Yotrisno Lang

Influence of Numerical Size Effect in Non-Linear Finite Element Analysis

Investigation of Different Configurations of Iterative-Incremental Method for Shear Failure Mode of Reinforced Concrete without Shear Reinforcement

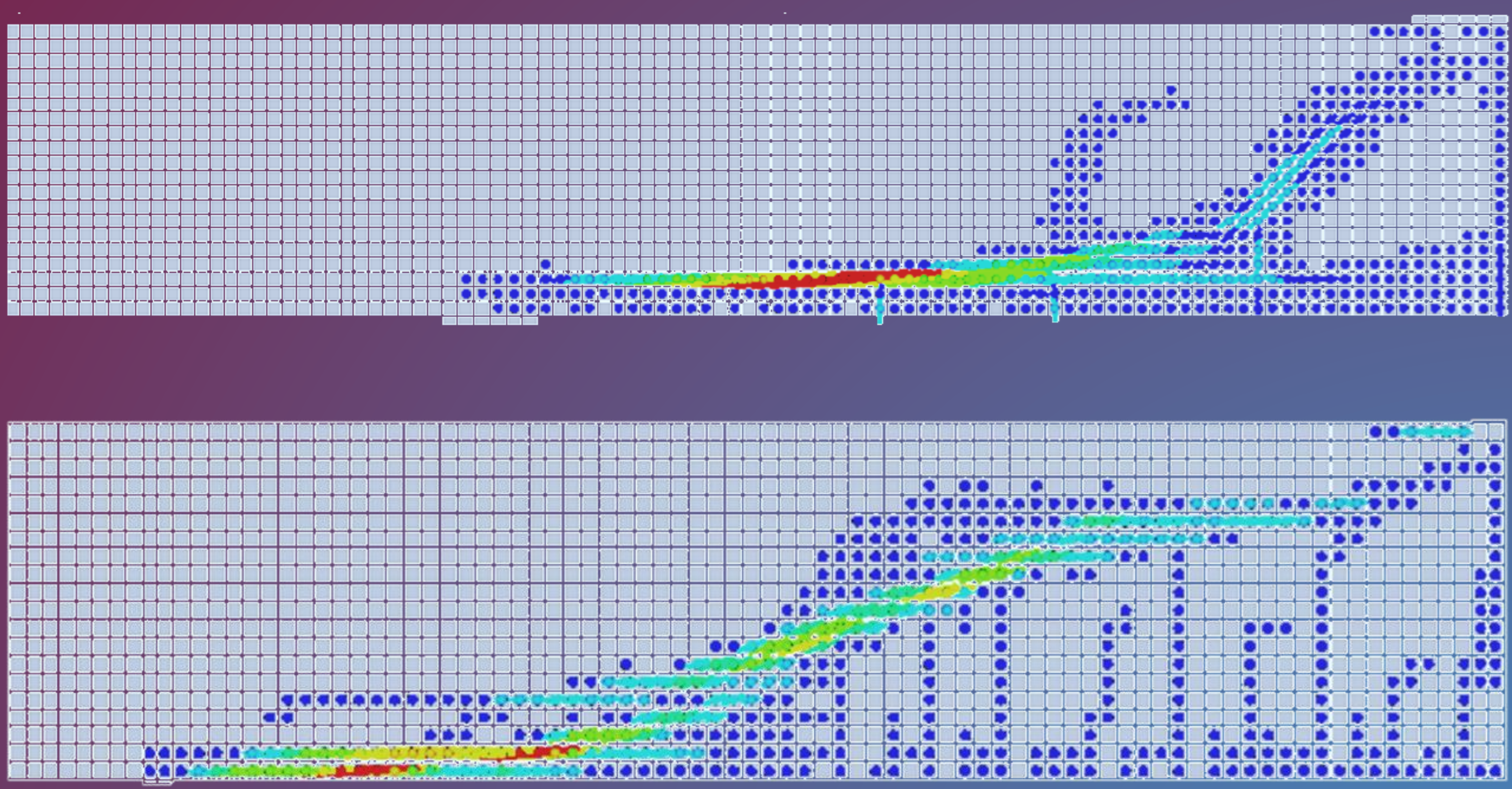

TU Delft

Influence of Numerical Size Effect in NLFEA

Investigation of Different Configurations of Iterative-Incremental Method for Shear Failure Mode of Reinforced Concrete without Shear Reinforcement

By

Yotrisno Lang

in partial fulfilment of the requirements for the degree of

Master of Science
in Civil Engineering and Geoscience

at the Delft University of Technology,
to be defended publicly on Wednesday, July 28th 2021 at 14:30.

Student number:	4903919	
Project duration:	November 1st 2020 – July 28th 2021	
Supervisor:	Yuguang Yang	TU Delft
Thesis committee:	Max Hendriks	TU Delft
	Joop den Uijl	TU Delft
	Cor Kasbergen	TU Delft

TU Delft

Preface

This thesis is the final requirement for completing my Master's degree in Civil Engineering at the Delft University of Technology. In the past 2 years, I have been challenged with a lot of things and learnt many valuable lessons through the process, especially during the process of completing this thesis. In the journey of completing this thesis, I was encouraged to learn and know more, explore and pay attention to a lot of details that I did not realise is important. I learnt that different actions will result in different responses, but what is more important is knowing and understanding why and how does something change. As there are a lot of problems that I probably have to deal with in the future, I should have a better understanding of these problems in order to be able to give an accurate and precise view of what is going on and how to solve problems at hand.

Finishing my thesis has been quite a challenge and I received a lot of help in the process. I want to thank my thesis committee, Yuguang Yang, Max Hendriks, Joop den Uijl and Cor Kasbergen for all the insights, remarks and supports that have been given to me from the thesis preparation to the finalization of the thesis report. I would like to give a special thanks to Joop den Uijl, as I spent a lot of my consultation with him and he was always very patient and understanding about myself and my confusion. I also want to thank my family, who always supporting me from the start to the end of my study journey at the Delft University of Technology. I will also not forget about my friends, Sam, Nut, Sun, Li and Siyuan, Ryohei, and Rhefa, who encourage and help me through difficult times during my study. This has been a very interesting journey that I am so grateful I got to experience and I will never forget.

In the end, I would like to apologize if there is/are some mistakes in the thesis. I hope that this thesis will be able to provide some new insights to help solve other problems, give benefits to the reader, and assist the advancement of knowledge in Civil Engineering, especially in the field of concrete structures.

Yotrisno Lang
Delft, July 2021

Contents

List of Tables

List of Figures

Notations

Latin

a	Beam Shear Span [mm]
a_d	Maximum Aggregate Size [mm]
a/d	Shear Slenderness
A	Beam Cross-Section Area [mm^2]
b	Beam Width [mm]
b_p	Loading and Support Plate Member Width [mm]
B_n	Dummy Normal Stiffness for Bond-Slip [N/mm^3]
B_t	Dummy Shear Stiffness for Bond-Slip [N/mm^3]
c	Stiffening Factor based on The Type of Reinforcement Bar
$CW_{t,u}$	The Ultimate Tensile Crack Width [mm] where the Remaining Fracture Energy of the Element is equal to 0; calculated based on the Guidelines for Nonlinear Finite Element Analysis of Concrete Structures (Hendriks & Roosen, 2020) and equal to 0.13 mm for specimen A123A1 and H123A
d	Beam Depth/Effective Height [mm]
E	Young's Modulus [MPa]
E_c	Concrete Young's Modulus [MPa]
E_{cm}	Concrete Mean Young's Modulus after 28 days [MPa]
E_{pl}	Loading and Support Plate Member Young's Modulus [MPa]
E_s	Reinforcement Young's Modulus [MPa]
E_{nn}	Young's Modulus of the n-surface in the n-direction [MPa]
E_{tt}	Young's Modulus of the t-surface in the t-direction [MPa]
E_{ss}	Young's Modulus of the s-surface in the s-direction [MPa]
E_{ns}	Young's Modulus of the n-surface in the s-direction [MPa]
E_{st}	Young's Modulus of the s-surface in the t-direction [MPa]
E_{nt}	Young's Modulus of the n-surface in the t-direction [MPa]
Ecw	Width of Crack Opening in the Principal Direction [mm]
EE	Relative Energy Variation per Step
$Eknn$	Crack Strain in The Perpendicular Direction to the Crack Opening
f_c	Concrete Compressive Strength [MPa]
f_{ck}	Concrete Characteristic Compressive Strength [MPa], if experimental data are available, the value of mean compressive strength is used instead
f_{ctm}	Concrete Mean Tensile Strength [MPa]
f_{st}	Intrinsic Shear Strength [MPa]
f_t	(uniaxial) Concrete Tensile Strength [MPa]
f_{tk}	Reinforcement Characteristic Ultimate Strength [MPa]
f_{tk} / f_{yk}	Ratio of Reinforcement Yield Strength to Ultimate Strength
$f_{t,red}$	Reduced Concrete Tensile Strength [MPa]
f_{yk}	Reinforcement Characteristic Yield Strength [MPa]
F_{cr}	Beam First Cracking Force [kN]
F_{err}	Force Tolerance/Norms
FE	Relative Out-Of-Balance Force per Step
G	(secant) Shear Modulus [MPa]

G_c	(uncracked) Concrete Shear Modulus [MPa]
G_{Ck}	Concrete Characteristic Compressive Fracture Energy [N/mm]
G_{err}	Energy Tolerance/Norms
G_F	Concrete Fracture Energy [N/mm]
G_{Fk}	Concrete Characteristic Tensile Fracture Energy [N/mm]
G_{ns}	Shear Modulus of the n-surface in the s-direction [MPa]
G_{st}	Shear Modulus of the s-surface in the t-direction [MPa]
$\overline{G_{st}}$	Intrinsic Shear Modulus due to cracks [MPa]
G_{nt}	Shear Modulus of the n-surface in the t-direction [MPa]
$Gknt$	Crack strain in The Parallel Direction to the Crack Opening
h	Beam Height [mm]
h_{ele}	Element Size [mm], equal to the square root of the area for non-square elements
h_p	Loading and Support Plate Member Height [mm]
I	Second Moment of Inertia of The Beam [mm^4]
$k_{dum,ax}$	Dummy Normal Stiffness for Plate-Beam Interface [N/mm^3]
$k_{dum,sh}$	Dummy Shear Stiffness for Plate-Beam Interface [N/mm^3]
$k_{FEM,nr}$	Linear Stiffness from Numerical Model Results without Reinforcement [kN/mm]
$k_{FEM,r}$	Linear Stiffness from Numerical Model Results with Bottom Reinforcement [kN/mm]
$k_{init.}$	Initial Beam Stiffness without The Contribution of The Reinforcement [kN/mm]
L	Beam Length [mm]
L_p	Loading and Support Plate Member Length [mm]
LB	Lower-Bound value of an Error Tolerance, Pre-defined value (G_{err} or F_{err}) of Error Tolerance in Numerical Model
M_{cr}	Beam First Cracking Moment [kNm]
n_{max}	Maximum Number of Iterations
n_p	Number of Load Steps
P	Applied Force on the Specimen/Numerical Model [kN]
P_{norm}	Normalised Peak Load; calculated by dividing the peak load of the numerical models to the experimental peak load of the specimen
P_u	Experimental Shear Strength, Maximum Load Capacity of the Beam [kN]
P_δ	Total Beam Deformation in The Experiment [mm]
s	Local Slip between Concrete and Reinforcement [mm]
s_c	Stirrup Spacing [mm]
s_0	(assumed) End-Point of Linear Bond-Stress Development [mm]
$s_{1,ref}$	Yield-Point of Pull-Out Failure [mm]; used as a reference to calculate $\tau_{bu,split}$
s_1, s_2, s_3	Critical Slip Points on Bond-Slip Model [mm]
ss	Length of Side Span [mm]
SW_c	Concrete Self-Weight [kN/m^3]
SW_s	Reinforcement Self-Weight [kN/m^3]
SW_{pl}	Loading and Support Plate Member Self-Weight [kN/m^3]
$w_{cr,c}$	Compression Crack Opening [mm]
$w_{cr,t}$	Tensile Crack Opening [mm]

Greek

α	Exponential Coefficient for Bond-Slip Model
β	Shear Modulus Reduction Factor, Shear Stiffness Reduction, Shear Retention Factor
$\beta_{\sigma,min}$	Minimum Reduction Factor of Concrete Compressive Strength due to Lateral Cracking/Reduction due to Cracks
γ	Mean Shear Strain
γ_{ns}	Strain of the n-surface in the s-direction
γ_{st}	Strain of the s-surface in the t-direction
γ_{nt}	Strain of the n-surface in the t-direction
$\Delta\gamma_{nt}$	Total Strain of the n-surface in the t-direction in iterative-incremental analysis
$\Delta\gamma_{12}$	Total Strain of the principal 1-surface in the principal 2-direction in iterative incremental analysis
$\Delta\gamma_{23}$	Total Strain of the principal 2-surface in the principal 3-direction in iterative incremental analysis
$\Delta\gamma_{31}$	Total Strain of the principal 3-surface in the principal 1-direction in iterative incremental analysis
δ	Deformation of The Beam in Numerical Model below The Loading Point [mm]
$\delta_{ela.}$	Elastic Deformation of The Beam [mm]
δ_{bend}	Bending Deformation of The Beam [mm]
δ_{sh}	Shear Deformation of The Beam [mm]
δ_{norm}	Normalised Displacement; calculated by dividing the displacement of the numerical models to the experimental total displacement of the specimen (22.5 mm for A123A1 and 15 mm for H123A)
ε	Total Strain
ε_c	Compression Strain
ε_p	Plastic Tensile Strain
ε_t	Tensile Strain Normal to The Crack Plane
ε_{t0}	Cracking Strain, equal to $\frac{f_t}{E_c}$
$\overline{\varepsilon_{tu}}$	Minimum Concrete Tensile Strain to start Crack Formation
ε_{uk}	Reinforcement Ultimate Tensile Strain based on f_{tk} / f_{yk} ratio
ε_{nn}	Strain of the n-surface in the n-direction
ε_{ss}	Strain of the s-surface in the s-direction
ε_{tt}	Strain of the t-surface in the t-direction
Δ	Simulated Shear Displacement at the Mid-Height of the Flexural Shear Crack Opening of the Specimen [mm]
$\Delta\varepsilon_{nn}$	Total Strain of the n-surface in the n-direction in iterative-incremental
$\Delta\varepsilon_{tt}$	Total Strain of the t-surface in the t-direction in iterative-incremental analysis
$\Delta\varepsilon_{11}$	Total Strain of the principal 1-surface in the principal 1-direction in iterative incremental analysis
$\Delta\varepsilon_{22}$	Total Strain of the principal 2-surface in the principal 2-direction in iterative incremental analysis
$\Delta\varepsilon_{33}$	Total Strain of the principal 3-surface in the principal 3-direction in iterative incremental analysis
μ	Young's Modulus Reduction Factor

ρ_l	Longitudinal Reinforcement Ratio [%]
σ	Stress [MPa]
σ_t	Mean Tensile Stress Normal to the Cracks [MPa]
σ_{nn}	Stress of the n-surface in the n-direction [MPa]
σ_{tt}	Stress of the t-surface in the t-direction (perpendicular to the n-direction) [MPa]
σ_{ss}	Stress of the s-surface in the s-direction [MPa]
σ_{ns}	Stress of the n-surface in the s-direction [MPa]
σ_{st}	Stress of the s-surface in the t-direction [MPa]
σ_{nt}	Stress of the n-surface in the t-direction [MPa]
$\Delta\sigma_{nn}$	Total Stress of the n-surface in the n-direction in iterative-incremental analysis [MPa]
$\Delta\sigma_{tt}$	Total Stress of the t-surface in the t-direction in iterative-incremental analysis [MPa]
$\Delta\sigma_{nt}$	Total Stress of the n-surface in the t-direction in iterative-incremental analysis [MPa]
$\Delta\sigma_{11}$	Total Stress of the principal 1-surface in the principal 1-direction in iterative incremental analysis [MPa]
$\Delta\sigma_{22}$	Total Stress of the principal 2-surface in the principal 2-direction in iterative incremental analysis [MPa]
$\Delta\sigma_{33}$	Total Stress of the principal 3-surface in the principal 3-direction in iterative incremental analysis [MPa]
$\Delta\sigma_{12}$	Total Stress of the principal 1-surface in the principal 2-direction in iterative incremental analysis [MPa]
$\Delta\sigma_{23}$	Total Stress of the principal 2-surface in the principal 3-direction in iterative incremental analysis [MPa]
$\Delta\sigma_{31}$	Total Stress of the principal 3-surface in the principal 1-direction in iterative incremental analysis [MPa]
τ	Mean Shear Stress [MPa]
τ_{bf}	Residual Bond-Stress [MPa]
$\tau_{b,max}$	Maximum Bond-Stress of Pull-Out Failure [MPa]
$\tau_{bu,split}$	Maximum Bond-Stress of Splitting Failure [MPa]
υ	Poisson Ratio
υ_c	Concrete (initial) Poisson Ratio
υ_s	Reinforcement Poisson Ratio
Ø	Diameter of Reinforcement [mm]
υ_{pl}	Loading and Support Plate Member Poisson Ratio

Abbreviations

FEM	Finite Element Method
n-dir	Normal Direction
NLFEA	Non-Linear Finite Element Analysis
NR	Newton-Raphson
s,t-dir	Tangential Direction
SLA	Sequentially Linear Analysis

Abstract

In concrete structures, shear failure is one of the failure mechanisms that should be estimated carefully due to its brittle nature. As the technology advances, the capacity of shear in concrete structures can be calculated with the analytical formulation in codes and standards and simulated with NLFEA. The shear capacity is affected by the size which is a phenomenon observed from experiments where the change in the structure size does not have a linear relation to the structural strength. This can be referred to as the experimental size effect. When estimating the shear capacity with NLFEA, this effect must be included in order to avoid over-estimation of capacity. However, another size effect can be found from the result of NLFEA. The change in structural size has an influence on the global response of concrete structures with different numerical configurations in a simulation with NLFEA. A numerical configuration consists of several numerical parameters. This effect is referred to as the numerical size effect. Therefore, it is necessary to incorporate the experimental size effect and reduce the influence of the numerical size effect in a numerical model in order to increase the accuracy and precision of the simulation with NLFEA.

The aim of this study is to investigate how the numerical size effect influences the NLFEA results, which will help understand how to improve the accuracy of the simulation. The investigation is done by studying numerical models with a variation on several numerical parameters, such as load increment, error tolerance, the maximum number of iterations and mesh size. The study is focused on identifying the influence of these numerical parameters for cases with different structural sizes and comparable shear slenderness. This is done by observing the global behaviour of the structure and comparing NLFEA results to their respective experimental results. Any difference in the simulated global response is analysed by observing the difference between the experimental and the simulated crack pattern and the convergence state of the respective step.

The study is done in three stages. The study is initiated by investigating how the flexural shear failure mode can be obtained with NLFEA. Two specimens with comparable shear slenderness (a/d), 3.70 and 3.91 for beam A123A1 and H123A respectively, are used as a reference for the simulation model. It was found that bad convergence was achieved at the later stage of the analysis and by not accepting non-converged steps, the results became dependent on the convergence state of the analysis where different peak loads were achieved in different numerical configurations for the same case study.

The study continues by identifying the correlation of numerical parameters with the results of NLFEA by creating simulation models with different iterative incremental solutions, load increment, error tolerance, and the maximum number of iterations. All load steps are accepted in this stage, regardless of their convergence state, and the rotating crack model is used in these numerical models. The NLFEA results are post-processed by setting up an upper limit in the error tolerance in order to minimize the variation of the peak load and attain a higher consistency of the results.

At the last stage, another study is performed to identify the correlation between mesh sizes with the results of NLFEA by simulating several models with different mesh sizes. All load steps are also accepted in this stage, regardless of their convergence state, and the rotating crack model is used in these numerical models The NLFEA results are also post-processed with the same criteria attained in the previous stage.

It is concluded that the results of NLFEA are dependent on the following numerical parameters, the load increment, error tolerance, and the maximum number of iterations, due to different initiations and propagation of dowel crack in the non-converged steps, which influences the convergence condition in the later stage of the NLFEA. The formation and rapid propagation of the dowel crack results in the excessive change in the principal strain direction and magnitude, which induces high relative energy variation and out-of-balance force. These numerical parameters indirectly contribute to the error found in each step in the analysis. An additional study is done by replacing the crack model with a fixed crack model with a damage-based shear retention model, but it was found that this did not solve the problem due to the excessive change in the shear retention factor on the elements that lead to premature failure of the beam.

The observation related to the numerical size effect reveals that the mesh size controls the propagation rate of the dowel crack. The use of a smaller mesh size will reduce the propagation rate of the dowel crack after its initiation due to a smaller increment of the crack width between each load step. As a result, the increment of the crack width becomes smaller as the mesh size decrease. This becomes more pronounced due to the effect of excessive change of the principal stress-strain direction and magnitude.

Full Newton-Raphson method has been proven to give the smallest variation of the peak load ratio (P_{norm}), ranging from $0.887-1.140$ for specimen A123A1 and $1.055-1.246$ for specimen H123A, compared to the other iterative-incremental

method with the use of load increment ratio (load increment/experimental peak load) within $0.03-0.006$ in combination with evaluation of acceptable analysis step with error tolerance, where the predefined error tolerance must be set to $G_{err}=0.0001$ and $F_{err}=0.01$, and non-converged steps can still be accepted if the relative energy variation and out-of-balance force of the corresponding step are below 0.03 and 0.58 respectively.

An additional criterion related to the shear displacement on the major flexural shear crack (Δ) should be added to the evaluation of the acceptable analysis step in order to prevent an excessive crack opening on the major flexural shear crack at the peak load. The analysis step can still be considered valid if the respective step satisfies the criterion of the error tolerance and the vertical crack opening on the major flexural crack on the respective step is below the ultimate tensile crack width $(CW_{t,u})$, which can be calculated from the Guidelines for Nonlinear Finite Element Analysis of Concrete Structures (Hendriks & Roosen, 2020). A mesh size ratio which larger than $h/15$ is required to have the correct simulated failure.

Keywords: NLFEA, Numerical Size Effect, Load Increment, Error Tolerance, Maximum Number of Iterations, Mesh Size, Convergence State, Dowel Crack Initiation, Dowel Crack Propagation

1 Introduction

Reinforced concrete structures are the most commonly used construction type. Having a better understanding of the non-linear behaviour of concrete will help improve the accuracy of the simulation of the non-linear FEM on the non-linear behaviour of the concrete structure. The non-linear FEM has been commonly applied in designing and assessing concrete structures. As this study typically requires a lot more time, it is often applied in important projects that cannot be analysed with hand calculations or the linear FEM. Such structures are typically characterised by larger dimensions, complex boundary conditions and vulnerability to brittle failure. The vulnerability to brittle failure is considered important because the failure happens suddenly and there is no sign of when it will happen.

Despite the fact that the non-linear FEM has been well developed over the past 3 decades, its application in such structures is still questionable as most of the non-linear FEM were developed in the period when full-scale experimental data were not widely available. They were calibrated with typical academic experiments, featured by simple boundary conditions and small specimen sizes. Recent experimental and theoretical studies have shown that upscaling such experimental observation to large scale structures is not always straightforward. The shear failure mode can be taken as an example, as it is one of the basic and common failure mechanisms in a structure. A typical effect called the size effect may significantly affect the accuracy of both theoretical prediction and numerical prediction.

The size effect is the influence of structural size on the structural strength where the change in the structure size does not have a linear relation to the structural strength. Size effect can be categorized into two types, experimental and numerical size effect. The experimental size effect is found from observation of the experimental results. The numerical size effect is found from observation of results of numerical simulation and is typically associated with a numerical parameter such as mesh size.

Several studies from An, Maekawa, & Okamura (1997), Cervenka V., Cervenka, Pukl, & Sajdlova (2016), Choi & Kwak (1990), Shayanfar, Kheyroddin, & Mirza (1997), and Tavio (2008) indicate that the shear failure has not been able to be simulated correctly due to the influence of numerical size effect. Different numerical configurations are used in these studies and different results are obtained in every study. This problem is also encountered in the shear test modelling contest in 2019 where teams from different universities and consultancies around Europe participated (Yang, Boer, & Uijl, Postdiction of the Flexural Shear Capacity of a Deep Beam, 2021). The modelling referred to two reinforced concrete beams without stirrups, with a large depth of 1200 mm and The Guidelines for Nonlinear Finite Element Analysis of Concrete Structures (Hendriks & Roosen, 2020) is used as a modelling reference. It was found that most participants were not able to obtain good simulation results that are compatible with the experimental results. Therefore, further investigations are needed to give insight into which numerical configuration should be chosen. The chosen configuration of the NLFEA directly affects the simulation and could cause underestimation or overestimation of the structural capacity, which makes the method of modelling in the NLFEA is crucial to be defined and standardized.

There are a lot of things to considered and simplified from the physical conditions of the structure when building the numerical models, such as non-linearity applied on the structure, element types, crack model, solution procedure, convergence criteria, and type of analysis. The purpose of this research is to study the influence of numerical size effect on the numerical results when simulating shear failure by investigating the following numerical parameters: load increment, error tolerance, the maximum number of iterations and mesh size.

1.1. Aim of The Study

The size effect or can be referred to as the experimental size effect, is defined as a phenomenon observed from experiments where the change in the structural size does not have a linear relation to the structural strength. Shear strength is the resistance of concrete structures under shear force. When resisting this force, a certain mode is formed when the structure is unable to resist it anymore. This is known as a failure mode. This thesis is focused on one of the shear failure modes, the flexural shear failure mode. Several papers from Kani (1967), Bazant, Ozbolt, & Eligehausen (Fracture Size Effect: Review of Evidence for Concrete Structures, 1994), Collins & Kuchma (1999), Vecchio & Shim (2004), Bazant & Yu (Universal Size Effect Law and Effect of Crack Depth on Quasi-Brittle Structure Strength, 2009), Syroka-Korol & Tejchman (2014), and Yang (2014), have indicated that the experimental size effect on concrete structure related to shear strength must be considered. These papers also give suggestions on how to account for size effect experimentally. However, no paper has been able to give definitive instructions and suggestions on how to account for the experimental size effect on simulation with NLFEA.

Furthermore, several studies from An, Maekawa, & Okamura (1997), Bazant & Oh (Crack Band Theory for Fracture of Concrete, 1983), Cervenka V., Cervenka, Pukl, & Sajdlova (2016), Choi & Kwak (1990), Shayanfar, Kheyroddin, & Mirza (1997), and Tavio (2008) indicated that another form of size effect is found on the simulation with NLFEA. This effect is referred to as the numerical size effect. Therefore, the numerical size effect can be defined as changes in the global response of concrete structures due to the use of different numerical configurations in a simulation with NLFEA. A numerical configuration consists of several numerical parameters. In the literature, the numerical size effect is usually correlated to the change in the mesh size in the numerical configuration with NLFEA.

The main objective of this thesis is to improve the estimation of reinforced concrete shear strength without shear reinforcement on NLFEA by studying the influence of predefined numerical parameters, such as load increment, error tolerance, the maximum number of iterations per step, and element size, to give insight on how to reduce numerical size effect. The experimental size effect will be included in the numerical model by studying literature and summarising how to include this effect. The study will be focused on the 2D FEM with the smeared cracking model. The type of structure that will be simulated for the investigation in this thesis is a 3-point loaded simply supported beam. The study is done by simulating 2 specimens with different sizes in terms of shear span (a) and beam depth (d) but has comparable shear slenderness (a/d). Two types of smeared cracking models will be used in this study, fixed and rotating crack models. The rotating crack model is used in the reference model and the fixed crack model will be used as a comparison to see the difference in their performance. All components, such as material properties and constitutive models, related to the simulation of the structure are considered and calculated in accordance with the Guidelines for Nonlinear Finite Element Analysis of Concrete Structures (Hendriks & Roosen, 2020).

1.2. Research Questions

In order to reach the aim of this study, the study must be able to answer the research question of this thesis. The research question of this thesis is:

“How do different numerical parameters influence the result in the NLFEA?”

Several sub-questions are formulated in order to have a clear line of thought. These questions will be answered sequentially, as these questions represent the overall process of answering the research question and achieving the aim of this study.

1. *What are the main parameters in simulating shear failure in NLFEA?*

   This question can be answered by first identifying the important aspects of NLFEA and the possible failure mode in reinforced concrete without shear reinforcement. Afterwards, a literature review must be done in order to have an insight related to the key features of shear transfer and how does the NLFEA model these features.

2. *What information is available regarding the key correlations between the size effect and NLFEA?*

   In this question, the term “size effect” is referred to both experimental and numerical size effect, as both components must be understood well in order to have an appropriate numerical model that can be analysed. This question can be answered by first defining the definition of the term “size effect” in the available literature, as several works of literature use the same terms for different types of size effect. Afterwards, another literature review is done to see which parameters are the keys for including the experimental size effect and imposing numerical size effect to the numerical model. The literature review also includes a list of possible measures on calibrating the experimental size effect and how to reduce the effect of numerical size effect. Furthermore, the literature review should also include the remaining problems that have not been solved. In the end, the literature review will have the numerical configuration that will be used as a reference for further investigation related to the numerical size effect which has accounted for the experimental size effect.

3. *How do predefined numerical parameters influence the numerical size effect in NLFEA?*

   The first step to answer this question is identifying the problem related to the numerical size effect in the current numerical configuration. A certain numerical configuration is used to model two experimental results with comparable shear span to beam depth ratio but has significant differences in shear span and beam depth. Afterwards, several parameters are varied in accordance with the identified problems to solve these problems. In the end, the problems found in the literature will be analysed by studying several variations related to this problem.

At the end of this report, the conclusion will also give some recommendations on how to minimize the numerical size effect and what other studies should be performed to help improve these recommendations.

1.3. Research Methodologies

The study will be done in a quantitative manner which will focus on the in-depth knowledge of size effect on finite element analysis for concrete structures with flexural shear failure. The study starts with an extensive literature review for the first and second research sub-questions. All data needed for answering the first and second research questions are retrieved from literature studies of scientific papers and books with content analysis and search methods. The literature study is done in order to give a clear view of the connection of finite element analysis with the shear failure mechanism and some insight regarding how to account for experimental size effect and what has been found related to the numerical size effect.

The third main research question will be answered mainly based on observation and measurement results. This will be done by modelling two case studies with NLFEA with different numerical configurations to give insight into how the numerical size effect influences the results of NLFEA. The chosen structural object to study in this thesis is a simply supported beam with a 3-point bending test, which is the simplest case in the civil engineering field for investigating shear failure and has a lot of available experimental test data. The case studies are based on two experimental results with comparable shear span to beam depth ratio but have significant differences in shear span and beam depth. The observations are going to be done for convergence norms, crack pattern/damage evolution on structure, and failure mode. Results of NLFEA will be compared to its respective experimental data and post-processed in order to minimize the numerical size effect. It is expected that the numerical results could give a clear picture of how the shear failure progress. The measurements are going to be done for the error tolerance, reaction force, displacement of the structure, and crack width on the failure crack. The influence of the numerical size effect can be studied by comparing the results of NLFEA. The measurement will help understand what factors are affected by the numerical size effect and what can be done to the numerical model in order to increase the accuracy of the estimation of shear resistance.

All analysis will be done based on the result of numerical simulation of finite element analysis. Any software package can be used for this research. The non-linear FEM software package DIANA 10.4 is used for this thesis. However, the conclusion of this study can be extended to any other non-linear FEM making use of the smeared crack approach.

1.4. Thesis Outline

This thesis is divided into 7 chapters with the first chapter explaining the research background while the other chapters explaining the steps taken to answer the research questions and reach the research objective.

Chapter 2 The Correlation of NLFEA to Shear Failure
The second chapter gives several points of view on how NLFEA can be used to simulate shear failure and what are the key parameters.

Chapter 3 Literature Review of Size Effect Phenomenon on Finite Element Analysis
The third chapter help gives a summary of what has been done to solve the problem of size effect on shear strength of concrete structures and identify the starting point of the study regarding the size effect phenomenon.

Chapter 4 Identification of Problem Related to Convergence
In the fourth chapter, the numerical models are modelled based on two specimens. Several types of verification are done in order to ensure the validity of the result of the NLFEA. However, several problems are found related to the convergence and the study of simultaneous satisfaction of convergence and inclusion of top reinforcement are done in order to determine whether it is necessary to include those components in the NLFEA.

Chapter 5 Sensitivity Analysis of Convergence Parameters
The fifth chapter gives insight related to the influence of three numerical parameters, load increment, error tolerance, and the maximum number of iterations, and how do these parameters influence the peak load distribution and global behaviour. Furthermore, the results of the finite element analysis are post-processed with an upper value of error tolerance in order to minimize the influence of these parameters and obtain a reliable numerical configuration that can be used for further evaluation related to the mesh size.

Chapter 6 Sensitivity Analysis of Mesh Size
The sixth chapter gives insight into the influence of the mesh size and how it affects the peak load and global behaviour. Furthermore, the results of the finite element analysis are post-processed with an upper value of error tolerance and limitation on the vertical opening at the mid-height of the major flexural shear crack in order to minimize the influence of mesh size and obtain a realistic simulated crack opening at the peak load.

Chapter 7 Conclusion and Recommendation
The last chapter shows the conclusion of the research and what should be done next related to the study of numerical size effect on concrete structures.

2 The Correlation of Finite Element Analysis to Shear Failure

Simulation of shear failure in NLFEA required a deep understanding of the concept of NLFEA. In this chapter, the concept of NLFEA will be explained briefly in subchapter 2.1. Afterwards, the overview of all failure modes of the beam will be given in subchapter 2.2, which will be used to investigate the size effect in chapters 5 and 6. In order to fully understand each parameter on the NLFEA, the targeted failure modes (flexural shear failure mode) mechanisms are described in detail in subchapter 2.3 based on data available in the literature. These mechanisms are going to be correlated with each parameter available on NLFEA in subchapter 2.4.

2.1. Non-Linear Finite Element Analysis

Finite Element Analysis is a tool developed by engineers, in collaboration with mathematicians, to generate a numerical solution to a specific problem. The numerical solution is an approximation based on a set of algebraic equations. There are two types of numerical solutions of finite element analysis, linear and non-linear response. The linear response does not include the effect of plasticity and large deflection which could affect the overall response of the model. In other words, the response is directly proportional to the applied load on the model. On the other hand, a non-linear response could produce a more realistic response that incorporated the effect of plasticity and large deflection in the model. This response could be interpreted as a representation of real structure behaviour, as long as the correct assumption and simplification are used to construct the model. (Cook, Finite Element Modeling for Stress Analysis, 1995)

The NLFEA can be done by creating a model of structures with a set of non-linear equations and use a suitable solution procedure to approximate the model response. NLFEA can be used to do several types of analysis in the structural application, such as strength analysis, stability analysis, construction stage analysis, reserve strength analysis, and progressive failure analysis. These analyses are used to assess a structure performance, for example, investigate causes of structural failure, safety and serviceability assessment, structure optimization, simulate material processing and manufacturing, and assist the researcher to create a simple method of analysis and design of structures by understanding the basic behaviour of the structure and validate material models with experimental results. These performances can be assessed by either doing only one or several types of analysis based on the level of assessment needed to be done. (Cook, Malkus, Plesha, & Witt, 2002)

The model response is often represented in the load-deflection diagram. This diagram shows the overall behaviour of the structure according to the numerical solution of NLFEA, which is often referred to as the equilibrium path. The equilibrium path is created based on the reference state where it is assumed that the model is not subjected to stress dan deformation yet. In NLFEA, the equilibrium path may include several critical points, such as limit points (L), bifurcation points (B), turning points (T), and failure points (F). The limit points can be identified by looking for a point in the equilibrium path which has a horizontal tangent line. The bifurcation points often describe as points where several equilibrium paths cross each other. The turning points can be found by looking for a point in the equilibrium path which has a vertical tangent. The failure points can be seen where the equilibrium path suddenly stops due to the failure of the model.

NLFEA usually consists of four important components, the physical problem, mechanical model, finite element model, and solution, illustrated in Figure 2.1. The physical problem is referred to as the actual problem that needed to be solved or a case study of a certain phenomenon. The physical problem is idealized with several assumptions to create a mechanical model. The mechanical model usually consists of the structure geometry, material law, loading, boundary conditions, and source of nonlinearity. All components of the mechanical model must be created with a sound engineering judgement based on the physical problem and the purpose of the analysis.

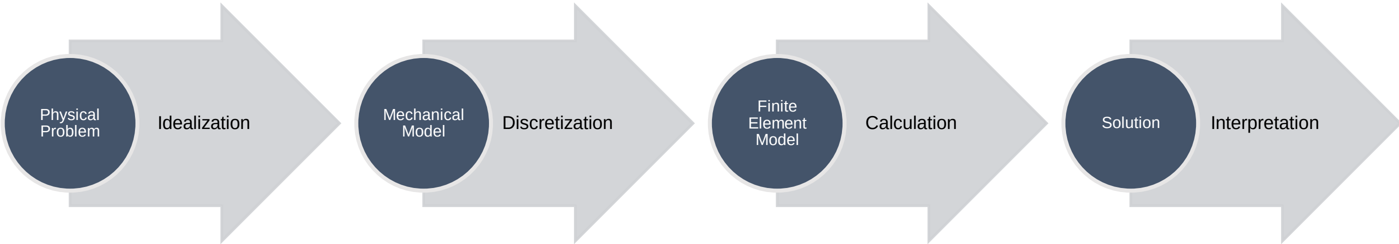

Figure 2.1 General Representation of NLFEA

Source: Lecture Slides “CIE5148 Computational Modelling of Structures”

In NLFEA, the way of applying load on the structure could affect the solution of NLFEA due to the equilibrium path of the structure. Applying load as a prescribed force, which is often called force controlled, would cause the equilibrium path to stop at the first limit point or first bifurcation point. On the other hand, applying load as a prescribed displacement, which is considered displacement controlled, would usually produce the complete equilibrium path until the failure points. However, a complete equilibrium path cannot be achieved even with displacement controlled in the case where the equilibrium path contains one or several turning points. This case could be solved by applying the arc-length method.

The source of nonlinearity is one of the key factors which greatly affect the results in NLFEA. There are several sources of nonlinearity such as material nonlinearity, geometric nonlinearity, and contact nonlinearity. The material nonlinearity can be described as the behaviour of the material in its current state which can be affected by its loading history and time-dependent factor. The material nonlinearity is expressed as the constitutive relationship between stress and strain in NLFEA. The geometric nonlinearity is described as the effect of large deformation on the structure where the small displacement assumption is not valid anymore. The large deformation could affect the loading direction and the internal action of the structure in resisting loads. The geometric nonlinearity is included in the NLFEA by finding the equilibrium on the structure based on its deformed shape. The contact nonlinearity can be described as a change in load distribution when two or more parts of a structure come in contact. This event is usually considered when there are gaps, contacts, and the sliding interface between two or more parts of a structure.

The mechanical model is discretised into a finite element model by choosing the suitable element type, mesh density, and solution parameters. The element types can be chosen based on the geometry, boundary conditions, and applied load in the mechanical model in combination with available elements on the software used. Based on Borst & Nauta (1985) works, the use of reduced integration should be avoided in concrete structures, as it could cause huge deviation on the damage progression and produce divergence on the results. Full gauss integration is recommended to be used in combination with 8-noded elements with 3x3 integration points for concrete structures, in order to avoid un-realistic zero-energy modes to occur which could cause divergence. This statement is confirmed by Balakrishnan & Murray (1986) where they stated that 2x2 integration points can only be used in the case where the elements are reinforced in two orthogonal directions, while 3x3 integration points can be used for other cases in order to prevent spurious zero-energy modes. The mesh density can be chosen based on the degree of element discretization is required, availability of time, and the acceptance level of the results. The mesh density is usually chosen based on trial and error in combination with checks on the sensitivity of the results.

The solution parameters are determined based on the iterative incremental solution method. Several parameters such as solution procedure, convergence method, step size, and the maximum number of iterations per step are chosen based on the available options on the software in combination with available recommendations made by the government. In the Netherland, this recommendation is referred to as Guidelines for Nonlinear Finite Element Analysis of Concrete Structures (Hendriks & Roosen, 2020). The most common solution procedures used for NLFEA are Full Newton-Raphson, Modified Newton-Raphson, and Newton’s Method. The details of these methods can be found on the analysis reference of corresponding software used. The convergence method is specified based on the convergence criteria and convergence tolerance. The convergence criteria can be chosen between force-based, displacement-based, and energy-based. The convergence criteria and level of convergence tolerance should be determined based on the level of accuracy needed for the results. The convergence criteria are evaluated based on the convergence state of NLFEA. The convergence state is defined as the level of relative energy variation and out-of-balance force on each step in the NLFEA. In order to reach convergence in the NLFEA, the convergence state of each step must be below the prescribed tolerance. The evaluation of the convergence criteria is done by defining the norms ratio. All norms are calculated as a part of the iteration process in the incremental procedure. The iterative-incremental procedure in the NLFEA is done based on Figure 2.2.

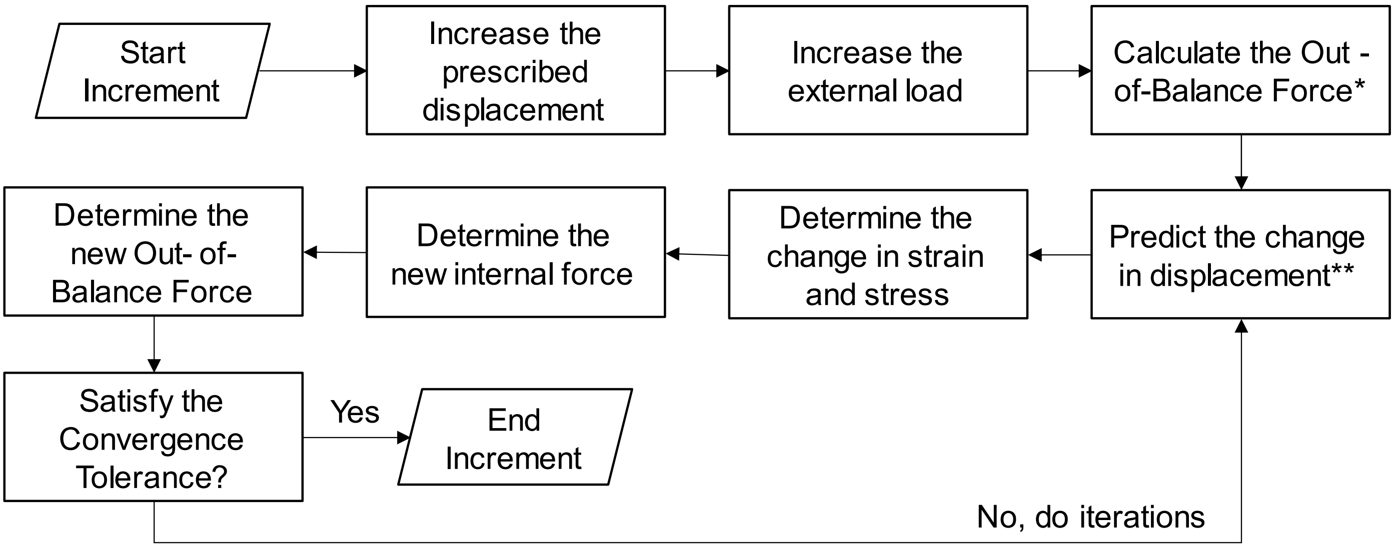

Figure 2.2 General Iterative-Incremental Procedure in Non-Linear Finite Element Analysis

Source: (DIANA FEA, 2020)

* The out-of-balance force is calculated based on the subtraction between the external load and the previous step internal force.
** The prediction of change in the displacement is done by multiplying the transpose stiffness matrix to the out-of-balance force vector.

According to (DIANA FEA, 2020), the force norm ratio is the ratio between the out-of-balance force of the current iteration (g_1) and the internal force after the first prediction (g_0). The displacement norm ratio is the ratio between the displacement change of the current iteration (δu_1) and the first prediction (Δu_0). The energy norm ratio is the ratio between the energy variation of the current iteration (δE_1) and after the first prediction (ΔE_0). The energy variation is calculated based on the internal forces (g_0 and g_1) and relative displacements (Δu_0 and δu_1). The illustration of these norms can be seen in Figure 2.3. The force and energy norm ratios are going to be referred to as relative out-of-balance force and relative energy variation in this document.

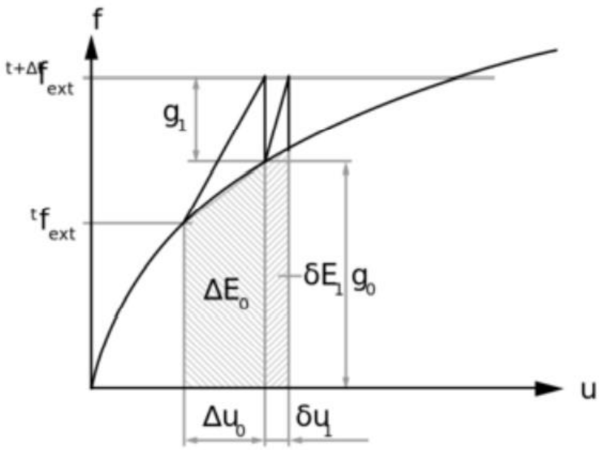

Figure 2.3 Norms Items

Source: (DIANA FEA, 2020)

The use of a single convergence criterion should be avoided in order to avoid high computational time (Cook, Malkus, Plesha, & Witt, 2002). The determination of step size and the maximum number of iterations per step must be done with consideration of the available time of the project and through trial and error to find the optimal value.

Another method that could be used to obtain the numerical solution is the SLA method (Slobbe, Hendriks, & Rots, 2013). SLA is used to simulate brittle failure on structure, specifically on concrete structure. SLA replaces the standard iterative-incremental solution procedure with a series of scaled linear analyses. The idea used for developing SLA is the numerical solutions are derived based on damage-controlled analysis. The non-linearity is captured by using a series of scaled linear elastic analyses until critical events on the critical integration points on the model are achieved. In every series of analyses, the critical event is traced to define the phenomenon of stiffness and strength reduction on the structure and applied it to its respective critical integration point. The critical events are predefined and related to the crack initiation and propagation. The SLA avoids the bifurcation phenomenon, which could happen in the standard iterative-incremental solution procedure. Furthermore, the use of reduced integration schemes does not cause any deviation due to the adopted positive secant stiffness on the SLA method. Furthermore, SLA is recommended by Yang (2014) to be used for simulating the shear failure of the reinforced concrete beam without shear reinforcement. On the other hand, there are several drawbacks to this method, such as the limitation on the unloading/reloading scheme to secant scheme only and a relatively long time for computation.

The finite element model is analysed and calculated on the software and a numerical solution will be generated. While using the iterative incremental solution method, the convergence of the solution could pose a problem in this stage, as it could be a very slow convergence or failed to reach convergence on a certain load step. These problems could be caused by high local stress, the failure of the structure, sudden change in stiffness, and various other reasons. The high local stress problem, which causes a lot of iteration to find convergence, can be resolved by using the high yield stress element on the region near the concentrated loads and point supports. All other reasons can be investigated by plotting the equilibrium path of the model and scanning through the log file of the numerical analysis. Any dramatic increase or decrease from one load step to another would usually lead to a problem in convergence. All important aspects of NLFEA are summarised in Figure 2.4. These give an illustration of how complex the process of determining the numerical configuration. Further study from available literature is done in chapter 3 and the numerical configuration that is used for the thesis is given in subchapter 4.1, 5.1, and 6.1.

De Putter (2020) indicates that convergence problem happens in a certain stage when analysing reinforced concrete beam without shear reinforcement, such as:

- crack localization – resulted in a small dip in the force-displacement diagram and cause convergence problem, which would end after crack open in a stable manner;
- crack inclination starts;
- reinforcement yield and concrete crush starts;
- failure of the beam.

The convergence problem could be solved by increasing the maximum number of iterations per step, assigning a smaller step size, re-evaluate the choice of the solution procedure, re-evaluate the choice of convergence criteria, or decrease convergence tolerance. However, these solutions will increase the amount of computational time and further study needs to be done in order to determine whether these solutions are applicable in every case, especially the simulation of the reinforced concrete beam without shear reinforcement. Furthermore, the numerical solution will also need to be evaluated by doing verification on the finite element model and validation of the mechanical model. In the end, the numerical solution would be interpreted based on the project interest or research purpose.

Figure 2.4 Mind Map of Important Aspects of NLFEA

2.2. Types of Failure in Reinforced Concrete Beam

There are two major types of failure in the reinforced concrete beam without shear reinforcement that could be identified, which are bending failure and shear failure, as indicated in Figure 2.5. In this thesis, the focus will be put on the shear failure with flexural shear failure mode, as it is more brittle and several sources of literature, such as Choi & Kwak (1990), Shayanfar, Kheyroddin, & Mirza (1997), Khalfallah, Charif, & Naimi (2004), Cervenka V., Cervenka, Pukl, & Sajdlova (2016) indicate that this failure has not been able to be simulated properly.

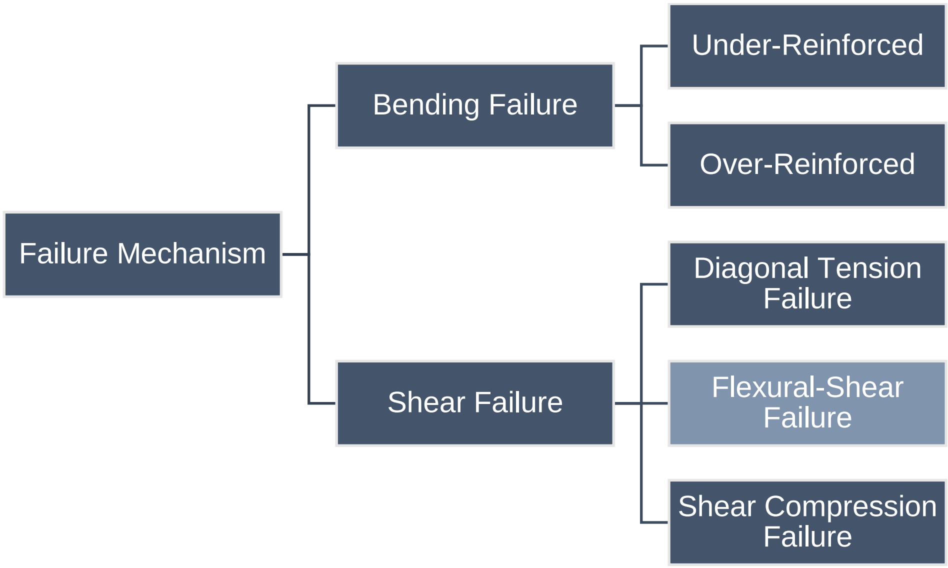

Figure 2.5 General Representation of Types of Failure

2.2.1 Bending Failure

Bending failure is derived from the inability of the cross-section to resist a certain level of bending moment. This will result in the formation of flexural cracks on the tension part of the beam. Without longitudinal reinforcement, the crack will propagate throughout the cross-section and cause failure. In the case of the reinforced concrete beam, the cracks will be stabilized, and the reinforcement starts to yield in one or some cracks. The continuation of yielding progression would produce large deformation on the beam while sustaining the load and will fail when the compression zone crushes (over-reinforced) or the reinforcement fail in tension (under-reinforced). (De Putter, 2020)

2.2.2 Shear Failure

Shear failure is derived from the inability of the cross-section to resist a combination of bending moment and shear force. Balakrishnan & Murray (1986) stated that shear failure happens due to the reduction of shear modulus above and below the neutral axis where shear strain can be produced on the same order of magnitude as normal strain. This statement is in line with Walraven (1980) where he stated that before failure, the propagation of crack opening would increase slower compared to shear deformation in the case of plain concrete. This indicates that shear failure accelerates the progression of shear deformation in the case of reinforced concrete without shear reinforcement.

There are three modes of shear failure, diagonal tension failure mode, flexural shear failure mode, and shear compression failure mode. The diagonal tension failure mode is described based on the classic beam theory where maximum shear stress is located in the neutral axis of the beam in the linear elastic stage. At the neutral axis, the principal stress is rotated in the diagonal direction, which causes the formation of diagonal cracks after reaching the concrete tensile strength. This phenomenon is not greatly influenced by bending moment and could only occur in a beam with limited flexural cracking where there is a drastic change in the width of the cross-section, such as prestressed hollow core slabs and T-beams.

The flexural shear failure mode is described based on the inclined flexural/flexural shear crack. The inclination of the flexural crack is caused by the increase of shear force, which resulted in the rotation of the principal stress direction. This crack reduces the resistance of the beam and caused a brittle failure. According to Yang (2014), the reduction is caused by the formation of secondary horizontal crack on the top which resulted in the loss of shear retention in the crack surface. Afterwards, the horizontal crack propagates quickly due to its unstable condition and causes failure of the beam. Flexural shear failure can also be interpreted as a significant reduction of shear modulus below the neutral axis, according to Balakrishnan & Murray (1986). On the other hand, it was mentioned by Sato, Tadokoro, & Ueda (2004) that the loss of shear retention is the result of increasing width of the shear crack, which is caused by the splitting tensile crack along the longitudinal reinforcement bars. The splitting crack caused the inability to transfer shear stress on the crack, which resulted in rapid propagation of shear crack on the beam.

Shear compression failure mode is described as a continuation of the flexural shear crack phenomenon, where the loss of shear retention in the crack surface does not cause immediate failure. This could happen due to the formation of arch structure within the beam, in which the arch takes over the load-bearing mechanism of the beam. If the arch can take over and achieved stability on the global level, then the beam could be imposed to a higher magnitude of loading. The imposed load can be increased until the concrete strut crush and failure happens due to the splitting crack of the concrete strut. On the other hand, if the arch cannot achieve stability, then it would fail almost immediately as the flexural shear failure mode takes place. Balakrishnan & Murray (1986) characterized shear compression failure as a condition where a significant reduction of shear modulus happens above the neutral axis when approaching failure. According to Vecchio & Shim (2004), the beam's behaviour with shear compression failure is greatly influenced by the crushing of the concrete located beneath and adjacent to the loading plate based on the experimental observation. One of the characteristics which differ from shear compression failure to flexural shear failure is that there is no splitting crack along with the tension reinforcement.

Based on these definitions, the flexural shear failure mode can be regarded as the lower bound and the shear compression failure mode as the upper bound of the load-carrying capacity in the case of shear failure. The diagonal tension failure is completely disregarded due to its non-relevance to the studied object on the thesis.

2.3. Shear Transfer Mechanism in Concrete Structures

According to Deng, Yi, & Tang (2017), there are five recognized shear transfer mechanisms in concrete structures, as illustrated in Figure 2.6: shear stress in the uncracked compression zone, interfacial shear transfer by aggregate interlock, dowel action of the longitudinal reinforcement, arch action, and residual tensile stress. Residual tensile stress can be transmitted directly across cracks when the crack width is sufficiently small. In a specific case such as reinforced concrete beam without shear reinforcement, Huber & Kollegger (2014) indicated that the behaviour of the beam is governed by uncracked compression zone, aggregate interlock, and dowel action of the longitudinal reinforcement when subjected to shear.

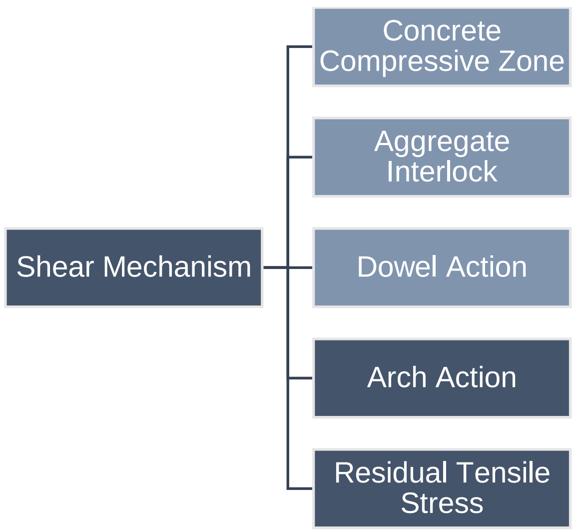

Figure 2.6 General Representation of Shear Mechanism

2.3.1 Aggregate Interlock

Yang (2014) defined aggregate interlock as a relationship of shear stress and compressive normal stress to the normal and tangential displacement along the crack respectively. The significance of aggregate interlock is still questionable as there are several different opinions regarding this. According to An, Maekawa, & Okamura (1997), aggregate interlocking contributes a non-significant resistance for beams larger than 1 m. This opinion is elaborated more by Sato, Tadokoro, & Ueda (2004), where it is clarified that the shear resistance from aggregate interlock is negligibly small for reinforced concrete beams without shear reinforcement $(a/d = 2.69)$, due to its inability to generate aggregate interlock mechanism after the occurrence of the flexural shear crack. However, the aggregate interlock mechanism can be expected to happen on deep reinforced concrete beams without shear reinforcement $(a/d = 1.76)$.

However, the experiment performed by Deng, Yi, & Tang (2017) produced different results, where aggregate interlock is said to contribute significant shear resistance for reinforced concrete beams ($a/d = 2.2$ and $a/d = 3$), especially for beams without shear reinforcement. In this experiment, it was also mentioned that even though the maximum aggregate size does not affect the concrete tensile strength significantly, but it is proven to be able to improve the shear resistance of a reinforced concrete beam without shear reinforcement. Yang (2014) also formulates the shear resistance based on the aggregate interlock capacity, which resulted in high accuracy on the prediction of shear resistance over a large range of beam size.

The increase of maximum aggregate size up to 40 mm leads to higher shear resistance due to the improvement of interlocking action on the crack surface. The maximum aggregate size effect on shear resistance can be incorporated into numerical simulation by modifying the fracture energy according to the aggregate size $G_F = a_d f_c^{0.7}$. Further increase in the maximum aggregate size would reduce the shear resistance.

2.3.2 Dowel Action

Walraven (1980) defined dowel action as the capacity of reinforcement to transfer force perpendicular to the bar axis, which would make this effect depends on the construction circumstances. Yang (2014) gives a more specific definition for dowel action in reinforced concrete beam, which is a differential tangential displacement in the concrete crack plane, resulted from the interaction between reinforcement and concrete.

The phenomenon of dowel action can be described as following: when a bar embedded in concrete is subjected to load perpendicular to its axis, the load would induce tensile stress on the concrete below the bar along the load axis and perpendicular to the load axis. The load and the dowel force are illustrated in Figure 2.7.

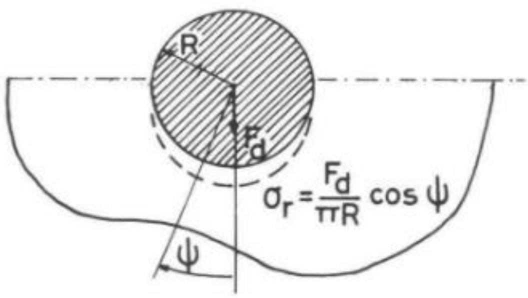

Figure 2.7 Illustration of Vertical Load on Steel Bar
Source: (Walraven, 1980)

*ψ is the force axis angle.

The load is proportionally divided into 34.4% on the load axis and 63.7% perpendicular to the load axis. When the concrete tensile strength is reached on the load axis, a crack will form and cause a change in the load-carrying system. When this occurs, there is one out of two phenomena that could happen (illustrated in Figure 2.8):

- Stress redistribution occurs on the concrete below the bar and cracks propagation continues slowly as the load increase, which in turns gradually decrease the stiffness until it reached the ultimate load. This phenomenon is indicated as the crushing failure mode of the dowel.
- No stress redistribution due to insufficient strength and area of the concrete below the bar and crack progression continue aggressively, which in turn decrease the load capacity of the structure. This phenomenon is indicated as the splitting failure mode of the dowel.

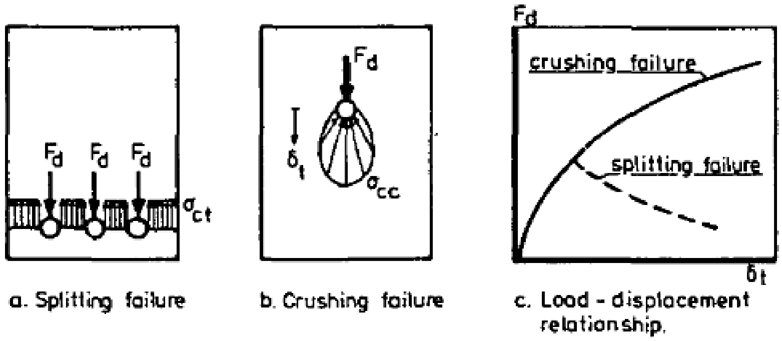

Figure 2.8 Failure Modes of Dowel

Source: (Pruijssers, 1988)

Based on the previous description, it can be said that dowel action can be estimated based on the stress around the bar, dowel force and the effect of tensile crack formation. In beams without shear reinforcement, the stress redistribution is usually not possible due to the small concrete area below the bars, which is insufficient to create an equilibrium with the dowel force and therefore cause the splitting failure to occur.

Sarkhosh, Uijl, Braam, & Walraven (2010) indicated that the contribution of dowel action can be significant if other mechanism contributions are relatively small, for example, the case of beams with a small amount of web reinforcement or post-peak loading stage. Yang (2014) stated that the effect of dowel action is more dominant and can be observed by observing shallow beam in size effect tests on the smallest specimens which reported by Kani (1967), Bažant & Kazemi (1991), and Collins & Kuchma (1999).

2.3.3 Contribution of Individual Shear Mechanism to Total Shear Resistance

The contribution of each shear transfer mechanism can be represented based on the response curve of the reinforced concrete subjected to shear. According to Tran (2020), the response can be explained in three stages as indicated in Figure 2.9. The first stage is the uncracked state, where no aggregate interlock, residual tensile stress and dowel action take place and the stress is distributed parabolically.

The second stage is the crack state where shear cracks have not reached the neutral axis. The stress is distributed parabolically on the uncracked zone with maximum value on the neutral axis and the stress decrease on the crack zone with respect to the crack width. In this stage, residual tensile stress, aggregate interlock and a minor dowel action exist. Yang (2014) stated that as the crack width increase, the dowel action contribution will reach a plateau while aggregate interlock contribution will decrease. These contributions are dependent on the shape of the crack, which correlated with the a/d ratio.

The third stage is the critical shear crack that develops in the compression zone where arch action, residual tensile stresses, aggregate interlock, and dowel action exists and the stress is distributed parabolically only on the uncracked zone. Point B and C, which is indicated in Figure 2.9, are often overlap for normal reinforced concrete without shear reinforcement and without prestressing.

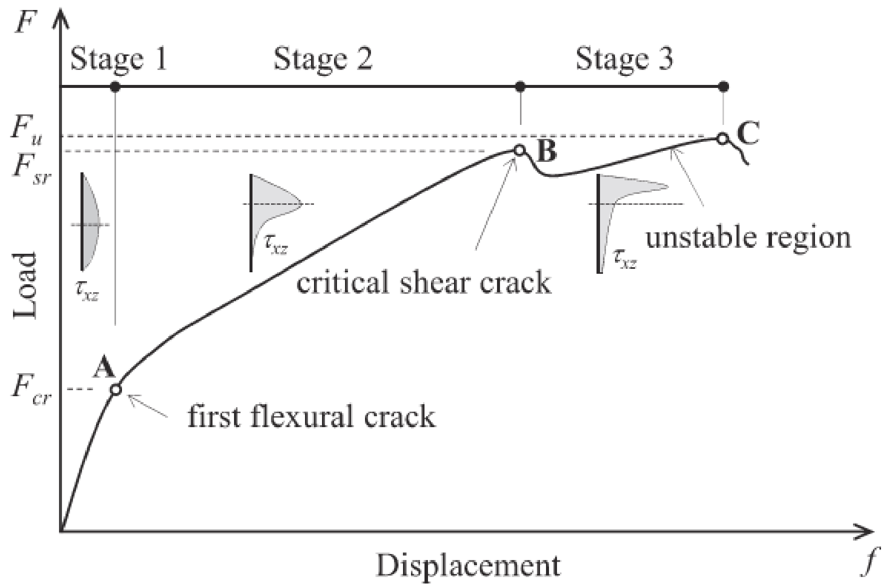

Figure 2.9 General Response Curve of Reinforced Concrete Beam with Shear Failure

Source: (Tran, 2020)

The response of a reinforced concrete beam with shear failure could be categorized further according to Fisker & Hagsten (2016). The response is categorized based on the major shear resistance mechanism, which related to the shear slenderness of the beam. There are two categories of shear slenderness, $a/d \leq 2.5$ and $a/d \geq 2.5$, which illustrated in Figure 2.10. Shear in beams with $a/d \leq 2.5$ is resisted with the strut and tie action within the beam, which resulted in a stable crack formation on the beams.

Shear in beams with $a/d \geq 2.5$ is majorly resisted with several mechanisms such as aggregate interlock, residual tensile stresses in cracks and dowel action. These mechanisms interact with the stress transfer within the compression zone, which results in an unstable crack formation on the beams. The sudden propagation of existing flexural shear crack into the compressive zone usually triggers the failure of the beams. Beams with $a/d \leq 2.5$ can be referred to as deep/short beams while beams with $a/d \geq 2.5$ can be referred to as slender beams.

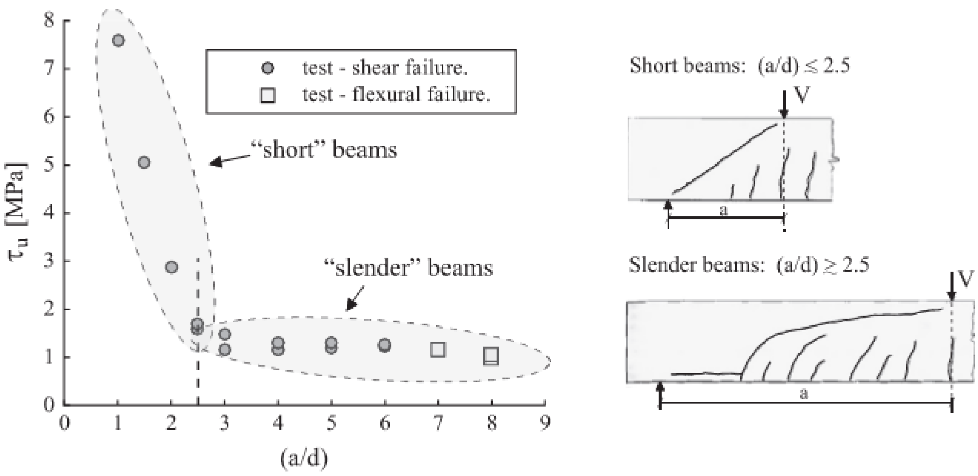

Figure 2.10 Slenderness Influence on the Shear Strength (Left) and Common Shear Failure Crack Pattern on Beams (Right)

Source: (Fisker & Hagsten, 2016)

2.4. Interpretation of Shear Transfer Mechanism in Finite Element Analysis

In the process of creating a mechanical model for concrete structure, material nonlinearity plays a significant role in NLFEA. Material properties determine the resistance level of a structure. In concrete structures, there are two materials used, concrete for the cross-section of the structure and steel for reinforcement of the structure. A plain concrete material exhibits different non-linear behaviour when subjected to compression and/or tension. On the other hand, steel has similar behaviour when subjected to compression and/or tension. Moreover, combining concrete and steel also means that there would be an interface between them and a combined action such as dowel action could occur.

These forms of resistance must be considered when making a model in order to be able to create a realistic and reasonable mechanical model in order to get a reliable result. Material properties often represented with constitutive relation in structural mechanics. This is also used in the mechanical model of finite element analysis where material nonlinearity is incorporated by creating a constitutive model based on experimental results. The suitable constitutive model can be known from literature and related papers. This thesis will mainly refer to the Guidelines for Nonlinear Finite Element Analysis of Concrete Structures (Hendriks & Roosen, 2020).

2.4.1 Concrete Cracks Determination

For concrete material, the damage occurring on it can be seen based on cracks. Cracks are formed due to softening process that resulted in geometrical discontinuity (Rots & Blaauwendraad, 1989). According to Teshome (2019), the formation and propagation of cracks in reinforced concrete without shear reinforcement are crucial when defining the resistance with NLFEA, which makes concrete properties is governing the process of shear failure in reinforced concrete without shear reinforcement.

In NLFEA, there are two types of commonly used cracking models, discrete cracking and smeared cracking. Discrete cracking model crack as a displacement continuity on the structure by using interface elements to separate the element into two (Borst & Nauta, 1985). The discrete model of splitting tensile crack and shear crack can be used to model the size effect of flexural shear failure on reinforced concrete beams without shear reinforcement (Sato, Tadokoro, & Ueda, 2004). However, this concept is strongly related to the prediction accuracy of the crack location on the structure (Rots & Blaauwendraad, 1989).

Smeared cracking model crack as a part of continuum element which happens due to change in stress-strain state on the element (Borst & Nauta, 1985). This concept is contradicting with the fact that crack is a geometrical discontinuity, which causes no stress relaxation on the surrounding element after the element is fully cracked, which called as stress locking phenomenon (Rots & Blaauwendraad, 1989). In this thesis, the focus would be on predicting a precise (high accuracy) crack pattern and location on the structure with the use of the smeared cracking model. The smeared cracking can be categorized into two types, fixed and rotating smeared crack.

Fixed smeared crack is created based on a reference to fixed principal axes on the normal direction (n-dir) of the crack (mode 1) and tangential direction (s,t-dir) of the crack (mode 2 and 3). Mode 1 correspond to tension stress transfer and mode 2 correspond to debonding and interlock stress. The principal axes are determined at the first formation of cracks with reference to the principal stress. After the first formation of the crack, no angle change on the principal axes of the element will be imposed. The stress-strain relation for fixed smeared crack is expressed mathematically in equations (2.1) and (2.2). (Rots & Blaauwendraad, 1989)

$$\begin{bmatrix} \sigma_{nn} \\ \sigma_{tt} \\ \sigma_{nt} \end{bmatrix} = \begin{bmatrix} E_{nn} & E_{nt} & 0 \\ E_{nt} & E_{tt} & 0 \\ 0 & 0 & G_{nt} \end{bmatrix} \begin{bmatrix} \varepsilon_{nn} \\ \varepsilon_{tt} \\ \gamma_{nt} \end{bmatrix} \qquad \text{2D} \qquad (2.1)$$

$$\begin{bmatrix} \sigma_{nn} \\ \sigma_{ss} \\ \sigma_{tt} \\ \sigma_{ns} \\ \sigma_{st} \\ \sigma_{nt} \end{bmatrix} = \begin{bmatrix} E_{nn} & E_{ns} & E_{nt} & 0 & 0 & 0 \\ E_{ns} & E_{ss} & E_{st} & 0 & 0 & 0 \\ E_{nt} & E_{st} & E_{tt} & 0 & 0 & 0 \\ 0 & 0 & 0 & G_{ns} & 0 & 0 \\ 0 & 0 & 0 & 0 & G_{st} & 0 \\ 0 & 0 & 0 & 0 & 0 & G_{nt} \end{bmatrix} \begin{bmatrix} \varepsilon_{nn} \\ \varepsilon_{ss} \\ \varepsilon_{tt} \\ \gamma_{ns} \\ \gamma_{st} \\ \gamma_{nt} \end{bmatrix} \quad \text{3D} \tag{2.2}$$

When the crack is initiated, both young's modulus (E) and shear modulus (G) will be reduced by introducing a reduction factor on the modulus. The young's modulus reduction factor (μ) is calculated from the softening behaviour of concrete and the shear modulus reduction factor (β) is determined as an additional input in material nonlinearity, which often called shear stiffness reduction or shear retention factor. The shear retention factors are not dependent on the concrete strength according to Walraven (1980).

According to Huber & Kollegger (2014), the shear retention factor for fixed crack can be determined as constant and variable. The constant shear retention factor can be calculated based on the crack normal stiffness of the tension softening curve. It was mentioned by Khalfallah, Charif, & Naimi (2004) that the use of $\beta = 0$ should be avoided as it would create an over-stiff behaviour on the load-displacement curve for over-reinforced concrete. The use of the $\beta < 1$ should produce satisfactory results for under-reinforced concrete. Khalfallah, Charif, & Naimi (2004) recommended the use of an average value of 0.4 to be used for the constant shear retention factor for all cases.

The variable shear retention factor is calculated based on the change in strain normal to the crack. The variable shear retention can be modelled based on several options, such as damage-based and aggregate size-based. As explained by de Putter (2020), the fixed crack model with damage-based model the aggregate interlock based on the change in strain normal to the crack. The fixed crack model with aggregate size-based model aggregate interlock by using linear relation of reduction factor of shear modulus from 1 at the crack opening to 0 at crack width equal to half of the mean aggregate size. In the work of Teshome (2019), the fixed crack model with damage-based and aggregate size-based shear retention would generally produce overestimation on the ultimate load. However, more problems are found with aggregate size-based where it could not predict shear and mixed-mode failure. Furthermore, the fixed crack model with aggregate size-based produces stiffer predictions compared to the experiment in 8 out of 9 cases. This happened because a fixed crack model with aggregate size-based overestimates the shear stiffness of the cracked plane, which slows down and delays the formation of flexural shear crack. On the other hand, the damage-based showed better results compared to aggregate size-based where it could predict the correct failure mode on 7 out of 9 experiments. The use of the correct shear retention factor would greatly influence the failure load only on beams with shear failure $a/d > 2.5$ according to Balakrishnan & Murray (1986). When comparing two types of shear retention factors, Huber & Kollegger (2014) found that the variable shear retention factor gives more reliable results compared to the constant shear retention factor for a fixed crack model.

The influence of shear retention factor in stress-strain relation can be expressed mathematically for 2D case in equation (2.3) (Rots & Blaauwendraad, 1989)

$$\begin{bmatrix} \Delta\sigma_{nn} \\ \Delta\sigma_{tt} \\ \Delta\sigma_{nt} \end{bmatrix} = \begin{bmatrix} \dfrac{\mu E}{1-\upsilon^2\mu} & \dfrac{\nu\mu E}{1-\upsilon^2\mu} & 0 \\ \dfrac{\nu\mu E}{1-\upsilon^2\mu} & \dfrac{E}{1-\upsilon^2\mu} & 0 \\ 0 & 0 & \dfrac{\beta E}{2(1+\upsilon)} \end{bmatrix} \begin{bmatrix} \Delta\varepsilon_{nn} \\ \Delta\varepsilon_{tt} \\ \Delta\gamma_{nt} \end{bmatrix} \tag{2.3}$$

The strain vector in the equation (2.3) indicates the total strain on the element, consist of crack strain and strain on the material. In order to incorporate particular crack laws which usually start from the definition of crack strain, the total strain is decomposed into 2 parts, crack strain and material strain. This concept is called fixed single crack or fixed crack. According to Borst & Nauta (1985), the problem with the fixed crack model is the possibility of excessive rotation of principal axes due to high shear stress on the crack, which would affect the numerical results. It was also mentioned by Rots & Blaauwendraad (1989) that the use of a fixed single crack will cause over stiff behaviour and can be eliminated by applying the shear softening function explicitly with the crack model. It was suggested to use a reduction factor equal to 0 when ultimate crack strain is reached. Little to no shear retention should be used for the fixed crack model to avoid excessive stress locking.

Another way to solve the problem is by implementing the decomposition concept even further on the crack strain by assuming that the crack strain is a summation of several multi-directional cracks occurring simultaneously on a sampling point. This extended concept of fixed single crack is called fixed multi-directional crack. (Rots & Blaauwendraad, 1989)

The process of initiation of a new crack, closing of an open crack and re-opening a closed crack is called a state change. A state change on one of the cracks becomes important in fixed multi-directional cracks because it could affect other cracks state change. Multiple state change on one strain increment is handled by tracing and handling the most critical state change first and postponed other cracks state change for the next strain increment.

This cause inconsistencies because postponing a crack state change would result in negative crack normal strain, which is physically meaningless. However, the fixed multi-directional crack is essential to implement due to the possibility of biaxial and triaxial tension on the element, in axisymmetric case, and plane-strain analysis. The use of different types of stress transfer models between modes 1, 2, and 3 in the fixed smeared crack is also possible. Furthermore, in the condition where the element is subjected to tension and shear, non-orthogonal cracks could be formed where a new crack will form when the angle of inclination between the existing crack(s) and the principal stress exceeds a certain threshold angle. A shear retention factor almost equal to 0 is recommended for a fixed smeared crack with a threshold angle of 60°. All formed cracks are monitored and recorded separately. The concept of fixed multi-directional crack is used as a base for rotating smeared cracks. (Rots & Blaauwendraad, 1989)

Rotating smeared crack is created based on rotating principal axes with reference to principal stress direction. It is assumed that the angle of principal stress rotation and principal strain rotation are equal, which called coaxiality. The stress-strain relation for rotating smeared crack is expressed mathematically in equation (2.4). (Rots & Blaauwendraad, 1989)

$$\begin{bmatrix} \Delta\sigma_{11} \\ \Delta\sigma_{22} \\ \Delta\sigma_{33} \\ \Delta\sigma_{12} \\ \Delta\sigma_{23} \\ \Delta\sigma_{31} \end{bmatrix} = \begin{bmatrix} \frac{\partial\sigma_{11}}{\partial\varepsilon_{11}} & \frac{\partial\sigma_{11}}{\partial\varepsilon_{22}} & \frac{\partial\sigma_{11}}{\partial\varepsilon_{33}} & 0 & 0 & 0 \\ \frac{\partial\sigma_{22}}{\partial\varepsilon_{11}} & \frac{\partial\sigma_{22}}{\partial\varepsilon_{22}} & \frac{\partial\sigma_{22}}{\partial\varepsilon_{33}} & 0 & 0 & 0 \\ \frac{\partial\sigma_{33}}{\partial\varepsilon_{11}} & \frac{\partial\sigma_{33}}{\partial\varepsilon_{22}} & \frac{\partial\sigma_{33}}{\partial\varepsilon_{33}} & 0 & 0 & 0 \\ 0 & 0 & 0 & \frac{\sigma_{11}-\sigma_{22}}{2(\varepsilon_{11}-\varepsilon_{22})} & 0 & 0 \\ 0 & 0 & 0 & 0 & \frac{\sigma_{22}-\sigma_{33}}{2(\varepsilon_{22}-\varepsilon_{33})} & 0 \\ 0 & 0 & 0 & 0 & 0 & \frac{\sigma_{33}-\sigma_{11}}{2(\varepsilon_{33}-\varepsilon_{11})} \end{bmatrix} \begin{bmatrix} \Delta\varepsilon_{11} \\ \Delta\varepsilon_{22} \\ \Delta\varepsilon_{33} \\ \Delta\gamma_{12} \\ \Delta\gamma_{23} \\ \Delta\gamma_{31} \end{bmatrix} \tag{2.4}$$

In this type of crack model, a new crack will be formed every time the angle of principal direction changes. Furthermore, a new crack will also trigger the inactivation of the previous cracks which cause every new crack is unique to its loading phase. The previous defects will be accounted for in the stress-strain relation and the formula of overall shear modulus will ensure coaxiality on the crack model. The rotating cracks can be conceived as a collection of several fixed cracks on different angle orientations. Strain decomposition also applied to this crack model in order to separate the crack strain and material strain.

The advantage of using the rotating crack model is that no specific shear transfer stress model is needed to be included in the model, which simplifies the model. Furthermore, according to Borst & Nauta (1985), the smeared crack model can be used to predict the position of dominant shear crack on shear failure with high accuracy. In Rots & Blaauwendraad (1989) experiment with the cracks model, it was also found that the over-stiff behaviour (on the model with fixed single crack) did not occur on the model with rotating crack, which makes it more acceptable. This is also found by Teshome (2019), where the use of the crack rotation concept is essential to create explicit shear softening and shear-normal coupling of the fixed single crack which could correctly display the strength degradation in the lateral direction. The use of a rotating crack model could produce a more accurate ultimate load even in combination with embedded reinforcement and less prone to stress locking compared to a fixed single crack model. Furthermore, according to de Putter (2020), the rotating crack model is the most suitable to model compressive shear and bending failure while the fixed crack model is the most suitable to model flexural shear failure.

On the other hand, there are some disadvantages to the model, such as the uniqueness of the crack, crack propagation bias, the simplicity of the model itself. The uniqueness of cracks on every loading phase can be interpreted as memory loss of damage orientation where old cracks cannot be reactivated in the later loading phase. This could pose a problem when non-proportional loading is applied which could cause a sudden shift of principal direction. The crack propagation with rotating crack is more influenced by directional bias (a phenomenon where crack propagates along the mesh line) compared to fixed single crack. Different types of stress transfer models in rotating crack could be used with reference to mode 1, as there are no shear stresses in the principal direction. The use of different shear stress transfer models must be done indirectly, such as modifying the tension stress transfer model of mode 1, which could cause unexpected incompatibility and error on the crack model. Furthermore, Huber & Kollegger (2014) found that even though the use of the fixed crack model resulted in great overestimation both in load resistance and midspan deflection, the response of FEM still better compared to FEM with rotating crack model. FEM with rotating crack model gives too soft response after cracking, which resulted in as lower load resistance and lower midspan deflection. Huber & Kollegger (2014) suggested that the overestimation of load resistance can be caused by increased shear stiffness due to smaller crack widths in numerical results. No considerations of dowel action and un-cracked compression zone are done in the respective numerical experiment. A brief description of the FEM configuration is given as follow. The failure criterion used on the FEM is the biaxial failure criterion for the concrete failure. The concrete tension softening is modelled with the Hordijk curve and the parabolic curve is used to model concrete compressive behaviour. The concrete stress interactions are modelled with the Vecchio and Collins model (1982) for the relation of compression-tension behaviour and Kupfer’s model for compression-compression and tension-tension behaviour.

Based on the recent works with the rotating crack model, there are some problems found on its use to model shear failure on beams without shear reinforcement. Teshome (2019) stated that a rotating crack model with embedded reinforcement prone to always produce delamination failure. The use of bond-slip reinforcement avoids the delamination problem and resulted in the correct failure mode. However, the use of the fixed crack model with damage-based still produces a better prediction of the failure mode due to its compatibility of the assumption and nature of the crack where the concrete crack is fixed at the same location and orientation and does not vanish or rotate based on the direction of the principal plane.

This problem also found by de Putter (2020) where for shear slenderness of 2.5-4, the failure mode is commonly mispredicted in combination with over-prediction of failure load with rotating crack model for beams without shear reinforcement due to over-rotation of the crack strain. The use of the rotating-to-fixed model or manual interpretation could help solve this problem.

Another problem is mentioned by de Putter (2020) where the use of the rotating crack model gives consistent over-prediction on the failure load for beams without and with shear reinforcement. It shows a large scatter on the result and over-prediction of almost equal to 2 times the experimental failure load. The over-predictions can be solved by creating two models for each crack model and using the lowest failure load as the outcome for beams without shear reinforcement.

In this thesis, both fixed and rotating crack models will be used to investigate the size effect because the fixed crack model could give higher precision on the results, while the rotating crack model is widely applied on NLFEA of concrete structures.

2.4.2 Concrete Compressive Behaviour

Concrete compressive behaviour is characterized by its compressive strength and the compression softening curve. Balakrishnan & Murray (1986) stated that the influence of the compressive stress-strain relationship is little to none on beams that fail in shear with $a / d > 2.5$. However, a subsequent study by Balakrishnan, Elwi, & Murray (1988) showed that the inclusion of compression softening is important in reinforced concrete beams without shear reinforcement with $a / d > 4$. This means that the influence of the compressive stress-strain relationship is not significant only for beams that fail in shear with shear slenderness between 2.5 and 4.

2.4.3 Concrete Tensile Behaviour

Concrete tensile behaviour is characterized by its tensile strength and tensile softening curve. Balakrishnan & Murray (1986) stated that tensile strength would influence the result of NLFEA. However, the influence of tensile strength to the failure load decrease as the shear span to depth ratio increase.

According to Khalfallah, Charif, & Naimi (2004), tension softening is an important feature that needs to be incorporated in the numerical model for reinforced concrete beams, especially for under-reinforced beams. The absence of tension softening behaviour would produce more mesh dependent results. This is proven by comparing models with the tension cut-off model against tension linear softening. The use of the tension linear softening model is less dependent on mesh size and can be mesh independent if the mesh size is smaller than $7a_g$ or roughly equal to 178 mm. In the specific case, such as reinforced concrete beam without shear reinforcement, Balakrishnan & Murray (1986) stated that the influence of tension softening is significant for small beams which fail in shear with $a / d > 2.5$.

Both statements are verified by Huber & Kollegger (2014), where they indicated that the simulation of shear behaviour of slender reinforced concrete beams without shear reinforcement is greatly affected by the tension softening behaviour and shear stiffness of cracked concrete assigned on the model. Broujerdian & Kazemi (2016) mentioned that the absence of tension strength will result in overestimation of the post-cracking deformation of the reinforced concrete, which also verifies Khalfallah, Charif, & Naimi (2004) statement regarding tension softening importance in NLFEA models.

2.4.4 Concrete Stress Interaction Behaviour

Concrete biaxial stress interactions such as compression-tension (reduction of compressive strength), compression-compression (confinement effect), tension-tension are not discussed in detail in any paper related to shear failure of reinforced concrete beams without shear reinforcement. Several papers only indicated what models of interaction are used on their NLFEA models, such as the works of Sato, Tadokoro, & Ueda (2004), Tavio (2008), Huber & Kollegger (2014), Broujerdian & Kazemi (2016), Ismail, Guadagnini, & Pilakoutas (2016), and de Putter (2020). The interaction models used by Sato, Tadokoro, & Ueda (2004) and Huber & Kollegger (2014) are described briefly in subchapters 2.4.5 and 2.4.1 respectively. All other interaction models can be seen in subchapter 3.3.

2.4.5 Reinforcement Behaviour

According to Channakeshava & Iyengar (1988), reinforcement can be modelled with three options. First, the reinforcement is modelled with discrete bar/beam element in combination with bond-slip model connected to the node of the beam on finite element model. According to de Putter (2020), the use of either truss or beam element does not give a significant difference in the ultimate load prediction and variation on average. Second, the reinforcement is modelled as a bar which is embedded within the concrete element on the finite element model to enforce displacement compatibility by interpolation and transformation. Third, the reinforcement is modelled as a composite material consisting of steel and concrete properties, which is useful for structures with distributed reinforcement along with the geometry. The second and third options cannot be used to model bond-slip behaviour on the interface between reinforcement and concrete. Yang (2014) indicated that in most cases with flexural shear failure, the rebars in a concrete beam are in the linear elastic stage.

The modelling of reinforcement as a composite material can be done by using the tension stiffening model and shear stiffening model based on An, Maekawa, & Okamura (1997). The models are constructed with equation (2.5). The tension stiffening model illustrated in Figure 2.11 (a) is constructed based on tension softening of cracked concrete and bond-slip of reinforcement to concrete. The shear stiffening model illustrated in Figure 2.11 (b) is constructed based on the contact density idealization and exclude the elastic deformation at the contact crack plane. The effective area of the composite material can be assumed as the effective embedment zone on the concrete which usually given as a function of reinforcement bar diameter. This model is not dependent on the mesh size of the structure.

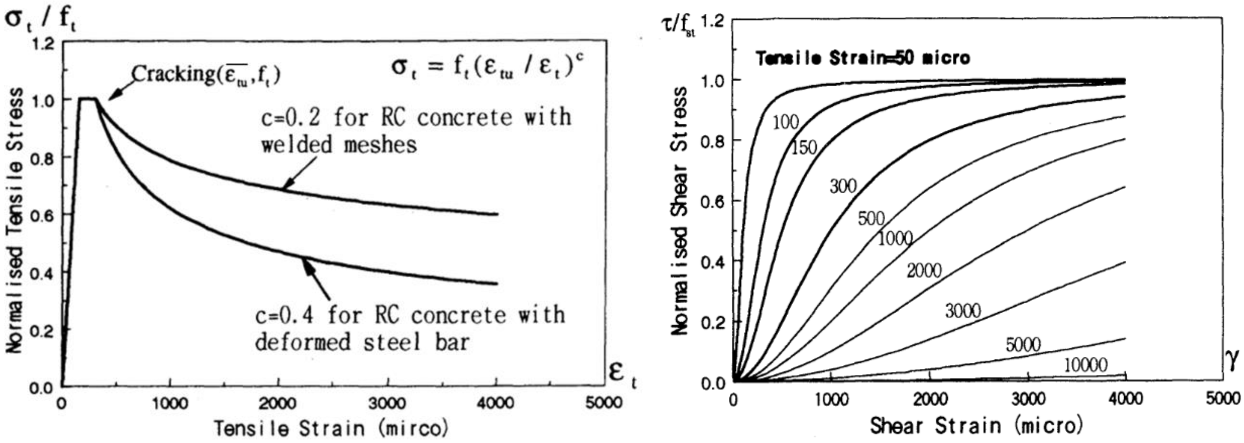

(a) (b)

$$\tau = G\gamma \qquad G = \frac{1}{\frac{1}{\overline{\overline{G_{st}}}} + \frac{1}{G_c}} \qquad \overline{G_{st}} = \frac{\tau_{st}}{\gamma} = f_{st}\frac{\overline{\beta}^2}{1+\overline{\beta}^2} \qquad \overline{\beta} = \frac{\gamma}{\varepsilon_t} \qquad f_{st} = 8.3\sqrt[3]{f_c} \tag{2.5}$$

Figure 2.11 (a) Tension Stiffening Model and (b) Shear Stiffening Model for Concrete in Reinforced Zone

Source: (An, Maekawa, & Okamura, 1997)

Broujerdian & Kazemi (2016) used smeared reinforcement in their paper and for the case of reinforced concrete without shear reinforcement, the load-displacement curve of the numerical results fit nicely with the experimental results, resulted in a small range of error from -10% to +4% (based on 3 samples). Furthermore, the crack pattern of numerical and experimental results is also similar.

However, according to Sato, Tadokoro, & Ueda (2004), using smeared reinforcement model for simulating flexural shear failure gives unacceptable results. In Sato, Tadokoro, & Ueda (2004) works, the crack on the reinforced concrete beam is modelled with the smeared crack model. The Maekawa model is adopted for the stress-strain relationship before cracking because the experimental observation on the stress-strain relation fits with this model. Niwa's model, Kupfer's model, and Aoyanagi and Yamada's model are used for the relation of compression-tension, compression-compression and tension-tension behaviour respectively. The tension softening curve of Reinhardt (1986) (equivalent to Hordijk tension softening curve) with secant-stiffness for unloading is used for the tension strength behaviour for unreinforced concrete element and tension softening curve of Tamai (1998) is used for reinforced concrete element, which implicitly indicates smeared reinforcement model is used.

The numerical model produced results with higher tensile strain compared to experimental results, which in return cause higher shear stress transfer on the model. This indicated that the results of NLFEA for flexural shear failure would greatly be affected by the shear retention factor for FEM with smeared reinforcement model. Furthermore, it is also mentioned that this FEM configuration cannot be used to produce accurate results of deformation at shear crack because the crack model does not include local deformation and fracture of dowel action. As a result, the FEM is overestimating the shear stiffness. This overestimation also connected indirectly to the incompatibility of the used assumption on the crack model, where Mode 1 and Mode 2 deformation are assumed to happen simultaneously while it is not the case for flexural shear failure.

2.4.6 Concrete-Reinforcement (Bond-Slip) Interaction Behaviour

The use of bond-slip relationship in beams for beams with $a/d > 2.5$ would reduce the failure load due to larger crack strains, which in turn cause higher shear stiffness reduction. When simulating reinforced concrete beams without shear reinforcement, the use of the bond-slip model is critical for shear slenderness between 2.5 and 4, according to Balakrishnan, Elwi, & Murray (1988) and Balakrishnan & Murray (1986). The use of bond-slip relationship in beams would reduce the failure load due to larger crack strains formation, which in turn cause higher shear stiffness reduction. The significance of using the bond-slip model is further explained in the work of Teshome (2019) and confirmed by de Putter (2020). The use of embedded reinforcement would mean that the relative displacement (slip) between concrete and reinforcement is considered as longitudinal strain, thus increasing the crack strain of the concrete. These cause problem when combined with rotating crack model where the longitudinal strain cause change in crack orientation to align in the longitudinal direction, thus makes the model always creating delamination failure.

Bond-slip behaviour can be modelled based on the Shima curve and FIB Model 2010. The Shima curve is a bond-slip model with relation to bar diameter and concrete strength. Shima curve has a higher bond stress capacity compared to FIB Model 2010 where a steep drop is given for concrete without confinement. De Putter (2020) mentioned that the steep drop is in accordance with the brittle nature of splitting failure but numerically more challenging, as would be more prone to convergence problem.

Based on de Putter (2020) works, the use of the FIB MC2010 bond-slip model in combination with the fixed (damage based) crack model gives the most consistent results (variation of 12% on the result) for reinforced concrete without shear reinforcement compared to embedded and Shima. On the other hand, the use of the Shima bond-slip model in combination with the rotating crack model gives the most consistent results (variation of 20% on the result) for reinforced concrete without shear reinforcement compared to embedded and FIB MC2010.

2.4.7 Relation to Shear Transfer Mechanism

According to Pruijssers (1988), the aggregate interlock is interpreted as tensile fracture of the concrete, where the development of small micro-cracks is defined based on the tension softening model. The stiffness of the element would greatly reduce as small micro-cracks began to appear. Two parameters are used to define this phenomenon: the descending branch stiffness on the tension softening model and the normal retention factor. Descending branch stiffness is used to clearly describe the increment on the stress-strain relation of a partially cracked element. The normal retention factor (or commonly known as the shear retention factor) is used to reduce the elastic modulus of the concrete. This concept is applied to the fixed crack model. The descending branch stiffness could also be expressed as a function related to the normal retention factor, which is used as a background for the rotating crack model. Both parameters are non-real parameters because it is derived based on experimental observation.

This interpretation of aggregate interlock also mentioned by Borst & Nauta (1985) and Channakeshava & Iyengar (1988) where aggregate interlock can be modelled with a positive shear modulus of cracked concrete by employing shear retention factor.

However, Borst & Nauta (1985) mentioned that the shear retention factor is also used to model the dowel action. A different opinion is given by Channakeshava & Iyengar (1988) where they stated that dowel action is not incorporated in the shear retention factor and modelled separately with normal stiffness of the bond-slip elements.

Pruijssers (1988) indicated that the dowel action mechanism is based on the response of bars and surrounding concrete due to lateral bar displacement. In the case of dowel action in bars perpendicular to the crack plane, the dowel action is a combination of resistance based on axial and lateral stiffness of the bars. Axial stiffness is based on the bond between steel and concrete. Lateral stiffness is based on the reaction stresses from concrete around the bar.

Dowel action can be modelled with the combination of 3 independent elements: steel bar element, bond element between bar and concrete, and the plain concrete element where slip between steel and concrete could happen. However, the modelling of the dowel action mechanism is strongly related to the bar elements described in the numerical program. Furthermore, Sarkhosh, Uijl, Braam, & Walraven (2010) indicated that a very fine mesh must be introduced to consider the concrete cover which would result in a huge number of elements.

On the other hand, Tavio (2008) indicated that smeared cracks model is unable to model any shear transfer mechanism discretely. Smeared cracks model only gives average responses on each element without considering the specific contributions of the individual mechanical effects, such as the aggregate interlock and dowel action at the crack location.

2.5. Summary

The reinforced concrete beams without shear reinforcement will be modelled with both crack models (fixed and rotating), as both crack models have different pros and cons, which can be very useful to create an acceptable model for a reinforced concrete beam without shear reinforcement. Several key parameters such as concrete tension softening, discrete model of reinforcement, and bond-slip interaction model will be included in the numerical models. However, further study is done in order to determine which components are necessary to be modelled in order to avoid complications on the model and large computational time. The use of the composite material model for reinforcement explained in subchapter 2.4.5 is served as an option in case the discrete reinforcement model is not suitable for simulating shear failure in NLFEA. The general representation of the mechanical model in NLFEA for modelling concrete structures is given in Figure 2.12. Its correlation to the shear transfer mechanism is illustrated in Figure 2.13.

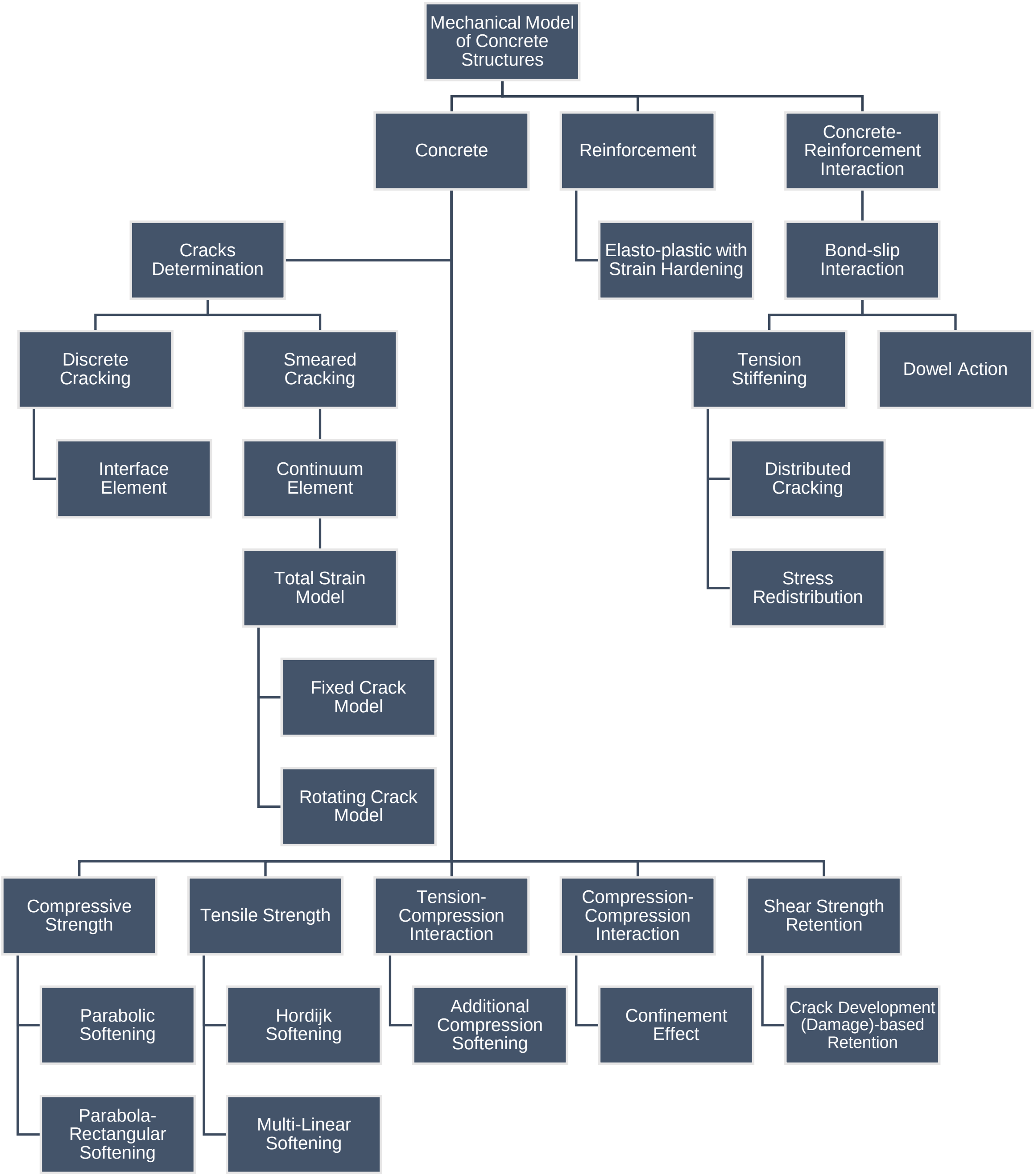

Figure 2.12 General Representation of Mechanical Model in NLFEA

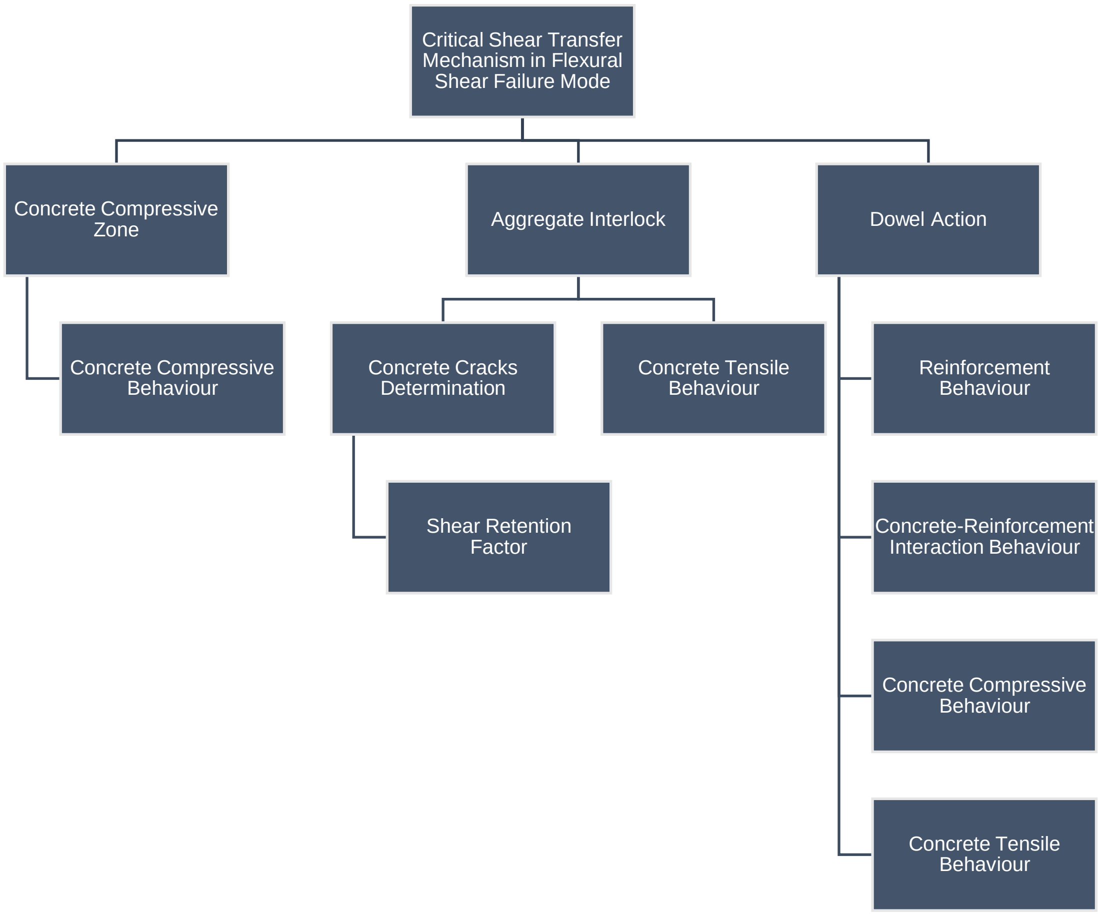

Figure 2.13 Mind Map of Interpretation of Shear Transfer Mechanism in NLFEA

3 Literature Review of Size Effect Phenomenon in Finite Element Analysis

Size effect on the shear resistance of reinforced concrete beam without shear reinforcement is an old issue that engineers have been dealing with for a long time. Bazant, Ozbolt, & Eligehausen (Fracture Size Effect: Review of Evidence for Concrete Structures, 1994) provided the collected evidence regarding this problem in his paper. The term “size effect” is used in many available pieces of literature with different meanings and understanding. Subchapter 3.1 aims to give more insight on what is the meaning of this term and how many variations that this term has in the literature. At the end of subchapter 3.1, a brief description is given to clarify which meaning of both experimental and numerical size effect is used in this thesis. Afterwards, subchapters 3.2.1 and 3.2.2 are describing the correlation between experimental size effect with structural geometry and material properties and constitutive model. Subchapter 3.2.1 specifically describes which are and are not the key parameters related to structural geometry. Subchapter 3.2.2 specifically describes the insights on how to calibrate material properties and constitutive model in order to account for experimental size effect on NLFEA. The study regarding numerical size effect and other problems of NLFEA are described in subchapter 3.3. Several insights related to how to solve these are also included in subchapter 3.3. In the end, subchapter 3.4 gives information regarding the starting point for modelling in NLFEA that is going to be used in chapters 4, 5 and 6.

3.1. Definition of Size Effect and its Influence in Finite Element Analysis

Tran (2020) indicates that the shear resistance of concrete structures is strongly dependent on the experimental size effect phenomenon. More specific dependency of shear resistance is given by Sarkhosh, Uijl, Braam, & Walraven (2010) where they indicated that the dominant parameters which influencing shear strength in beams without shear reinforcements are concrete strength, experimental size effect, span to depth ratio, longitudinal reinforcement ratio, and axial force. According to Syroka-Korol & Tejchman (2014), the experimental size effect can be defined as a decrement of both nominal structure resistance and material brittleness as the element size in tension increases, in which beams would become ductile on a small scale and brittle on a sufficiently large scale. Bazant, Ozbolt, & Eligehausen (Fracture Size Effect: Review of Evidence for Concrete Structures, 1994) stated that the experimental size effect on concrete structures must be considered for diagonal shear failure and torsional shear failure of longitudinally reinforced beams without stirrups, punching shear failure of slabs, pull-out failures of deformed bars and headed anchors, and failure of short and slender tied columns.

The experimental size effect consists of two parts, statistical/stochastic size effect and energetic/deterministic size effect. The experimental size effect is formulated based on the combination of the statistical and energetic size effect and its relevance to the total depth of the concrete members. The statistical size effect can be explained by Weibull with the theory of random local material strength according to Bazant & Yu (Universal Size Effect Law and Effect of Crack Depth on Quasi-Brittle Structure Strength, 2009). The statistical size effect can be determined empirically, which denotes the significancy of empirical factors to be incorporated in the formulation of the shear resistance model without shear reinforcement for reinforced concrete members.

The energetic size effect, according to Tran (2020), can be defined as the dependency of material strength to the structure size, which can also be interpreted as a release of energy in cracks associated with material damage to failure. In order to determine the material failure, the decisive mechanism of failure (in this thesis is flexural shear failure mode) and its location must be identified. There are several dominant mechanisms for resisting shear force, such as compression zone, tension zone, aggregate interlock, dowel action, and the interaction between each mechanism. The energetic size effect would affect the reinforced concrete beams without shear reinforcement where diagonal shear and tensile fracture occur as mentioned by (Syroka-Korol & Tejchman (2014).

On the other hand, in Bazant & Yu (Universal Size Effect Law and Effect of Crack Depth on Quasi-Brittle Structure Strength, 2009) works, the categorization of the experimental size effect is slightly different, where the experimental size effect is divided into two types, Type I and Type II, as illustrated in Figure 3.1. Type I occurs on the structure that fails at the crack initiation from a smooth surface while Type II occurs on structure with a deep notch where crack can form stably before reaching failure.

Type I size effect associated with both statistical and energetic size effect (Energetic-Statistical) while type II only associated with energetic size effect. The effect of statistical size effect is governing in the case where the total depth of the structure is large while the energetic size effect is governing when the total depth is small.

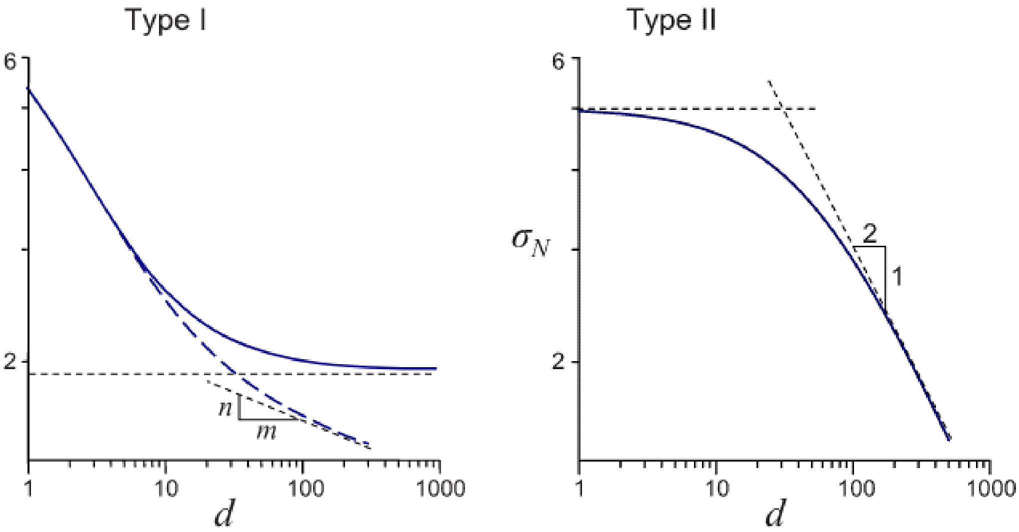

Figure 3.1 Illustration of The Influence of Numerical Size Effect on Nominal Stress based on Fracture Mechanics: Type I (Left) and Type II (Right)

Source: (Bazant & Yu, Universal Size Effect Law and Effect of Crack Depth on Quasi-Brittle Structure Strength, 2009)

Another probable source of the experimental size effect is the aggregate size and its shape. However, the shear resistance had been proven to be independent of the maximum aggregate size and its shape by Fenwick & Paulay (1968). Furthermore, Fenwick & Paulay (1968) also indicated that the crack response to shear load is also independent of the load history and the crack opening path.

In this thesis, the experimental size effect is correlated to the size change on the cross-section and length, which strongly correlates with the energetical size effect. Therefore, the statistical size effect is completely disregarded in this thesis.

The numerical size effect is never mentioned explicitly in any papers. The numerical size effect is only implicitly referred to in An, Maekawa, & Okamura (1997), Cervenka V. , Cervenka, Pukl, & Sajdlova (2016), Choi & Kwak (1990), Shayanfar, Kheyroddin, & Mirza (1997), and Tavio (2008) as mesh dependency/mesh dependency/element size effect. These papers will be discussed more extensively in subchapter 3.2.1-3.3. However, the numerical size effect is also related to the convergence problem and numerical parameters that are defined in NLFEA. The problems related to the convergence and numerical parameters are mentioned by Choi & Kwak (1990) and Malm & Holmgren (2008). In this thesis, the numerical size effect is correlated to the sensitivity of the numerical parameters, such as load step, error tolerance, the maximum number of iterations, and mesh size.

3.2. Experimental Size Effect

As mentioned in subchapter 3.1, the source of the experimental size effect is from the difference in the geometry, material properties and constitutive models. Several works of literature give some insight regarding what is found in the experimental results and their correlation to the experimental size effect. Furthermore, several different numerical configurations are also suggested to be used for including the experimental size effect in the NLFEA.

3.2.1 Experimental Size Effect – Structure Geometry

Structure geometry is considered as the source of the experimental size effect. As stated by Balakrishnan, Elwi, & Murray (1988), the shear failure is dependent on the shear slenderness (a/d). For reinforced concrete beams without shear reinforcement, flexural shear failure usually occurs for shear slenderness in the range of 2-2.5. Beams with $a/d<2$ will have a significant increase in shear resistance as the ratio continue to decrease. This statement is also given by Ismail, Guadagnini, & Pilakoutas (2016), which said that the important parameter for estimating shear resistance of reinforced concrete deep beam is shear slenderness and concrete strength.

When a beam is loaded, the beam will certainly deform. The deformation consists of bending deformation and shear deformation. Based on Huang, et al. (2018), the shear deformation of the shear-critical reinforced concrete beam is negligible when the beam does not has shear reinforcement. However, in the case of a beam with shear reinforcement, the shear deformation must be considered.

Based on Broujerdian & Kazemi (2016), reinforcement ratio will affect the average stress-strain relation of cracked concrete both in tension and compression. The use of bilinear uniaxial stress-strain without strain hardening for bare steel reinforcement would result in the overestimation of load resistance in analysing reinforced concrete. On the other hand, the reinforcement spacing will not affect the post-cracking behaviour of reinforced concrete.

3.2.2 Experimental Size Effect – Material Properties and Constitutive Models

Material properties and constitutive models are considered as a tool for calibrating the experimental size effect in NLFEA. Based on the explanation given in subchapter 2.5, the tensile strength could play a significant role to reduce the size effect. However, several studies, as mentioned in subchapter 2.4.3, raise doubts of its effectivity to include experimental size effect, because its influence on the results decrease as the a/d ratio increase.

On the other hand, according to An, Maekawa, & Okamura (1997), the experimental size effect has been included on numerical analysis in the constitutive models of the material: tensile stress transfer on the bond-slip mechanism of reinforcement and strain softening of concrete tension and shear. The strain-softening of concrete tension and shear greatly influence the experimental size effect because these parameters indirectly represent the aggregate interlock mechanism and dowel action (in the case where the bond-slip mechanism is not included in the model). Both mechanisms greatly influence the inclusion of experimental size effect in numerical model.

Several suggestions are given in some papers on how to account for the experimental size effect for simulating shear failure. Tavio (2008) suggested that the concrete is modelled with a custom tension softening curve, in combination with smeared cracks assumption with fixed crack direction. The reinforcement component is modelled with a bilinear strain hardening curve. The concrete stress interactions are modelled with Niwa’s model, Kupfer’s model, and Aoyanagi and Yamada’s model for the relation of compression-tension, compression-compression and tension-tension behaviour respectively. The custom tension softening curve can be constructed based on equation (3.1). The results in terms of stiffness are very similar to the experimental results, while the peak load is still over-estimated and the peak displacement is underestimated.

$$\sigma_{cx'} = \begin{cases} E_c \varepsilon_{x'} & \varepsilon_{x'} \le \varepsilon_{t0} \\ f_t & \varepsilon_{t0} \le \varepsilon_{x'} \le \varepsilon_{t0} + \varepsilon_p \\ f_t \left(\dfrac{\varepsilon_{t0}}{\varepsilon_{x'} - \varepsilon_p} \right)^{\beta} & \varepsilon_{x'} \ge \varepsilon_{t0} + \varepsilon_p \end{cases} \tag{3.1}$$

$$\beta = \frac{2G_f + f_t \varepsilon_{t0} h_{ele}}{2G_f - f_t \varepsilon_{t0} h_{ele}} \qquad \varepsilon_p = \min\left(0.55 + 2.27e^{-\frac{h_{ele}}{87}}, 1.4\right)\varepsilon_{t0}$$

Broujerdian & Kazemi (2016) suggested that the use of interactive constitutive laws for concrete and reinforcement (or also known as smeared reinforcement) would help improve shear failure simulation results from NLFEA. The input for reinforcement behaviour is modelled with a trilinear strain hardening curve. The input for concrete compressive behaviour, which is also used for plain concrete, is modelled with a modified parabolic curve. The slip between reinforcement and concrete is not considered in the model. The FEM used smeared rotating crack approach in combination with secant-stiffness-based NLFEA. The interaction between concrete and reinforcement are implicitly modelled by using interactive constitutive laws where the stress-strain relation is modified based on the concrete material characteristic and the existence of reinforcement. For the case of reinforced concrete without shear reinforcement, the load-displacement curve of the numerical results fit nicely with the experimental results, resulted in a small range of error from -10% to +4% (based on 3 samples). Furthermore, the crack pattern of numerical and experimental results is also similar.

According to Huber & Kollegger (2014) and Ismail, Guadagnini, & Pilakoutas (2016), the use of different failure criteria for concrete failure would help improve shear failure simulation results. Two options of failure criterion are explored by Ismail, Guadagnini, & Pilakoutas (2016), the nonlinear elastic damage-based approach SBETA model with biaxial failure criterion based on Kupfer criterion model and the combined fracture-plastic model with Rankine criterion for tensile fracture and three-parameter failure surface based on Menetrey-William criterion for concrete crushing. In general, the damaged plasticity model used the concept of isotropic damaged elasticity in combination with isotropic tensile and compressive plasticity. The main failure mechanism of concrete is assumed to be tensile cracking and compression crushing. Huber & Kollegger (2014) found that the use of FEM with the combined fracture-plastic model gives better predictions compared to the SBETA model when simulating shear failure in terms of load resistance, deformation, crack pattern and failure mode. Furthermore, Huber & Kollegger (2014) suggested the use of tensile strength equal to $f_t = 0.33\sqrt{f_c}$, which shows a better prediction of initial crack development with no significant influence on the load resistance. Another option to improve the results of NLFEA is using a shear factor of 10 for the combined fracture-plastic model, as it gives the most accurate results compared to SBETA models and other models with the combined-fracture model with other values of the shear factor.

However, according to Ismail, Guadagnini, & Pilakoutas (2016), in the case of deep beams, the development of high shear stress and lateral tensile stress on the shear span of reinforced concrete deep beams are producing softer behaviour on the concrete compared to uniaxial stress condition. This effect reduces the overall stiffness of the beam and increases shear deformation, which cannot be estimated well by either the SBETA model or the combined fracture-plastic model.

3.3. Numerical Size Effect

As mentioned in subchapter 3.1, the source of the numerical size effect is commonly known from the mesh size. The influence of load step, error tolerance, and iterations are often ignored as only a few works of literature mentioned this. Several works of literature have claimed to solve the problem related the mesh size dependency, while other sources claim that the solution is not able to solve this problem in other cases.

3.3.1 Numerical Size Effect – Load Step, Error Tolerance and Iterations

The numerical size effect is rarely correlated to the load step, error tolerance, and the maximum number of iterations, as it is considered not important. In Choi & Kwak (1990) works, the influence of numerical parameters such as load step and integration orders are considered not as significant as the influence of mesh size. Another literature that mentions this problem is the works of Malm & Holmgren (2008). It is implicitly mentioned that there is a problem related to the convergence where a common problem is found in the static analysis, where it is hard to reach convergence during the loading phase.

3.3.2 Numerical Size Effect – Mesh Size

The numerical size effect is closely related to mesh size dependency. When discussing mesh dependencies on NLFEA, according to Slobbe, Hendriks, & Rots (2013), it can be categorized into 2 categories, directional mesh bias and mesh size sensitivity. Directional mesh bias can be defined as the preference of strain localization to follow the mesh lines. Strain localization is a phenomenon of a sudden change from smooth strain patterns to a rapid increase in strain distributions on the localized band with a decrement of strain in the adjacent parts of the structure. In order to solve this problem, Bazant & Oh (Crack Band Theory for Fracture of Concrete, 1983) recommend using uniform square mesh for unknown crack path, because the element width is equal and would not introduce any bias due to favourable crack paths on the element. Balakrishnan & Murray (1986) gave a more precise range on the element aspect ratio, which should be between 1 and 2 to reduce the directional bias on the crack formation. In this thesis, this limitation of element aspect ratio will be considered because the problem with directional mesh bias will not be addressed and discussed further.

Mesh size sensitivity is related to the sensitivity of the result to the change of used element size in the finite element model. Mesh size sensitivity should have been solved with crack band theory. According to Bazant & Oh (Crack Band Theory for Fracture of Concrete, 1983), the crack band theory can be applied for crack mode 1 in order to solve the problem with mesh dependencies. The use of crack bandwidth on the tension softening modulus can only be applied for element size less than $\frac{2G_F E_c}{f_t^2}$. The use of a larger element size could be done by reducing the tensile strength and assuming a sudden stress drop to 0 after reaching tensile strength. The reduction of tensile strength can be calculated with $f_{t,red} = \sqrt{\frac{2E_c G_F}{h_{ele}}}$.

However, several papers still indicate problems with mesh size sensitivity. In Choi & Kwak (1990) works, the mesh size influences the load-displacement curve, especially post-cracking stage behaviour. In order to solve this problem, a modification is added to either the stress-strain curve of the reinforcement or adding a linear descending branch to the stress-strain curve of the concrete. This proves to solve the problem when combined with fixed crack with constant shear retention of 0.4 on beams with $a = 900$ mm; $h = 300$ mm; $a/d = 3$ and $a = 1800$ mm; $h = 500$ mm; $a/d = 3.6$.

This problem also came up in Shayanfar, Kheyroddin, & Mirza (1997) works where it was mentioned that mesh size influence not only the load-displacement curve, but also load-strain characteristic, crack pattern and the failure load. 2 specimens are studied in this paper: under-reinforced Beam A ($a = 900$ mm; $d = 270$ mm; $a/d = 3.33$; $h = 300$ mm) and over-reinforced Beam B ($a = 900$ mm; $d = 260$ mm; $a/d = 3.46$; $h = 300$ mm). Variation on the mesh size in terms of element is employed to study this problem: 4 (450 x 300 mm)

$[h]$, 20 (150 mm) $[h/2]$, 30 (125 mm) $[h/3]$, 80 (75 mm) $[h/4]$, 120 (60 mm) $[h/5]$, 320 (35 mm) $[h/9]$ elements. As a result, a smaller mesh model produces a lower failure load in under-reinforced concrete with the overall response is influenced by mesh size. The change in overall response is caused by the rate of crack progression where it would decrease when the mesh size increase and in turns makes the structure has more energy dissipation capacity compared to smaller mesh size. In over-reinforced concrete, the failure loads are not significantly influenced by the mesh size due to its high ratio of tensile reinforcement. This reduces the influence of cracking on the material non-linearity of the concrete to the overall response. The problem can either be solved by changing the tensile strength or the ultimate strain. The results in the paper indicated that the influence of change in tensile strength is not as significant as the influence of change in ultimate strain. The ultimate strain can be modified based on the following expression to get a better result with linear strain-softening: $\varepsilon_{tu} = 0.004e^{-0.2h_{ele}} \geq \varepsilon_{cr}$.

Khalfallah, Charif, & Naimi (2004) also found a problem regarding mesh size sensitivity and recommend the use of a tension linear softening model in order to completely avoid mesh dependency. Khalfallah, Charif, & Naimi (2004) suggested that the use of the tension linear softening model would be mesh independent if the mesh size is smaller than $7a_g$ (≈ 178 mm).

Cervenka V., Cervenka, Pukl, & Sajdlova (2016) suggested another way to solve the mesh dependency problem, where the tension softening is modelled with the use of exponential function according to the Hordijk model. This still creates a problem regarding mesh size sensitivity. This is observed from comparison study of one specimen ($b = 250$ mm; $h = 4000$ mm; $a = 12000$ mm; $a/d = 3.12$) which is modelled with a variation on the mesh size of $h/80$, $h/40$, $h/20$, and $h/10$. The mesh refinement cause increase in stiffness on the load-displacement curve due to the difference in cracked concrete contribution to the reinforcement stiffness, which strongly relates to concrete tension stiffening, where bigger mesh size has smaller reinforcement stiffness due to larger volume of cracked concrete. The influence of mesh size sensitivity is dependent on the crack path from strain localization of different mesh sizes and element types. The recommendation on optimal mesh size for strength prediction is 100 mm $[h/40]$ for linear square element and 200 mm $[h/20]$ for quadratic element. This is further proven by de Putter (2020) where the model uncertainty increases as the element size decrease on reinforced beams without shear reinforcement with rotating and fixed (damage based) crack model. The recommended mesh size is $h/20$ with quadratic element, which is in line with the recommendation given by Cervenka V., Cervenka, Pukl, & Sajdlova (2016). It was also mentioned that the element size of 60 mm is too large to objectively model beams without shear reinforcement, which also indicates that minimum element size might be required to be specified.

Another insight regarding this problem is also given by Cervenka & Laserna (2018), where the magnitude of the crack band in tension should also consider the spacing of reinforcement and element size. The use of a mechanical model of strain-softening to represent non-linear behaviour would have severe mesh dependency and a tendency of going to zero energy dissipation as the element size reduce. In order to reduce the mesh dependencies, limitations based on aggregate size and reinforcement spacing on the crack bandwidth could be applied to the model. In the element with tension stress, the crack bandwidth should be limited below the stirrup spacing s_c (the typical range of 150-300 mm) and above $1.5a_g$ (the typical range of 10-50 mm).

Another suggestion regarding NLFEA in terms of computation time is given by Teshome (2019). In order to reduce computation time in NLFEA, Teshome (2019) suggested the use of a combination of big mesh with mesh refinement along the shear span, as it has been proven to give better prediction in terms of load-displacement curve and failure mode compared to uniform big mesh.

3.4. Modelling Strategies for Size Dependencies Observation

Several modelling strategies have been given in subchapter 3.2.2. However, the input of numerical parameters used in combination with the material and constitutive models are not defined clearly in these works of literature. Therefore, those modelling strategies are not used and remain an option in case the chosen modelling strategies encountered a problem where the failure mode cannot be simulated properly.

The modelling strategies used as a starting point of this study is based on de Putter (2020) works. The recommended modelling strategies for beams without shear reinforcement (limited to $h = 600$ mm) are to use the mesh size of $h/20$, a maximum of 100 iterations per step, include the FIB unconfined bond-slip model, and use convergence tolerance of $G_{err} = 0.0001$ and $F_{err} = 0.01$ which must be satisfied simultaneously. In de Putter (2020) works, the highest retained load in a converged load step can be assumed as the failure load. This strategy is chosen because all concrete properties and reinforcement are also modelled based on the Guidelines for Nonlinear Finite Element Analysis of Concrete Structures (Hendriks & Roosen, 2020). These recommendations give results with a small error range from -18% to +2% for fixed crack and -13% to +5% for rotating crack (based on 101 samples).

3.5. Summary

The experimental size effect has been recognized as a constant phenomenon that always influences the beam shear strength. Several works of literature provide insight on how to account for and calibrate this effect on NLFEA, but no papers have been able to prove that their solution could work on a bigger variation of geometries. Furthermore, some papers results contradict each other, such as the use of other forms of tension softening curve and the use of smeared reinforcement. As there is no clear explanation can be found regarding how each component on NLFEA works and influence the results, an explicit numerical model will be used where all components will be modelled separately with details that are in line with the Guidelines for Nonlinear Finite Element Analysis of Concrete Structures (Hendriks & Roosen, 2020). Furthermore, as this study focuses on observing the numerical size effect, the classification defined by Bazant & Yu (Universal Size Effect Law and Effect of Crack Depth on Quasi-Brittle Structure Strength, 2009) regarding two types of experimental size effect will not be discussed further.

As there is little information related to the problem of convergence and analysis configuration in NLFEA, this thesis will focus on investigating this problem. The investigation will be done for several factors that have not been specified in the Guidelines for Nonlinear Finite Element Analysis of Concrete Structures (Hendriks & Roosen, 2020) will also be evaluated, such as load steps, error tolerance, and non-converged steps. This is also done to clarify the opinion given by Choi & Kwak (1990) regarding its non-significance influence on the results and help gives some insights to solve the problem implicitly mentioned by Malm & Holmgren (2008).

The mesh size dependency problem has claimed to be solved by Bazant & Oh (Crack Band Theory for Fracture of Concrete, 1983). However, several papers still found the same problem even after applying the offered solution by Bazant & Oh (Crack Band Theory for Fracture of Concrete, 1983). Some papers give insights on how to minimize this effect, such as modifying fracture energy with ultimate tensile strain and defining limits on the mesh size. The limit of mesh size will be re-evaluated in order to see whether the current limit can be used to simulate shear failure in NLFEA. The modification of fracture energy will not be done as this could change the failure mechanism.

In order to study all these problems, the modelling strategies of de Putter (2020) in subchapter 3.4 will be used as a starting point in this thesis, as it provides a small error range for both crack models based on a large range of samples.

4 Identification of Problem Related to Convergence

The investigation of the numerical size effect begins with identifying the problem related to convergence. The problem related to the convergence is identified in this chapter. All details regarding the simulation in the NLFEA is specified in subchapter 4.1. In order to be able to evaluate the result of NLFEA and avoid a mistake in the modelling process, several types of verifications must be done. There are three components that are going to be verified in the result of NLFEA, the simulated elastic stiffness, the simulated first crack occurrence, and the convergence state of the steps in NLFEA. The verification of the first two components is done by comparing the simulated value to the analytical value. These verifications are done in subchapter 4.3. The verification of the convergence state is done by checking the status of convergencies in each step of the analysis and the simulated global behaviour in the load-displacement curve. The detail of this verification is given in subchapter 4.4. The verification of the convergence state has a problem that will be investigated further in chapter 5. In order to reduce the computational time, the number of elements and components should be reduced. The numerical model can be simplified by investigating the effect of simultaneous satisfaction of the convergence norms and the inclusion of top reinforcement, which are done in subchapters 4.6 and 4.7. Subchapter 4.5 will gives an explanation regarding the simulated process of crack propagation in the reinforced concrete beam without shear reinforcement with flexural shear failure mode. This subchapter will be used as an aid for the study in subchapters 4.6 and 4.7 and chapters 5 and 6. It must be noted that any figure with a crack pattern, such as Figure 4.14, is only used to be studied qualitatively. The value of Ecw always indicates a range from uncracked element $(Ecw = 0)$ to fully cracked element $(Ecw = CW_{t,u})$. A fully cracked element is defined as an element which has lost all its fracture energy. The value of Ecw should not be used as a reference for any study related to the experimental crack width because it does not consider the effect of localised reinforcement, which should have decreased the crack opening around the reinforcement.

4.1. Experimental Set-Up for Convergence Problem Identification

In order to be able to observe the influence of numerical size effect in NLFEA, the case study must be modelled with finite element analysis with a certain configuration and analyse with a certain procedure. Two beams are chosen for the study of numerical size effect, where both beams have comparable shear slenderness with a large difference in both shear span (a) and beam depth (d). Furthermore, both beams also have a significant difference in shear strength, which can be seen in Table 4.1. The configuration of the beams is illustrated in Figure 4.1. The red line in Figure 4.1 indicated the position of the reinforcement. All components of the beam are modelled explicitly, where the concrete, reinforcement, loading plate, support plate, and the interaction of each component are modelled separately. The geometries of the beams, reinforcement and loading and support plate are presented in detail in Table 4.2 and Table 4.3 respectively.

Table 4.1 Beam Experimental Shear Strength

Test Specimen	P_u	P_δ
A123A1	136.5	25
H123A	445	17
Dimension	[kN]	[mm]

Source: (Koekkoek & Yang, 2016) and (Yang, Shear Behaviour of Deep RC Slab Strips (Beams) with Low Reinforcement Ratio, 2020)

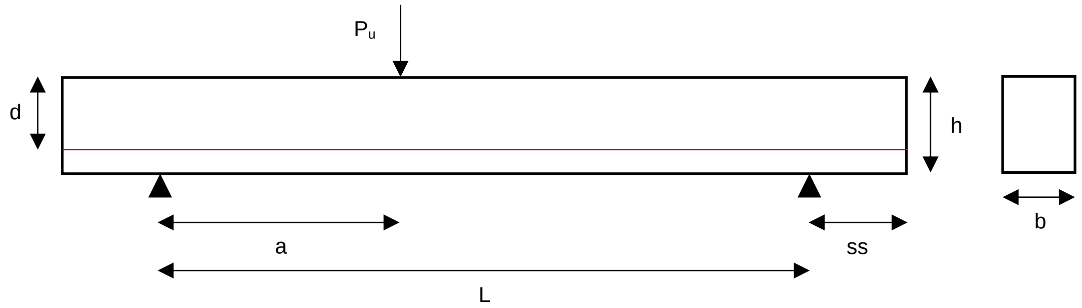

Figure 4.1 Beam Configuration and the Boundary Conditions

Table 4.2 Beam Geometry

Test Specimen	b	h	a	L	d	$M/Vd\ (a/d)$	ss
A123A1	300	300	1000	5000	270	3.70	500
H123A	300	1200	4500	9000	1150	3.91	500
Dimension	[mm]	[mm]	[mm]	[mm]	[mm]	-	[mm]

Source: (Koekkoek & Yang, 2016) and (Yang, Shear Behaviour of Deep RC Slab Strips (Beams) with Low Reinforcement Ratio, 2020)

Table 4.3 Reinforcement and Plate Geometry

Test Specimen	Top Rebar Config.	Btm Rebar Config.	ρ_l	b_p	L_p	h_p
A123A1	$3Ø20$	$3Ø20$	1.16	300	100	10
H123A	$2Ø20$	$8Ø25(2L)*$	1.14	300	100	10
Dimension	-	-	[%]	[mm]	[mm]	[mm]

Source: (Koekkoek & Yang, 2016) and (Yang, Shear Behaviour of Deep RC Slab Strips (Beams) with Low Reinforcement Ratio, 2020)

* $(2L)$: 2 layer of reinforcement

All models would only consider physical non-linear effects. The material properties are derived based on Guidelines for Nonlinear Finite Element Analysis of Concrete Structures (Hendriks & Roosen, 2020). All non-linear material properties for concrete are calculated based on available experimental data of mean concrete compressive strength. For the case of reinforcement, the experimental data of yield strength and ultimate strength are used. These experimental data are referred to as primary material properties and all derived properties are referred to as secondary material properties. The primary material properties are shown in Table 4.4. The secondary material properties for concrete and reinforcement are shown in Table 4.5 and Table 4.6 respectively. These properties are used for constructing the constitutive model in the numerical model. All constitutive models are chosen based on the recommendation given in Guidelines for Nonlinear Finite Element Analysis of Concrete Structures (Hendriks & Roosen, 2020) in combination with the modelling strategies of de Putter (2020). Figure 4.2 and Figure 4.3 gives an illustration of the constitutive model for concrete and reinforcement respectively.

Table 4.4 Primary Material Properties

Test Specimen	f_{ck}	f_{yk}	f_{tk}	SW_c	SW_s	SW_{pl}
A123A1	56.94	550	613	23.9	78.5	0
H123A	60.05	550	613	23.9	78.5	0
Dimension	[MPa]	[MPa]	[MPa]	[kN/m^3]	[kN/m^3]	[kN/m^3]

Source: (Koekkoek & Yang, 2016) and (Yang, Shear Behaviour of Deep RC Slab Strips (Beams) with Low Reinforcement Ratio, 2020)

Table 4.5 Concrete Secondary Material Properties

Test Specimen	E_{cm}	υ_c	f_{ctm}	G_{Fk}	G_{Ck}	$\beta_{\sigma,min}$
A123A1	38564.21	0.2	4.270011	0.11	33.92	0.4
H123A	39108.81	0.2	4.35615	0.11	34.42	0.4
Dimension	[MPa]	-	[MPa]	[N/mm]	[N/mm]	-

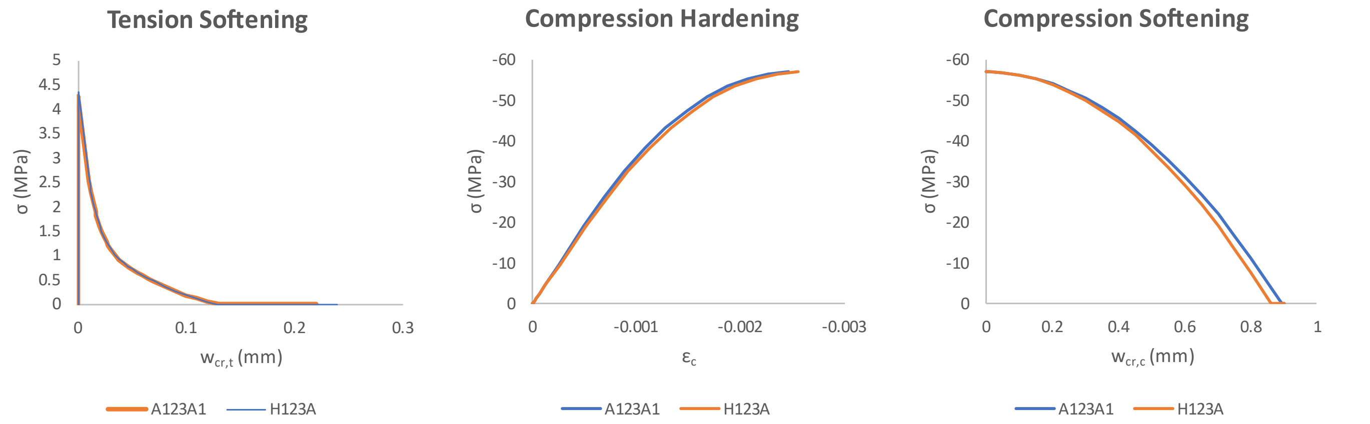

Figure 4.2 Constitutive Models for Concrete Element in the Numerical Model

The non-linear behaviour of the concrete is presented with reference to $w_{cr,t}$ and $w_{cr,c}$ as it can give a general illustration which is independent from the mesh size. $w_{cr,t}$ and $w_{cr,c}$ are calculated from the multiplication of crack strain to the mesh size.

Table 4.6 Reinforcement Secondary Material Properties

Test Specimen	E_s	υ_s	f_{tk} / f_{yk}	Class*	ε_{uk}
A123A1	200000	0.3	1.11	B	5
H123A	200000	0.3	1.11	B	5
Dimension	[MPa]	-	-	-	[%]

* Class = the hardening class of reinforcement based on f_{tk} / f_{yk} ratio

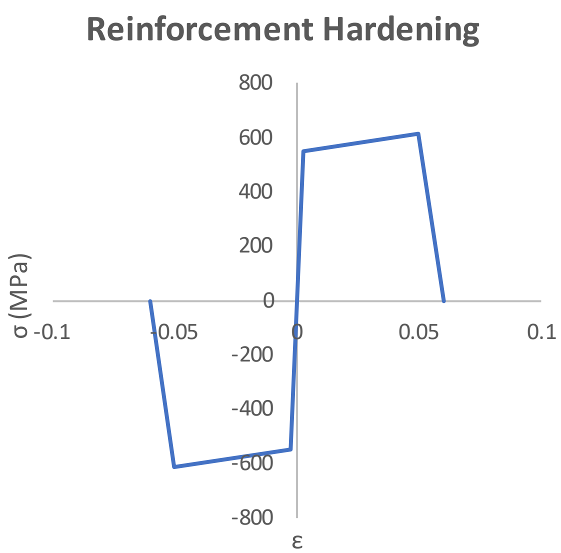

Figure 4.3 Constitutive Models for Reinforcement Element in the Numerical Model

The loading and support plates are modelled only to avoid singularities phenomena on the beam. Therefore, the non-linear behaviour of the beam is not necessary to be modelled. The material properties of the plates are given in Table 4.7.

Table 4.7 Loading and Support Plate Member Material Properties

Test Specimen	E_{pl}	υ_{pl}
A123A1	200000	0.3
H123A	200000	0.3
Dimension	[MPa]	-

In this thesis, it is assumed that the concrete and the reinforcement is perfectly bonded for top reinforcement and not perfectly bonded for bottom reinforcement, where some slip could occur between these components. This assumption is recommended to be used by de Putter (2020), where the assumption of a perfect bond between concrete and reinforcement would cause over-rotation on the direction of the principal stress near the reinforcement that would always create de-lamination failure on most of the finite element model for three-point loaded beam. The bond-slip behaviour is modelled with FIB Model Code 2010 local bond-slip model for ribbed bars. The first part of the bond-slip model is constructed from exponential equations, which would cause a numerical problem when there is no slip $(s=0)$. In order to avoid this problem, the software package DIANA assumed that up until a certain magnitude of slip (s_0), linear relation of bond stress and slip is used. A dummy stiffness also needs to be assigned to the bond-slip model based on the software package DIANA requirement. The dummy stiffness can be calculated with equations (4.1) and (4.2). All parameters value used for the bond-slip model is given in Table 4.8. The illustration of the constitutive model of FIB Model Code 2010 local bond-slip model is given in Figure 4.4. The assumption of the linear bond-slip in DIANA must be checked with the reference in FIB Model Code 2010 to see whether the value of s_0 is sufficiently small, as given in Figure 4.4 where the difference in the bond-slip is very small.

$$B_n = \frac{100E_{cm}}{h_{ele}} \tag{4.1}$$

$$B_t = 0.1B_n \tag{4.2}$$

Table 4.8 Parameters for Local Bond-Slip Model for Ribbed Bars

Test Specimen	$\tau_{b,max}$	$\tau_{bu,split}$	τ_{bf}	s_0	$s_{1,ref}$	s_1	s_2	s_3	α	B_n	B_t
A123A1	20.15	8.89	0.001	0.01	1	0.13	0.13	0.16	0.4	257095	25709.5
H123A	20.62	8.99	0.001	0.01	1	0.13	0.13	0.15	0.4	65181.3	6518.13
Dimension	[N/mm^2]	[N/mm^2]	[N/mm^2]	mm	mm	mm	mm	mm	-	[N/mm^3]	[N/mm^3]

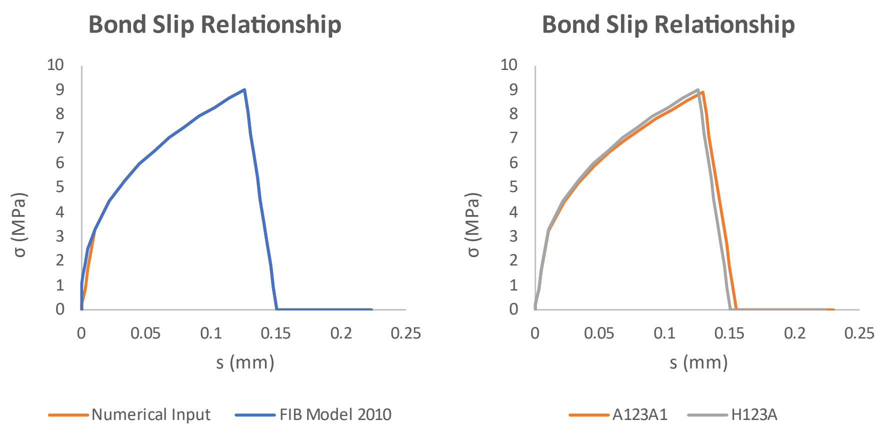

Figure 4.4 Constitutive Models for Local Bond-Slip of the Bottom Reinforcement in the Numerical Model

In order to diminish plate contributions to the beam stiffness and prevent any localized tensile stress to build up on the corner of the plate where it connects to the beam, an interface with the properties of 'no-tension with shear stiffness reduction' is assigned on the connection between the beam and the plate. A dummy stiffness needs to be assigned to the interface for the linear behaviour. The dummy stiffness can be calculated with equations (4.3) and (4.4), according to (Teshome, 2019). The value of the parameters of the interface is given in Table 4.9.

$$k_{dum,ax} = \frac{E_{cm}}{h_{ele}} \tag{4.3}$$

$$k_{dum,sh} = 0.01 k_{dum,ax} \tag{4.4}$$

Table 4.9 Parameters for Plate-Beam Interface

Test Specimen	$k_{dum,ax}$	$k_{dum,sh}$	critical interface opening for a reduction in tension	critical interface opening for a reduction in shear	normal stiffness reduction factor	shear stiffness reduction factor
A123A1	2570.95	25.71	0.001	0.001	0	0
H123A	651.81	6.52	0.001	0.001	0	0
Dimension	[N/mm^3]	[N/mm^3]	mm	mm	-	-

The beams are modelled with quadratic (8-noded) plane stress elements. The reinforcement is modelled with equivalent axial stiffness, where the total area of the bars is converted into 1 bar, and the element have the same behaviour as a beam element. All models would be subjected to an external load. The external load is applied as a prescribed displacement equal to the total beam deformation in the experiment in Table 4.1.

The solution procedure used for the analysis is the iterative-incremental procedure, as indicated in subchapter 2.1 Non-Linear Finite Element Analysis. The load would be applied progressively (displacement-controlled analysis) with a certain number of load steps as indicated in Table 4.10. The error tolerance/convergence norms must be defined in order to use the selected solution procedure. Guidelines for Nonlinear Finite Element Analysis of Concrete Structures (Hendriks & Roosen, 2020) gives the recommendation to use both energy norms and force norms. All parameters related to the solution procedures are given in Table 4.10.

Table 4.10 Load Step and Convergence Norms

Test Specimen	n_p	n_{max}	F_{err}	G_{err}	Satisfy All Norms
A123A1	100	100	0.01	0.0001	Yes
H123A	100	100	0.01	0.0001	Yes

Several variations are made for this study in order to identify the source of problems in NLFEA, which are cracking models, simultaneous satisfaction of all norms, the inclusion of top reinforcement, and different type of iterative-incremental procedures. Two different cracking models are explored in this subchapter in order to see their impact on the global behaviour of the beam. The effect of satisfying all norms at the same time is also investigated to see its importance on the numerical models. The necessity to model top reinforcement also investigated at the global level in order to see its importance on the numerical models.

Three different iterative-incremental procedures are explored in this subchapter, the Quasi-Newton – Crisfield type method and Full Newton-Raphson. Teshome (2019) indicated that the Quasi-Newton method is more suitable to be used for the analysis of concrete structures. Full Newton-Raphson is the solution procedure used by de Putter (2020). The overview of the model variations is given in Table 4.11.

Table 4.11 Model Variations 1

Variation	Cracking Model	Satisfy All Norms	Top Reinf. Inclusion	Iterative-Incremental Procedure
R	Rotating	Yes	No	Quasi-Newton
F	Fixed	Yes	No	Quasi-Newton
R_NO SIMULT	Rotating	No	No	Quasi-Newton
F_ NO SIMULT	Fixed	No	No	Quasi-Newton
R_TR	Rotating	Yes	Yes	Quasi-Newton
F_TR	Fixed	Yes	Yes	Quasi-Newton
R_NR	Rotating	Yes	No	Full Newton-Raphson
F_NR	Fixed	Yes	No	Full Newton-Raphson

4.2. Verification Method for Results of Finite Element Analysis

The results of NLFEA are verified with the initial stiffness of the beam, the first crack occurrence on the beam, and the convergence state of each step. The initial stiffness can be calculated analytically based on the formulation of the Timoshenko Beam with equation (4.5), which accounts for both bending and shear deflection of the beam. The first crack occurrence can be calculated based on the maximum tensile strength of the concrete with equation (4.6). The magnitude of the initial stiffness and the first crack occurrence on the beam are given in Table 4.12. The convergence state that would be accepted as a valid result is the steps that either satisfy both norms, only one of the norms or non-converged only on one step and followed with converged steps afterwards.

$$k_{init.} = \frac{P_u}{\delta_{ela}}$$
$$\delta_{ela.} = \delta_{bend} + \delta_{sh}$$
$$\delta_{bend} = \frac{P_u (L-a)^2 a^2}{3E_{cm} IL} \qquad \delta_{sh} = \frac{P_u (L-a) a}{G_c AL} \tag{4.5}$$
$$I = \frac{1}{12} bh^3 \qquad A = bh \qquad G_c = \frac{E_{cm}}{2(1+\upsilon_c)}$$

$$F_{cr} = \frac{M_{cr} L}{(L-a)a}$$
$$M_{cr} = \frac{1}{6} bh^2 f_{ctm} \tag{4.6}$$

Table 4.12 Analytical Initial Stiffness and First Crack Occurrence of the Beam

Test Specimen	$\delta_{ela.}$	$k_{init.}$	M_{cr}	F_{cr}
A123A1	5.67	24.08	19.22	24.02
H123A	4.17	106.69	219.55	97.58
Dimension	[mm]	[kN/mm]	[kNm]	[kN]

4.3. Stiffness and First Crack Verification

The results of NLFEA that are used for verification of initial stiffness and first crack occurrence are results with linear analysis, as this verification confirms whether the input is correct or not. The results of the NLFEA for the verification of initial stiffness can be seen in Table 4.13.

Table 4.13 Elastic Stiffness Verification

Test Specimen	$k_{init.}$	$k_{FEM,nr}$	$k_{FEM,r}$	$k_{FEM,nr}$ / $k_{init.}$	$k_{FEM,nr}$ / $k_{init.}$
A123A1	24.08	23.86	26.07	0.99	1.09
H123A	106.69	104.82	116.28	0.98	1.11
Dimension	[kN/mm]	[kN/mm]	[kN/mm]	-	-

When the stiffness from the NLFEA results without reinforcement is compared to the initial stiffness, the stiffness value is very similar, as indicated by the relative value of the stiffness that almost equal to 1 for both specimens. This indicates that all inputs are correct. Furthermore, the inclusion of reinforcement would slightly increase the overall stiffness of the beam.

The results of the NLFEA for the verification of the first crack occurrence can be seen in Table 4.14. The difference in the first cracking forces of the NLFEA and the analytical cracking force is caused by the size of the load step and the lack of initial imperfection on the model. The use of smaller load steps would be able to decrease the first cracking force on the beam. The use of different cracking models does not show any significant difference in any variations, which indicates that the first crack occurrence in the simulation is independent of the concrete cracking models. The difference between the first cracking forces on each variation of the model shows a similar pattern on both specimens, where the difference becomes larger when top reinforcement is included in the model. Furthermore, a higher difference can also be seen when the norms are not simultaneously satisfied, and the Full Newton-Raphson method is used.

Table 4.14 First Crack Occurrence Verification

Test Specimen	A123A1	H123A	Dimension
F_{cr}	24.02	97.58	[kN]
R	29.19	160.26	[kN]
R_NO SIMULT	32.65	189.03	[kN]
R_TR	31.58	149.46	[kN]
R_NR	32.65	189.04	[kN]
F	29.47	160.01	[kN]
F_NO SIMULT	32.65	189.03	[kN]
F_TR	31.27	149.44	[kN]
F_NR	32.65	189.04	[kN]

The inclusion of top reinforcement on the beam would increase the overall stiffness of the beam, where a similar effect can be observed in Table 4.13 with numerical models with and without bottom reinforcement. The increase of stiffness would indicate that the magnitude of the load resistance would be higher when the magnitude of the beam displacement is the same for these variants. However, a higher force due to change in norms satisfaction condition and the use of another iterative-incremental method indicate that the solution procedure configuration has a certain influence on the simulation of non-linear behaviour.

4.4. Convergence State Verification

The convergence state of all steps in the analysis must be verified. It is common to accept only the steps that are converging. However, it is hard to achieve fully converged analysis when simulating the failure of both specimens. This problem has been addressed by de Putter (2020) and a solution is given where the steps should be still considered valid up to the point where continuous non-convergence is spotted in the analysis. Figure 4.5 illustrates the difference in the load-displacement curve with and without the consideration of the convergence state in the analysis.

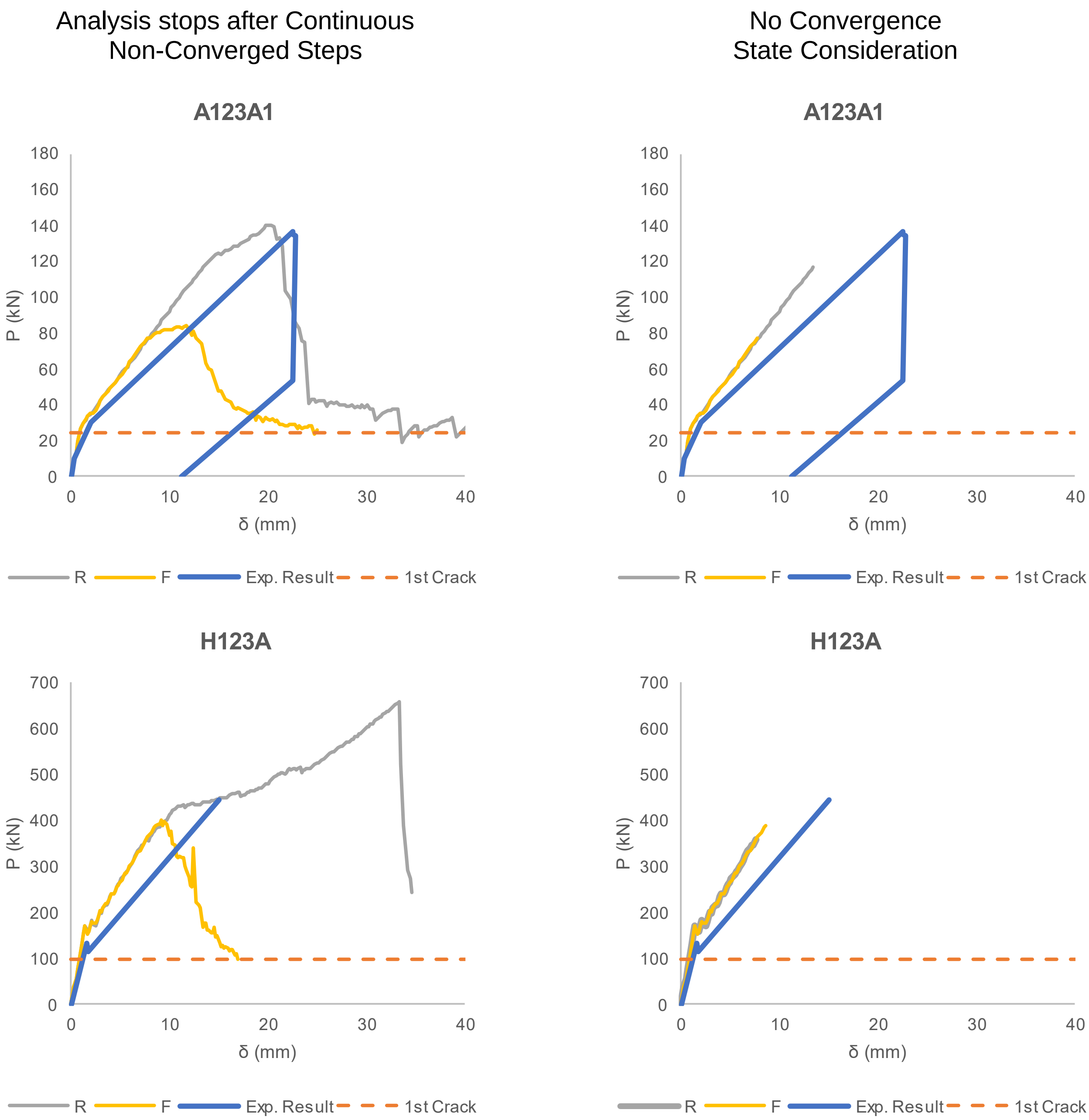

Figure 4.5 Load-displacement Curve with and without the Consideration of Convergence State

In Figure 4.5, a significant difference in the peak load can be seen in the numerical model with the rotating crack model while a small difference can be seen in the numerical model with the fixed crack model. Furthermore, the change in the non-linear stiffness cannot be observed in the numerical model with the rotating crack model and the peak load will be dependent on the convergence state of the analysis. The dependency on the convergence state of the step in the analysis should be avoided, as it will create a variety of peak loads with different numerical configurations. This problem can be solved by accepting all steps in the analysis regardless of its convergence state and investigate what is the cause of the non-convergencies of the steps at the later stage of the analysis.

Based on the results of the analysis, the convergence state of each variation is different compared to each other, where the continuous non-convergence starts at different load levels with different numerical configurations for one specimen. No model can achieve 100% convergence in all steps. As this thesis focuses on the estimation of the peak load and does not analyse the post-peak behaviour, the simulated behaviour up to the peak load is considered important and a comparison of the convergence state is done up to this point in order to have an insight of the overall pattern of the convergence state. There are 3 aspects that would be observed, the total number of steps, the total number of non-convergence steps, and the convergence level. The convergence level is defined as the percentage of converged steps based on the total number of steps up to the simulated peak load. The convergence level is calculated in order to see whether there is a consistent pattern between different numerical configurations and see the effect of change in the numerical configuration. These aspects can be observed in Figure 4.6. The load-displacement curve is also given in Figure 4.7 for specimen A123A1 and Figure 4.8 for specimen H123A to help understand the difference in the simulated global behaviour and whether it has a relation to the convergence state of the analysis.

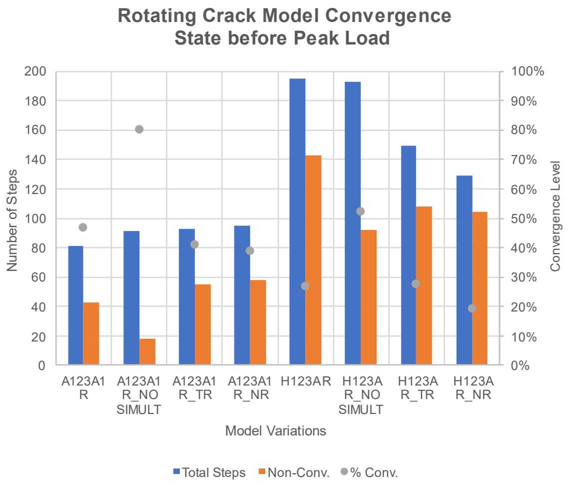

(a)

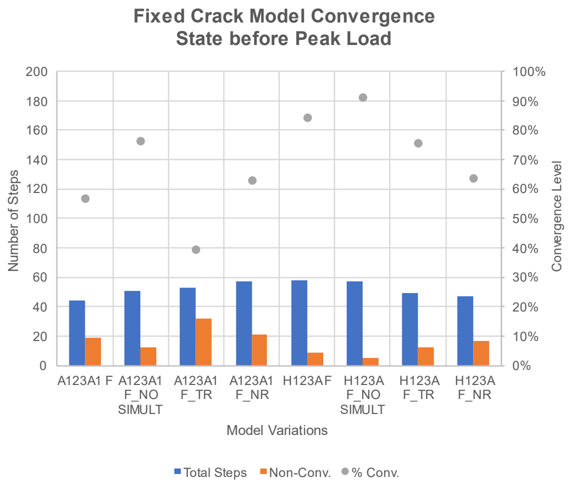

(b)

Figure 4.6 (a) Rotating and (b) Fixed crack model Convergence State

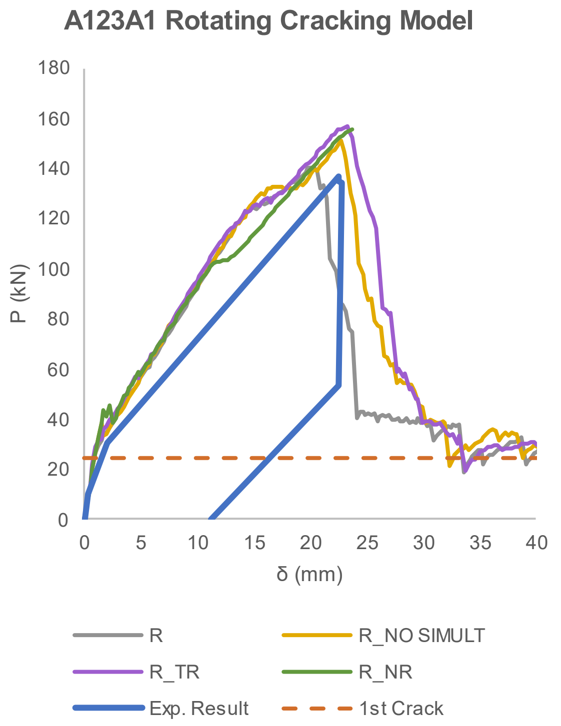

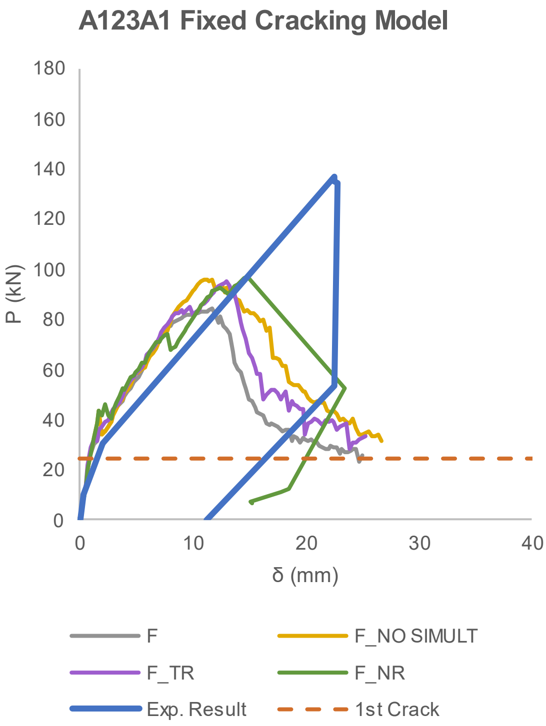

Figure 4.7 Load-displacement Curve Model A123A1 with Rotating and Fixed crack model

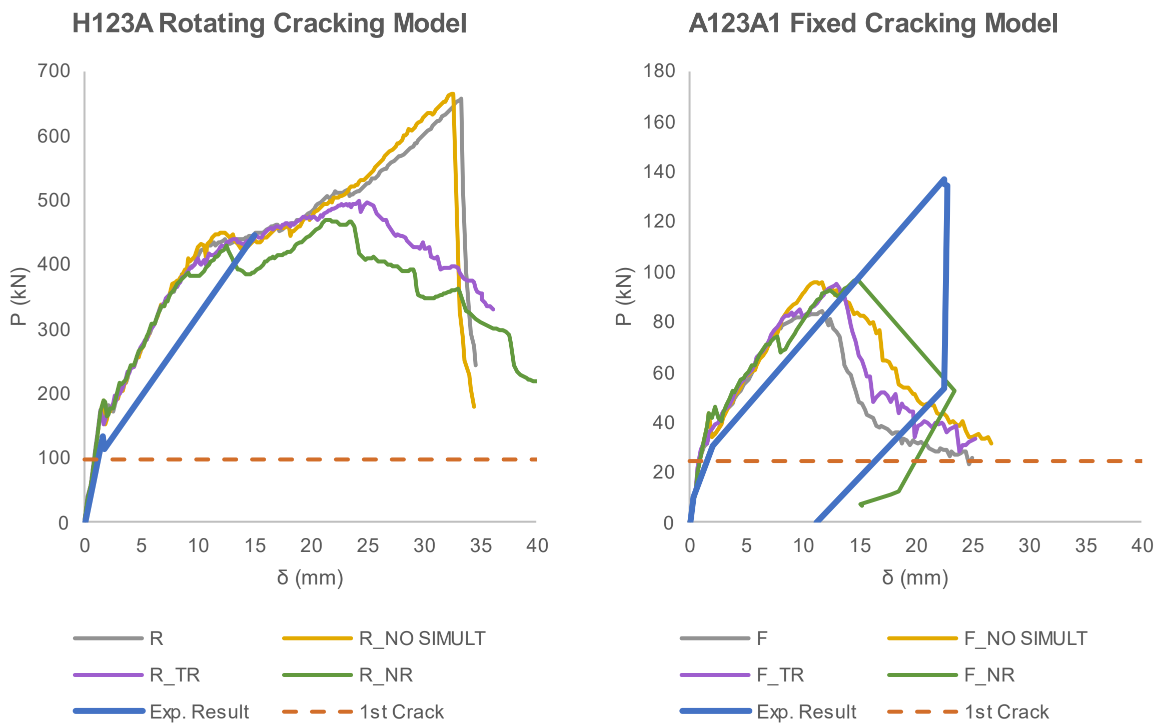

Figure 4.8 Load-displacement Curve Model H123A with Rotating and Fixed crack model

Figure 4.6 (a) shows that the overall model for specimen A123A1 need a smaller number of steps to reach its peak load compared to the overall model for specimen H123A1. The percentage of converged steps shows a similar pattern for both specimens, where the variation of R_NO SIMULT has a higher level of convergencies compared to other models. Furthermore, overall models of specimen A123A1 has a lower percentage of converged steps compared to specimen H123A. The variation of R_TR does not affect the convergence level of the model, as it has a comparable convergence level to variation R. The variation of R_NR also has a comparable level of convergence to variation R, which indicates that the use of both Quasi-Newton and Full Newton-Raphson method for rotating crack model would give comparable convergence level.

Figure 4.6 (b) shows a different pattern in terms of the number of steps required to achieve peak load and the influence of the iterative-incremental method on the convergence level. Overall results show that the number of steps required to reach its peak load is comparable in both specimens. The variation of F_NR shows that the level of convergence for both specimens is comparable. On the other hand, the variation of F for both specimens shows a huge difference in the convergence level.

On the other hand, it can be seen that Figure 4.6 (a) and (b) have a significant difference in the convergence level. This indirectly caused by a fewer number of steps in the numerical model with the fixed crack model, where fewer steps also mean less probability of the step becoming non-converged. Furthermore, the low total number of steps also indicate that the numerical model with a fixed crack model reached its peak faster compared to the numerical model with a rotating crack model. This is proven in Figure 4.7 and Figure 4.8 where the numerical model with the rotating crack model has a significantly higher peak load compared to the numerical model with the fixed crack model. Furthermore, the overestimation seems to be increasing from model for specimen A123A1 to specimen H123A in Figure 4.7 and Figure 4.8 for both types of cracking model.

In order to understand the difference in the convergence level between each variant, the convergence state of the analysis of each variant is plotted. An example of this plot can be seen in Figure 4.9. This figure illustrates the convergence state of each step in the analysis, whether a step reach convergence (this is when the relative energy variation and out-of-balance force are below its respective tolerance) or not. The determination of the convergence in a step is independent of its previous step and the connecting line is only used to show how the convergence change during the analysis.

The significant difference in convergence level of variation R and F to variation R_NO SIMULT and F_SIMULT can be explained by observing Figure 4.9 and Figure 4.10. These figures show that several load steps have already reach convergency after several iterations if the condition of simultaneous satisfaction of norms is not applied. This indicates that the convergence state on several steps change when a higher number of iterations is used on the steps. Another phenomenon that can be observed is that most of the steps only reach convergence in terms of energy variation. The dependency of the results to the number of iterations, force tolerance/norms and energy tolerance/norms would be investigated further in the next subchapter.

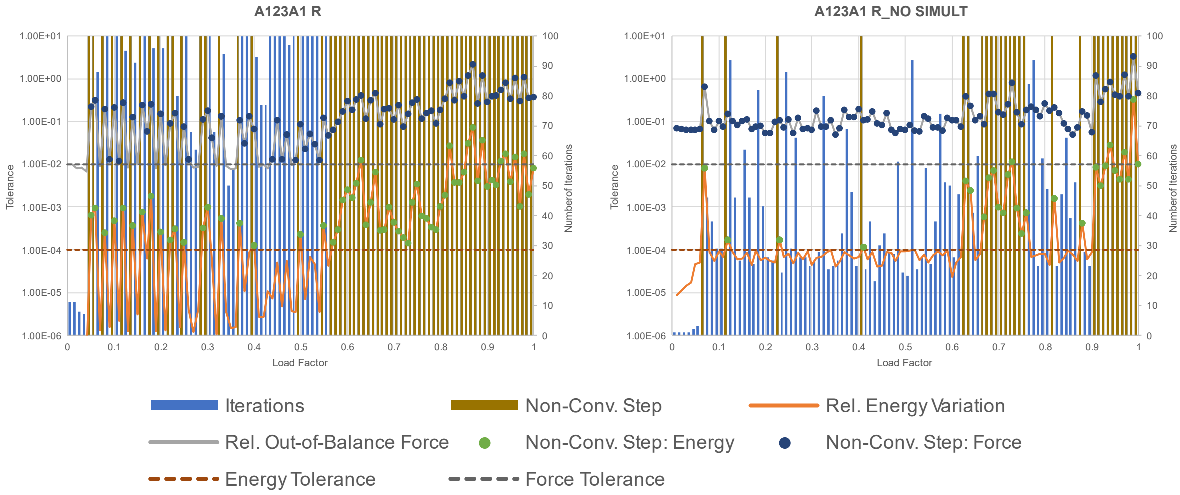

Figure 4.9 Convergence Behaviour of Variation R and R_NO SIMULT

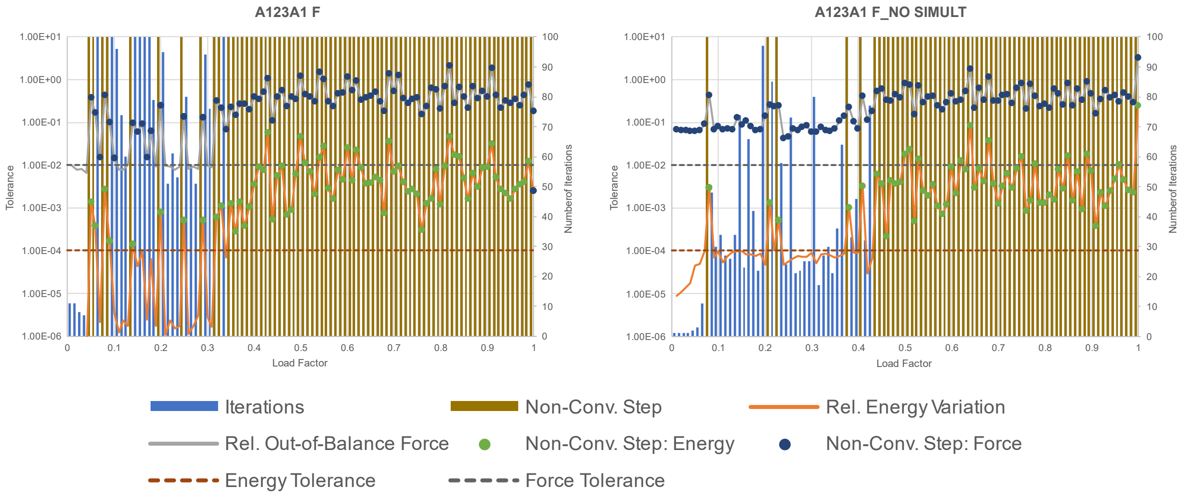

Figure 4.10 Convergence Behaviour of Variation F and F_NO SIMULT

The significant difference of convergence behaviour between different iterative-incremental method can be explained by observing Figure 4.11 and Figure 4.12. In any cracking model, the variation of R and F almost have all its converged steps at the beginning of the analysis. After exceeding load factor 0.5, almost little to none of the steps are converging anymore. On the other hand, the variation of R_NR and F_NR shows that the converged steps are distributed arbitrarily during the analysis. This phenomenon could be caused by the way these iterative-incremental methods form its stiffness matrix, where the Full Newton-Raphson method form a new stiffness matrix on every iteration in every step while the Quasi-Newton method derived the stiffness matrix based on the previous step stiffness matrix. This implicitly implies that the Quasi-Newton method would reach convergence more easily due to the small relative difference in terms of energy and force compared to the Full Newton-Raphson method. This phenomenon can be observed in H123A R and H123A F in Figure 4.11 and Figure 4.12 respectively. Furthermore, the relative difference in terms of energy and force would indirectly be carried as the load increase, thus reducing the chance of the steps to converge after a non-converged step with a relatively high difference in terms of energy and force, which can be observed in Figure 4.12.

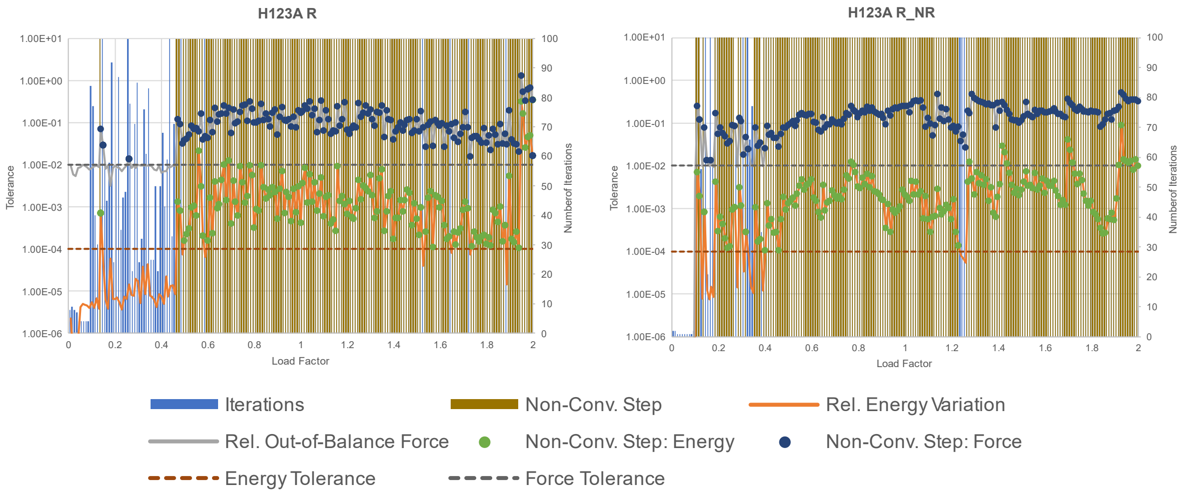

Figure 4.11 Convergence Behaviour of Variation R and R_NR

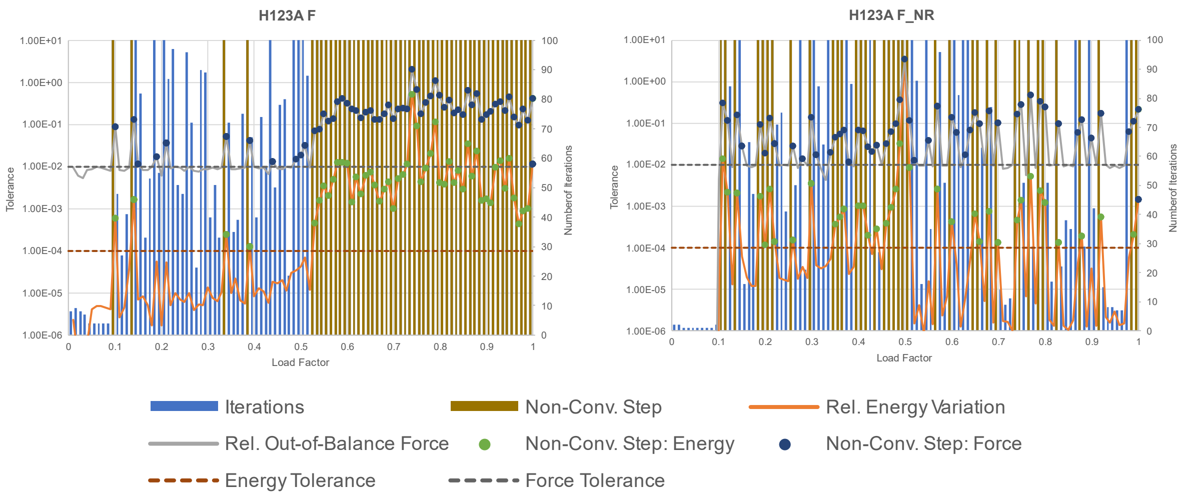

Figure 4.12 Convergence Behaviour of Variation F and F_NR

The problem of non-converged steps can be solved by refining the load increment and/or increase the maximum number of iterations per step. However, this would cause the proposed solution method to be time-consuming and impractical to be applied. In order to avoid this, further study regarding the effect of load increment would be studied further in the next subchapter. Increasing the maximum number of iterations would only be done if there is a significant difference when a small load increment is applied to the models.

In order to continue the analysis of the results of the NLFEA, it can be assumed that all steps give valid results regardless of its convergence state, as the difference between converged and non-converged steps in the results of the NLFEA can be assumed to be small, as indicated by de Putter (2020). In order to verify this assumption, sensitivity analysis will be done for the load increment, convergence norms (both energy and force norms), and the number of iterations for three methods of the iterative-incremental method, Quasi-Newton (Crisfield), Full Newton-Raphson, and Modified Newton-Raphson. Modified Newton-Raphson is also investigated as it is one of the popular choices for the iterative-incremental method. All numerical models will be using a rotating crack model in order to avoid severe underestimation from the use of a fixed crack model.

Some observations on the results of NLFEA for several models are presented in the next subchapter in order to see whether any simplification can be made on the models.

4.5. Correlation of Crack Propagation to the Beam Global Response

In order to be able to have a better understanding of the results of the NLFEA, the global response of the beam is observed through the load-displacement curve of the specimen. Another global response that would strongly be connected to the beam global response is the crack propagation process. In order to have a better understanding of the cracking progression and its effect on the load-displacement curve, the results of NLFEA for model A123A1 R is used to describe several phenomena on the cracking progression. The global response would be observed up to the peak capacity of the beam and no observation would be done for the post-peak behaviour of the beam. The load-displacement curve of model A123A1 R is illustrated in Figure 4.13. These observations focus on giving aid to the process of model simplification in subchapter 4.6 Effect of Simultaneous Satisfaction of the Convergence Norms and 4.7 Effect of the Inclusion of Top Reinforcement and help the analysis in chapter 5 Sensitivity Analysis of Convergence Parameters and 6 Sensitivity Analysis of Mesh Size.

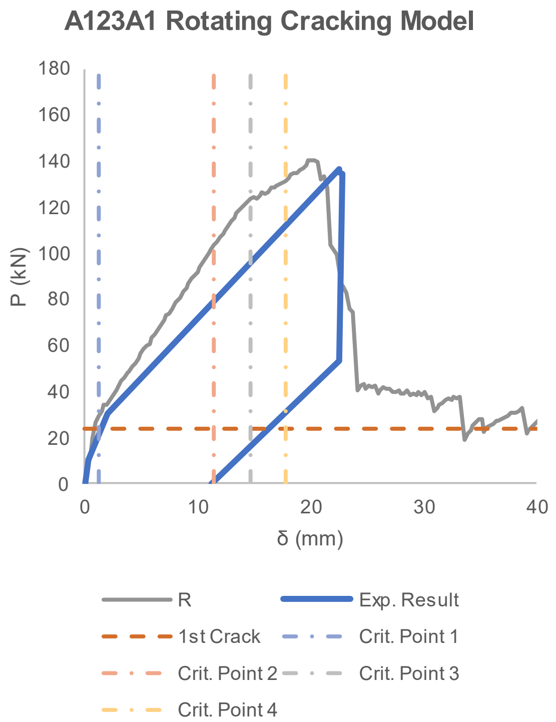

Figure 4.13 Load-displacement Curve of Model A123A1 R

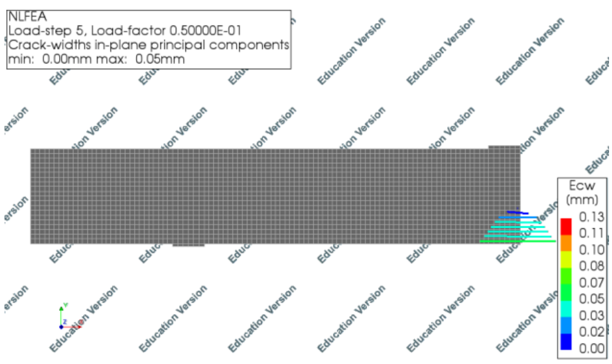

Figure 4.14 The Crack Pattern at Critical Point 1 of Model A123A1 R

At the first critical point, cracks start to form on the models. The first crack that forms on critical point 1 is flexural crack. The crack opening is mostly in the longitudinal direction. This marks the change in the overall stiffness of the beam, which causes a shift in the load-displacement curve in Figure 4.13. The illustration of the crack formation is given in Figure 4.14.

At the second critical point, one of the major cracks starts to turn into an inclined crack. As a result, the principal direction of the cracks on the inclined crack shift into diagonal, which indicates that the crack is opening in the longitudinal and vertical direction. At the low end of the inclined crack, small dowel cracks start to form. The crack inclination process does not affect the load-displacement curve in Figure 4.13.

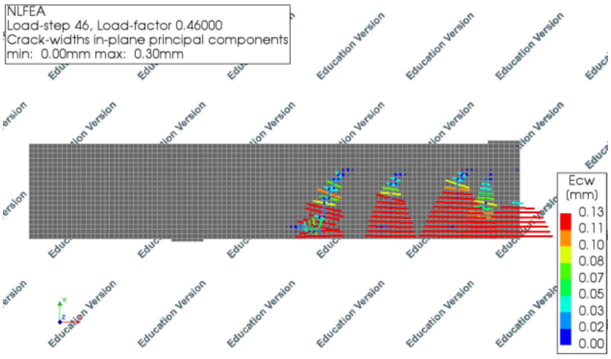

Figure 4.15 The Crack Pattern at Critical Point 2 of Model A123A1 R

At the third critical point, the major inclined crack has been formed. The dowel crack has formed halfway up to the support plate. The horizontal branch of the inclined crack starts developing at the top end of the inclined crack. These phenomena can be seen in Figure 4.16. At this cracking stage, the load-displacement curve is heavily influenced, as the overall stiffness of the model change and cause a shift on the curve, which can be seen in Figure 4.13.

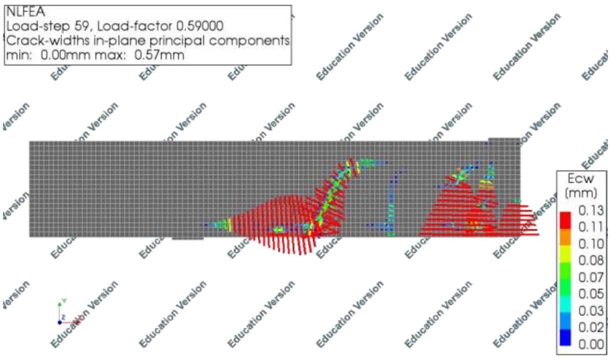

Figure 4.16 The Crack Pattern at Critical Point 3 of Model A123A1 R

At the fourth critical point, the major inclined crack has been fully formed. Furthermore, another major flexural crack formed another inclined crack. The dowel crack on the low end of the major inclined crack has formed up to the support plate. The horizontal branch of the inclined crack has developed halfway to the loading plate. These phenomena can be observed in Figure 4.17 (a). However, even with the formation of a new inclined crack, there is no significant change on the load-displacement curve, as the overall stiffness of the model does not change and no big shift on the curve can be spotted in Figure 4.13. At the peak load, the horizontal branch of the major inclined crack has propagated up to the loading point, as indicated in Figure 4.17 (b). An overview of these critical points is given in Table 4.15.

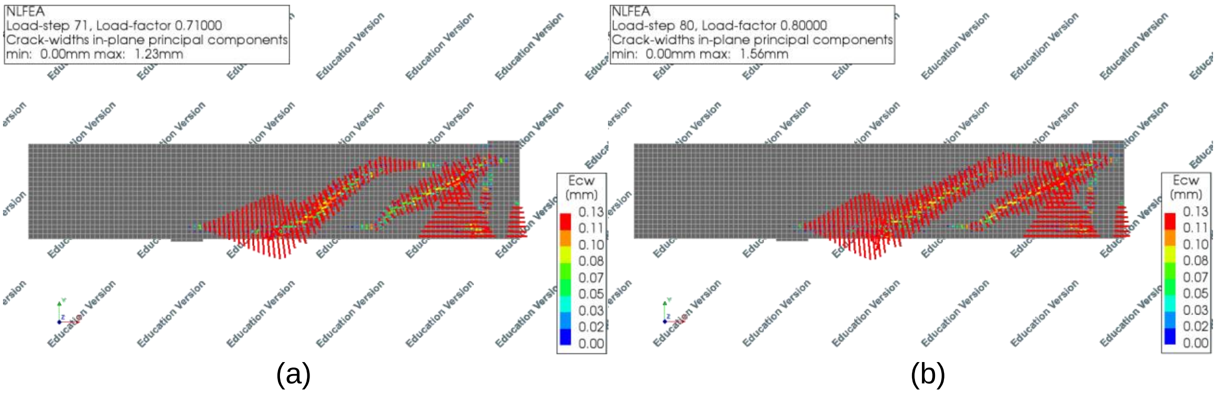

Figure 4.17 The Crack Pattern at (a) Critical Point 4 and (b) the Peak Load of Model A123A1 R

Table 4.15 Overview of each Critical Points of Figure 4.13

Critical Point	Events	Effects	Reference
1	Formation of flexural crack	Change in the simulated beam stiffness	Figure 4.14
2	Formation of inclined crack and dowel crack	-	Figure 4.15
3	Propagation of inclined crack, dowel crack halfway to support plate, and formation of horizontal crack at the top end of the inclined crack	Change in the simulated beam stiffness	Figure 4.16
4	Propagation of horizontal crack at the top end of the inclined crack	-	Figure 4.17 (a)
Peak Load	Fully formed flexural shear crack	Failure of the simulated beam	Figure 4.17 (b)

4.6. Effect of Simultaneous Satisfaction of the Convergence Norms

The effect of simultaneous satisfaction of the convergence norms is quite significant in terms of the load steps convergence state, as explained in 4.4 Convergence State Verification. However, when comparing the global response of the beam, the difference in the results is not very significant for either the rotating or fixed crack model. These results can be seen in Figure 4.18 and Figure 4.28 for the rotating and fixed crack model respectively. There are some small differences that can be spotted in both Figure 4.18 and Figure 4.28. These differences will be discussed further in this subchapter.

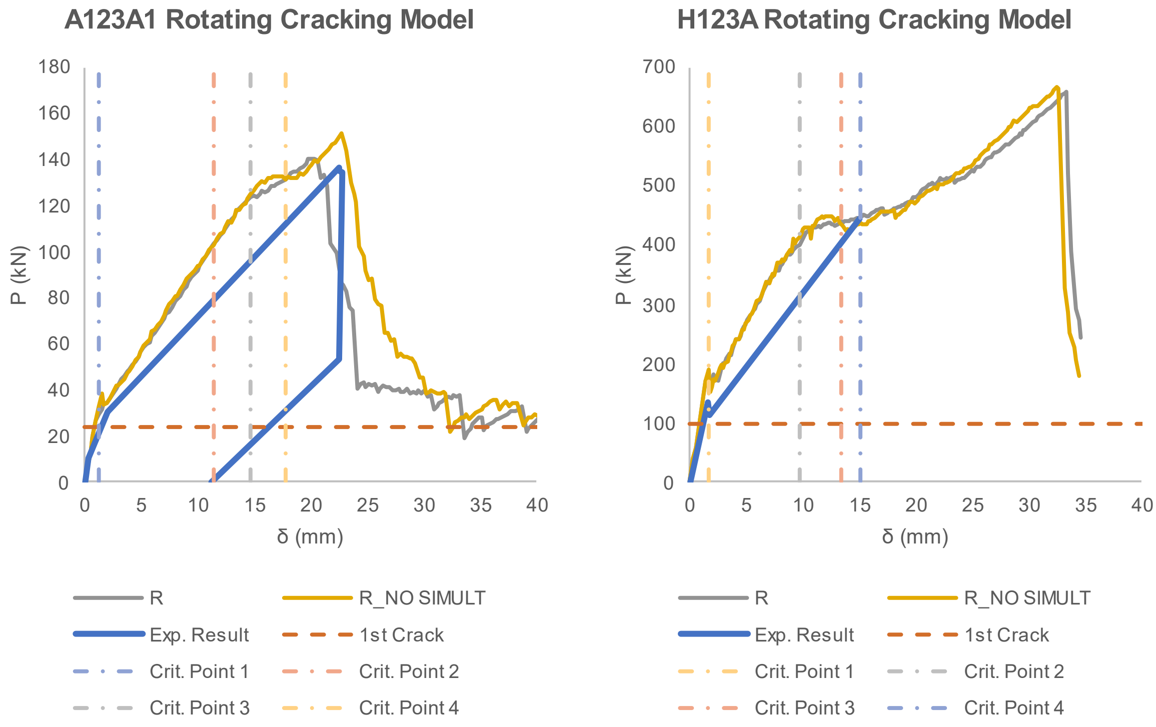

Figure 4.18 Comparison of the Global Behaviour of Model Variant R and R_NO SIMULT

In Figure 4.18, there are some deviations on critical points 1, 3 and 4 for specimen A123A1. Critical point 2 of specimen A123A1 is observed in order to clarify whether the cracking pattern is similar for both models when the load-displacement curves show a similar pattern. On the other hand, for specimen H123A in Figure 4.18, no significant difference can be seen in the load-displacement curve. Critical point 1 of specimen H123A is used to indicate the first cracking phenomenon. Critical points 2 and 3 are chosen to represent the change in stiffness on the load-displacement curve. Critical point 4 is chosen where the peak load from the experimental result coincide with the load-displacement curve of the numerical models.

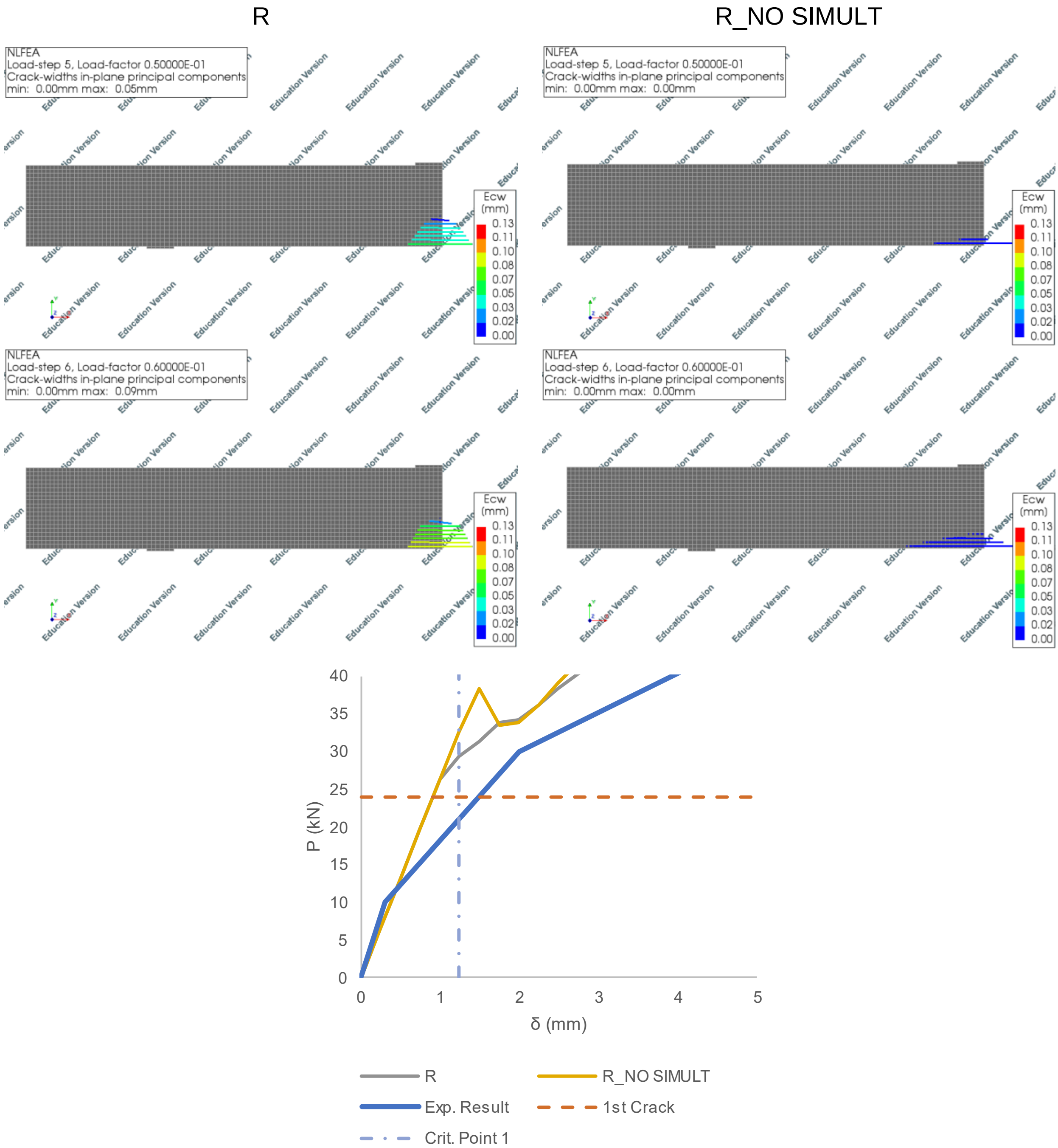

Figure 4.19 Critical Point 1 of Model A123A1 R and R_ NO SIMULT

The first set of models to be observed are model A123A1 R and A123A1 R_NO SIMULT. Figure 4.19 indicated that on critical point 1, a different crack formation is produced in model A123A1. A localized single crack formed on the model A123A1 R while several small cracks formed on the model A123A1 R_NO SIMULT. The formation of localized single crack from the first crack occurrence causes a sudden jump in the load capacity. However, this phenomenon does not affect the non-linear response from critical point 1 to critical point 3, as can be seen in Figure 4.18.

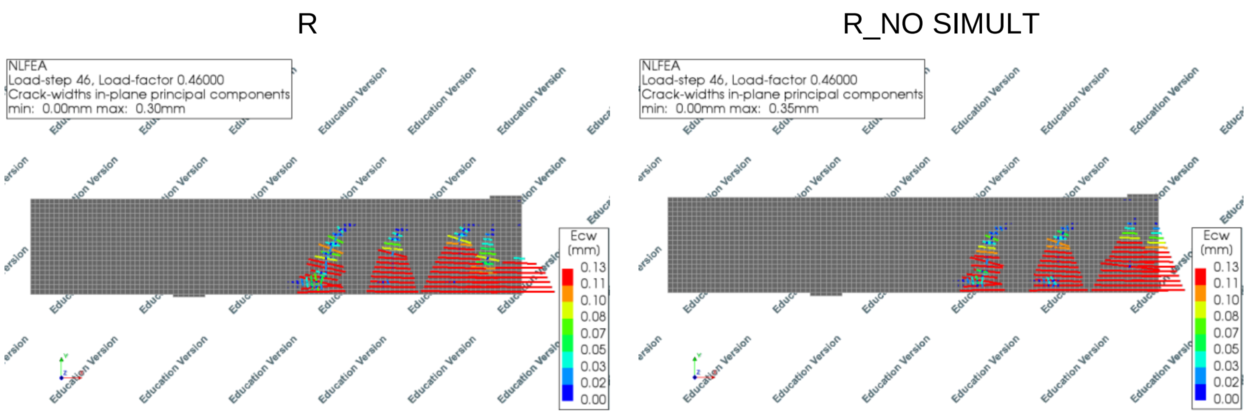

Figure 4.20 Critical Point 2 of Model A123A1 R and R_ NO SIMULT

Figure 4.20 indicates that there is no significant difference in the cracking pattern in critical point 2 between model A123A1 R and model A123A1 R_NO SIMULT. This also implies that a similar pattern of cracking can be expected when the load-displacement curves show a similar pattern.

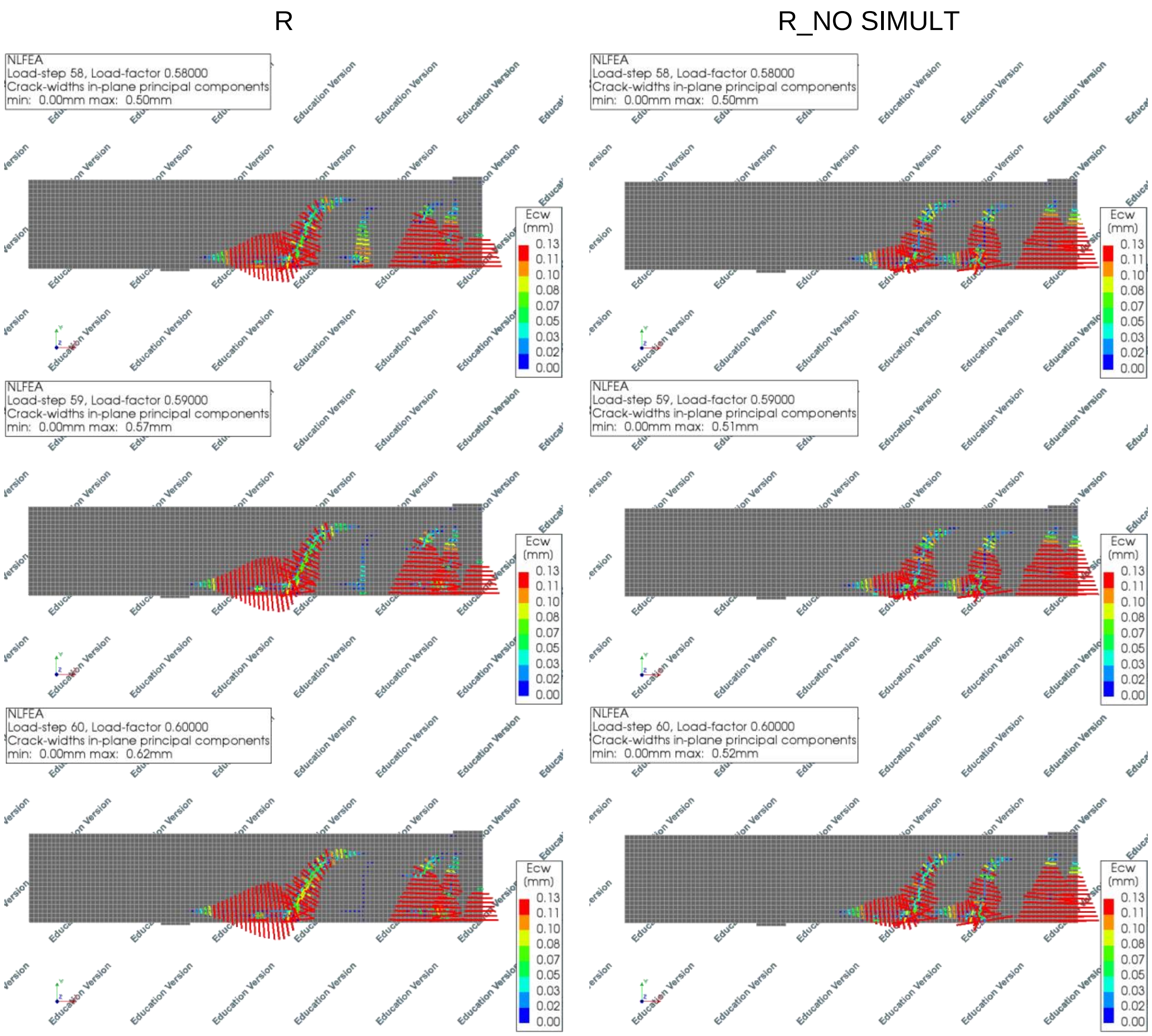

Figure 4.21 Critical Point 3 of Model A123A1 R and R_ NO SIMULT

In critical point 3, the cracking pattern of both A123A1 models started with 2 inclined critical cracks, which can be seen in Figure 4.21 for load step 58. However, on load step 59 in Figure 4.21, the crack pattern in these models change where the crack progression is less stable in model A123A1 R compared to model A123A1 R_NO SIMULT. The stability is determined based on the magnitude of the crack width and the crack pattern. Model A123A1 R shows a significant increase in the crack width, from 0.50 mm to 0.57 mm. Furthermore, one of the inclined cracks becomes more dominant and generate bigger crack width. On the other hand, the crack width in model A123A1 R_NO SIMULT only shows a small increase, from 0.50 mm to 0.51 mm and both inclined critical cracks are still propagating at the same time.

The difference in both crack width and crack pattern can be attributed to the consumption of fracture energy of the element on the model. In model A123A1 R, it can be seen that on one of the inclined cracks, the crack width has exceeded 0.13 mm, the ultimate tensile crack width of the concrete element. On the other hand, this is not the case for model A123A1 R_NO SIMULT, where on both inclined cracks, the crack width on the upper part of the inclined crack has not exceeded the ultimate crack width. This resulted in a smaller area of uncracked concrete in model A123A1 R compared to model A123A1 R_NO SIMULT, which makes it harder for model A123A1 R to reach an equilibrium state on the beam. This leads to higher crack width propagation and a different crack pattern is formed. Furthermore, this phenomenon also indirectly contributes to the load-displacement curve behaviour, where an increase of capacity from critical point 3 to critical point 4 can be seen in Figure 4.18.

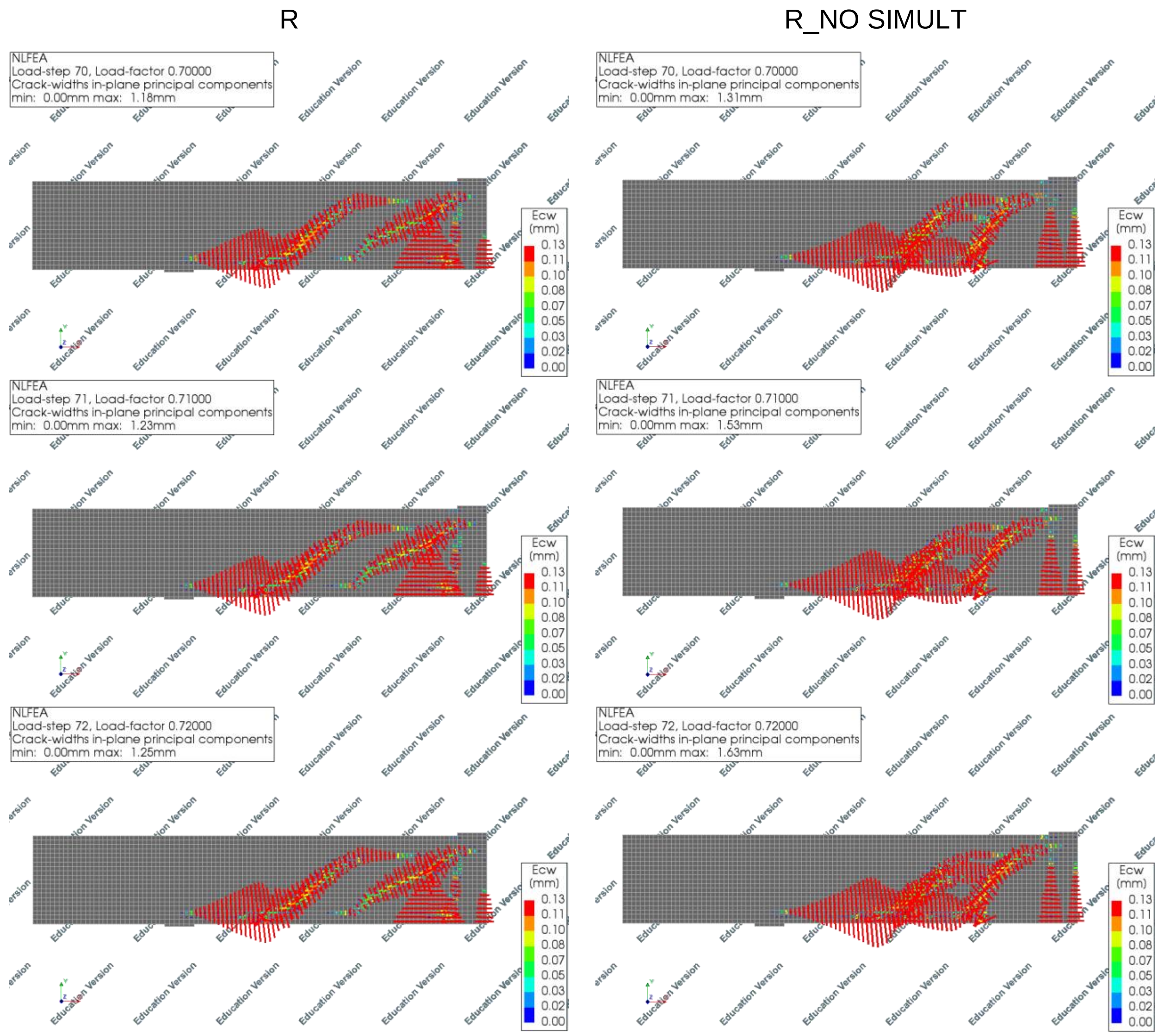

Figure 4.22 Critical Point 4 of Model A123A1 R and R_NO SIMULT

R R_NO SIMULT

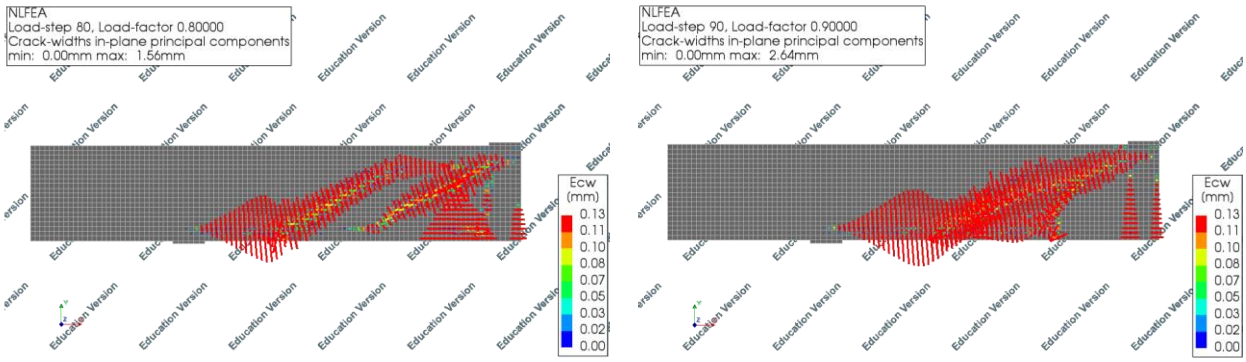

Figure 4.23 Crack Pattern at the Peak Load of Model A123A1 R and R_NO SIMULT

After reaching critical point 4, another shift happens on the load-displacement curve of model A123A1 R_NO SIMULT in Figure 4.18. The cracking pattern in Figure 4.22 shows that the major inclined crack in model A123A1 R is propagating at the top end of the inclined crack in the horizontal direction and it reached its peak when the top horizontal crack meets another inclined crack that connects it to the support plate, forming a complete flexural shear crack in Figure 4.23. However, model A123A1 R_NO SIMULT developed another inclined crack adjacent to the major inclined crack. This can be spotted in Figure 4.22 where another horizontal crack has formed on the adjacent inclined crack.

Furthermore, no significant crack propagation can be observed in the major inclined crack, while the adjacent inclined crack continues to propagate in the horizontal direction. This indicates that the model is able to maintain its equilibrium state with the existence of the major inclined cracks and continue the crack propagation phase of the adjacent inclined crack. This gives an explanation of why the load capacity keeps increase in model A123A1 R_NO SIMULT in Figure 4.18. At the peak load of model A123A1 R_NO SIMULT in Figure 4.23, the crack pattern shows that approximately 3 fully formed flexural shear cracks can be produced on one beam. This result is very contradictive to the test results, where only one flexural shear crack exists after beam failure.

R R_NO SIMULT

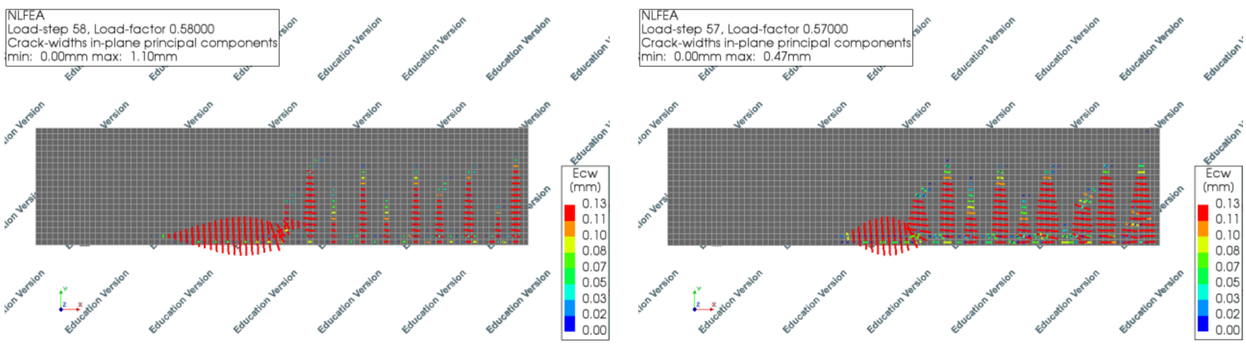

Figure 4.24 Critical Point 2 of Model H123A R and R_NO SIMULT

The next set of models to be observed are H123A R and H123A R_NO SIMULT. No further analysis is given for critical point 1, as it shows a similar phenomenon between model A123A1 R and A123A1 R_NO SIMULT in Figure 4.19. In critical point 2, which is shown in Figure 4.24, the dowel crack propagation rate is higher in H123A R and the crack width is larger in model H123A R compared to model H123A R_NO SIMULT. This phenomenon has been observed in 4.5 Correlation of Crack Propagation to the Beam Global Response, where the formation of a certain amount of the dowel crack causes a change in the beam overall stiffness. The stiffness change can be observed in the load-displacement curve in Figure 4.18.

R R_NO SIMULT

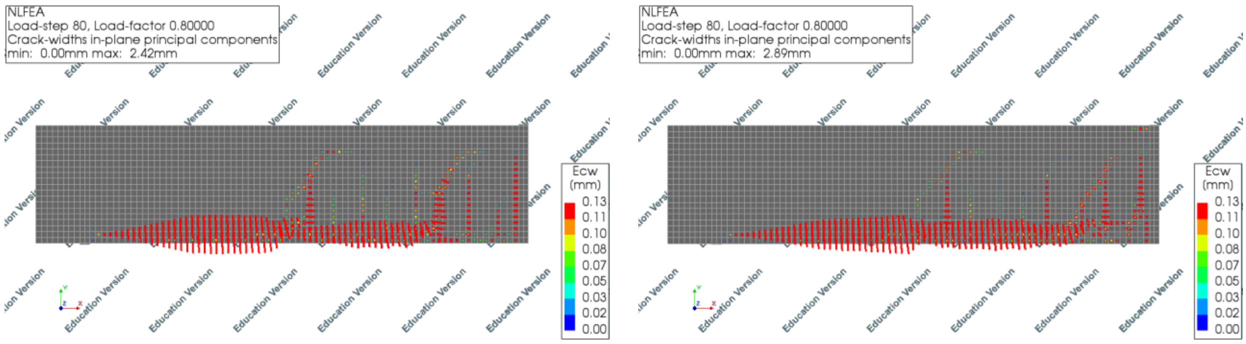

Figure 4.25 Critical Point 3 of Model H123A R and R_NO SIMULT

In critical point 3, the major crack formed on the model is the dowel crack, which can be seen in Figure 4.25. There are two inclined cracks on each model, but no significant difference can be seen in the crack pattern. The magnitude of the crack width is also similar for both models. This corresponds to the load-displacement curve in Figure 4.18 where no significant shift happens on the curve as well.

R R_NO SIMULT

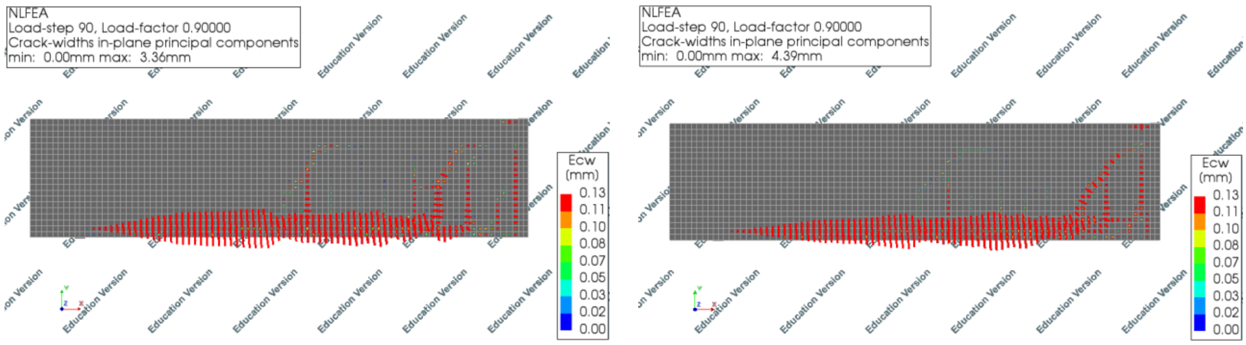

Figure 4.26 Critical Point 4 of Model H123A R and R_NO SIMULT

R R_NO SIMULT

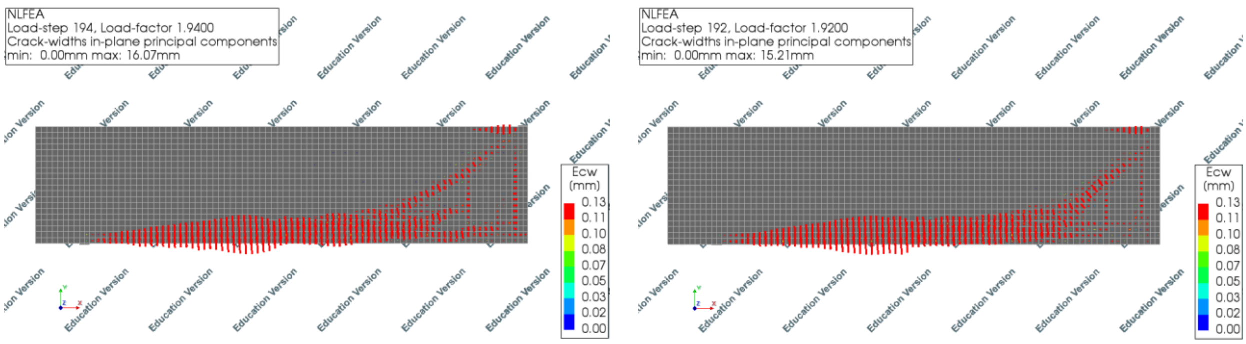

Figure 4.27 Crack Pattern at the Peak Load of Model H123A R and R_NO SIMULT

In critical point 4, the flexural shear crack has almost completely formed in both models. These crack patterns can be seen in Figure 4.26. No significant difference can be seen in either Figure 4.26 or Figure 4.27. All observations for model H123A R and R_NO SIMULT show that there is no significant difference in the results of NLFEA when the norms are simultaneously satisfied or not for specimen H123A.

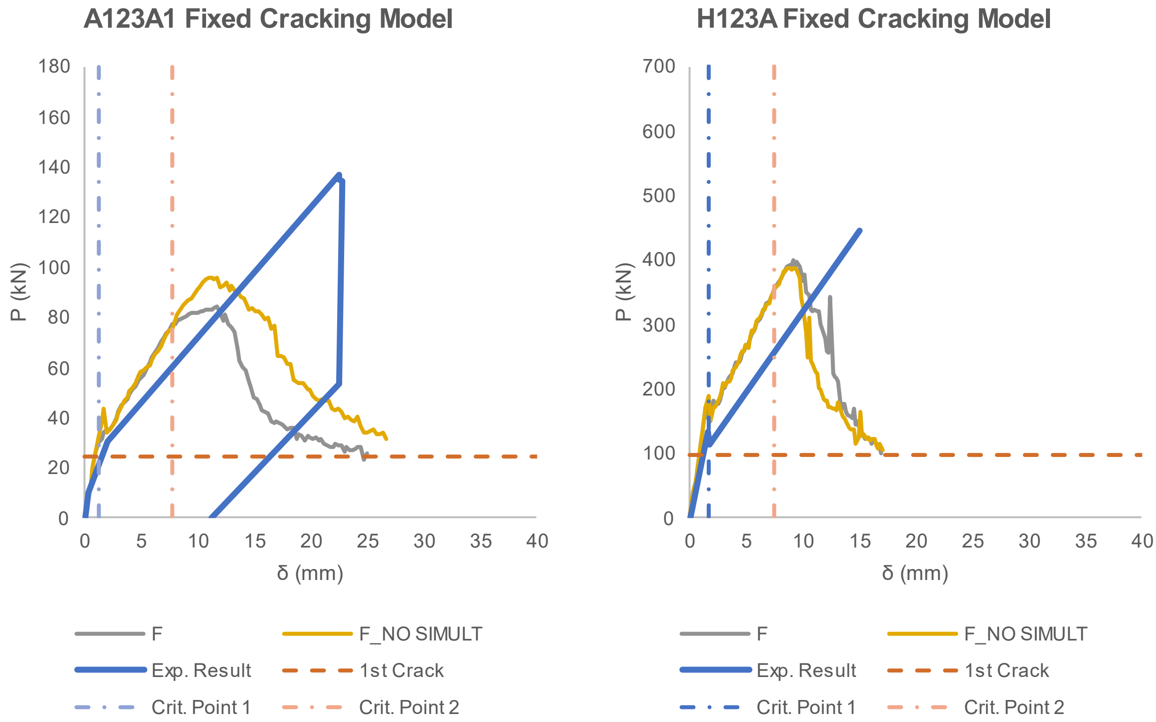

Figure 4.28 Comparison of the Global Behaviour of Model Variant F and F_NO SIMULT

When observing Figure 4.18 and Figure 4.28 together, a similar pattern can be observed between the models using a fixed crack model and rotating crack models, where the effect of simultaneous satisfactions of norms in specimen A123A1 is greater compared to specimen H123A. Critical point 1 in Figure 4.28 represents the first cracking occurrence, where this phenomenon has been explained in Figure 4.19. Critical point 2 in Figure 4.28 gives an indication of when the curve starts to deviate for specimen A123A1 and observation on the crack pattern before peak load is reached for specimen H123A.

F F_NO SIMULT

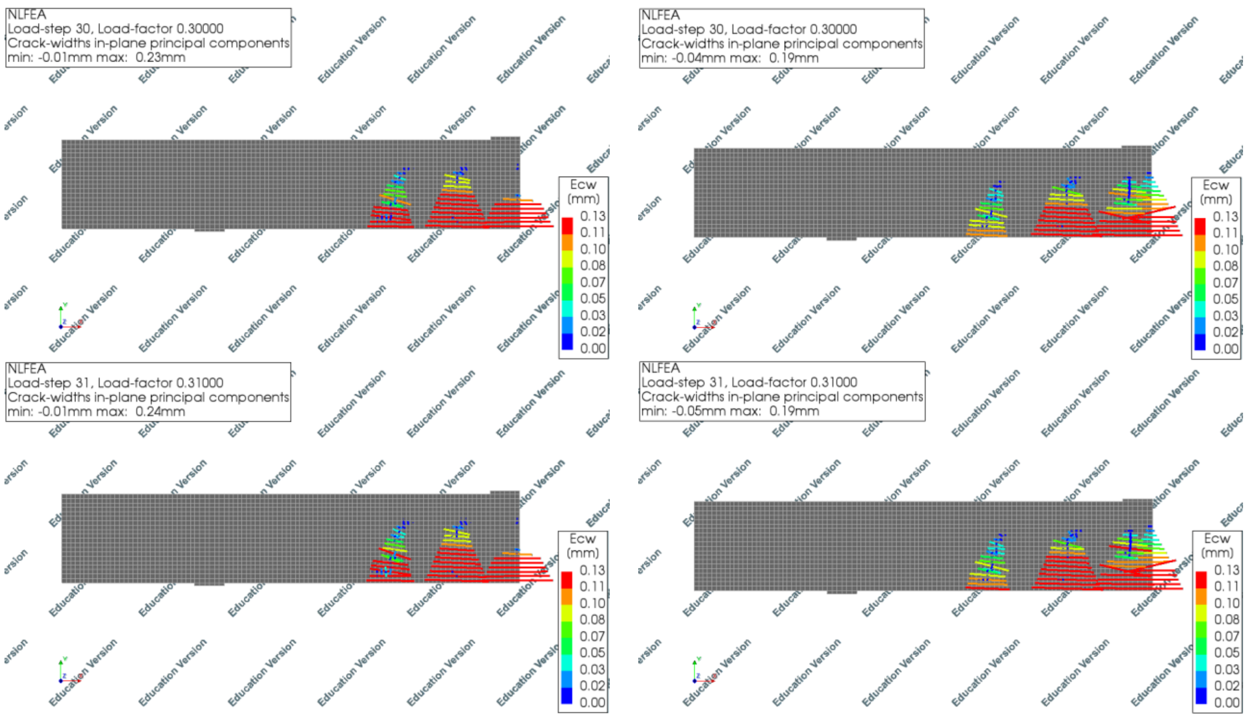

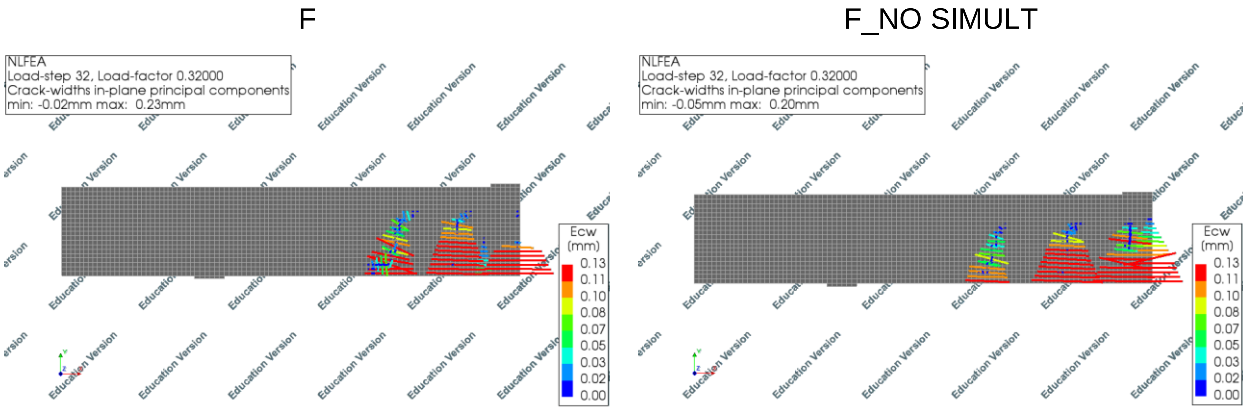

Figure 4.29 Critical Point 2 of Model A123A1 F and F_NO SIMULT

The third observation is done for models A123A1 F and F_NO SIMULT. At critical point 2 in Figure 4.31, the difference in the crack pattern can be observed in both models. Model A123A1 F has formed an inclined flexural crack with dowel crack at the low-end propagating to the support plate, while model A123A1 F_NO SIMULT has formed several flexural cracks without inclination. This difference implies that model A123A1 F_NO SIMULT will have a higher load capacity, as the formation of the inclined crack and dowel crack propagation would exist on a higher load level. This effect can also be seen in Figure 4.28, where the load-displacement curve of model A123A1 F starts to have a change in stiffness while the load-displacement curve of model A123A1 F_NO SIMULT still has a similar stiffness to the previous load step.

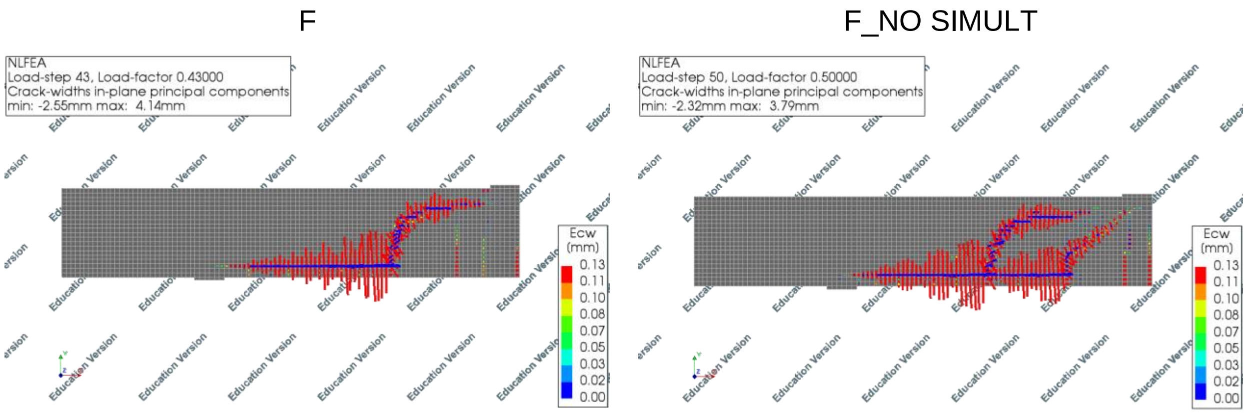

Figure 4.30 Crack Pattern at Peak Load of Model A123A1 F and F_NO SIMULT

At the peak load, Figure 4.30 shows a relatively same crack pattern as Figure 4.23, where model A123A1 F only formed one flexural shear crack while model A123A1 F_NO SIMULT formed two flexural shear cracks. This also indicates that one beam can have more than one flexural shear crack, which is contradictory to the experimental result.

The fourth observation is done for models H123A F and H123A F_NO SIMULT. Figure 4.31 describes the crack pattern on critical point 2, where no significant difference can be seen on the crack pattern and the magnitude of the crack width. This phenomenon can also be observed in the load-displacement curve in Figure 4.28. At the peak load, there are some differences that can be observed in the magnitude of the crack width, according to Figure 4.32. The magnitude of the crack width is higher in model H123A F_NO SIMULT compared to H123A F. However, the crack pattern is similar in both models. As explained in subchapter 4.5 Correlation of Crack Propagation to the Beam Global Response, the crack formation has a significant influence on the load-displacement curve. This gives an explanation of why the load-displacement curve in Figure 4.28 has a very similar peak load for these models. No significant influence can be observed when specimen H123A1 is simulated with or without simultaneous satisfaction of the norms.

F F_NO SIMULT

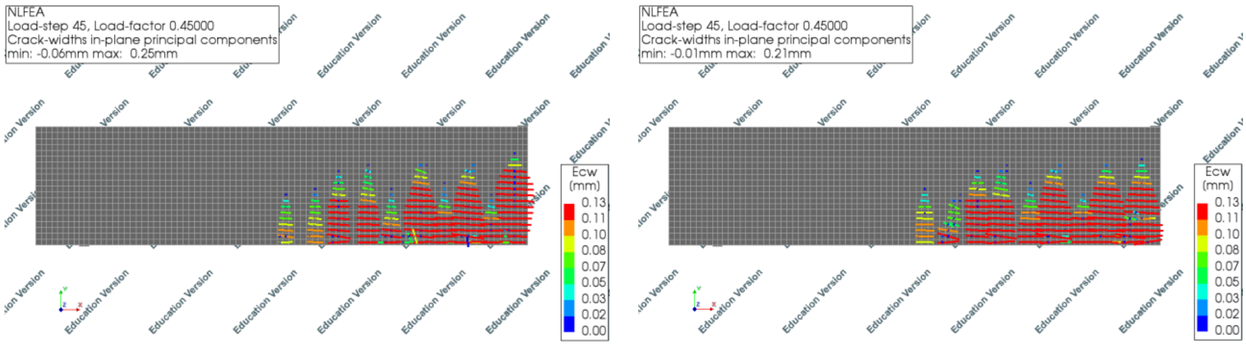

Figure 4.31 Critical Point 2 of Model H123A F and F_NO SIMULT

F F_NO SIMULT

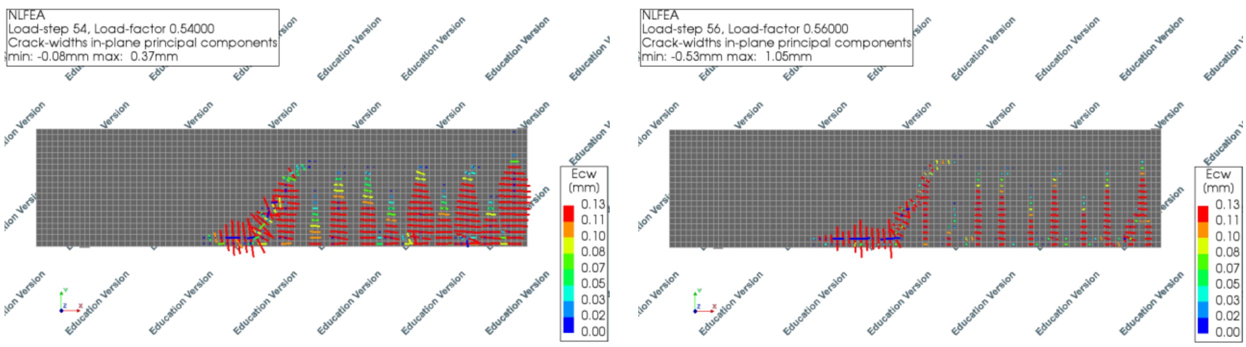

Figure 4.32 Crack Pattern at Peak Load of Model H123A F and F_NO SIMULT

All observations show that the use of the rotating and fixed crack model does not influence the effect of simultaneous satisfaction of the norms on numerical models. Two phenomena can be highlighted in these observations. The first is that the simultaneous satisfaction of norms has a significant impact on the simulated global behaviour of the beam. This can be observed clearly in the results of numerical model for specimen A123A1, where the load capacity has a significant difference due to late critical cracking formation and multiple formations of flexural shear cracks. The second is that the effect of simultaneous satisfaction of norms become less pronounced as the specimen size increase. This can be observed clearly by comparing the simulated global results of numerical models for specimens A123A1 and H123A, where H123A has a larger size in terms of height and shear span. In order to have a general configuration that can be used for all beam sizes, the simultaneous satisfaction of norms must be used for the numerical models.

4.7. Effect of the Inclusion of Top Reinforcement

The inclusion of the top reinforcement on the numerical model would increase the number of elements and nodes. An increase in the number of elements and nodes will result in higher computational time. In order to see whether this addition is necessary or not, the effect of the inclusion of top reinforcement is studied for both rotating and fixed crack models on two specimens, A123A1 and H123A.

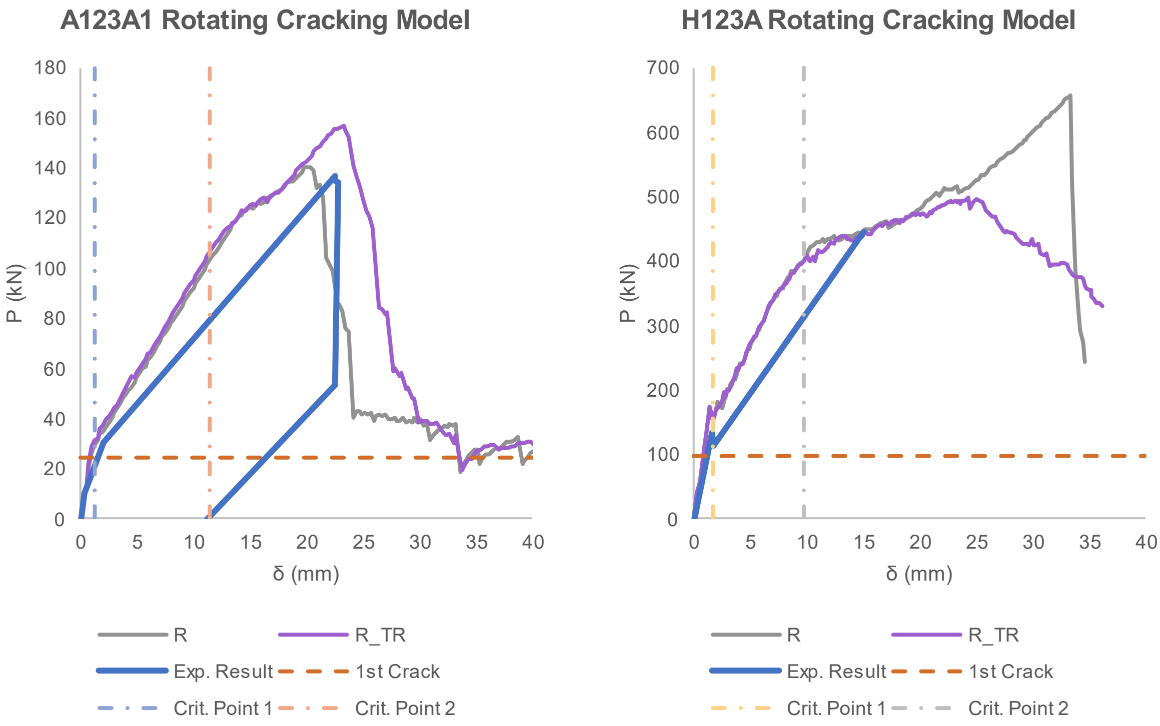

Figure 4.33 Comparison of the Global Behaviour of Model Variant R and R_TR

According to Figure 4.33, the inclusion of top reinforcement would cause a significant increase for specimen A123A1 and a decrease for H123A in load capacity with a rotating crack model. These phenomena are a contradiction between specimen A123A1 and H123A. These phenomena are studied by observing the cracking pattern on the simulated non-linear behaviour, which represented by critical point 2, and the cracking pattern and stress distribution on the peak load of each model. Critical point 1 indicates the first cracking phenomenon, which has been explained in subchapter 4.3 Stiffness and First Crack Verification.

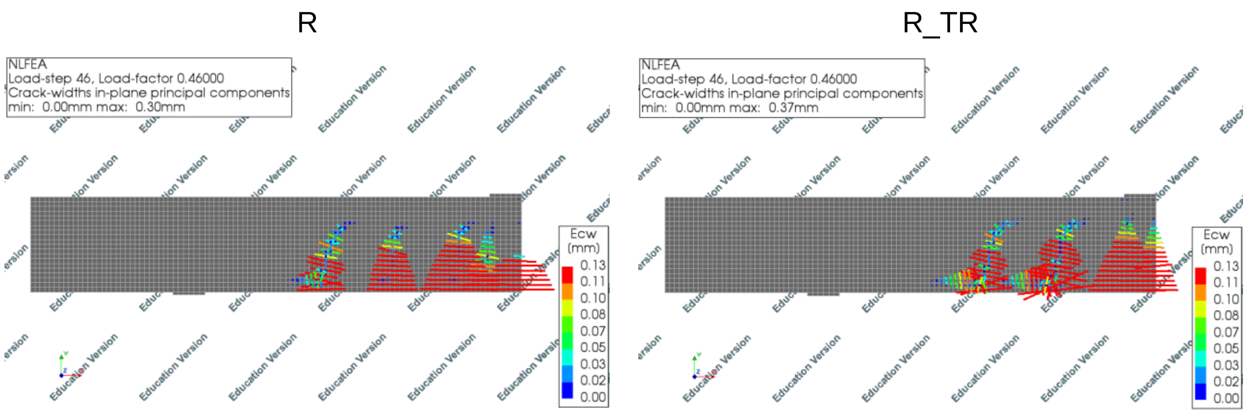

Figure 4.34 Critical Point 2 of Model A123A1 R and R_TR

The cracking pattern on critical point 2 can be observed in Figure 4.34. It can be seen that there is a difference in the cracking pattern of model A123A1 R and A123A1 R_TR, where there are less inclined cracks in model

A123A1 R compared to model A123A1 R_TR. However, this difference does not affect the load-displacement curve in Figure 4.33, which indicates that the number of inclined cracks on the model will not affect the simulated global behaviour.

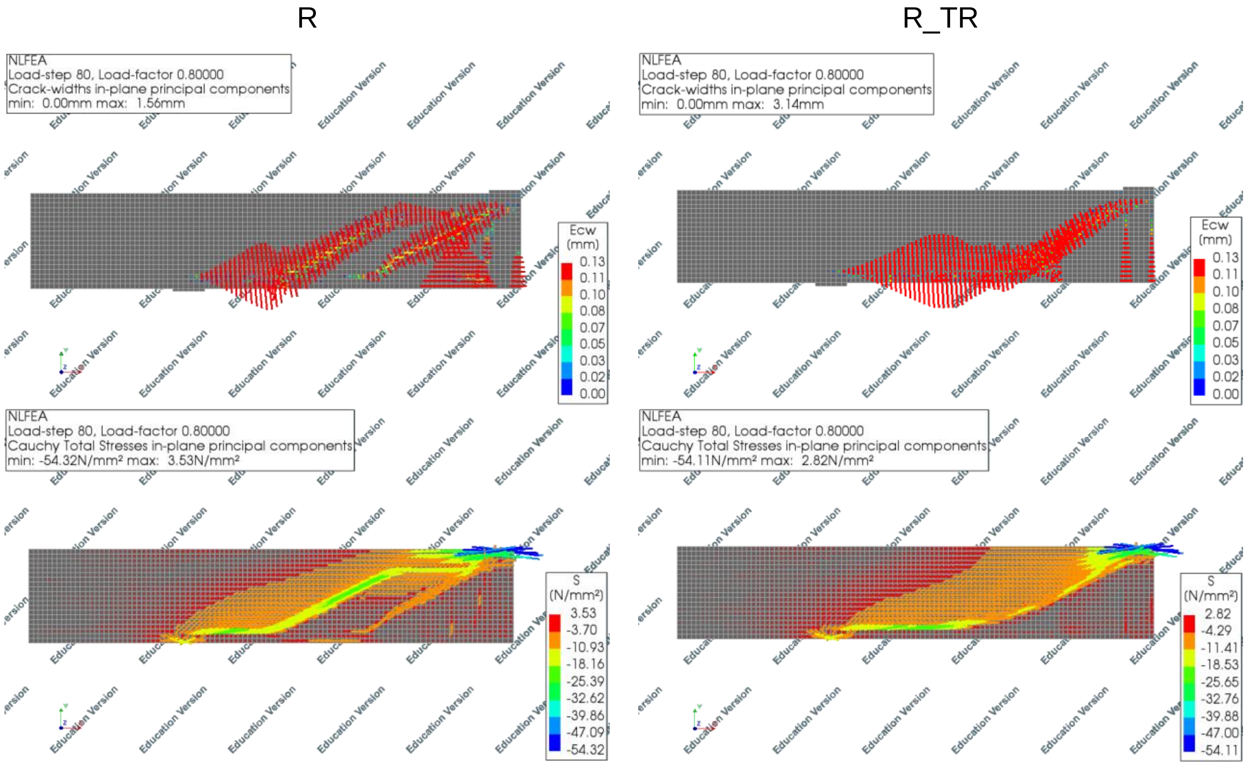

Figure 4.35 Crack Pattern (Top) and Stress Distribution (Bottom) at the Peak Load of Model A123A1 R

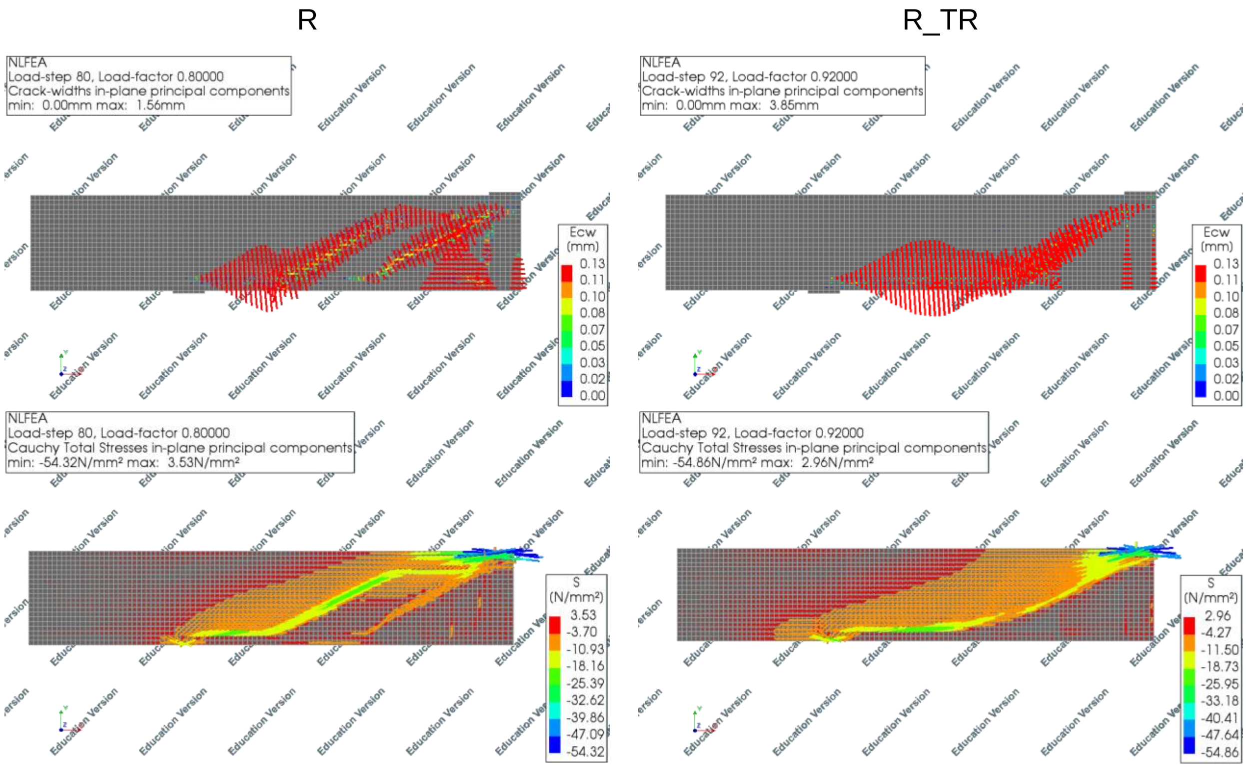

Figure 4.36 Crack Pattern (Top) and Stress Distribution (Bottom) at the Peak Load of Model A123A1 R and R_TR

At the peak load of the model A123A1 R, a different crack pattern can be seen forming on model A123A1 R and A123A1 R_TR, according to Figure 4.35. Model A123A1 R formed a flexural shear crack with top and bottom horizontal cracks, while model A123A1 R_TR formed a flexural shear crack with bottom horizontal cracks. If the stress distribution is observed in Figure 4.35, it can be seen that the compression strut forming on the side of the flexural shear crack is smaller in model A123A1 R compared to model A123A1 R_TR. A larger compression strut would indirectly imply higher load capacity.

Since model A123A1 R_TR has a larger compression strut, this causes the simulated beam not to fail immediately after a fully flexural shear crack has formed. The crack pattern and the stress distribution at the peak load of both models can be seen in Figure 4.36. A relatively larger crack width on the dowel crack can be seen in model A123A1 R_TR. This phenomenon changes the failure mode of model A123A1 R_TR from flexural shear failure to shear compression failure, which causes the difference in load capacity that is shown in Figure 4.33.

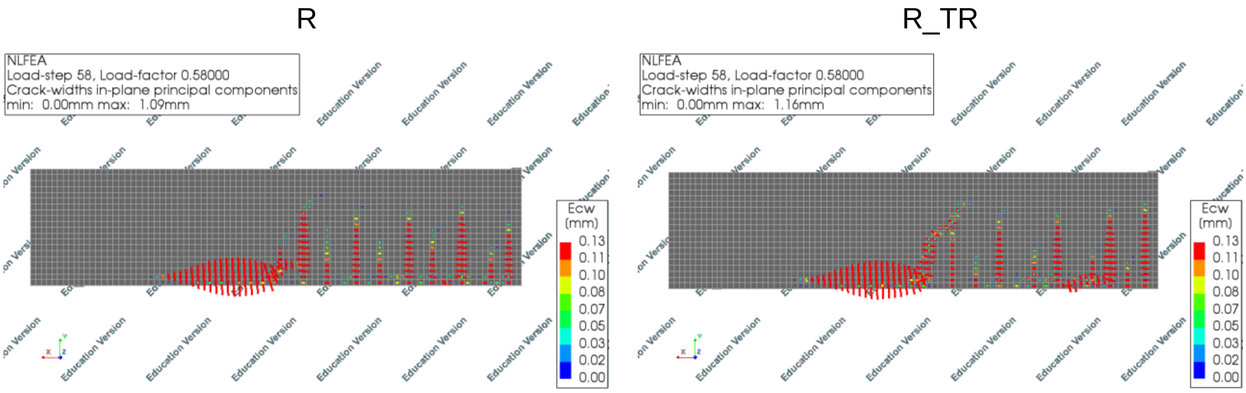

Figure 4.37 Critical Point 2 of Model H123A R and R_TR

The next observation is done for models H123A R and H123A R_TR. On critical point 2, there is no significant difference that can be spotted in Figure 4.37. However, it should be noted that the inclined crack on model H123A R is less developed compared to model H123A R_TR.

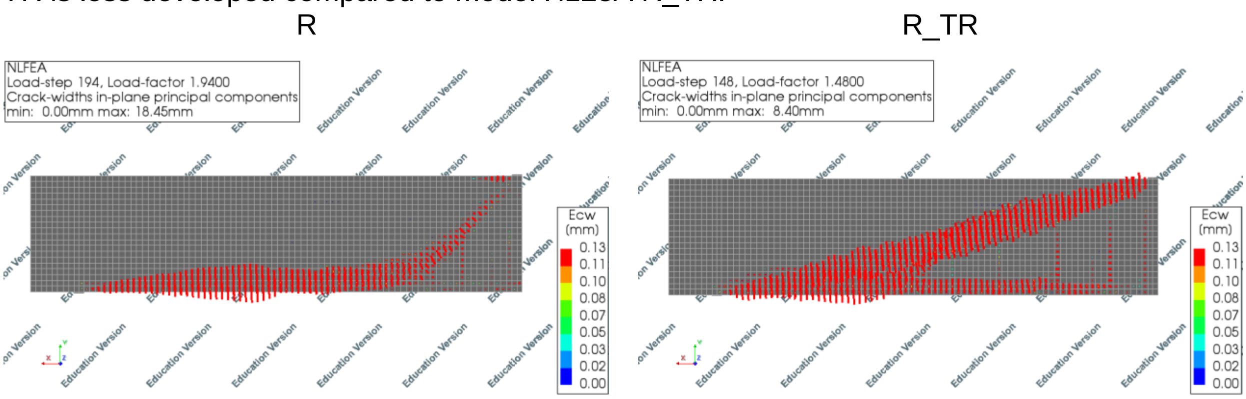

Figure 4.38 Crack Pattern at the Peak Load of Model H123A R and R_TR

The difference in the peak load of both models H123A R and H123A R_TR are caused by a different cracking pattern on the model, which can be seen in Figure 4.38. The crack pattern in model H123A R indicated that the peak load is reached when the flexural shear crack has been formed and the model cannot maintain its equilibrium state any further. On the other hand, the crack pattern in model H123A R_TR indicated that the model has been shattered into two parts due to cracks and can only maintain its equilibrium state with the top and bottom reinforcement. These represent 2 different failure modes, where model H123A R produce the same failure mode as the experimental results while model H123A R_TR produce a completely different failure mode from the experimental results.

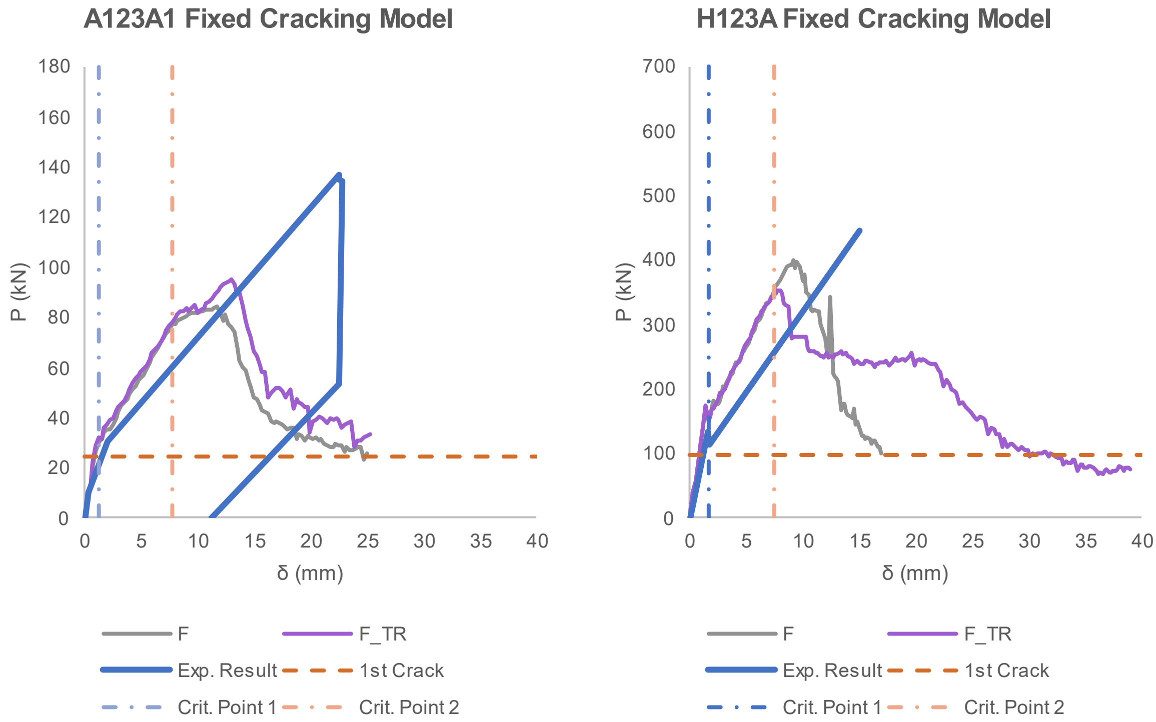

Figure 4.39 Comparison of the Global Behaviour of Model Variant F and F_TR

When observing Figure 4.39 and Figure 4.33, a similar pattern can be observed between the models using the fixed crack model and rotating crack models, where the effect of the inclusion of top reinforcement is inconsistent between specimen A123A1 and H123A. Critical point 1 in Figure 4.39 represents the first cracking occurrence, where this phenomenon has been explained with Figure 4.19. Critical point 2 in Figure 4.39 used for observation on the crack pattern before peak load is reached for specimen A123A1 and gives an indication of when the curve starts to deviate for specimen H123A.

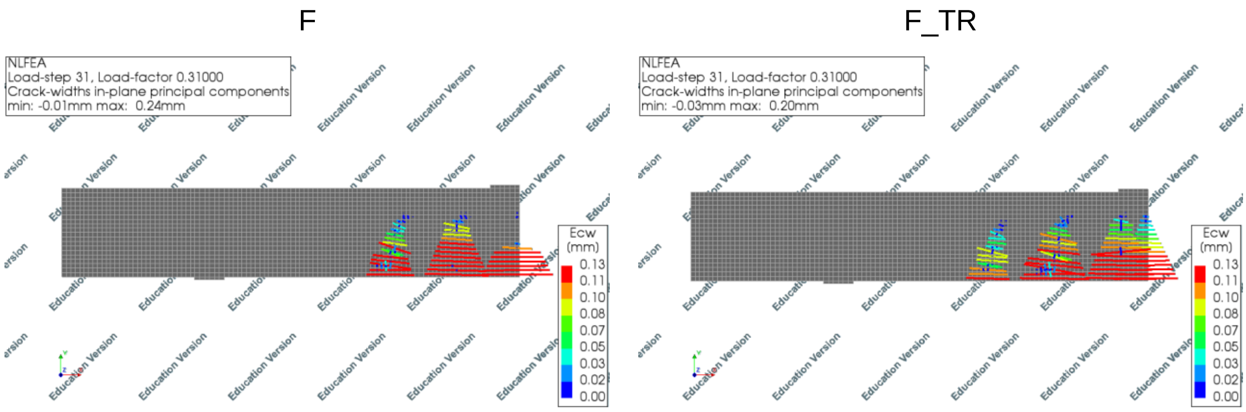

Figure 4.40 Critical Point 2 of Model A123A1 F and F_TR

The third observation is done for models A123A1 F and A123A1 F_TR. Figure 4.43 illustrates the cracking pattern on both models. It can be seen that no significant difference can be seen on critical point 2, which corresponds to the load-displacement curve in Figure 4.42, which is also similar for both models.

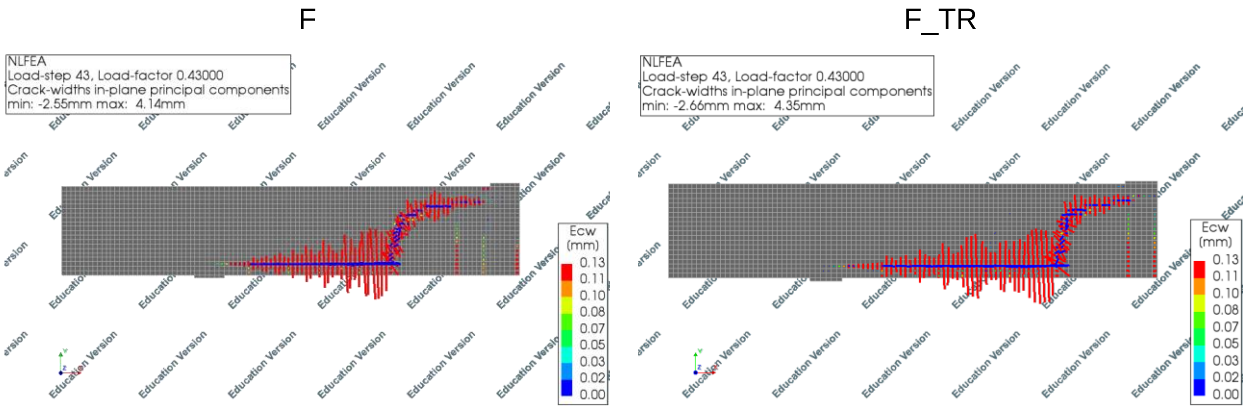

Figure 4.41 Crack Pattern at the Peak Load of Model A123A1 F

The same phenomenon also happens in Figure 4.41 where at the same load step where model A123A1 F reached its peak load, the cracking pattern is very similar as well. However, this contradicted the observation in Figure 4.39 where the load-displacement starts to change its trend for both models. This problem can be answered by observing Figure 4.42.

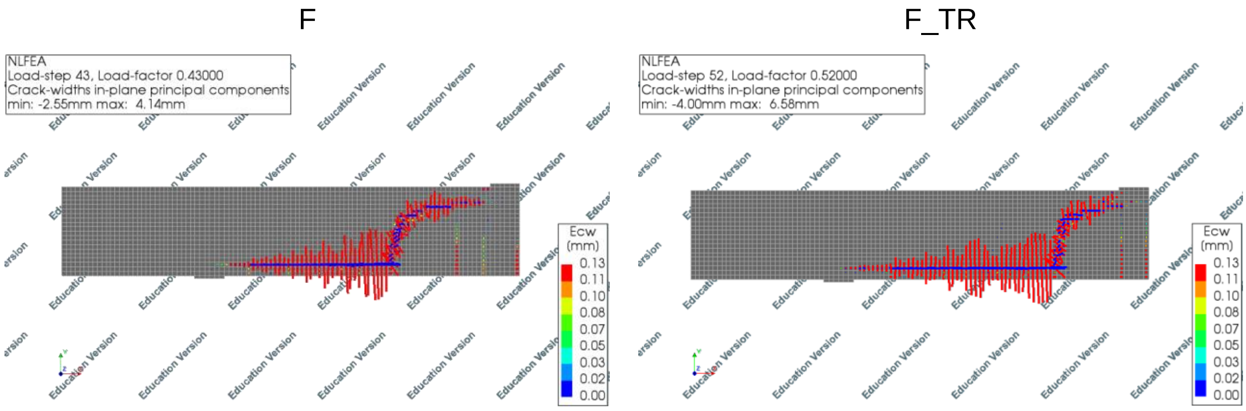

Figure 4.42 Crack Pattern at the Peak Load of Model A123A1 F and F_TR

In Figure 4.42, it can be seen that the crack on model A123A1 F_TR has propagated through the beam where the beam is shattered into two parts. This phenomenon only happens in model A123A1 F_TR because of the existence of top reinforcement, which allows for stress to be transferred via reinforcement even if the beam is shattered into two parts. This allows for an increase in the load capacity of the beam in model A123A1 F_TR, which can be observed in Figure 4.39.

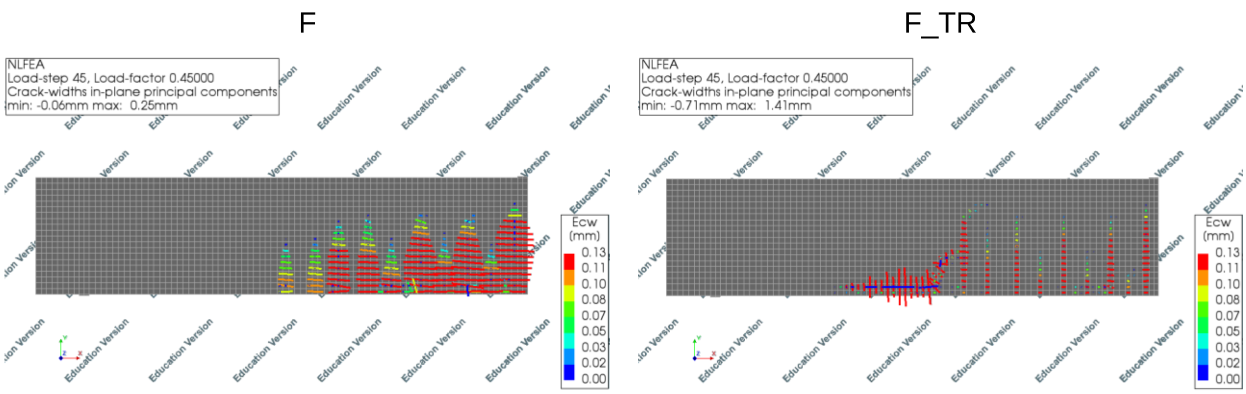

Figure 4.43 Critical Point 2 of Model H123A F and F_TR

The last observation is done for models H123A F and H123A F_TR. The cracking pattern on critical point 2 can be observed in Figure 4.43, where it can be seen that model H123A has not developed an inclined crack, while model H123A F_TR has developed an inclined crack and dowel crack. This difference is quite significant because the formation of the inclined crack would affect the load-displacement curve, as explained in subchapter 4.5 Correlation of Crack Propagation to the Beam Global Response. This phenomenon causes a change in the load-displacement curve that can be observed in Figure 4.39.

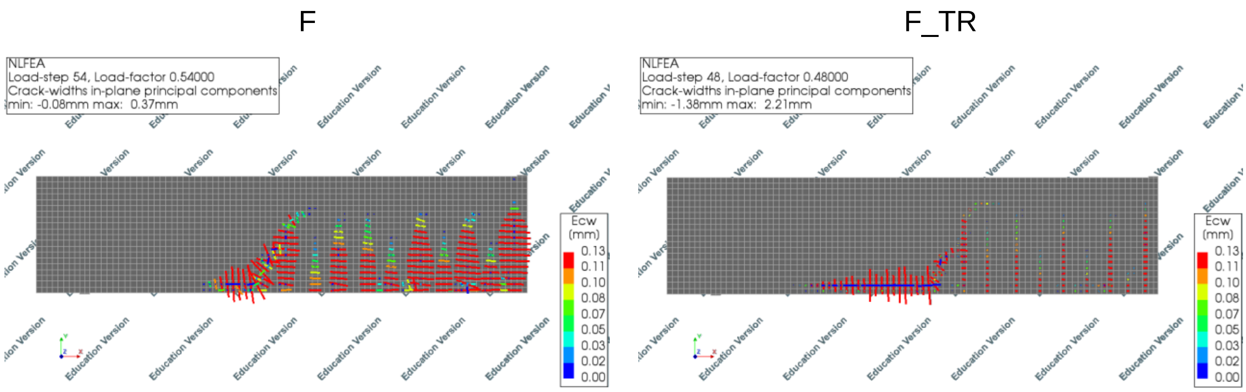

Figure 4.44 Crack Pattern at the Peak Load of Model H123A F and F_TR

At the peak load of both models, according to Figure 4.44, it can be seen that similar behaviour occurs on both models where the peak load is reached before the flexural shear crack is fully formed. In terms of crack width magnitude, the crack width is smaller in model H123A F compared to model H123A F_TR which indicates that the crack opening process in model H123A F is more stable compared to model H123A F_TR.

All observations show that even though a similar behaviour can be seen in rotating and fixed crack models for both specimen A123A1 and H123A, the reason for its behaviour is different for each case. However, it can be concluded that there are two phenomena that constantly influence the results of the numerical models, which are crack over-propagation that leads to beam shattered into two parts and induce different failure mode and early cracking progression. In order to avoid these problems, the top reinforcement should not be included in the numerical models.

4.8. Summary

The problem identification related to the convergence is done by studying 16 variations of the numerical configurations. The numerical models are modelled based on two specimens with different shear span (a) and beam depth (d). However, both specimens have a comparable shear slenderness (a/d). Two types of cracking models are used, the rotating and fixed crack models. Furthermore, the numerical model is varied with different criteria of convergence, reinforcement configuration and iterative-incremental analysis.

Three verifications are done for the result of the numerical model, elastic stiffness, first cracking moment and convergence state. The simulated elastic stiffness is similar to the analytical value, which means that all inputs are correct. The simulated first cracking moment happens on a higher load level compared to the analytical value due to the load step size and lack of initial imperfection on the numerical model, which indicates that this should be studied further in order to see its influence on the simulated non-linear behaviour. The study of the first crack occurrence in subchapter 4.6 has proven that this does not cause a change in the simulated non-linear behaviour. In the NLFEA, the numerical models are not able to achieve 100% convergence on all load steps. Furthermore, if the common method of evaluation is used, where the analysis is stopped when continuous non-convergence in the analysis steps is spotted, then it will result in peak load dependency to the convergence state where different peak loads can be achieved with different numerical configurations. In order to avoid this problem, all load steps will be accepted regardless of their convergence state and sensitivity analysis will be performed on the numerical parameters, such as load increment, error tolerance and the maximum number of iterations.

In order to study the change in the global behaviour of the simulated beam, the simulated process of flexural shear crack formation is investigated. There are four critical steps in the formation of the flexural shear crack. The flexural shear crack starts from the formation of flexural crack. The flexural crack starts to change into an inclined crack due to a change in the principal direction of the crack propagation. After the inclined crack has been formed, a small dowel crack starts forming at the low-end of the inclined crack and propagating along with the bottom reinforcement. The dowel crack propagation causes a change in the simulated non-linear behaviour of the beam. After the dowel crack propagates to the support, a horizontal crack starts to form at the top-end of the inclined crack and propagate to the loading point. As this process is completed, the beam has reached its peak load and fails afterwards.

As there will be a lot of variations to simulate and in order to reduce the computational time, the effect of simultaneous satisfaction of convergence norms and inclusion of top reinforcement are studied in order to decide whether these are necessary to be included in the numerical model. The study has proven that the simultaneous satisfaction of convergence norms is necessary for the numerical model, as it affects the critical cracking formation in the numerical model. The inclusion of top reinforcement is considered to be unnecessary, as it will change the crack over-propagation and induce different failure modes.

5 Sensitivity Analysis of Convergence Parameters

The investigation of the numerical size effect continues with solving the problem related to convergence. The identified problem related to convergence is studied by analysing the sensitivity of the numerical parameters, such as load increment (subchapter 5.3), error tolerance (subchapter 5.4), and the maximum number of iterations (subchapter 5.5). The details regarding the sensitivity analysis are specified in subchapter 5.1. Based on the observation and analysis in subchapters 5.3, 5.4 and 5.5, the main source of the problem related to the convergence is the formation of the dowel crack. The correlation and the causal relationship between the formation of the dowel crack and the convergence state are studied in subchapter 5.6. The sensitivity analysis is concluded by deriving the convergence criteria for the simulation of shear failure in the reinforced concrete beam without shear reinforcement in subchapter 5.7. Additional study is done in subchapter 5.8 to see whether the fixed crack model has a better performance compared to the rotating crack model when used to simulate shear failure in the reinforced concrete beam without shear reinforcement. It must be noted that any figure with a crack pattern, such as Figure 5.12, is only used to be studied qualitatively. The value of Ecw always indicates a range from uncracked element $(Ecw = 0)$ to fully cracked element $(Ecw = CW_{t,u})$. A fully cracked element is defined as an element which has lost all its fracture energy. The value of Ecw should not be used as a reference for any study related to the experimental crack width because it does not consider the effect of localised reinforcement, which should have decreased the crack opening around the reinforcement.

5.1. Case Study Details for Convergence State Study

As mentioned in subchapter 4.4 Convergence State Verification, the convergence state would be analysed further by performing sensitivity analysis on the models. This analysis would be done for the rotating crack model, as it is a more common cracking model used on numerical models. The sensitivity analysis will be done based on the relative energy variation and out-of-balance force, which are controlled as the convergence norms in the models. The purpose of the sensitivity analysis is to find relatively constant results for the peak load of specimens A123A1 and H123A.

The sensitivity analysis is done by varying the load increment, convergence tolerance/norms, and the number of iterations. The specimens used for the study are the same as specimens defined in chapter 4 Identification of Problem Related to Convergence. All material properties and beam geometry would also be the same as defined in subchapter 4.1 Experimental Set-Up for Convergence Problem Identification, except for the top reinforcement, which is excluded from the model. 11 variations of load increment are created for analysing the dependency of load increment to the results of numerical models, ranging from 0.1 to 0.004. The variation details are given in Table 5.1. 6 variations of error tolerance are created for analysing the dependency of error tolerance to the results of numerical models, which are detailed in Table 5.2. 5 variations of the maximum number of iterations are created to analyse the dependency of the maximum number of iterations to the results of numerical models, which are detailed in Table 5.3. Several sub-variations are also created for the variation of error tolerance and number of iterations in order to see the consistency of the results of numerical models. The sub-variations are detailed in Table 5.4.

Table 5.1 Model Variation 2

Code	Imp. Disp. per Step		n_p	n_{max}	G_{err}	F_{err}	Cracking Model	Iterative-Incremental Method
	A123A1	H123A						
LI0.1	2.5 mm	1.7 mm	10	100	0.0001	0.01	Rotating	(1) Quasi-Newton (2) Full Newton-Raphson (3) Modified Newton-Raphson
LI0.08	2 mm	1.36 mm	13	100	0.0001	0.01	Rotating	
LI0.06	1.5 mm	1.02 mm	17	100	0.0001	0.01	Rotating	
LI0.04	1 mm	0.68 mm	25	100	0.0001	0.01	Rotating	
LI0.03	0.75 mm	0.51 mm	34	100	0.0001	0.01	Rotating	
LI0.02	0.5 mm	0.34 mm	50	100	0.0001	0.01	Rotating	
LI0.016	0.4 mm	0.272 mm	63	100	0.0001	0.01	Rotating	
LI0.01	0.25 mm	0.17 mm	100	100	0.0001	0.01	Rotating	
LI0.008	0.2 mm	0.136 mm	125	100	0.0001	0.01	Rotating	
LI0.006	0.15 mm	0.102 mm	167	100	0.0001	0.01	Rotating	
LI0.004	0.1 mm	0.068 mm	250	100	0.0001	0.01	Rotating	

Table 5.2 Model Variation 3

Code	G_{err}	F_{err}
ET1	0.005	0.01
ET2	0.001	0.01
ET3	0.0005	0.01
ET4/FT3	0.0001	0.01
FT1	0.0001	0.1
FT2	0.0001	0.05

Table 5.3 Model Variation 4

Code	n_{max}	G_{err}	F_{err}
NI10	10	0.0001	0.01
NI25	25	0.0001	0.01
NI50	50	0.0001	0.01
NI75	75	0.0001	0.01
NI100	100	0.0001	0.01

Table 5.4 Sub-Variation of Model Variation 3 and 4

Code	Iterative-Incremental Method	Specimen	Load Increment
R11	Quasi-Newton	A123A1	0.08
R12	Quasi-Newton	A123A1	0.04
R13	Quasi-Newton	A123A1	0.02
R21	Quasi-Newton	H123A	0.06
R22	Quasi-Newton	H123A	0.04
R23	Quasi-Newton	H123A	0.03
R31	Full NR	A123A1	0.02
R32	Full NR	A123A1	0.016
R33	Full NR	A123A1	0.01

Code	Iterative-Incremental Method	Specimen	Load Increment
R41	Full NR	H123A	0.03
R42	Full NR	H123A	0.02
R43	Full NR	H123A	0.016
R51	Modified NR	A123A1	0.03
R52	Modified NR	A123A1	0.02
R53	Modified NR	A123A1	0.016
R61	Modified NR	H123A	0.02
R62	Modified NR	H123A	0.016
R63	Modified NR	H123A	0.01

5.2. Analysis Method for Studying the Convergence Parameters

The sensitivity analysis will be done in three stages. The first stage is reducing the distribution of the peak load from the results of NLFEA. This will be done by doing a statistical analysis on the distribution of the peak load. The chosen method of the statistical analysis for this study is the study with box plot (or commonly known as box-and-whisker plot). The box plot is used as a tool that can be used for displaying a data distribution. This plot is constructed based on 5 values, the minimum, maximum, first and third quartile, and median value. The minimum and maximum values are evaluated based on the minimum and maximum values found on the data and the boundary defined by the interquartile range. The data beyond this boundary is considered as an outlier. The illustration of the box plot can be seen in Figure 5.1. The box plot is suitable to be used for comparing the data distribution before and after a certain modification, which is in line with the current objective where a new criterion will be applied in order to reduce the distribution of the peak load. (DeCoursey, 2003)

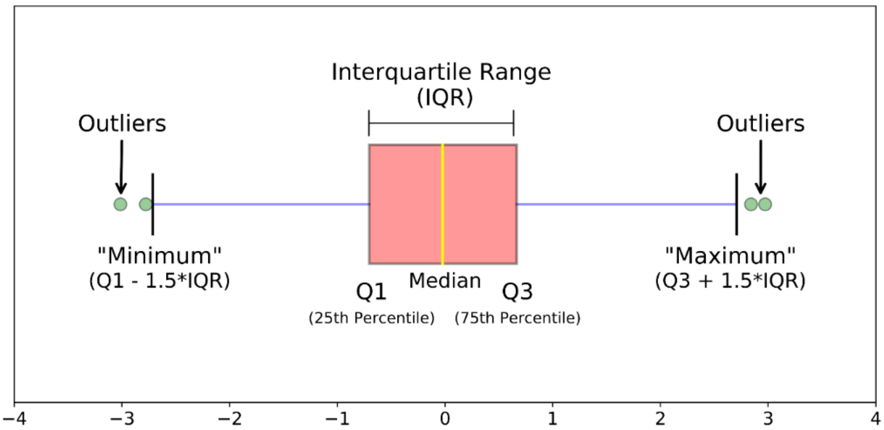

Figure 5.1 Illustration of Box Plot and its Components

Source: https://towardsdatascience.com/understanding-boxplots-5e2df7bcbd51

However, as the plot only shows the overall distribution of the result, it cannot shows the individual change of the data before and after a certain modification. In order to compensate for this drawback, a scatter plot is also used in order to see the individual change of the data. Figure 5.2 gives an example of how the data will be represented during the study of convergence parameters.

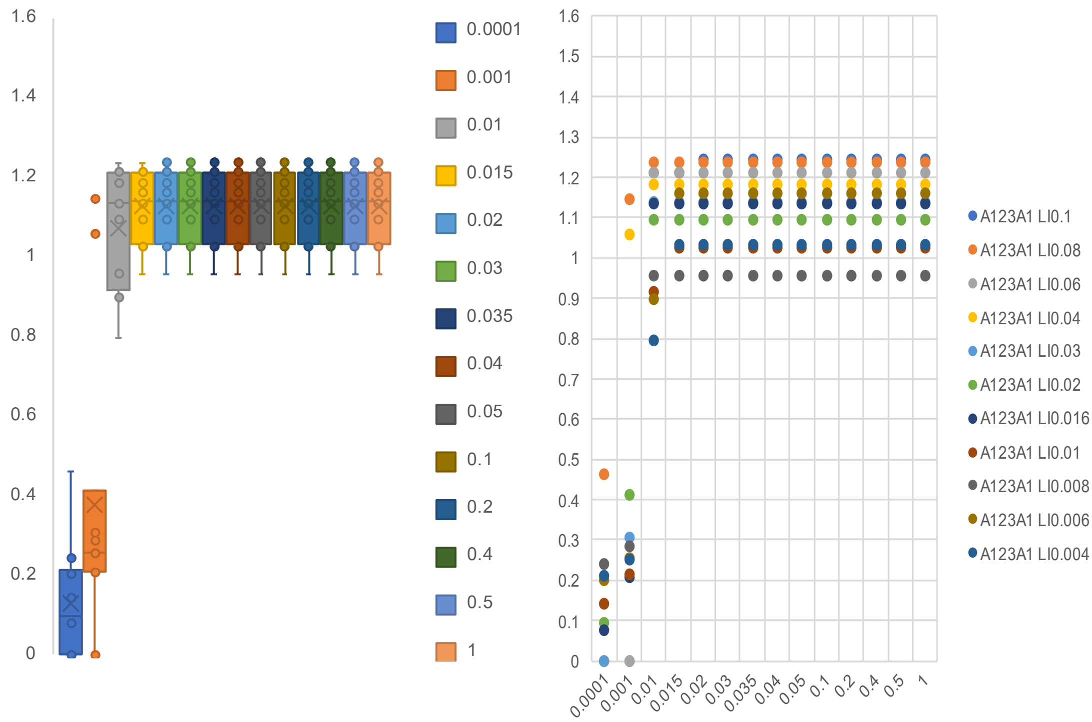

Figure 5.2 Example of Box and Scatter Plots

In Figure 5.2, the left graph consists of several box plots which give an illustration of how the distribution of the data change after a certain criterion is applied and what happens if the criterion is changed. The value of the distribution of the data can be seen on the vertical axis of the graph. In the right graph, the data from different models are represented with several dots with different colours. The change in the result of a particular numerical model can be seen as the criterion is applied and changed. This graph helps to give insight on the trend of the change in a particular numerical model and whether there is a common trend that can be seen from all results of numerical models.

The first stage is only going to be done for the study of load increment, as it will help clarify the dependency of peak load to this numerical parameter. The study of error tolerance and the maximum number of iterations will not be included in the first stage due to two reasons. The first reason is that in order to do this stage of analysis, it will need more than three sub-variation of load step per variation in order to have a more representative data distribution, which consumed more than the available time. The second reason is that the necessity of studying the distribution of the data for both variations (error tolerance and the maximum number of iterations) has not been identified yet. Therefore, the study of both variations will focus more on identifying the influence of the change on global behaviour.

The second stage is to observe the global behaviour of the simulated beam and the convergence state of the analysis. The purpose of this stage is to find whether there is a connection between change in the global behaviour to the change in the convergence state of the analysis. Two types of global behaviour are going to be observed in this stage, the load-displacement curve and the crack propagation process. The process of flexural shear crack formation has been studied and clarified into 4 steps in subchapter 4.5 Correlation of Crack Propagation to the Beam Global Response. Understanding the process of flexural shear crack formation will help identify the source of the problem with the convergence. The second stage is done for all variations and at the end, the correlation and causal relationship of the convergence state to the change in the global behaviour will be analysed in order to have an insight of what is the root of the problem.

The last stage is to derive new convergence criteria that should be satisfied in order to have a smaller distribution of data with the correct failure mode. This stage evaluates all results from the first and second stages of the analysis and tries to derive a set of criteria that can be used in any case. An additional study will also be done in order to see whether the use of a different crack model will be able to increase the performance of the simulation and reduce the dependency of the global behaviour to the numerical parameters (load increment, error tolerance, and the maximum number of iterations).

5.3. Effect of Load Increment Variation

The influence of load increment can be observed in the peak load of the numerical models and the global behaviour of the beam. Furthermore, its influence on different types of iterative-incremental methods would also be observed. An additional criterion is needed in order to define a limit of acceptance of non-converged steps. The upper bound value for the convergence norms is needed to be defined for each iterative-incremental method. The use of the upper bound value of convergence norms is expected to cause a change in the peak load distribution over the variation of load increment.

5.3.1 Effect of Load Increment Variation in Quasi-Newton Method

The first observation is done for numerical models with the Quasi-Newton method. The change in peak load distribution due to different values of upper bound for energy tolerance can be observed in Figure 5.3 and Figure 5.4 for specimens A123A1 and H123A respectively.

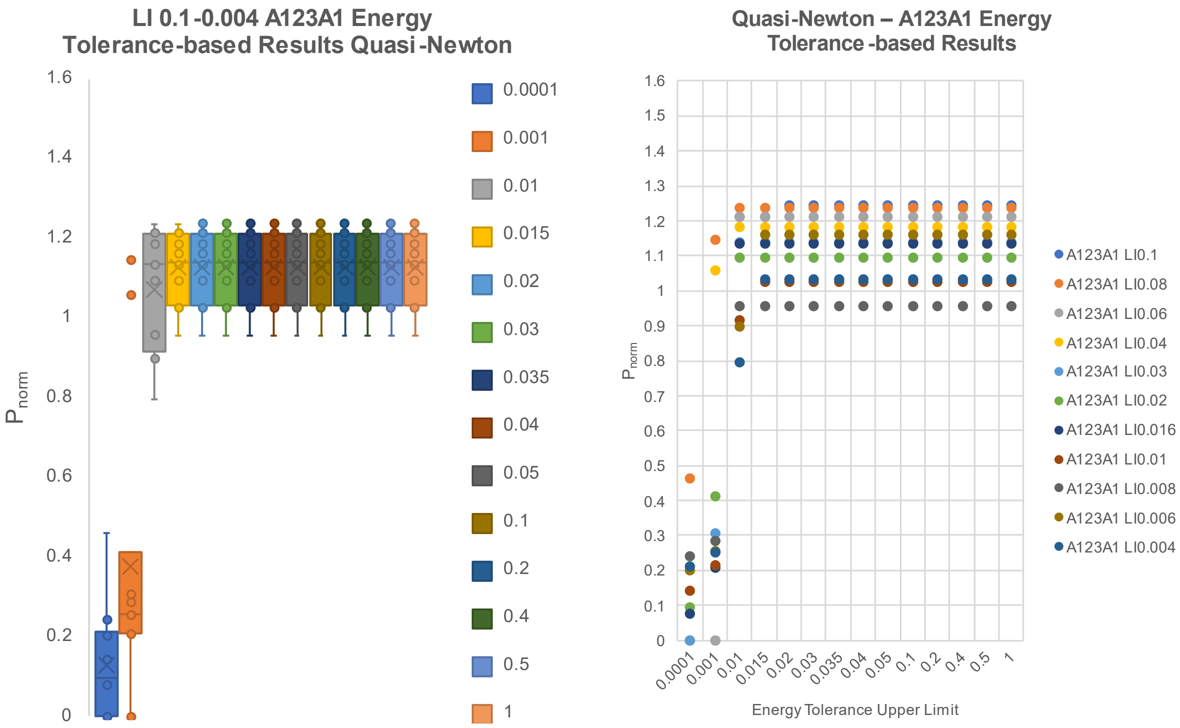

Figure 5.3 Peak Load Distribution for Model A123A1 – Quasi-Newton with Upper Bound Energy Tolerance

The peak load distribution in terms of statistics is given on the left and how does the peak load value change with different value of upper bound for energy tolerance is given on the right.

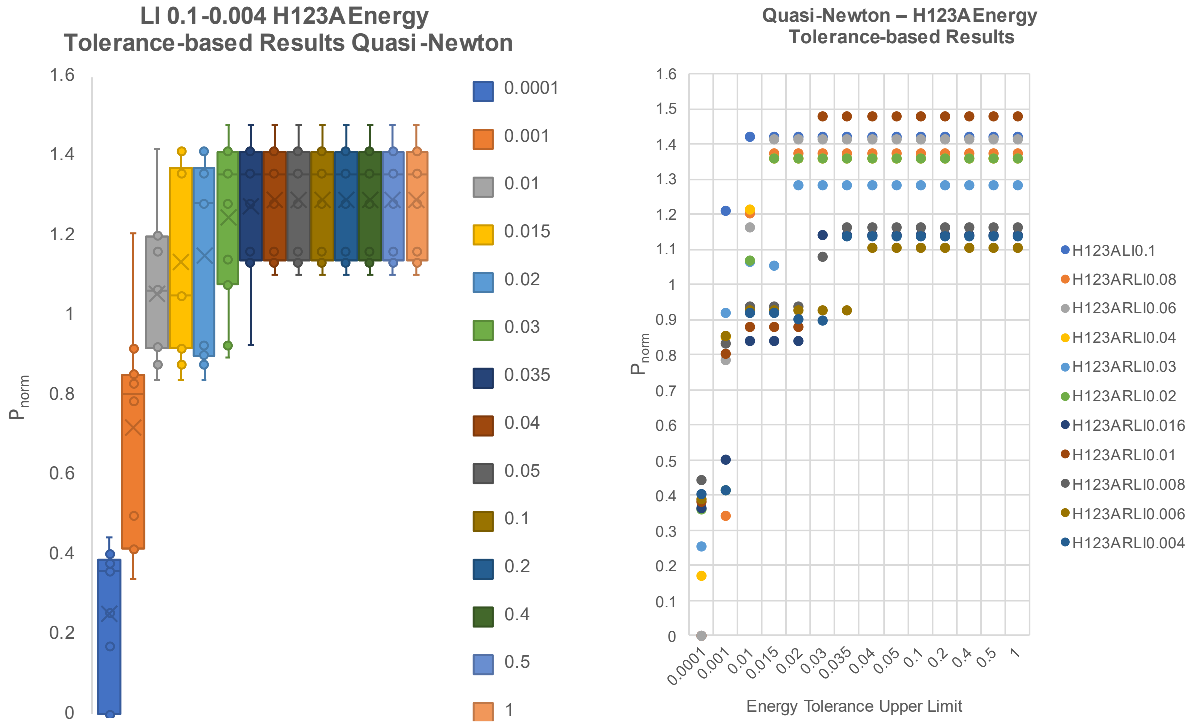

Figure 5.4 Peak Load Distribution for Model H123A – Quasi-Newton with Upper Bound Energy Tolerance

The peak load distribution in terms of statistics is given on the left and how does the peak load value change with different value of upper bound for energy tolerance is given on the right.

Both Figure 5.3 and Figure 5.4 indicate that the use of a single value of energy tolerance would cause a large underestimation of relative load capacity, ranging from 0-0.462 for specimen A123A1 and 0-0.444 for specimen H123A. Accepting several non-converged steps by imposing an upper bound value on the energy tolerance is able to improve the overall distribution of the peak load. Figure 5.3 shows that the upper limit of 0.015 is sufficient to prevent any significant change in the peak load distribution and give the smallest distribution of peak load for specimen A123A1. However, if the same upper limit value is used for specimen H123A, Figure 5.4 shows a relatively high distribution on the peak load. A higher value of the upper limit is needed to achieve the same behaviour as specimen A123A1 for specimen H123A. The upper limit of 0.04 is required to achieve this target. This indicates that the upper limit value for energy tolerance might be dependent on the specimen size, where a small specimen size requires a smaller upper limit compared to large specimen size.

Furthermore, it can be seen that a different range is attained for both cases, where the relative peak value of numerical models for specimen A123A1 is ranging from 0.958-1.237 while for specimen H123A is ranging from 1.106-1.479. The difference is not only on the minimum and maximum value but also on the total range of the peak load. These differences make it not possible to combine the results of specimen A123A1 and H123A and observe the peak load distribution together. Figure 5.3 and Figure 5.4 also show that no pattern can be seen in the distribution of the peak load, which means that the use of smaller load increment does not immediately produce a higher/smaller peak load.

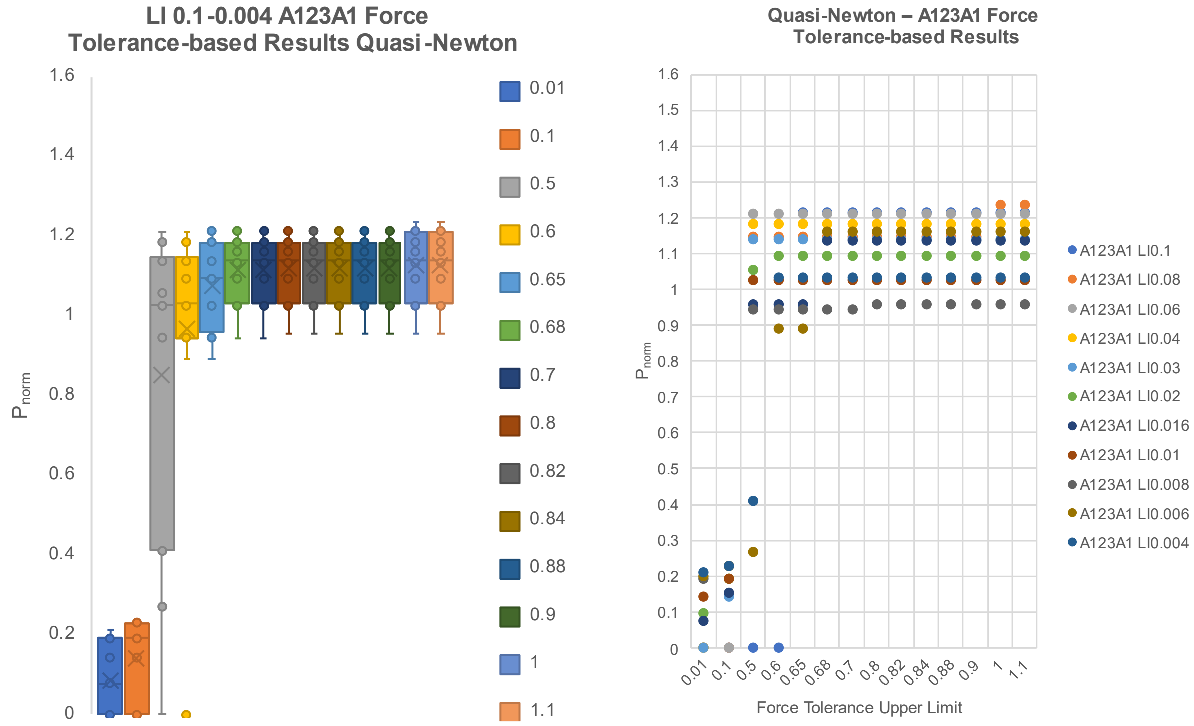

Figure 5.5 Peak Load Distribution for Model A123A1 – Quasi-Newton with Upper Bound Force Tolerance

The peak load distribution in terms of statistics is given on the left and how does the peak load value change with different value of upper bound for force tolerance is given on the right.

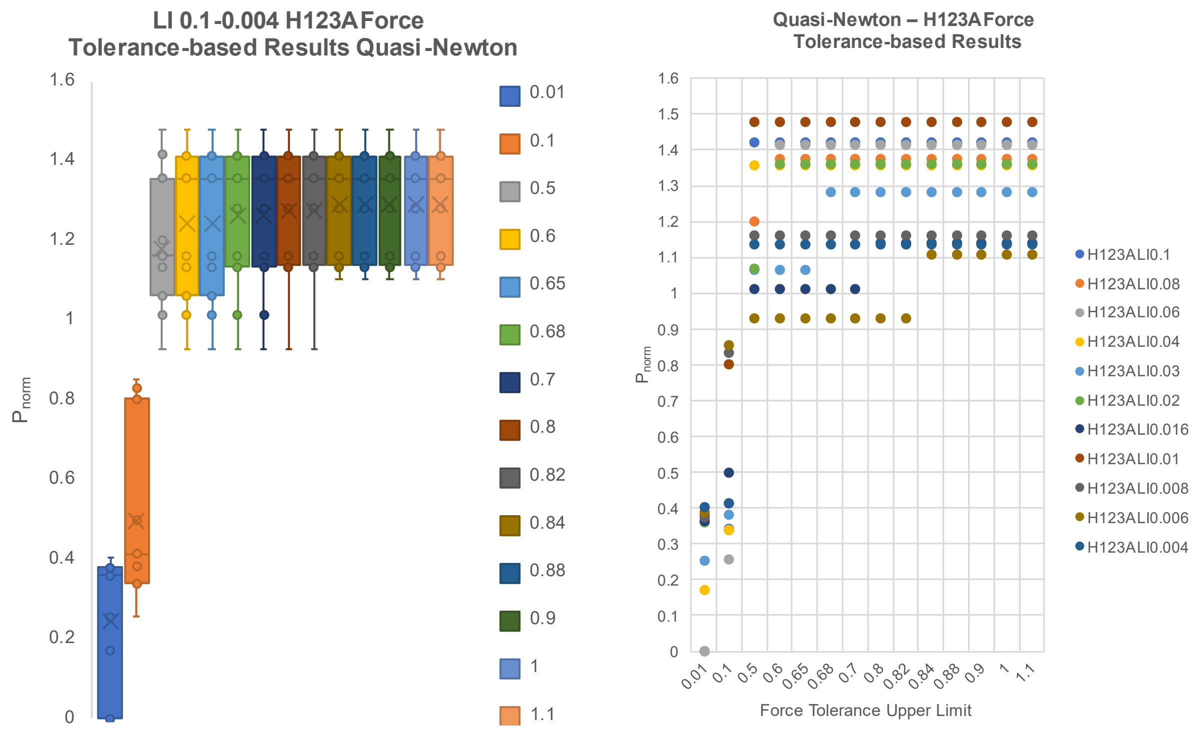

Figure 5.6 Peak Load Distribution for Model H123A – Quasi-Newton with Upper Bound Force Tolerance

The peak load distribution in terms of statistics is given on the left and how does the peak load value change with different value of upper bound for force tolerance is given on the right.

A different distribution result is attained when an upper bound value is imposed on the force tolerance, which can be seen in Figure 5.5 and Figure 5.6. A smaller range of peak load distribution, compared to the single value of energy tolerance, is achieved when a single value of force tolerance is used, ranging from 0-0.211 for specimen A123A1 and 0-0.403 for specimen H123A. Accepting several non-converged steps by imposing upper bound value on the force tolerance also improve the overall distribution of the peak load. The optimum upper bound for specimen A123A1 for force tolerance is 0.68 while for specimen H123A is 0.84. This also indicates that the upper limit value for force tolerance might be dependent on the specimen size, where a small specimen size requires a smaller upper limit compared to large specimen size.

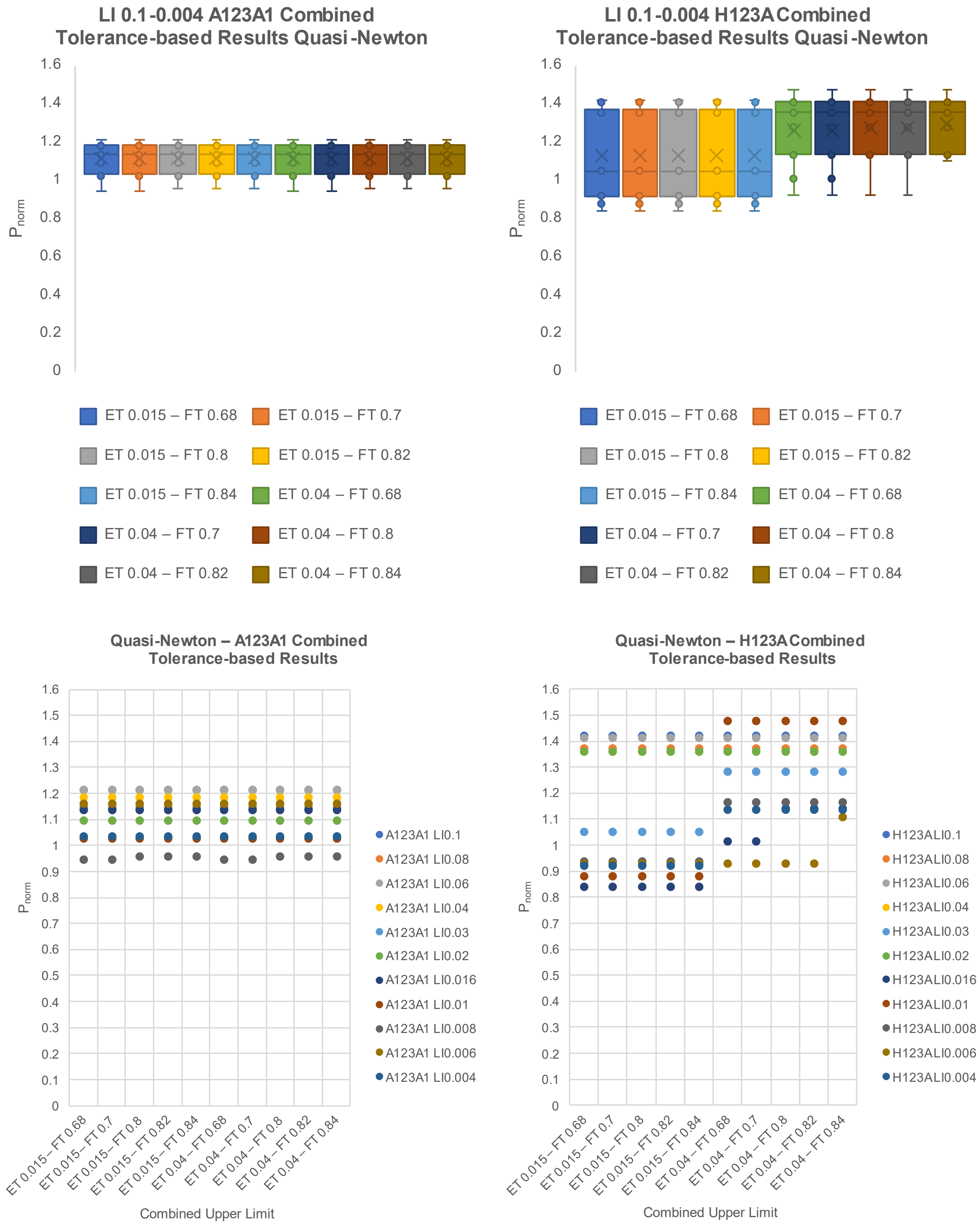

Figure 5.7 Peak Load Distribution for Quasi-Newton Method with Combined Upper Bound

The peak load distribution in terms of statistics is given on the top and how does the peak load value change with different value of upper bound for error tolerance is given on the bottom.

Furthermore, a different range is also attained for both cases, where the relative peak value of numerical models of specimen A123A1 is from 0.946 to 1.214 while for specimen H123A is from 1.106 to 1.479. No pattern can be seen on the distribution of the peak load with load increment variation. The relative peak value range of numerical models for each specimen is similar in both cases. A single upper bound value is not recommended to be used, because the numerical models rarely have a single step that would exceed the upper bound value of energy and force tolerance at the same time. An example can be seen by comparing Figure 5.3 and Figure 5.5 for model A123A1 LI0.08. Model A123A1 LI 0.08 has a relative peak load of 1.237 when the optimal upper bound of energy tolerance is used, while a relative peak load of 1.147 is achieved when the optimal upper bound of force tolerance is used. In order to find a general upper bound for numerical models and reduce variation of the results, the upper bound limit is applied to both energy and force tolerance.

Figure 5.7 shows the combination of upper bound values from the optimal value of specimen A123A1 and H123A where a single upper bound type is applied. For specimen A123A1, Figure 5.7 indicates that the use of 0.015-0.04 and 0.68-0.84 for upper bound of energy and force tolerance respectively do not change the peak load distribution, which is in accordance with the results in Figure 5.3 and Figure 5.5. Figure 5.3 and Figure 5.5 show a similar distribution of peak load results, which means that the use of combined tolerance would not significantly change the peak load distribution for specimen A123A1. On the other hand, specimen H123A does not produce the same result as specimen A123A1. Slight variation can be seen between the upper bound of 0.015 and 0.04 for energy tolerance. This also can be explained by observing Figure 5.4 and Figure 5.6 where a significant difference in range can be seen between the upper bound of 0.015 and 0.04 for energy tolerance and an almost constant range between the upper bound of 0.68 and 0.84 for force tolerance. The most optimal combined tolerance is 0.04 and 0.84 for energy and force tolerance respectively. The optimal combination for the upper bound value of the tolerance gives a range of 0.958-1.214 for specimen A123A1 and 1.106-1.479 for specimen H123A.

A better result can be attained by specifying a specific range of load increment where the peak load has less variation compared to the current range of load increment. Figure 5.8 gives an improved peak load distribution where the range of load increment is reduced from 0.1-0.004 to 0.1-0.02. The change in the range of load increment causes a change in the optimally combined tolerance, from 0.04 and 0.84 to 0.04 and 0.68 for energy and force tolerance respectively. The change in the range of load increment improves the peak load distribution from 0.958-1.214 and 1.106-1.479 to 1.096-1.214 and 1.283-1.420 for specimen A123A1 and H123A respectively.

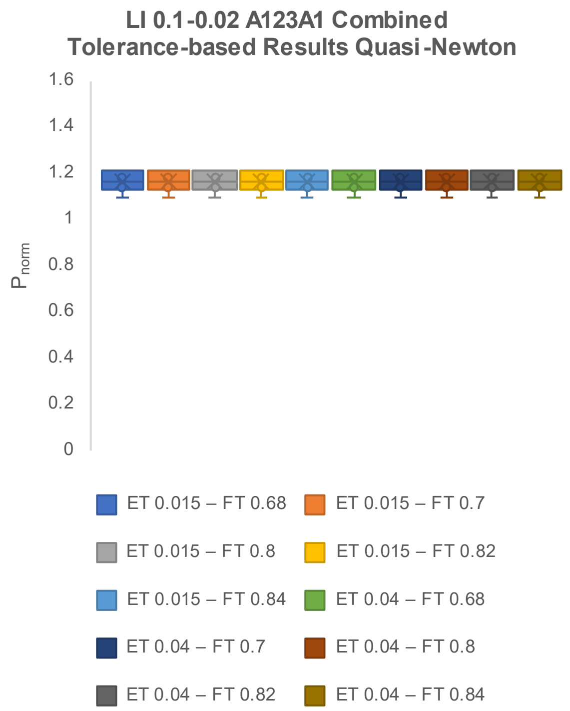

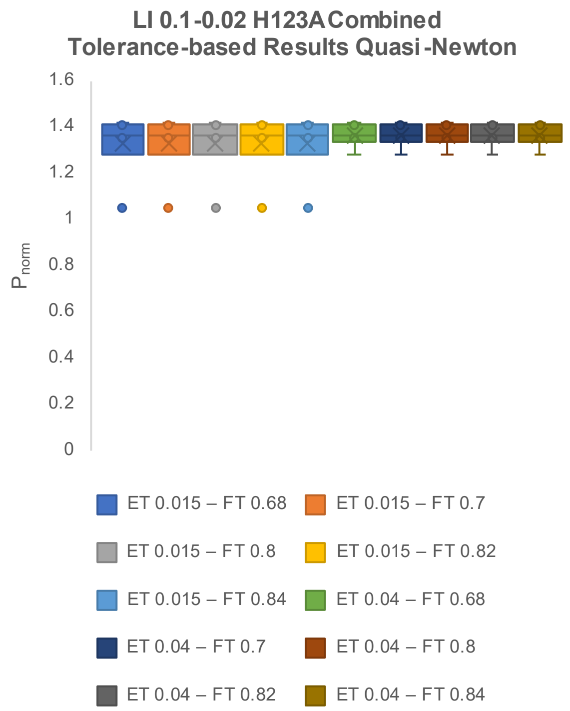

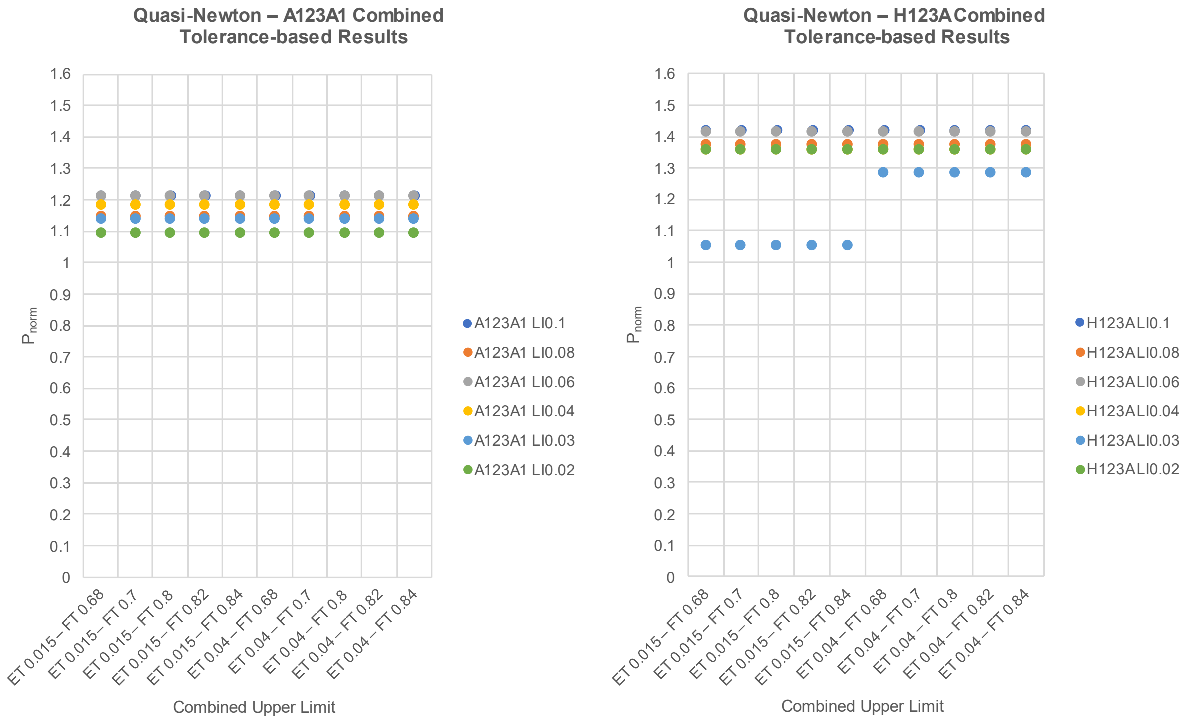

Figure 5.8 Peak Load Distribution for Quasi-Newton Method with Combined Upper Bound and LI 0.1-0.02

The peak load distribution in terms of statistics is given on the top and how does the peak load value change with different value of upper bound for energy tolerance is given on the bottom.

The simulated global behaviour of the beam with the Quasi-Newton method is observed based on the results of NLFEA which has lower relative energy variation and relative out-of-balance force than the defined upper bound for both energy and force tolerance. Figure 5.9 gives an illustration of the simulated global behaviour of the beam with the Quasi-Newton method based on the load-displacement curve.

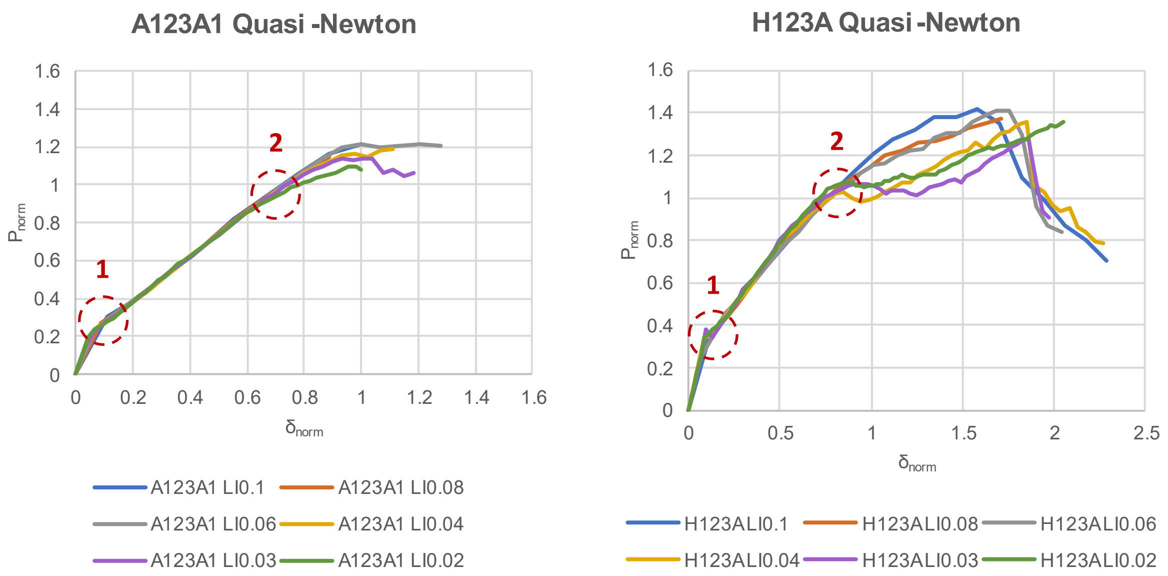

Figure 5.9 Load-displacement Curve for Load Increment Variance – Quasi-Newton Method

In the load-displacement curve in Figure 5.9, there are 2 critical points that show some deviation due to change in load increment. The first critical point is considered not important because the deviation in critical point 1 does not affect the overall simulated behaviour of the beam in the non-linear region. This can be seen by observing the load-displacement curve between critical point 1 and critical point 2, where the simulated non-linear behaviour is similar for all models with specimen A123A1 and H123A. On critical point 2, a significant deviation can be seen between the results on both specimens. The deviation on the curve is considered significant due to its effect on the simulated non-linear behaviour and the peak load of the model. Three models, LI0.06, LI0.03, and LI0.02 are chosen as the representative of all results for specimen A123A1 and two models, LI0.06 and LI0.04, for specimen H123A. The load-displacement curve for these models is given in Figure 5.10.

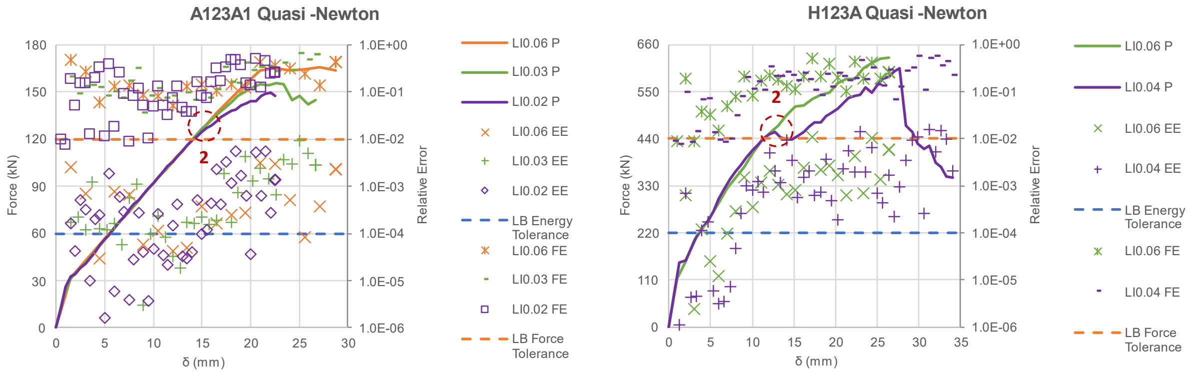

Figure 5.10 Load-displacement Curve with the Convergence State for Quasi-Newton Method

Figure 5.10 indicates that most of the steps are converging in relative energy variation. Furthermore, higher relative energy variation and out-of-balance force can be seen by comparing convergence state at δ = 15-25 mm to δ = 5-15 mm for specimen A123A1 and δ = 10-30 mm to δ = 5-10 mm for specimen H123A, where the curve is near its peak.

The first critical point 2 that would be analysed is for specimen A123A1. Detailed illustration for critical point 2 of specimen A123A1 is given in Figure 5.11. 4 load steps are going to be observed in Figure 5.11. These load steps indicate the shift in the load-displacement curve and will be called shifting points A, B, C and D for displacement at 13.48 mm, 14.98 mm, 16.48 mm and 17.98 mm respectively.

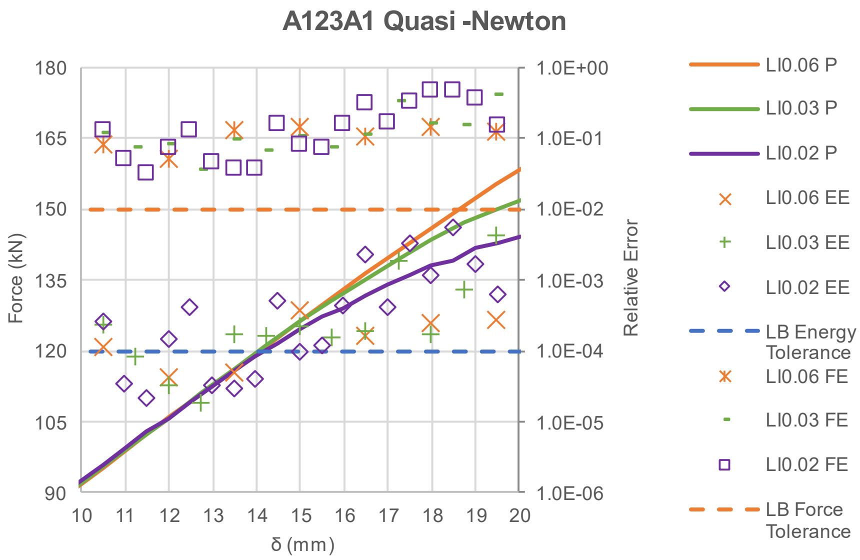

Figure 5.11 Load-displacement Curve on Critical Point 2 of Specimen A123A1 for Quasi-Newton Method

LI0.06

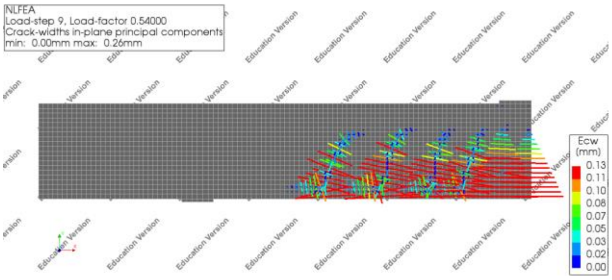

LI0.03

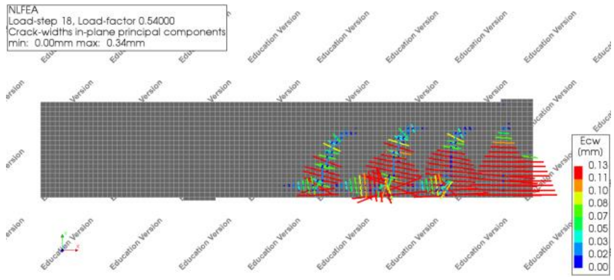

LI0.02

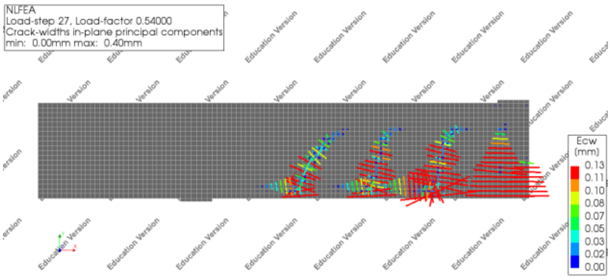

Figure 5.12 Crack Pattern Specimen A123A1 with Quasi-Newton Method at δ = 13.48 mm (Shifting Point A)

LI0.06

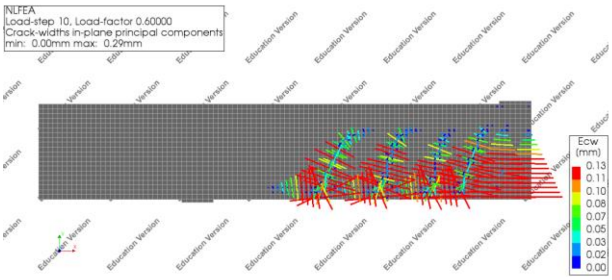

LI0.03

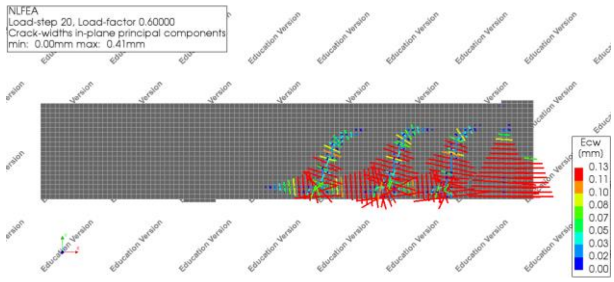

LI0.02

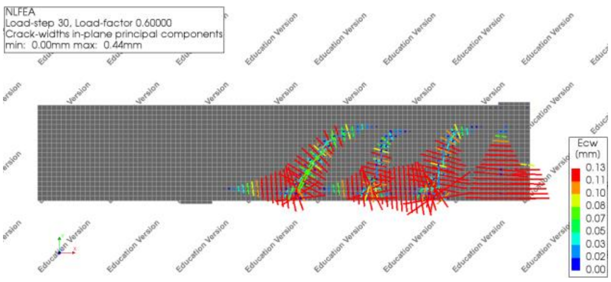

Figure 5.13 Crack Pattern Specimen A123A1 with Quasi-Newton Method at δ = 14.98 mm (Shifting Point B)

LI0.06

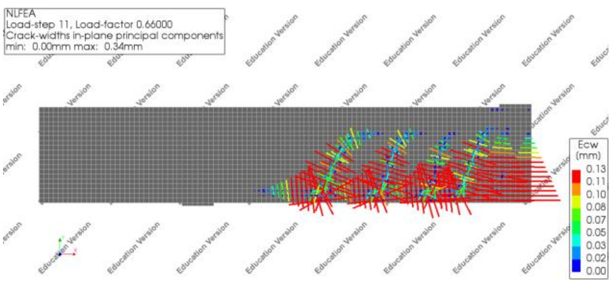

LI0.03

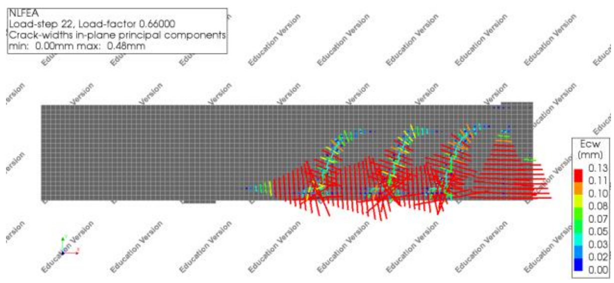

LI0.02

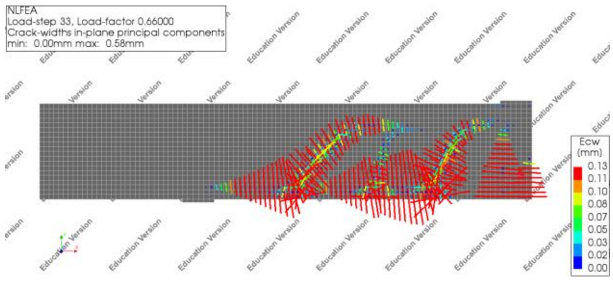

Figure 5.14 Crack Pattern Specimen A123A1 with Quasi-Newton Method at δ = 16.48 mm (Shifting Point C)

LI0.06

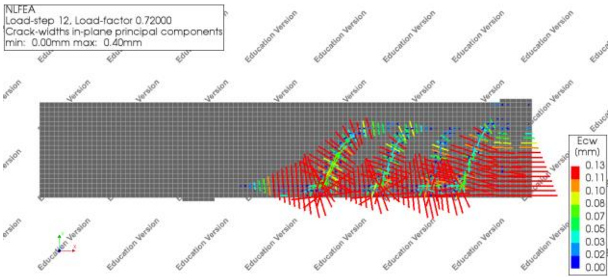

LI0.03

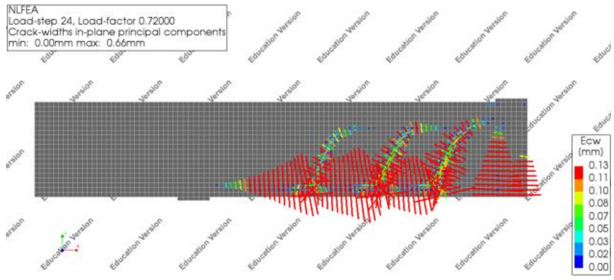

Figure 5.15 Crack Pattern Specimen A123A1 with Quasi-Newton Method at δ = 17.98 mm (Shifting Point D)

LI0.06

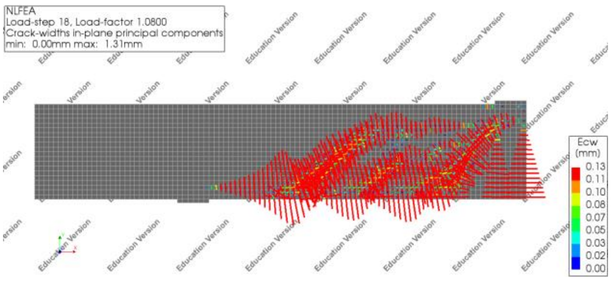

LI0.03

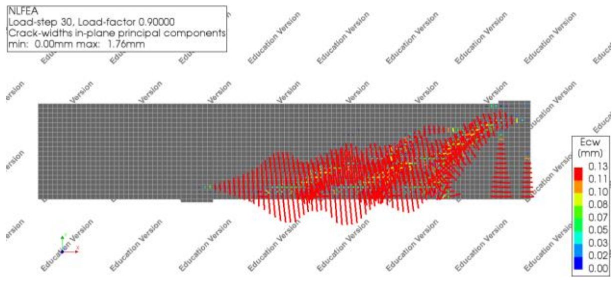

LI0.02

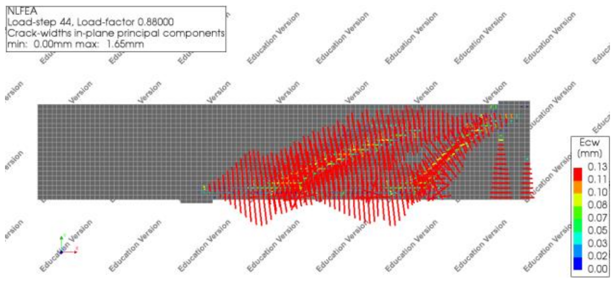

Figure 5.16 Crack Pattern Specimen A123A1 with Quasi-Newton Method at Peak Load

The relative energy variation in Figure 5.11 is relatively constant for model A123A1 LI0.06 and LI0.03, and constantly increasing in model A123A1 LI0.02 from shifting point A to shifting point C. The relative out-of-balance force in model A123A1 LI0.06 and LI0.03 is relatively constant through all shifting points. However, in model A123A1 LI0.02, the relative out-of-balance force is constantly increasing from shifting point A to shifting point C. The convergence state for model A123A1 LI0.03 starts to change from shifting point C to D, where an increase in relative energy variation and out-of-balance force can be seen, which does not happen in model A123A1 LI0.06.

In terms of crack pattern, the model A123A1 LI0.06 and LI0.03 show similar crack progression in Figure 5.12, Figure 5.13, and Figure 5.14, where several inclined cracks with dowel crack are propagating. On the other hand, model A123A1 LI0.02 shows a different crack pattern where several inclined cracks are transformed into major inclined cracks, which the dowel crack in shifting point C in Figure 5.14 has almost reached the support. This transformation also happens to model A123A1 LI0.03 on a later stage in shifting point D in Figure 5.15. However, the cracking pattern at the peak load is similar between model A123A1 LI0.06, LI0.03, and LI0.02, according to Figure 5.16. The change in convergence state seems to follow the crack progression on the concrete where the constant level of relative energy variation and out-of-balance force indicates stable crack propagation on the model and increased level of relative energy variation and out-of-balance force indicates the model is approaching its peak capacity.

The next critical point 2 in Figure 5.10 that would be analysed is for specimen H123A. Detailed illustration for critical point 2 of specimen H123A is given in Figure 5.17. 4 load steps are going to be observed in Figure 5.17. These load steps indicate the shift in the load-displacement curve and will be called shifting points A, B, C and D for displacement at 12.07 mm, 13.08 mm, 14.09 mm and 16.13 mm respectively.

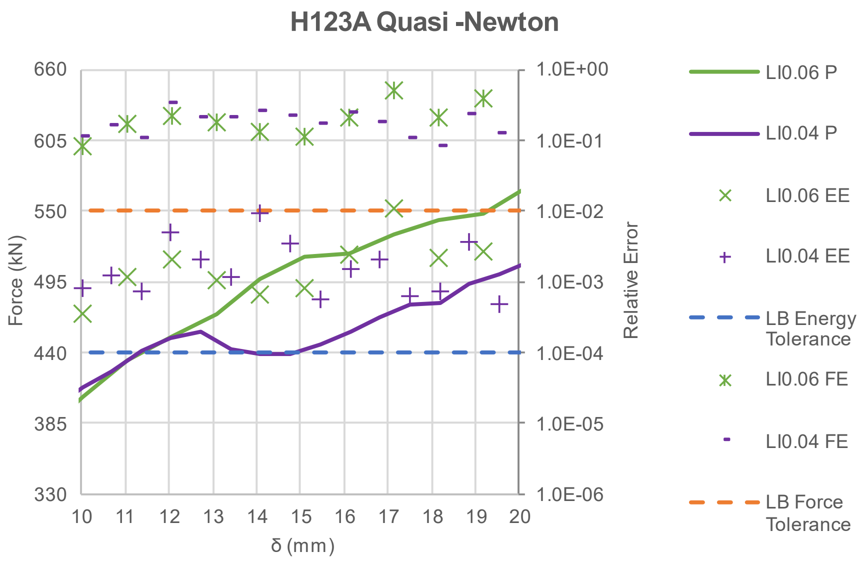

Figure 5.17 Load-displacement Curve on Critical Point 2 of Specimen H123A for Quasi-Newton Method

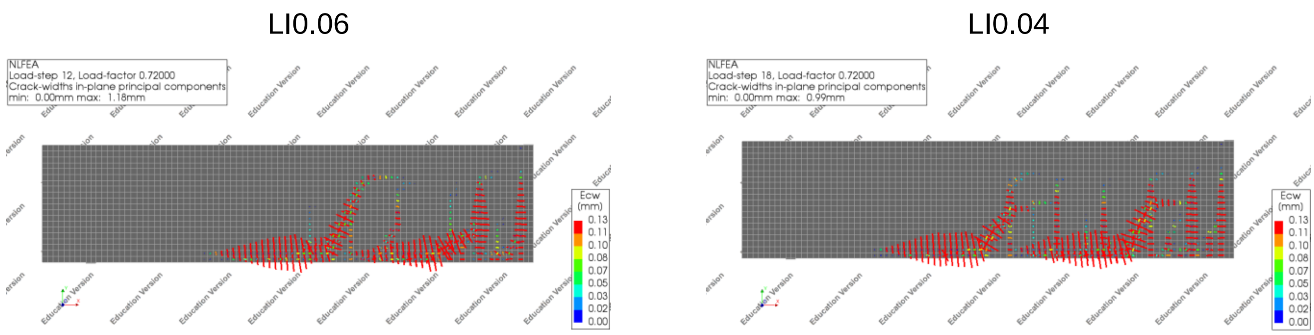

Figure 5.18 Crack Pattern Specimen H123A with Quasi-Newton Method at δ = 12.07 mm (Shifting Point A)

LI0.06 LI0.04

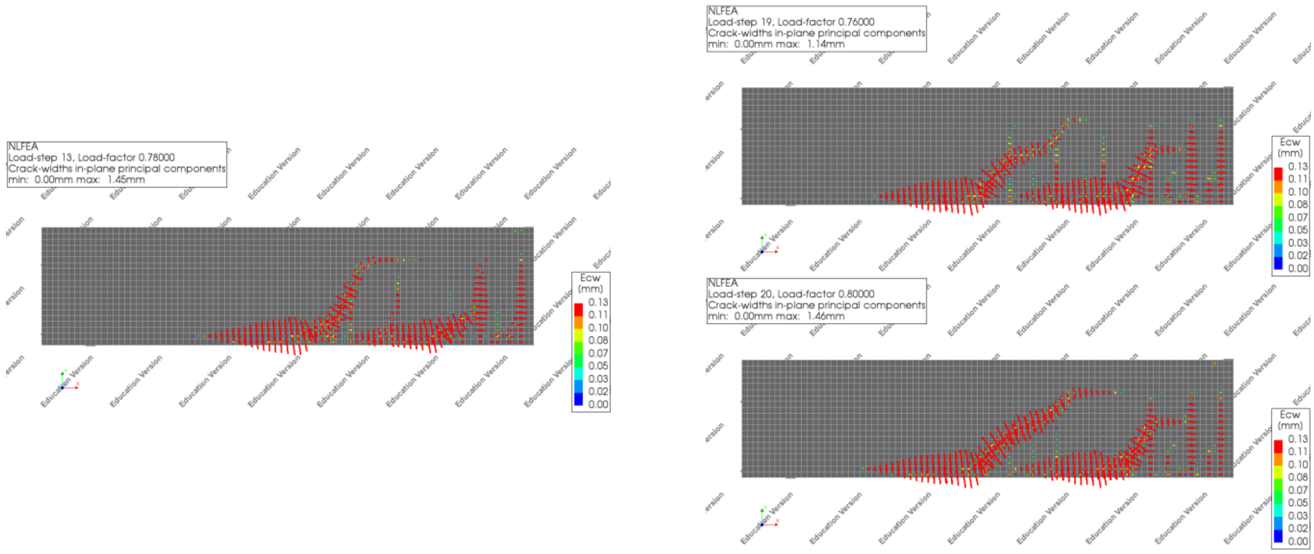

Figure 5.19 Crack Pattern Specimen H123A with Quasi-Newton Method at δ = 13.08 mm (Shifting Point B)

LI0.06 LI0.04

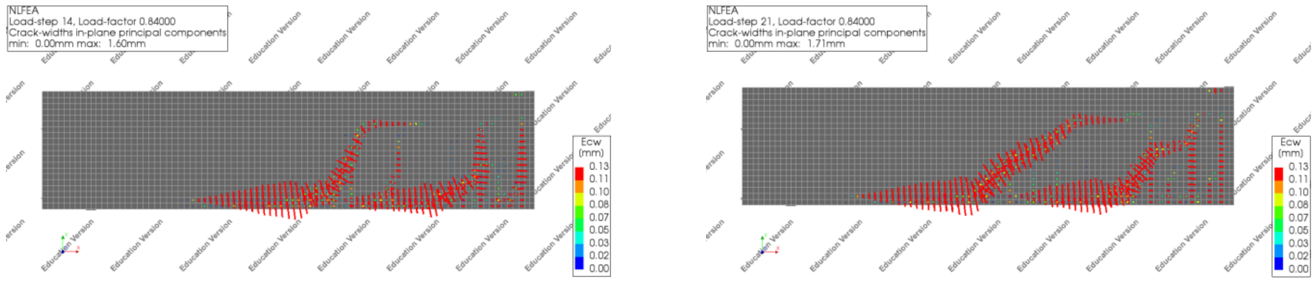

Figure 5.20 Crack Pattern Specimen H123A with Quasi-Newton Method at δ = 14.09 mm (Shifting Point C)

LI0.06 LI0.04

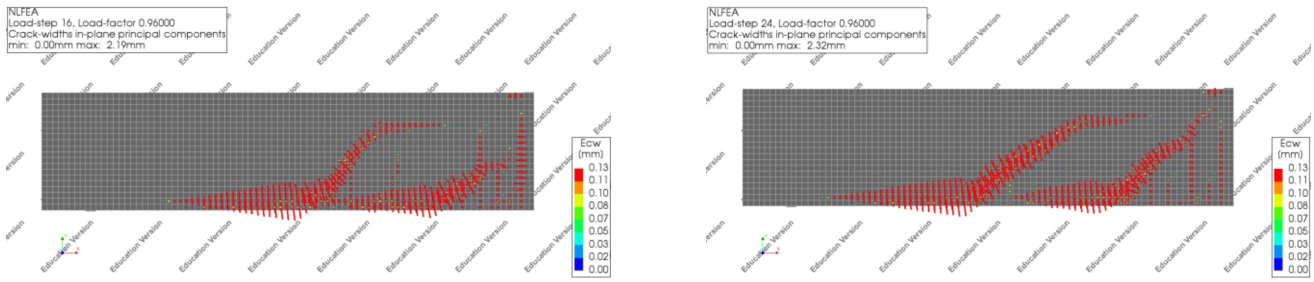

Figure 5.21 Crack Pattern Specimen H123A with Quasi-Newton Method at δ = 16.13 mm (Shifting Point D)

LI0.06 LI0.04

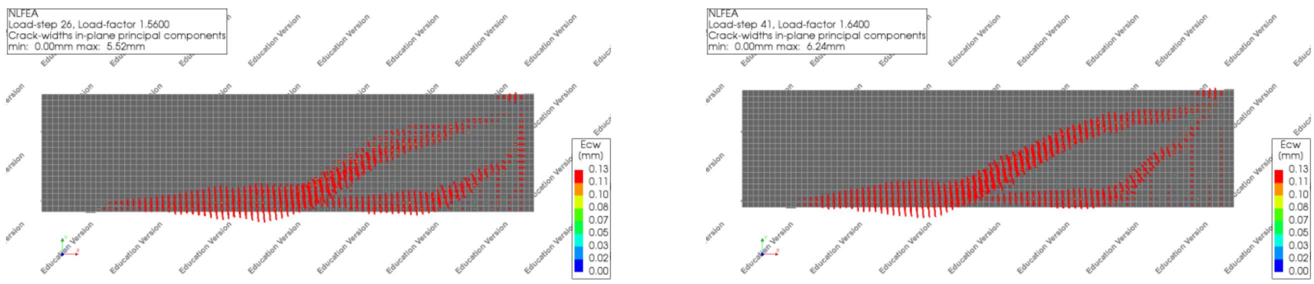

Figure 5.22 Crack Pattern Specimen H123A with Quasi-Newton Method at Peak Load

The relative energy variation in Figure 5.17 shows a similar pattern between model H123A LI0.06 and LI0.04, and relatively constant through all shifting points. However, a significant difference in relative energy variation in model H123A1 LI0.06 can be seen from shifting point B to C. The relative out-of-balance force in model H123A1 LI0.06 and LI0.04 is relatively constant through all shifting points.

In terms of crack pattern, models H123A LI0.06 and LI0.04 show similar crack progression with small differences in maximum crack width in shifting point A in Figure 5.18. The similarity of the crack progression can also be seen in other shifting points in Figure 5.19, Figure 5.20, and Figure 5.21. However, the difference in maximum crack width becomes larger from shifting point B to C in model H123A LI0.04. The crack propagation in model H123A LI0.04 is less stable compared to model H123A LI0.06. This phenomenon can be observed by comparing the maximum crack width in both models in Figure 5.18, Figure 5.19, and Figure 5.20. The maximum crack width in model H123A LI0.06 is larger in shifting point A compared to model H123A LI0.04 in Figure 5.18, while model H123A LI0.06 has smaller maximum crack width in shifting point B compared to model H123A LI0.04 in shifting point C in Figure 5.20. The shifting point of this phenomenon happens between shifting points B and C, where the maximum crack width is increased by 0.15 mm in model H123A LI0.06, while in model H123A LI0.04 is increased by 0.25 mm. This indirectly implied that model H123A LI0.04 has more concrete elements that reached its ultimate tensile strain, which cause higher relative energy variation between the current step and the previous step. This phenomenon is captured in the relative energy variation in Figure 5.17. The similarity of the cracking pattern between each shifting point can also be seen in the relative energy variation and out-of-balance force. Furthermore, the crack pattern at the peak load also similar for both models in Figure 5.22, which is also consistent with the similarity of the convergence state of both models in Figure 5.10.

Based on the observation for both specimen A123A1 and H123A, it can be concluded that the variation on the peak load of models with the Quasi-Newton method and different load increment is caused by the different rates of crack propagation on the models. This can be observed in the change of the convergence state of the models where the shift from constant to linear growth of both relative energy variation and out-of-balance force indicates that the model is approaching its peak capacity. The shifting point of this phenomenon is considered important because the shifting point controls when the numerical models would reach their peak capacity.

5.3.2 Effect of Load Increment Variation in Full Newton-Raphson Method

The second observation is done for numerical models with the Full Newton-Raphson method. The change in peak load distribution due to different values of upper bound values for energy tolerance can be observed in Figure 5.23 and Figure 5.24 for specimens A123A1 and H123A respectively.

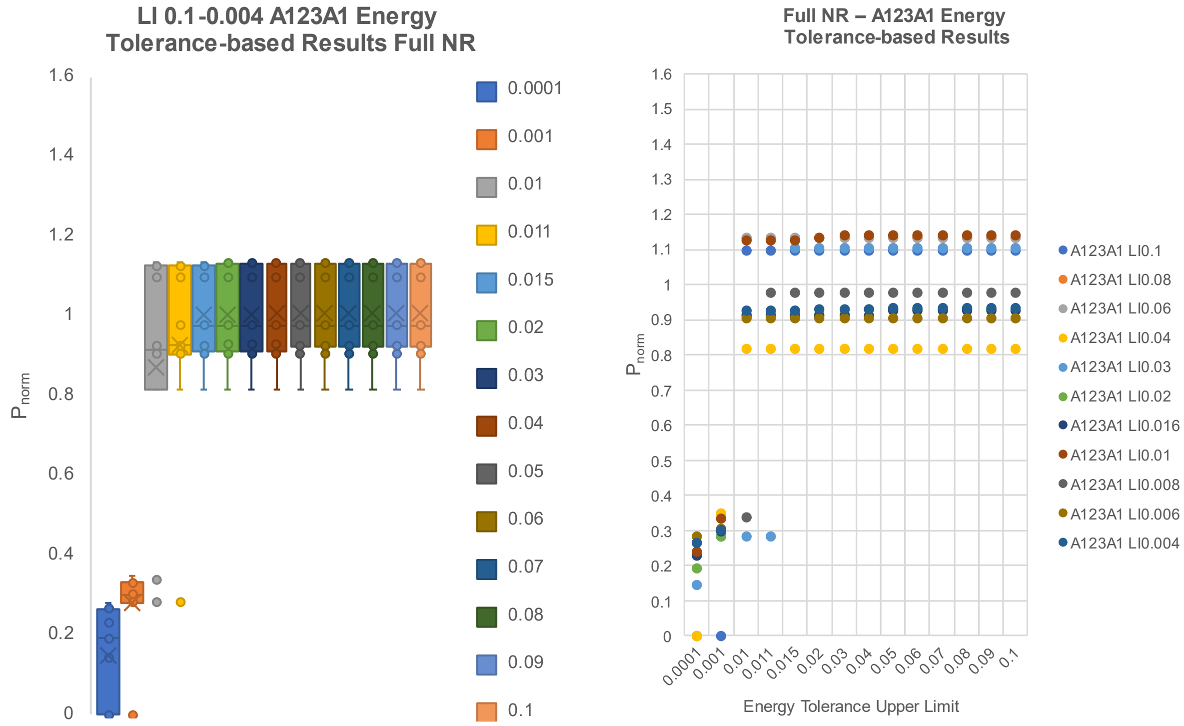

Figure 5.23 Peak Load Distribution for Model A123A1 – Full NR with Upper Bound Energy Tolerance

The peak load distribution in terms of statistics is given on the left and how does the peak load value change with different value of upper bound for energy tolerance is given on the right.

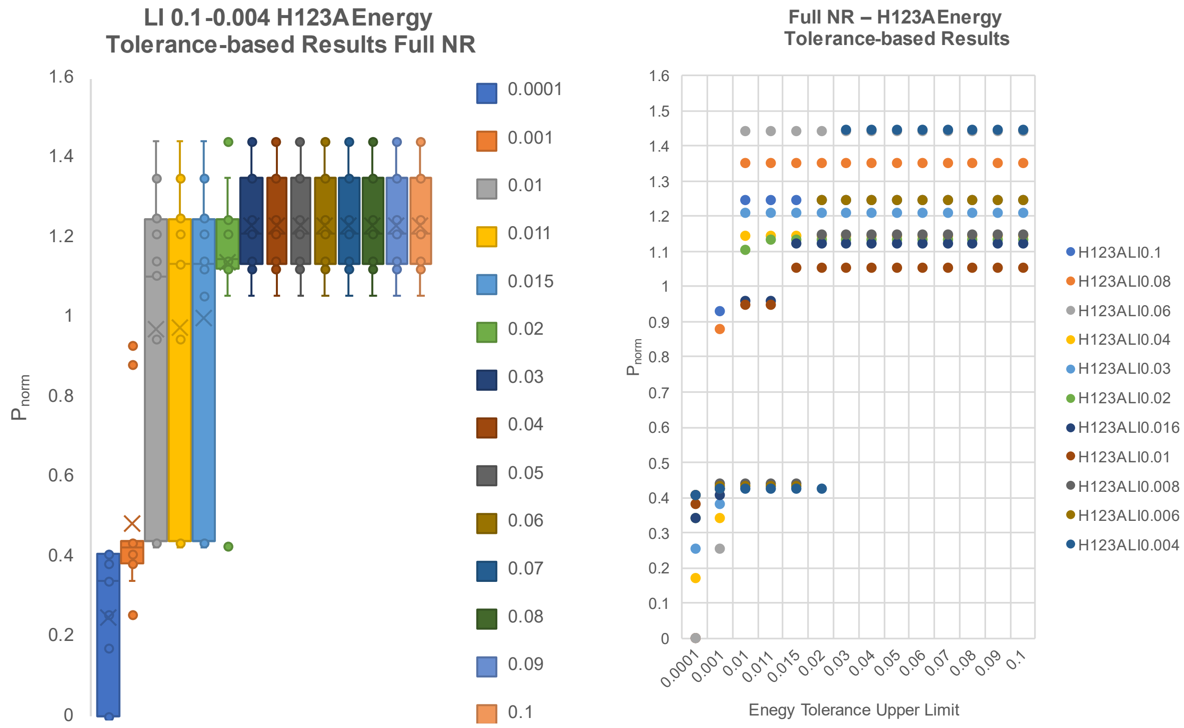

Figure 5.24 Peak Load Distribution for Model H123A – Full NR with Upper Bound Energy Tolerance

The peak load distribution in terms of statistics is given on the left and how does the peak load value change with different value of upper bound for energy tolerance is given on the right.

Both Figure 5.23 and Figure 5.24 indicate that the use of a single value of energy tolerance would cause a large underestimation of relative load capacity, ranging from 0-0.282 for specimen A123A1 and 0-0.408 for specimen H123A. Accepting several non-converged steps by imposing an upper bound value on the energy tolerance is able to improve the overall distribution of the peak load. Figure 5.23 shows that the upper limit of 0.015 is sufficient to prevent any significant change in the peak load distribution and give the smallest distribution of peak load for specimen A123A1. However, if the same upper limit value is used for specimen H123A, Figure 5.24 shows a relatively high distribution on the peak load. A higher value of the upper limit is needed to achieve the same behaviour as specimen A123A1 for specimen H123A. The upper limit of 0.03 is required to achieve this target. This indicates that the upper limit value for energy tolerance might be dependent on the specimen size, where a small specimen size requires a smaller upper limit compared to large specimen size.

Furthermore, it can be seen that a different range is attained for both cases, where the relative peak value of numerical models for specimen A123A1 is ranging from 0.817-1.135 while for specimen H123A is ranging from 1.055-1.449. The difference is not only on the minimum and maximum value but also on the total range of the peak load. These differences make it not possible to combine the results of specimen A123A1 and H123A and observe the peak load distribution together. Figure 5.23 and Figure 5.24 also show that no pattern can be seen in the distribution of the peak load, which means that the use of smaller load increment does not immediately produce a higher/smaller peak load.

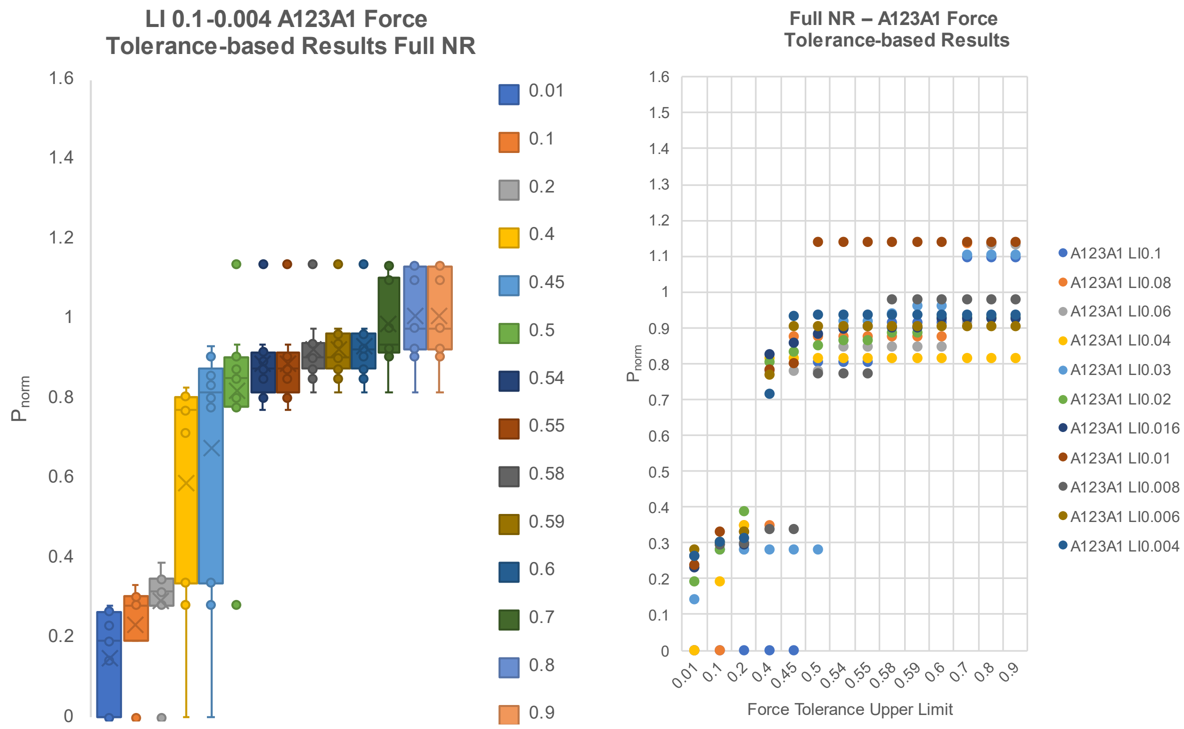

Figure 5.25 Peak Load Distribution for Model A123A1 – Full NR with Upper Bound Force Tolerance

The peak load distribution in terms of statistics is given on the left and how does the peak load value change with different value of upper bound for force tolerance is given on the right.

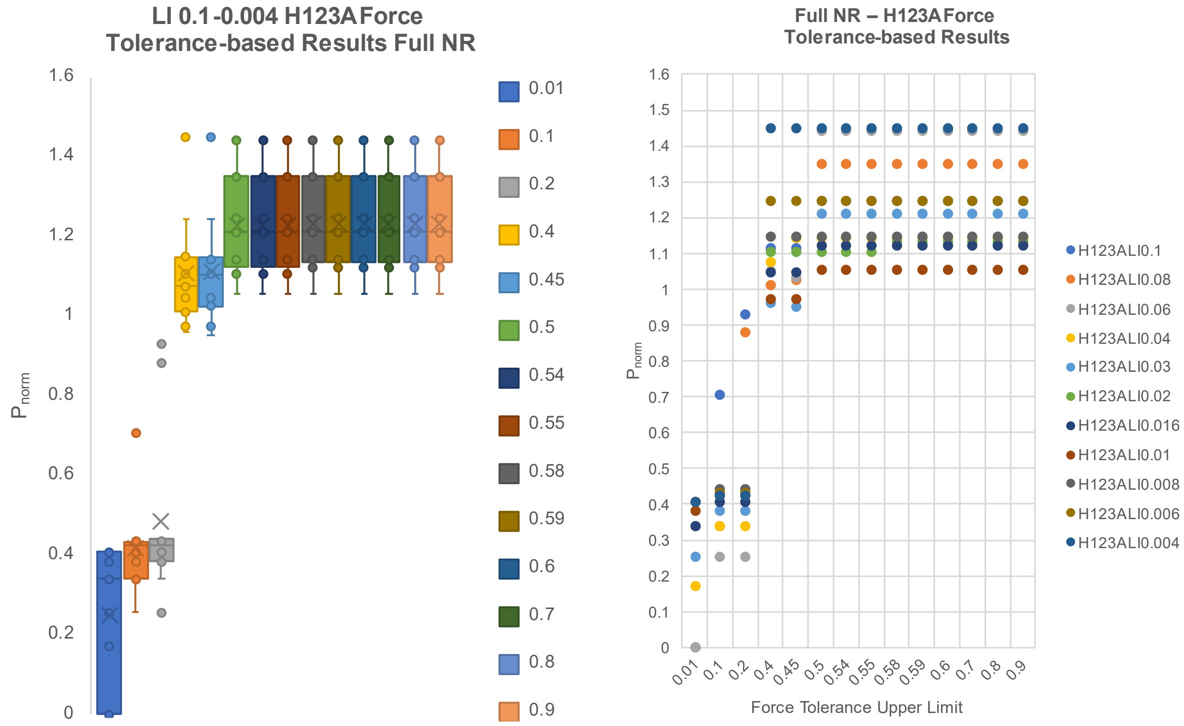

Figure 5.26 Peak Load Distribution for Model H123A – Full NR with Upper Bound Force Tolerance

The peak load distribution in terms of statistics is given on the left and how does the peak load value change with different value of upper bound for force tolerance is given on the right.

A different distribution result is attained when an upper bound value is imposed on the force tolerance, which can be seen in Figure 5.25 and Figure 5.26. The same range of peak load distribution, compared to the single value of energy tolerance, is achieved when a single value of force tolerance is used, ranging from 0-0.282 for specimen A123A1 and 0-0.408 for specimen H123A. Accepting several non-converged steps by imposing upper bound value on the force tolerance also improve the overall distribution of the peak load. However, in comparison to Figure 5.23 and Figure 5.24, Figure 5.25 and Figure 5.26 do not exhibit the same behaviour where a higher value of upper bound means less variation on the peak load distribution. The upper bound value is needed to be within a certain range of values in order to have the most optimum peak load distribution, where the minimum value of the range is used for the upper bound value. The optimum upper bound for specimen A123A1 for force tolerance is ranged between 0.58-0.6 while for specimen H123A is 0.4-0.45. This still indicates that the upper limit value for force tolerance might be dependent on the specimen size, where a small specimen size requires a smaller upper limit compared to a large specimen size.

Furthermore, a different range is also attained for both cases, where the relative peak value of numerical models of specimen A123A1 is from 0.817 to 0.978 while for specimen H123A is from 0.962 to 1.246. No pattern can be seen on the distribution of the peak load with load increment variation and both results have an outlier. The relative peak value range of numerical models for each specimen is similar in both cases. A single upper bound value is not recommended to be used, because the numerical models rarely have a single step that would exceed the upper bound value of energy and force tolerance at the same time. An example can be seen by comparing Figure 5.3 and Figure 5.5 for model A123A1 LI0.03. Model A123A1 LI 0.03 has a relative peak load of 1.103 when the optimal upper bound of energy tolerance is used, while a relative peak load of 0.940 is achieved when the optimal upper bound of force tolerance is used. In order to find a general upper bound for numerical models, reduce variation of the results, and eliminate the outliers, the upper bound limit is applied to both energy and force tolerance.

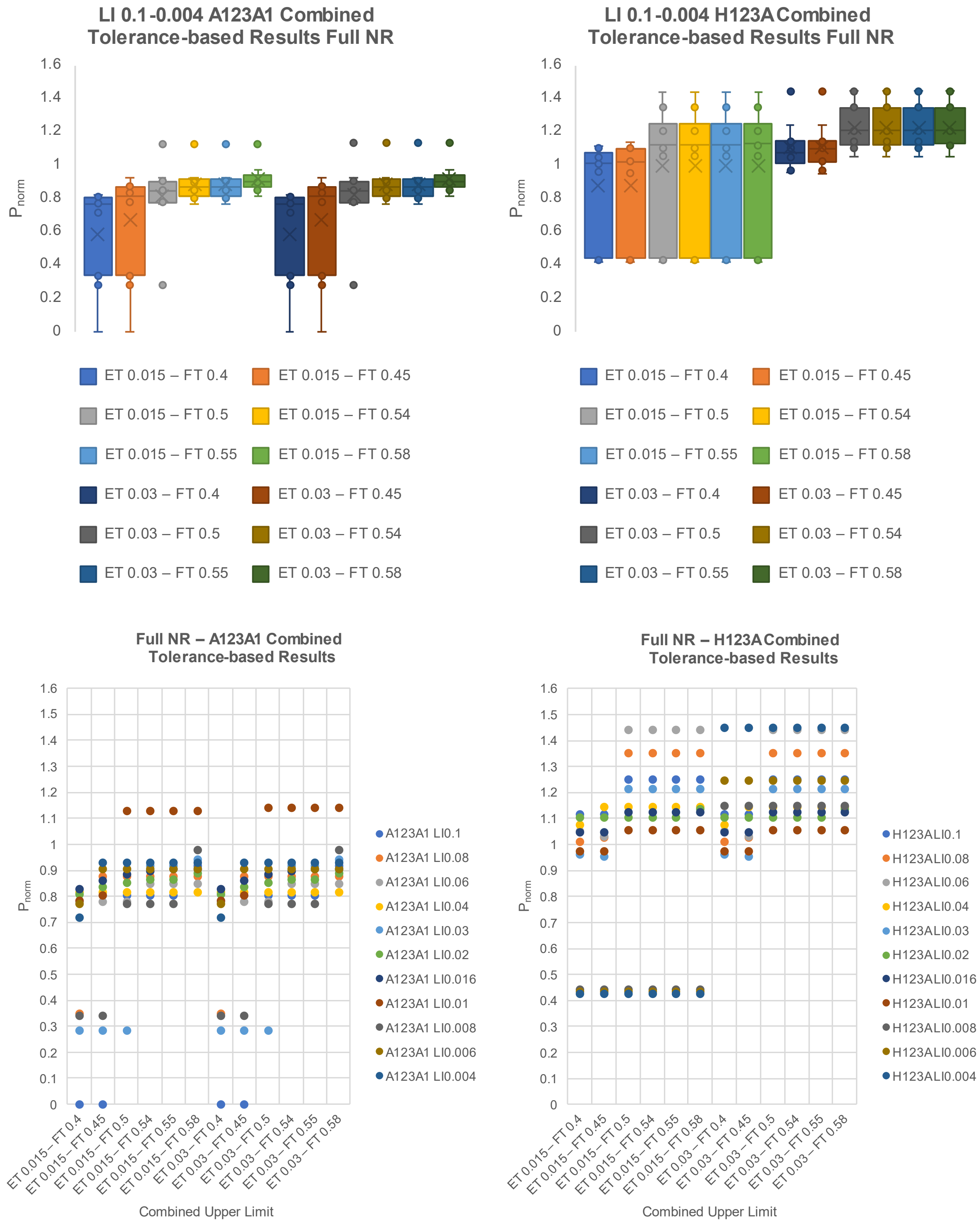

Figure 5.27 Peak Load Distribution for Full NR Method with Combined Upper Bound

The peak load distribution in terms of statistics is given on the top and how does the peak load value change with different value of upper bound for error tolerance is given on the bottom.

Figure 5.27 shows the combination of upper bound values from the optimal value of specimen A123A1 and H123A where a single upper bound type is applied. For specimen A123A1, Figure 5.27 indicates that the use of 0.015 and 0.03 for the upper bound of energy tolerance in combination with the upper bound of 0.58 for force tolerance respectively do not change the peak load distribution, which is in accordance with the results in Figure 5.23. Figure 5.23 shows a similar distribution of peak load results for both upper bound values of energy tolerance, which means that the use of combined tolerance would not significantly change the peak load distribution for specimen A123A1. On the other hand, specimen H123A does not produce the same result as specimen A123A1. A large variation can be seen between the upper bound of 0.015 and 0.03 for energy tolerance in combination with the upper bound of 0.58 for force tolerance. This also can be explained by observing Figure 5.24 where a significant difference in range can be seen between the upper bound of 0.015 and 0.03 for energy tolerance. The most optimal combined tolerance is 0.03 and 0.58 for energy and force tolerance respectively. The optimal combination for the upper bound value of the tolerance gives a range of 0.817-0.978 for specimen A123A1 and 1.055-1.449 for specimen H123A.

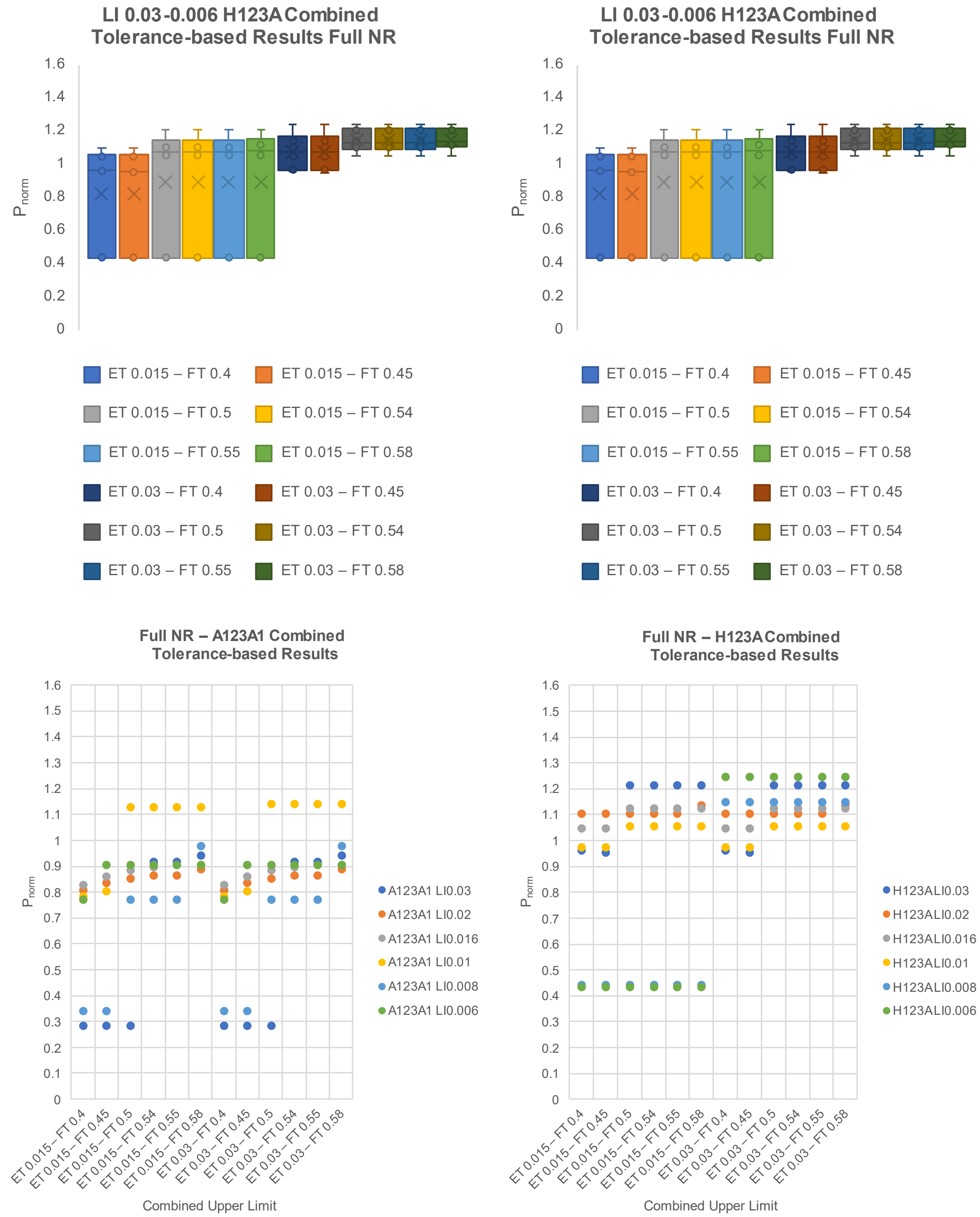

Figure 5.28 Peak Load Distribution for Full NR Method with Combined Upper Bound and LI 0.03-0.006

The peak load distribution in terms of statistics is given on the top and how does the peak load value change with different value of upper bound for error tolerance is given on the bottom.

A better result can be attained by specifying a specific range of load increment where the peak load has less variation compared to the current range of load increment. Figure 5.28 gives an improved peak load distribution where the range of load increment is reduced from 0.1-0.004 to 0.03-0.006. The change in the range of load increment improves the peak load distribution for the optimally combined tolerance of 0.03 and 0.58 for energy and force tolerance, from 0.817-0.978 and 1.055-1.449 to 0.887-1.140 and 1.055-1.246 for specimen A123A1 and H123A respectively.

The simulated global behaviour of the beam with the Full Newton-Raphson method is observed based on the results of NLFEA which has lower relative energy variation and relative out-of-balance force than the defined upper bound for both energy and force tolerance. Figure 5.29 gives an illustration of the simulated global behaviour of the beam with the Full Newton-Raphson method based on the load-displacement curve.

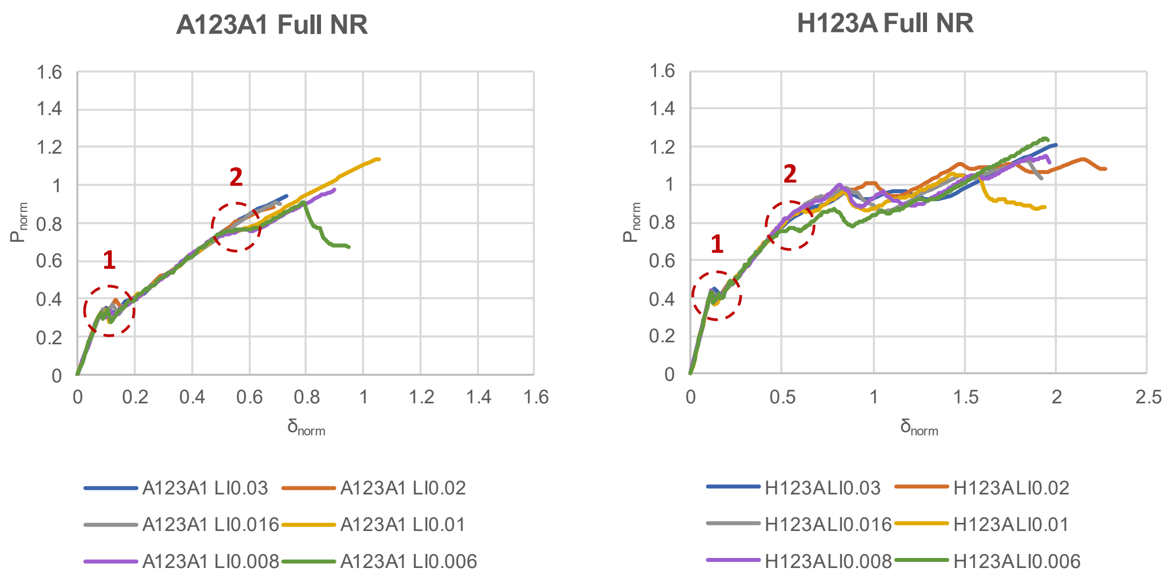

Figure 5.29 Load-displacement Curve for Load Increment Variance – Full NR Method

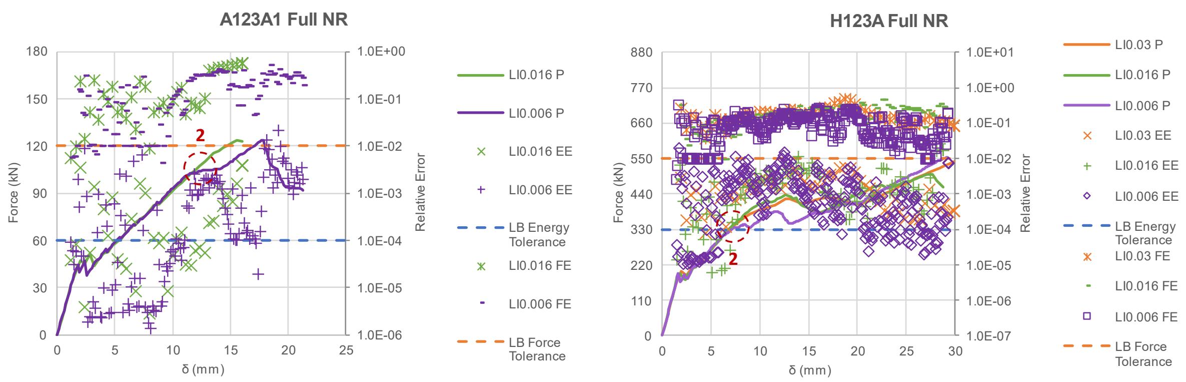

Figure 5.30 Load-displacement Curve with the Convergence State for Full Newton-Raphson Method

In the load-displacement curve in Figure 5.29, there are 2 critical points that show some deviation due to change in load increment. The first critical point is considered not important because the deviation in critical point 1 does not affect the overall simulated behaviour of the beam in the non-linear region. This can be seen by observing the load-displacement curve between critical point 1 and critical point 2, where the simulated non-linear behaviour is similar for all models with specimen A123A1 and H123A. On critical point 2, a significant deviation can be seen between the results on both specimens. The deviation on the curve is considered significant due to its effect on the simulated non-linear behaviour and the peak load of the model. Two models, LI0.016 and LI0.006, are chosen as the representative of all results for specimen A123A1 and three models, LI0.03, LI0.016, and LI0.006, for specimen H123A. The load-displacement curve for these models is given in Figure 5.30.

Figure 5.30 indicates that most of the steps are converging in both relative energy variation and out-of-balance force for model simulating specimen A123A1 and only in energy variation for model simulating specimen H123A. Furthermore, higher relative energy variation and out-of-balance force can be seen by comparing convergence state at δ = 10-20 mm to δ = 5-10 mm for specimen A123A1 and δ = 10-20 mm to δ = 5-10 mm, where the curve is near its peak for specimen A123A1 and during non-linear stiffness change in specimen H123A. The overall relative energy variation is reducing at δ = 20-30 mm for specimen H123A while the overall out-of-balance force is similar at δ = 20-30 mm to δ =10-20 mm.

The first critical point 2 that would be analysed is for specimen A123A1. Detailed illustration for critical point 2 of specimen A123A1 is given in Figure 5.31. 3 load steps are going to be observed in Figure 5.31. These load steps indicate the shift in the load-displacement curve and will be called shifting points A, B, and C for displacement at 11.19 mm, 11.59 mm, and 11.99 mm respectively.

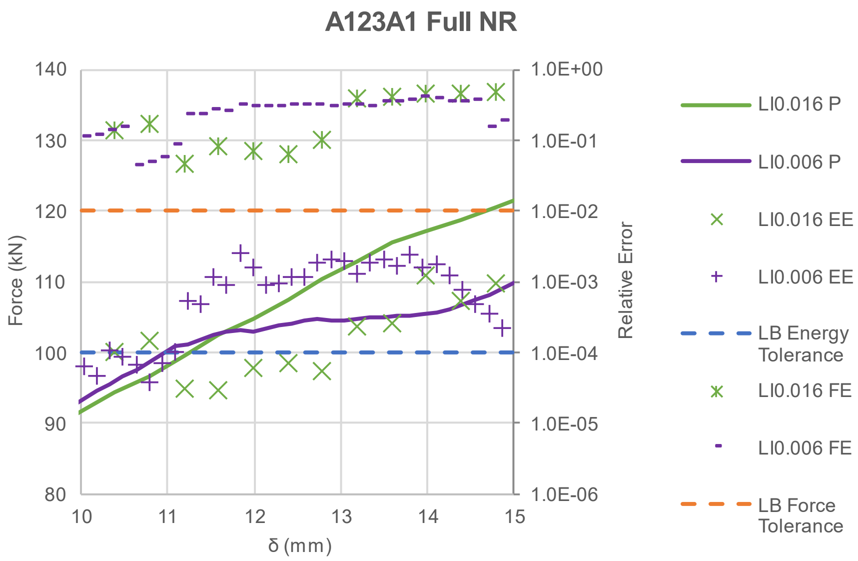

Figure 5.31 Load-displacement Curve on Critical Point 2 of Specimen A123A1 for Full NR Method

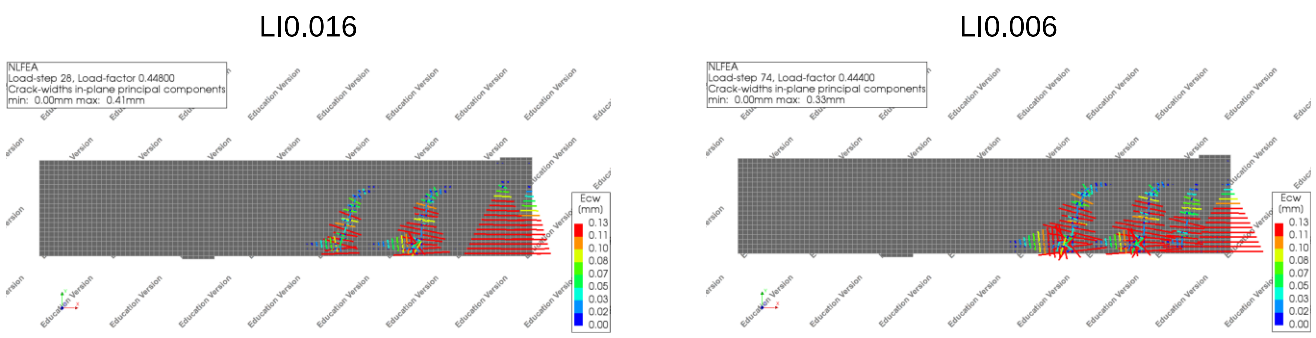

Figure 5.32 Crack Pattern Specimen A123A1 with Full NR Method at δ = 11.19 mm (Shifting Point A)

LI0.016 LI0.006

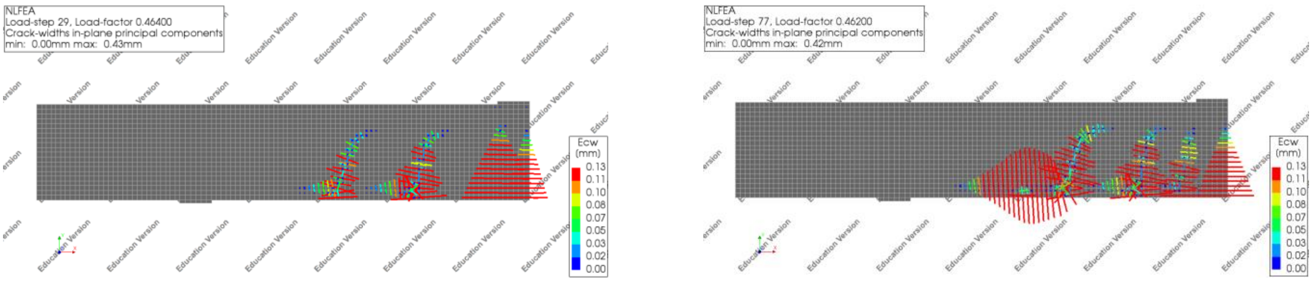

Figure 5.33 Crack Pattern Specimen A123A1 with Full NR Method at δ = 11.59 mm (Shifting Point B)

LI0.016 LI0.006

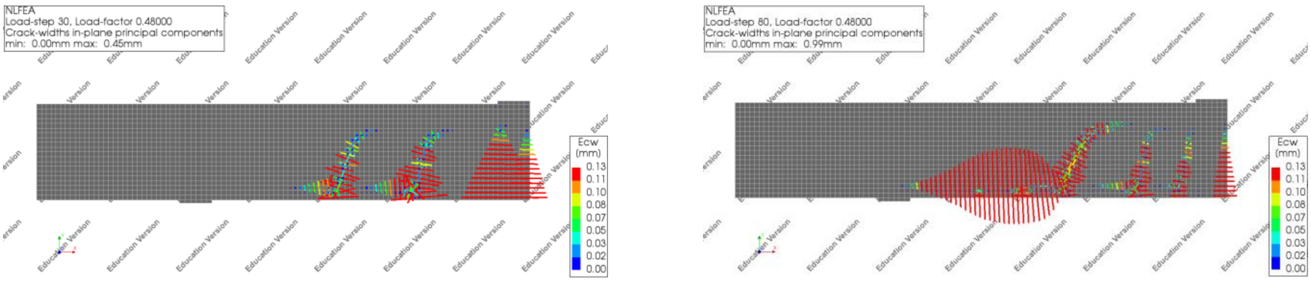

Figure 5.34 Crack Pattern Specimen A123A1 with Full NR Method at δ = 11.59 mm (Shifting Point C)

LI0.016 LI0.006

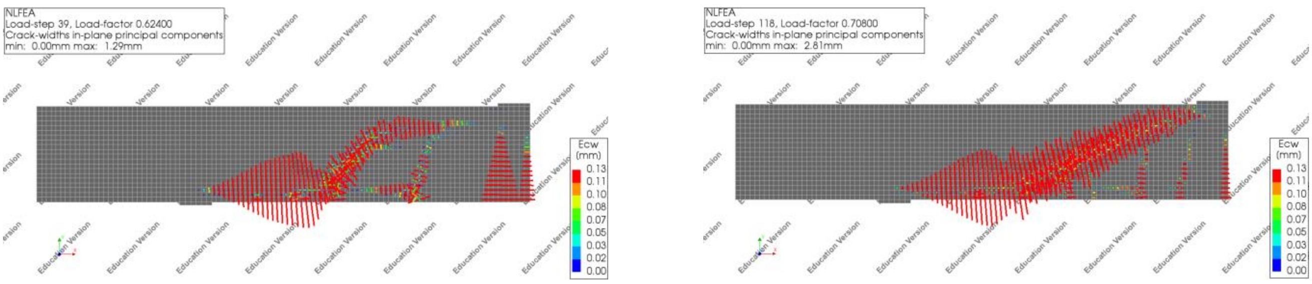

Figure 5.35 Crack Pattern Specimen A123A1 with Full NR Method at Peak Load

The relative energy variation in Figure 5.31 is relatively constant for model A123A1 LI0.016 and constantly increasing in model A123A1 LI0.006 from shifting point A to shifting point C. The relative out-of-balance force in model A123A1 LI0.06 and LI0.03 is constantly increasing through all shifting points. A significant difference of both relative energy variation and out-of-balance force can be seen between model A123A1 LI0.016 and LI0.006, where higher energy variation and out-of-balance force can be seen in model A123A1 LI0.016 compared to LI0.006.

In terms of crack pattern, models A123A1 LI0.016 and LI0.006 show a similar crack progression on shifting point A in Figure 5.32. However, the rate of crack progression in model A123A1 LI0.016 is slower compared to model A123A1 LI0.006. This can be seen in Figure 5.33 and Figure 5.34 where the trend of the maximum crack width changes where the maximum crack width is larger in model A123A1 LI0.016 compared to model A123A1 LI0.006 in Figure 5.32 to the maximum crack width is smaller in model A123A1 LI0.016 compared to model A123A1 LI0.006 in Figure 5.33 and Figure 5.34. Furthermore, it can be seen that the location of the maximum crack width is different between model A123A1 LI0.016 and LI0.006 in Figure 5.33 and Figure 5.34 compared to Figure 5.32, where the maximum crack width is located in the flexural crack opening in Figure 5.32 for both models, while in Figure 5.33 and Figure 5.34, the maximum crack width is located in flexural crack opening for model A123A1 LI0.016 and dowel crack opening for model A123A1 LI0.006. The change in the rate of crack width propagation in model A123A1 LI0.006 is due to the absence of vertical reinforcement, causing the crack width increment in the vertical direction (dowel crack) is higher compared to the crack width increment in the horizontal direction (flexural crack). These phenomena can be correlated to the observation results of Figure 5.31. The relative energy variation is smaller in model A123A1 LI0.016 is due to the lower rate of crack propagation and cause fewer elements to lose their tensile fracture energy. Higher crack propagation rate in model A123A1 LI0.006 cause more elements to lost their tensile fracture energy, which in turn increase the relative energy variation of the step as well. The significant difference in the relative out-of-balance force is correlated to different types of crack propagation. This correlation can be verified by the observation results of critical point 2 for numerical models with the Quasi-Newton method, where in Figure 5.11 (specimen A123A1) and Figure 5.17 (specimen H123A), a similar magnitude of the relative out-of-balance force is reflected in the similarity of the cracking progression on the numerical models in Figure 5.12, Figure 5.13, Figure 5.14 and Figure 5.15 for specimen A123A1 and Figure 5.18, Figure 5.19, Figure 5.20 and Figure 5.21 for specimen H123A. Even with all differences in the cracking progression, both models still produce similar cracking patterns at the peak load in Figure 5.35.

The next critical point 2 in Figure 5.30 that would be analysed is for specimen H123A. Detailed illustration for critical point 2 of specimen H123A is given in Figure 5.36. 4 load steps are going to be observed in Figure 5.36. These load steps indicate the shift in the load-displacement curve and will be called shifting points A, B, C, and D for displacement at 5.99 mm, 6.49 mm, 7.00 mm, and 7.51 mm respectively.

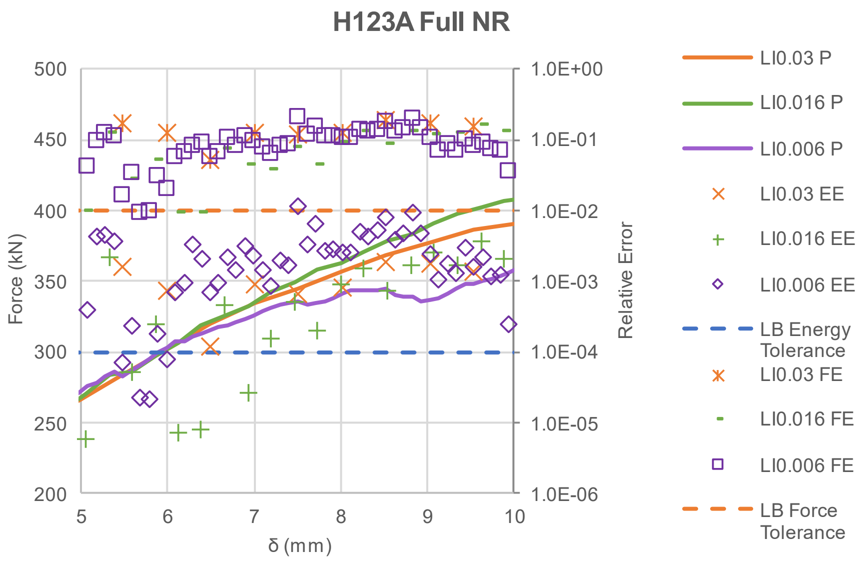

Figure 5.36 Load-displacement Curve on Critical Point 2 of Specimen H123A for Full NR Method

LI0.03

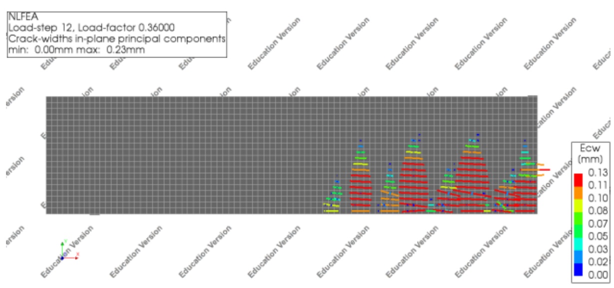

LI0.016

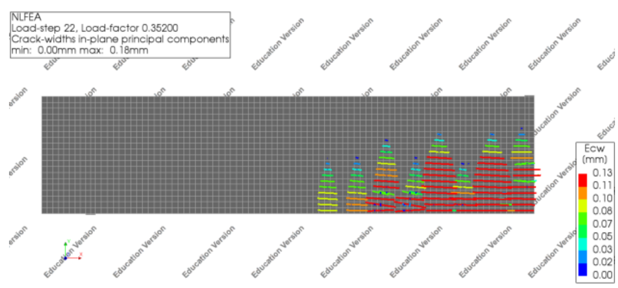

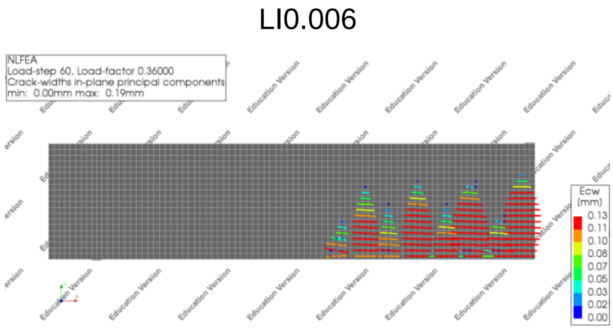

Figure 5.37 Crack Pattern Specimen H123A with Full NR Method at δ = 5.99 mm (Shifting Point A)

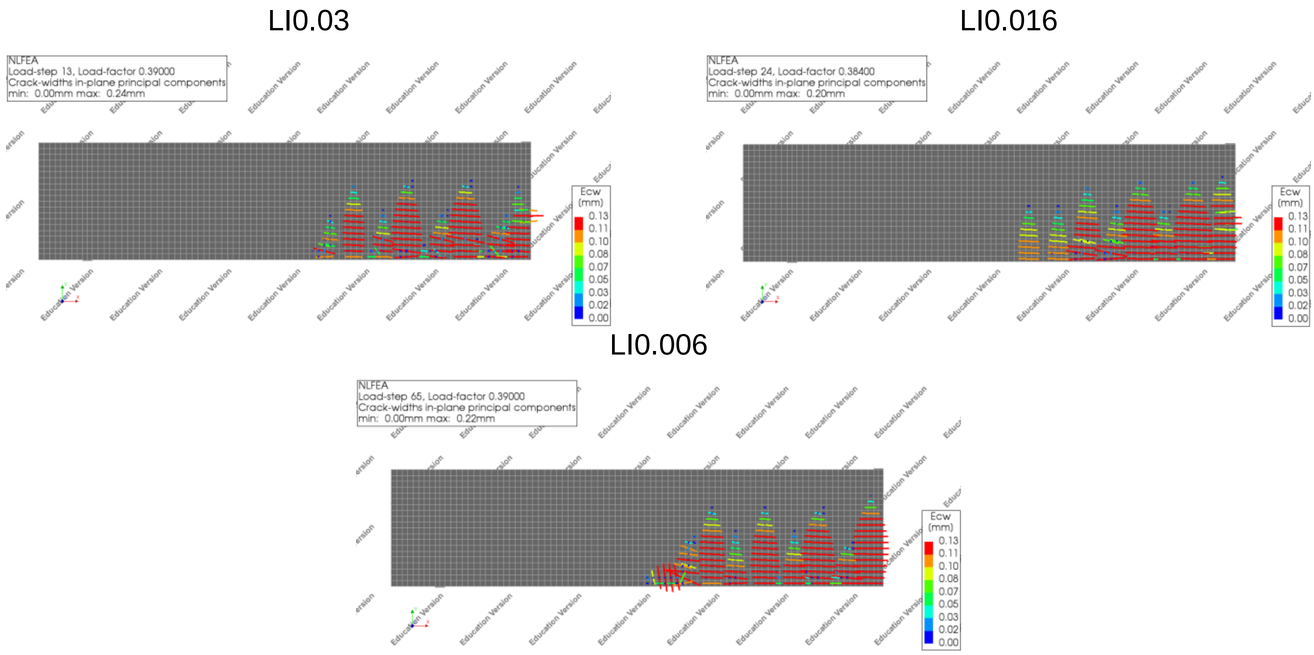

Figure 5.38 Crack Pattern Specimen H123A with Full NR Method at δ = 6.49 mm (Shifting Point B)

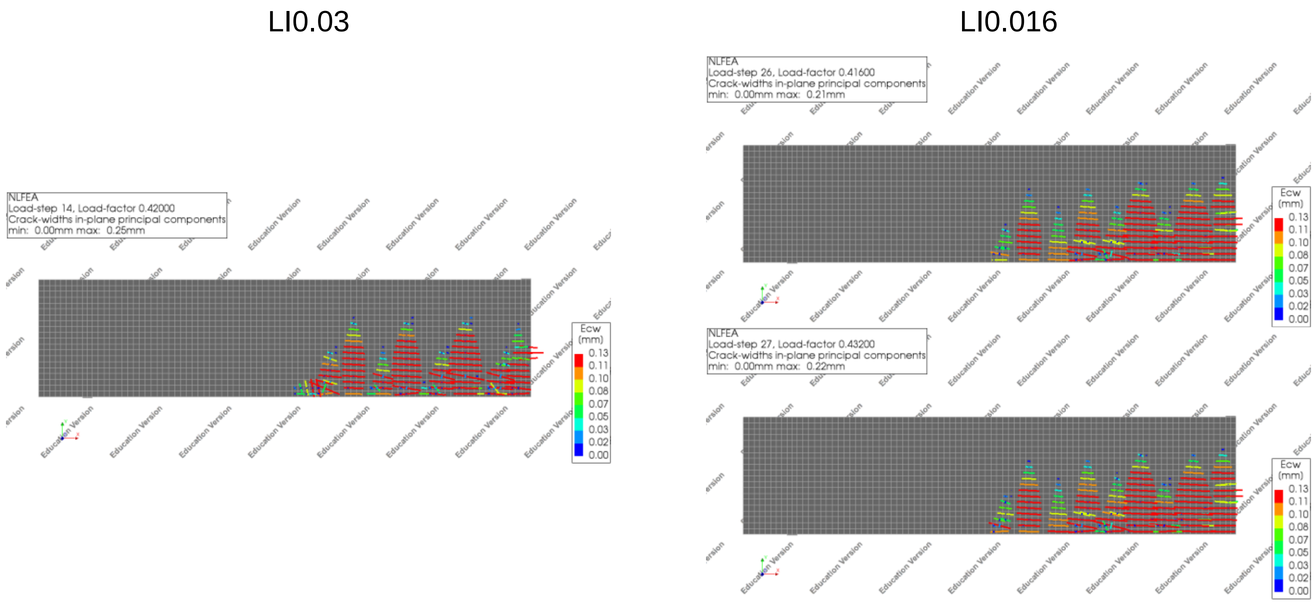

LI0.006

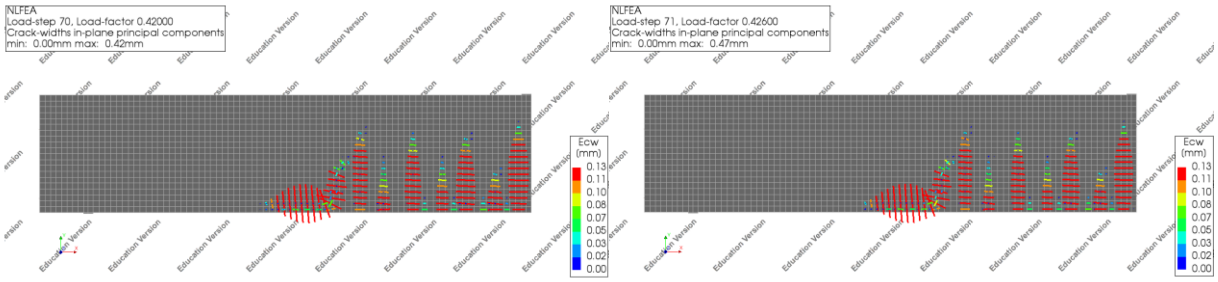

Figure 5.39 Crack Pattern Specimen H123A with Full NR Method at δ = 7.00 mm (Shifting Point C)

LI0.03

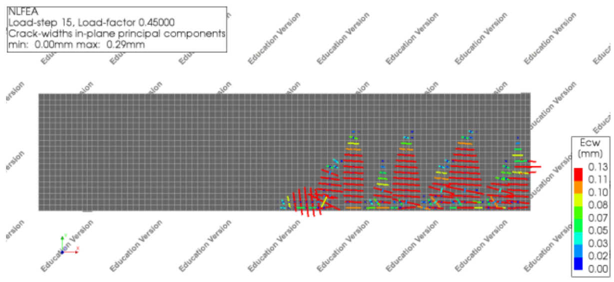

LI0.016

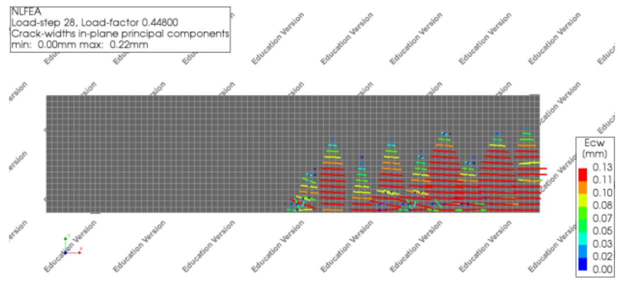

LI0.006

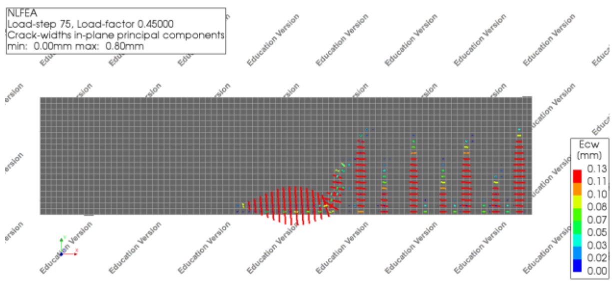

Figure 5.40 Crack Pattern Specimen H123A with Full NR Method at δ = 7.51 mm (Shifting Point D)

LI0.03

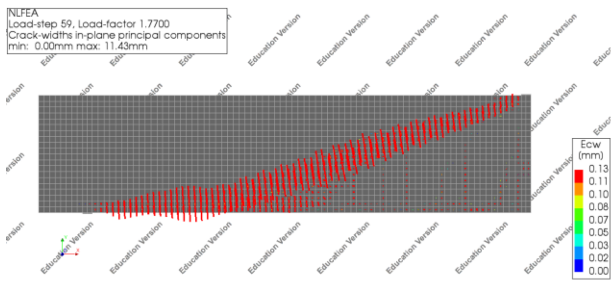

LI0.016

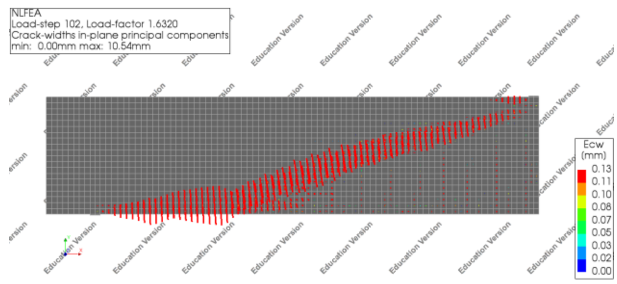

LI0.006

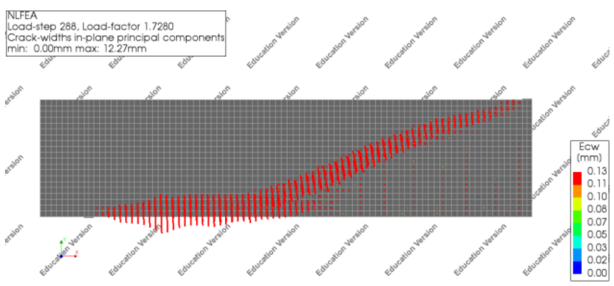

Figure 5.41 Crack Pattern Specimen H123A with Full NR Method at Peak Load

The relative energy variation and the relative out-of-balance force in Figure 5.36 show a similar pattern between all models, where models H123A LI0.03, LI0.016 and LI0.006 show a constant trend through all shifting points. However, in shifting points B and C where model H123A LI0.006 and LI0.03 load-displacement curve deviate, both relative energy variation and out-of-balance force for the correspondent model are highest compared to other models.

In terms of crack pattern, models H123A LI0.03, LI0.016 and LI0.006 show similar crack progression with small differences in maximum crack width in shifting point A in Figure 5.37. The crack pattern of model H123A LI0.006 starts to change from shifting point B in Figure 5.38 where dowel crack has propagated in the model, where other models have not had dowel crack at this stage. Model H123A LI0.03 starts to change from shifting point C in Figure 5.39 where dowel crack also has propagated in this model, similar to model H123A LI0.006. In Figure 5.40, the major crack propagation in both model H123A LI0.03 and H123A LI0.006 is dowel crack, while in model H123A LI0.016 is flexural crack. Model H123A LI0.016 does not experience any changes through all shifting points. The formation of the dowel crack can be correlated to the value of the relative energy variation and out-of-balance force. The formation of the dowel crack is reflected by higher relative energy variation and out-of-balance force compared to the model without dowel crack. This phenomenon can be seen in shifting points B and C where model H123A LI0.006 has higher relative energy variation and out-of-balance force compared to model H123A LI0.03 and LI0.016 and model H123A LI0.03 has higher relative energy variation and out-of-balance force compared to model H123A LI0.016. However, this phenomenon does not change the crack pattern at the peak load for all models, where all models have a similar crack pattern in Figure 5.41.

Based on the observation for both specimen A123A1 and H123A, it can be concluded that variation on the peak load of models with the Full Newton-Raphson method and different load increment is caused by the initiation of dowel crack formation. This can be observed by comparing the relative energy variation and out-of-balance force of each model, where the steps on the model with the formation of dowel crack typically have higher relative energy variation and out-of-balance force compared to the model with only flexural cracks. The difference in the relative energy variation and out-of-balance force is increasing as the dowel crack propagation becomes more dominant in the model. This can be seen in Figure 5.35 and Figure 5.41 where the dowel crack propagation is more dominant in the model with specimen A123A1 compared to the model with specimen H123A. The shifting point of this phenomenon is considered important because the shifting point controls when the numerical models would reach their peak capacity.

5.3.3 Effect of Load Increment Variation in Modified Newton-Raphson Method

The last observation is done for numerical models with the Modified Newton-Raphson method. The change in peak load distribution due to different values of upper bound value for energy tolerance can be observed in Figure 5.42 and Figure 5.43 for specimen A123A1 and H123A respectively.

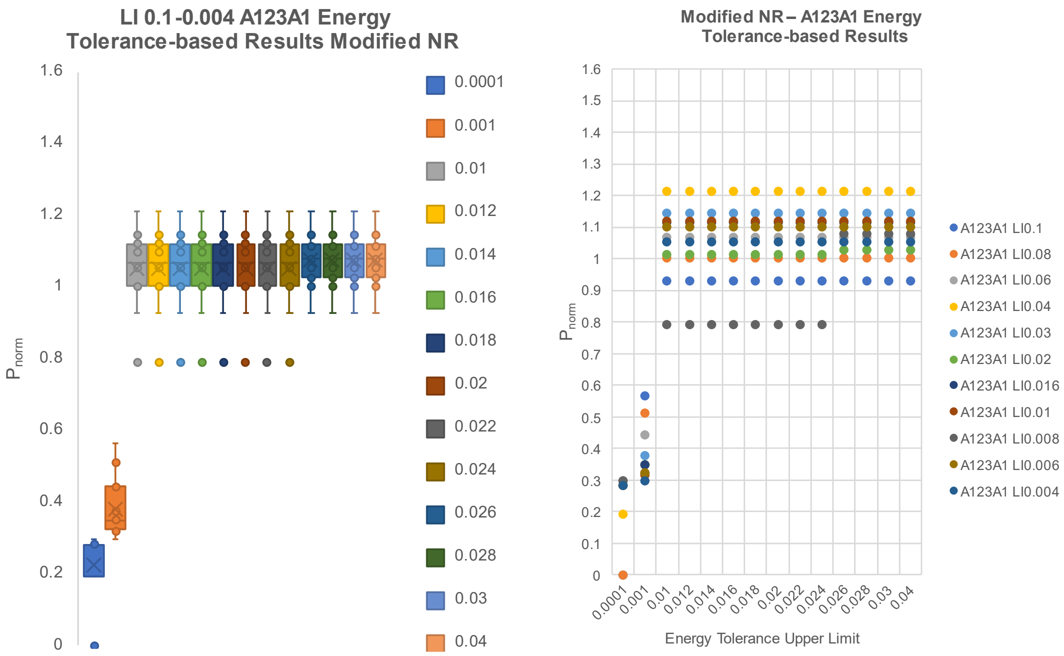

Figure 5.42 Peak Load Distribution for Model A123A1 – Modified NR with Upper Bound Energy Tolerance

The peak load distribution in terms of statistics is given on the left and how does the peak load value change with different value of upper bound for energy tolerance is given on the right.

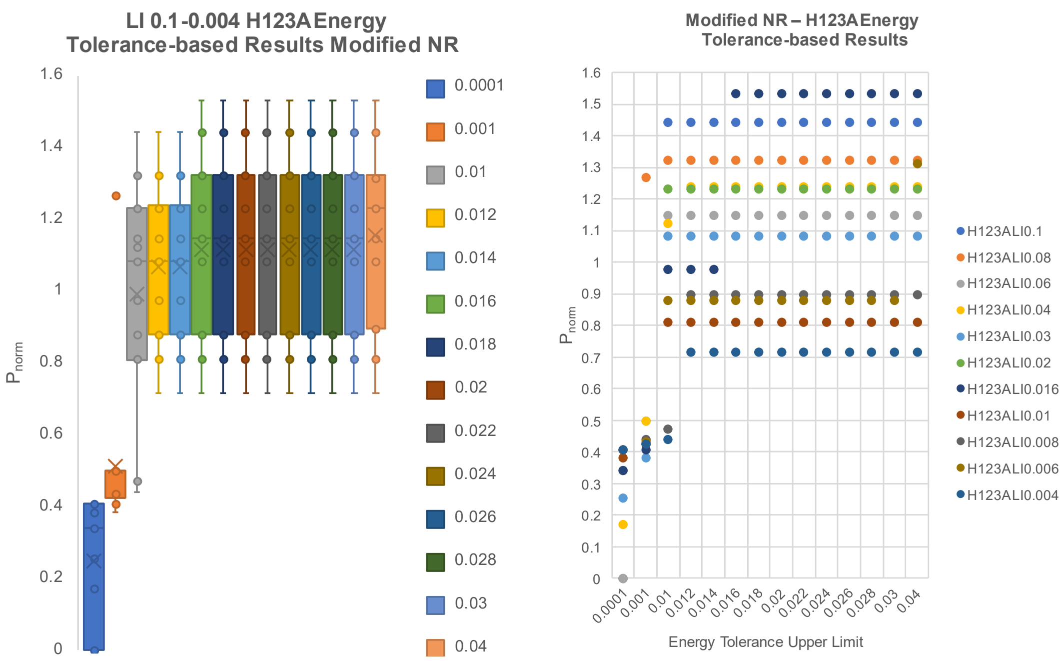

Figure 5.43 Peak Load Distribution for Model H123A – Modified NR with Upper Bound Energy Tolerance

The peak load distribution in terms of statistics is given on the left and how does the peak load value change with different value of upper bound for energy tolerance is given on the right.

Both Figure 5.42 and Figure 5.43 indicate that the use of a single value of energy tolerance would cause a large underestimation of relative load capacity, ranging from 0.192-0.297 for specimen A123A1 and 0-0.408 for specimen H123A. Accepting several non-converged steps by imposing an upper bound value on the energy tolerance is able to improve the overall distribution of the peak load. Figure 5.42 shows that the upper limit of 0.026 is sufficient to prevent any significant change in the peak load distribution and give the smallest distribution of peak load for specimen A123A1. However, a lower value of the upper limit can be applied for specimen H123A to achieve the same behaviour as specimen A123A1. The upper limit of 0.012 for specimen H123A is sufficient to achieve this target. This indicates that the upper limit value for energy tolerance might be dependent on the specimen size, where a small specimen size requires a higher upper limit compared to large specimen size.

Furthermore, it can be seen that a different range is attained for both cases, where the relative peak value of numerical models for specimen A123A1 is ranging from 0.929-1.214 while for specimen H123A is ranging from 0.717-1.532. The difference is not only on the minimum and maximum value but also on the total range of the peak load. These differences make it not possible to combine the results of specimen A123A1 and H123A and observe the peak load distribution together. Figure 5.42 and Figure 5.43 also show that no pattern can be seen in the distribution of the peak load, which means that the use of smaller load increment does not immediately produce a higher/smaller peak load.

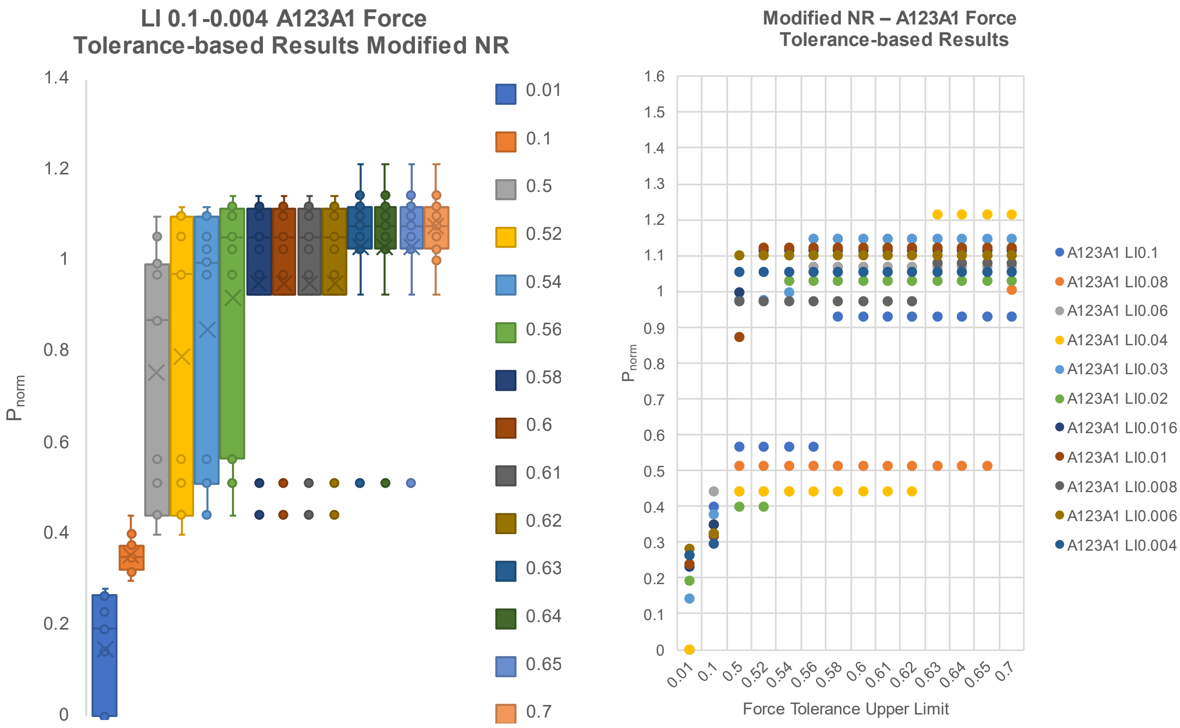

Figure 5.44 Peak Load Distribution for Model A123A1 – Modified NR with Upper Bound Force Tolerance

The peak load distribution in terms of statistics is given on the left and how does the peak load value change with different value of upper bound for force tolerance is given on the right.

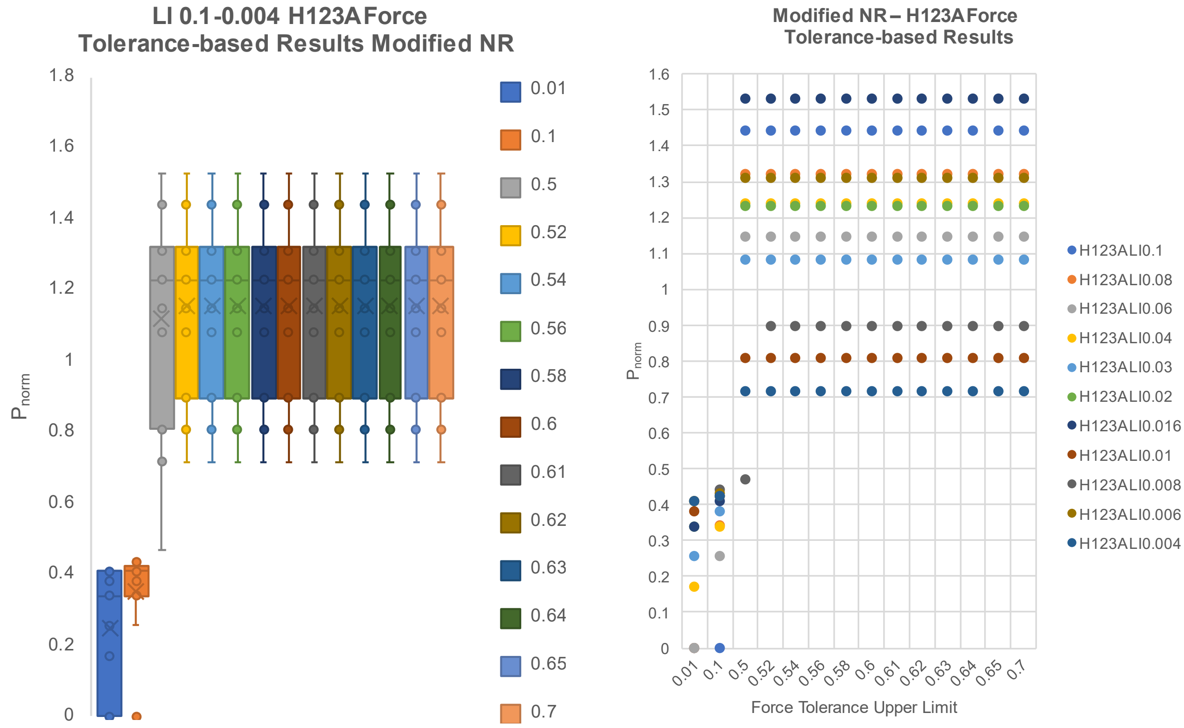

Figure 5.45 Peak Load Distribution for Model H123A – Modified NR with Upper Bound Force Tolerance

The peak load distribution in terms of statistics is given on the left and how does the peak load value change with different value of upper bound for force tolerance is given on the right.

A different distribution result is attained when an upper bound value is imposed on the force tolerance, which can be seen in Figure 5.44 and Figure 5.45. A different range of peak load distribution, compared to the single value of energy tolerance, is achieved when a single value of force tolerance is used, ranging from 0-0.282 for specimen A123A1 and 0-0.408 for specimen H123A. Accepting several non-converged steps by imposing upper bound value on the force tolerance also improve the overall distribution of the peak load. However, in comparison to Figure 5.42, Figure 5.43 and Figure 5.45, Figure 5.44 do not exhibit the same behaviour where a higher value of upper bound means less variation on the peak load distribution. The upper bound value is needed to be within a certain range of values in order to have the most optimum peak load distribution for specimen A123A1, where the minimum value of the range is used for the upper bound value. The optimum upper bound for specimen A123A1 for force tolerance is ranged between 0.58-0.62 while for specimen H123A is 0.52. This still indicates that the upper limit value for force tolerance might be dependent on the specimen size, where a small specimen size requires a smaller upper limit compared to a large specimen size.

Furthermore, a different range is also attained for both cases, where the relative peak value of numerical models of specimen A123A1 is from 0.929 to 1.145 while for specimen H123A is from 0.717 to 1.532. No pattern can be seen on the distribution of the peak load with load increment variation and the results for specimen A123A1 contains an outlier. The relative peak value range of numerical models for each specimen is similar in both cases. A single upper bound value is not recommended to be used, because the numerical models rarely have a single step that would exceed the upper bound value of energy and force tolerance at the same time. An example can be seen by comparing Figure 5.42 and Figure 5.44 for model A123A1 LI0.04. Model A123A1 LI0.04 has a relative peak load of 1.214 when the optimal upper bound of energy tolerance is used, while a relative peak load of 0.442 is achieved when the optimal upper bound of force tolerance is used. In order to find a general upper bound for numerical models, reduce variation of the results, and eliminate the outliers, the upper bound limit is applied to both energy and force tolerance.

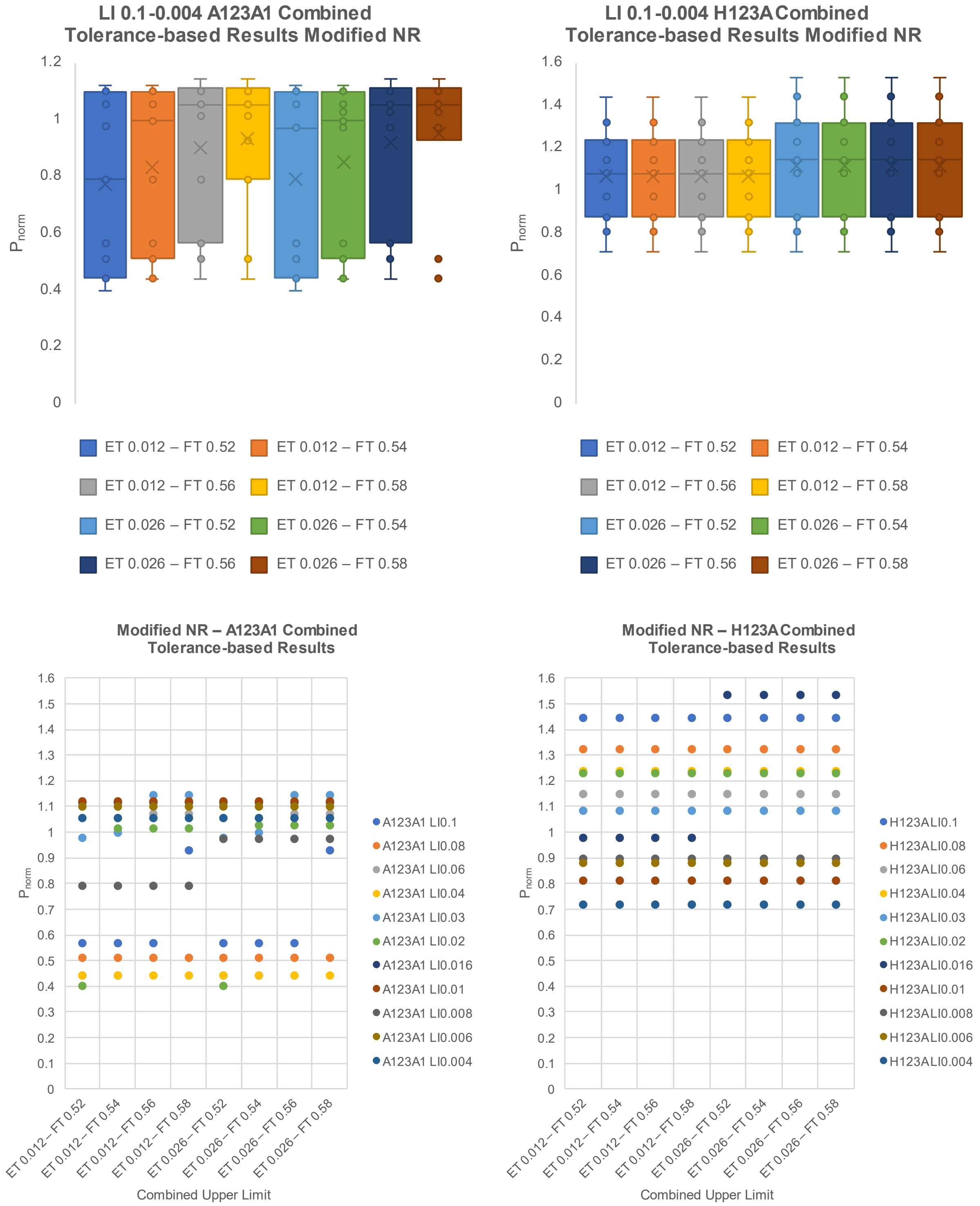

Figure 5.46 Peak Load Distribution for Modified NR Method with Combined Upper Bound

The peak load distribution in terms of statistics is given on the top and how does the peak load value change with different value of upper bound for error tolerance is given on the bottom.

Figure 5.46 shows the combination of upper bound values from the optimal value of specimen A123A1 and H123A where a single upper bound type is applied. For specimen A123A1, the peak load distribution is reduced when the upper bound of force tolerance is increased from 0.52 to 0.58 and combined with the upper bound of energy tolerance of either 0.012 or 0.026. This can be explained by observing Figure 5.42 and Figure 5.44, where Figure 5.42 has no significant difference in peak load distribution with the upper bound of 0.012 and 0.026 for energy tolerance, while Figure 5.44 shows that the range peak load distribution is becoming smaller as the upper bound for force tolerance increase, from 0.52 to 0.57. On the other hand, specimen H123A does not produce the same result as specimen A123A1. Specimen H123A1 produce constant results for the upper bound of 0.012 and 0.026 for energy tolerance, in combination with the upper bound of 0.52-0.58 for force tolerance. However, the peak load distribution is different when the results with an upper bound of 0.012 are compared to the upper bound of 0.026 for energy tolerance. This also can be explained by observing Figure 5.43 where a significant difference in range can be seen between the upper bound of 0.012 and 0.026 for energy tolerance. The most optimal combined tolerance is 0.026 and 0.58 for energy and force tolerance respectively. The optimal combination for the upper bound value of the tolerance gives a range of 0.929-1.145 for specimen A123A1 and 0.717-1.532 for specimen H123A.

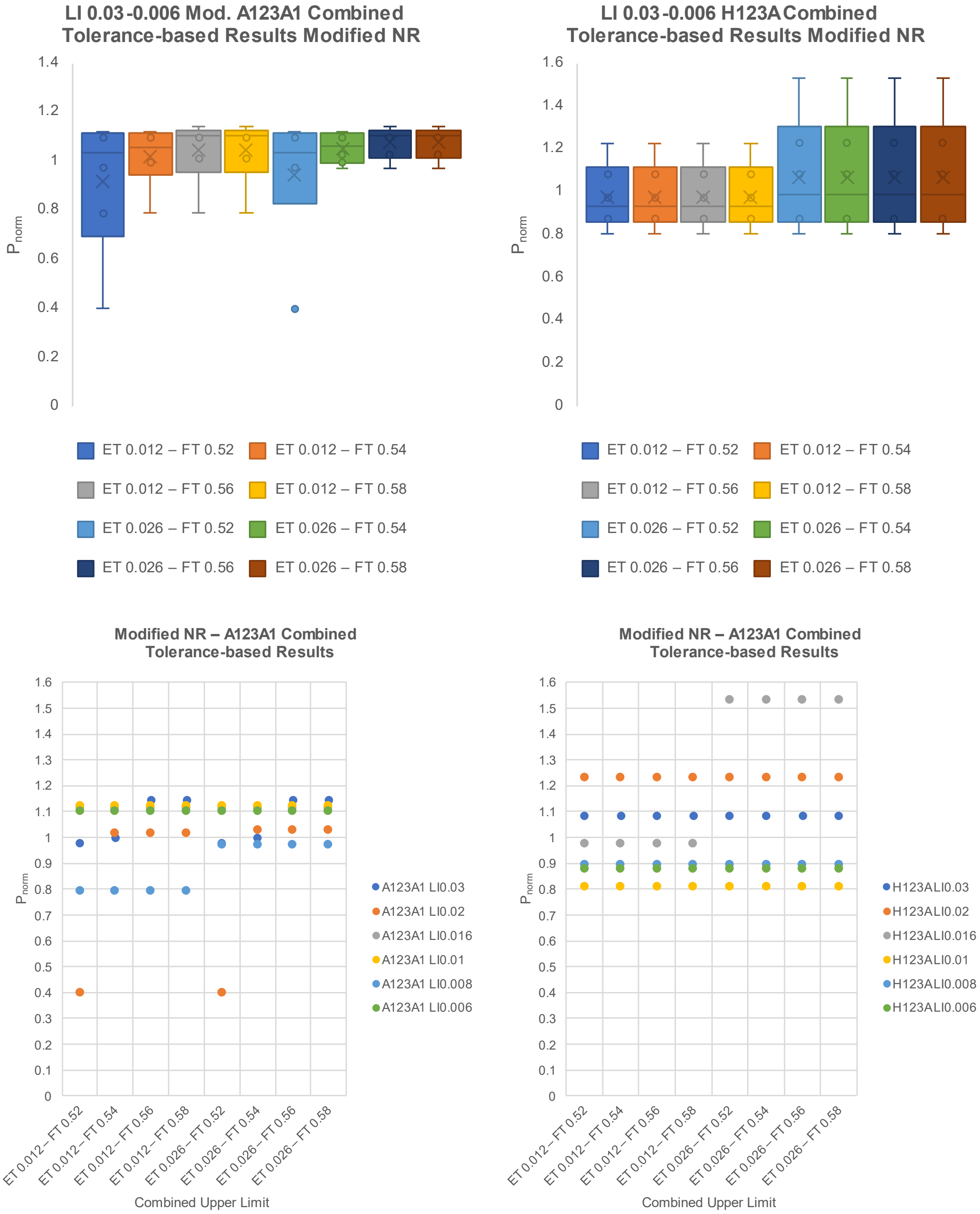

Figure 5.47 Peak Load Distribution for Modified NR Method with Combined Upper Bound and LI 0.03-0.006

The peak load distribution in terms of statistics is given on the top and how does the peak load value change with different value of upper bound for error tolerance is given on the bottom.

A better result can be attained by specifying a specific range of load increment where the peak load has less variation compared to the current range of load increment. Figure 5.47 gives an improved peak load distribution where the range of load increment is reduced from 0.1-0.004 to 0.03-0.006. The change in the range of load increment causes a change in the optimally combined tolerance in terms of energy tolerance, from 0.026 and 0.58 to 0.012 and 0.54 for energy and force tolerance respectively. The change in the range of load increment improves the peak load distribution from 0.929-1.145 and 0.717-1.532 to 0.791-1.121 and 0.809-1.231 for specimen A123A1 and H123A respectively.

The simulated global behaviour of the beam with the Modified Newton-Raphson method is observed based on the results of NLFEA which has lower relative energy variation and relative out-of-balance force than the defined upper bound for both energy and force tolerance. Figure 5.48 gives an illustration of the simulated global behaviour of the beam with the Modified Newton-Raphson method based on the load-displacement curve.

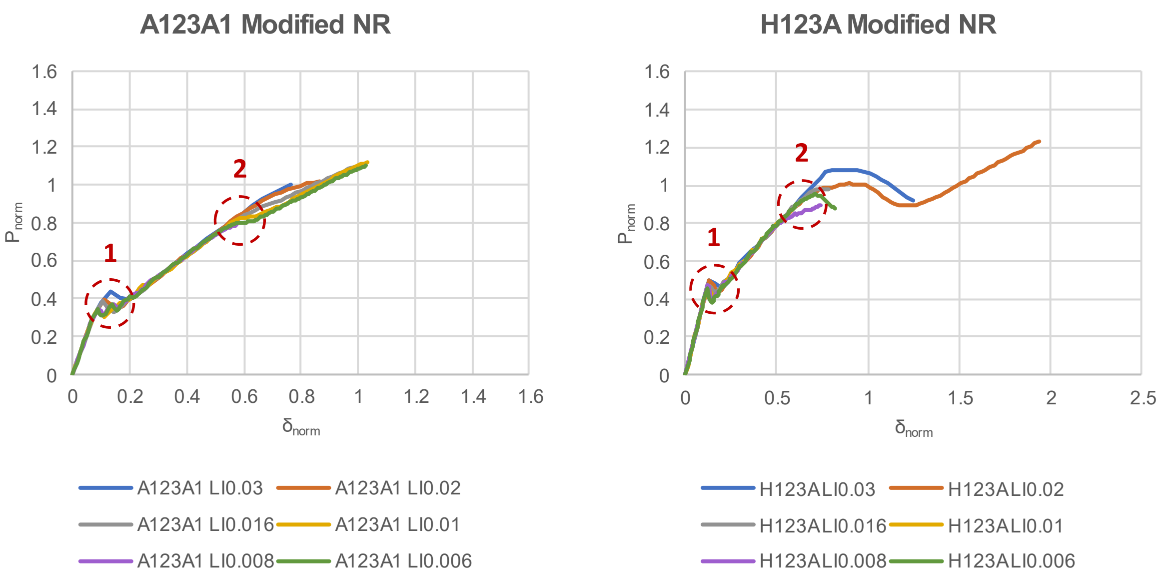

Figure 5.48 Load-displacement Curve for Load Increment Variance – Modified NR Method

In the load-displacement curve in Figure 5.48, there are 2 critical points that show some deviation due to change in load increment. The first critical point is considered not important because the deviation in critical point 1 does not affect the overall simulated behaviour of the beam in the non-linear region. This can be seen by observing the load-displacement curve between critical point 1 and critical point 2, where the simulated non-linear behaviour is similar for all models with specimen A123A1 and H123A. On critical point 2, a significant deviation can be seen between the results on both specimens. The deviation on the curve is considered significant due to its effect on the simulated non-linear behaviour and the peak load of the model. Two models, LI0.016 and LI0.006, and LI0.008 and LI0.006 are chosen as the representative of all results for specimen A123A1 and H123A respectively. The load-displacement curve for these models is given in Figure 5.49.

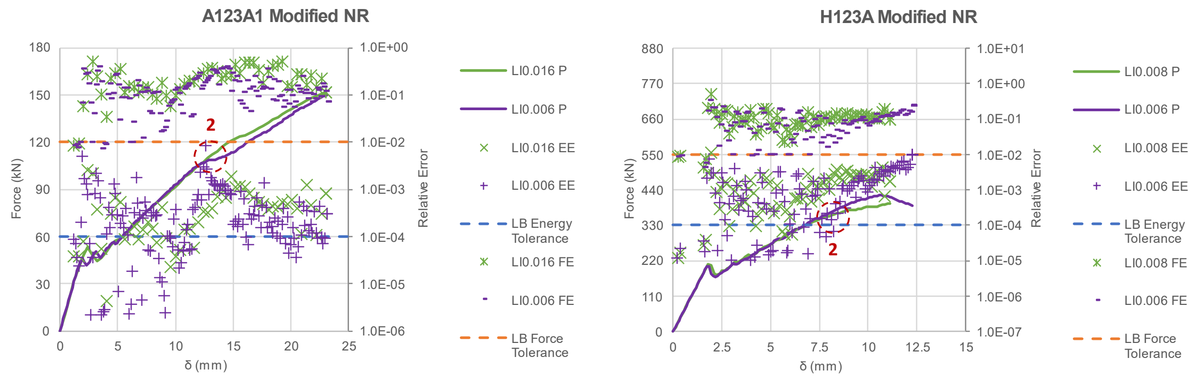

Figure 5.49 Load-displacement Curve with the Convergence State for Modified Newton-Raphson Method

Figure 5.49 indicates that most of the steps are converging in relative energy variation. Furthermore, the relative energy variation and out-of-balance force are significantly higher compared to the tolerance in both specimens.

The first critical point 2 that would be analysed is for specimen A123A1. Detailed illustration for critical point 2 of specimen A123A1 is given in Figure 5.50. 3 load steps are going to be observed in Figure 5.50. These load steps indicate the shift in the load-displacement curve and will be called shifting points A, B, and C for displacement at 11.59 mm, 11.99 mm, and 12.39 mm respectively.

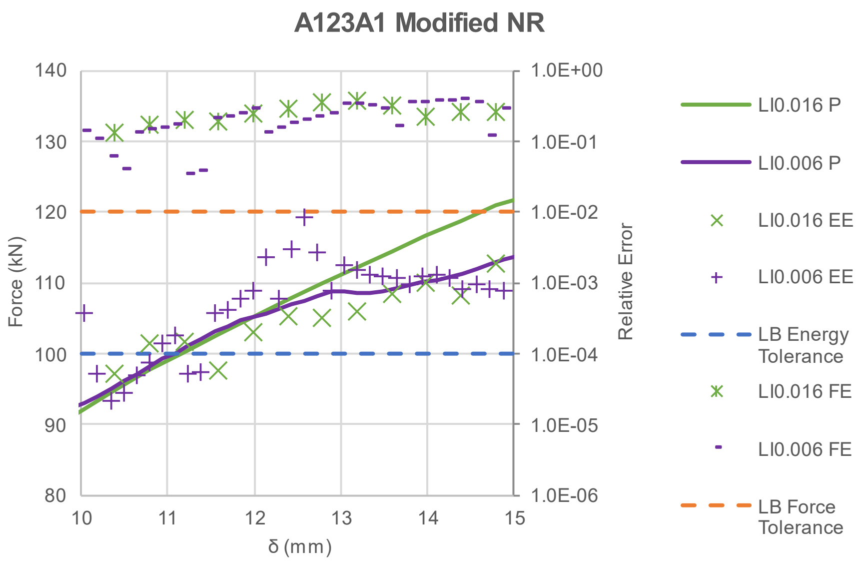

Figure 5.50 Load-displacement Curve on Critical Point 2 of Specimen A123A1 for Modified NR Method

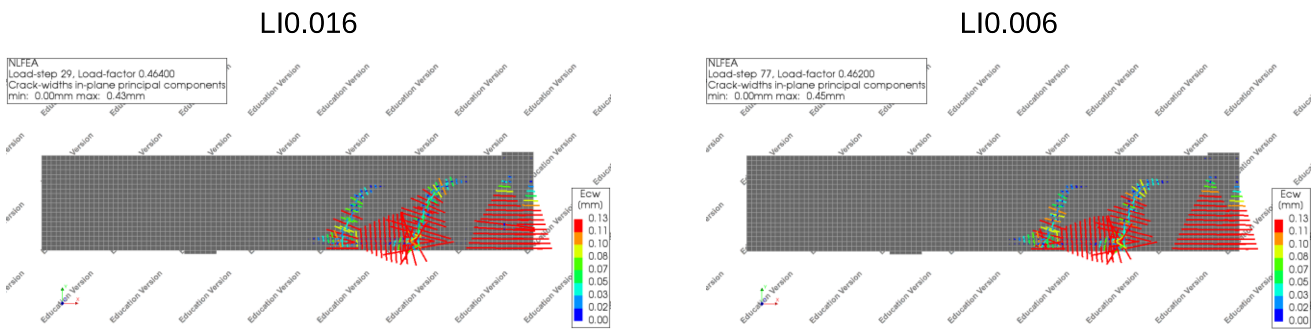

Figure 5.51 Crack Pattern Specimen A123A1 with Modified NR Method at δ = 11.59 mm (Shifting Point A)

LI0.016 LI0.006

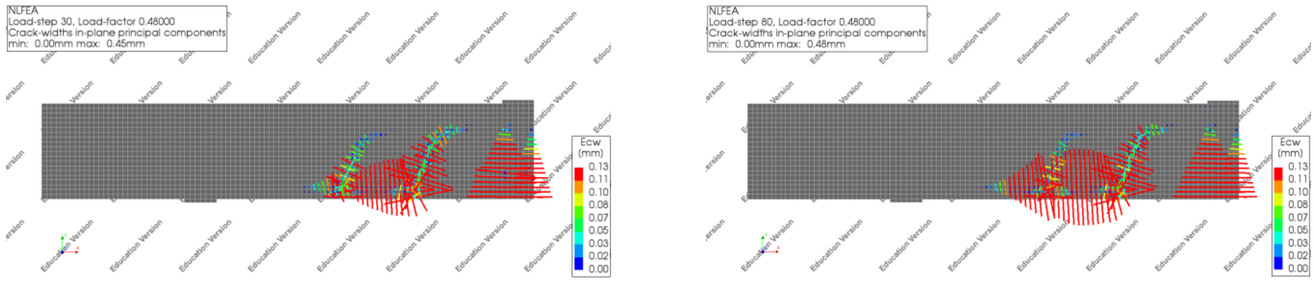

Figure 5.52 Crack Pattern Specimen A123A1 with Modified NR Method at δ = 11.99 mm (Shifting Point B)

LI0.016 LI0.006

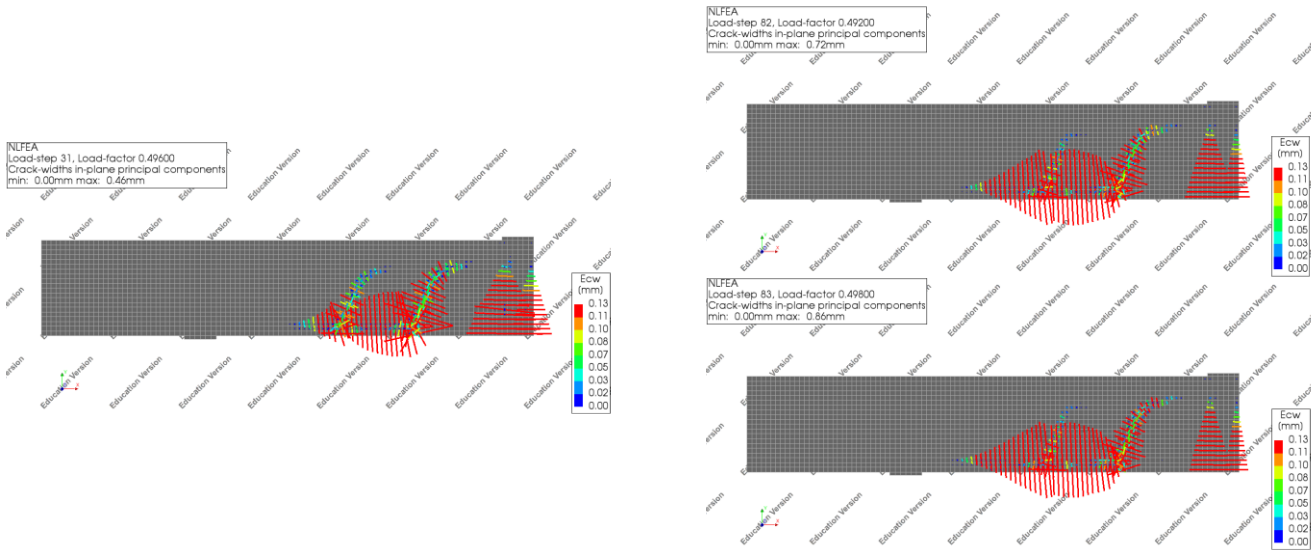

Figure 5.53 Crack Pattern Specimen A123A1 with Modified NR Method at δ = 12.39 mm (Shifting Point C)

LI0.016 LI0.006

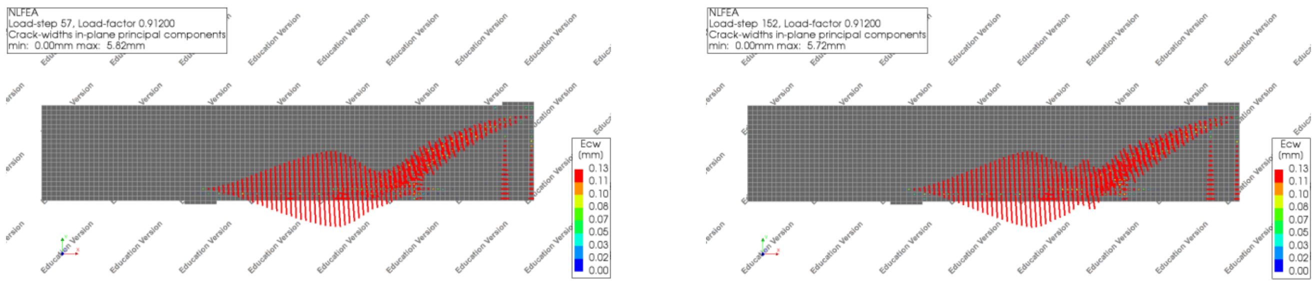

Figure 5.54 Crack Pattern Specimen A123A1 with Modified NR Method at Peak Load

The relative energy variation in Figure 5.50 is linearly increasing for both models A123A1 LI0.016 and LI0.006 from shifting point A to shifting point C. The relative out-of-balance force in model A123A1 LI0.016 and LI0.006 is constant through all shifting points. A significant increase in relative energy variation for model A123A1 LI0.006 can be seen from shifting point B to C.

In terms of crack pattern, models A123A1 LI0.016 and LI0.006 show a similar crack progression on shifting point A in Figure 5.51. It can be seen that the maximum crack width of model A123A1 LI0.016 is slightly higher than model A123A1 LI0.006 in Figure 5.51 and Figure 5.52. This trend continues through all shifting points and its difference is becoming larger from shifting point A to C. Although the difference in maximum crack width in Figure 5.52 is small, the crack pattern is slightly different where the overall dowel crack in model A123A1 LI0.016 is smaller compared to model A123A1 LI0.006. The shifting point B is followed by shifting point C in Figure 5.53 where the largest differences can be spotted through all shifting points where the crack propagation is governed by dowel crack. This phenomenon can be seen in the changes of the convergence state in terms of relative energy variation. At shifting point B, the overall dowel crack opening is smaller in model A123A1 LI0.016 compared to A123A1 LI0.006, thus resulting in a smaller number of cracked elements in the model A123A1 LI0.016 and reduce the relative energy variation of the step at the shifting point. A123A1 LI0.006 has more cracked elements that resulted in higher relative energy variation on the shifting point. However, this phenomenon does not affect the cracking pattern at the peak load in Figure 5.54. A similar crack pattern and maximum crack width can be seen on both models.

The next critical point 2 in Figure 5.49 that would be analysed is for specimen H123A. Detailed illustration for critical point 2 of specimen H123A is given in Figure 5.55. 4 load steps are going to be observed in Figure 5.55. These load steps indicate the shift in the load-displacement curve and will be called shifting points A, B, C and D for displacement at 6.66 mm, 7.06 mm, 7.33 mm and 8.41 mm respectively.

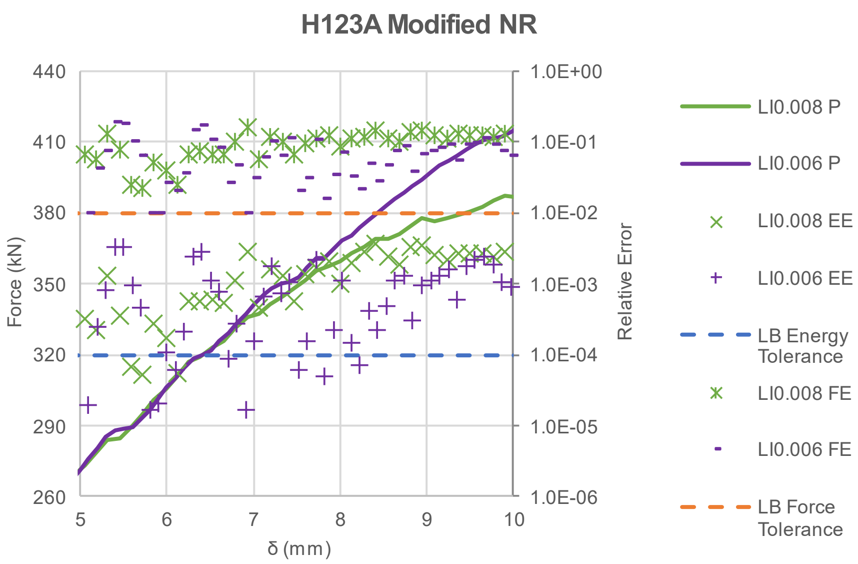

Figure 5.55 Load-displacement Curve on Critical Point 2 of Specimen H123A for Modified NR Method

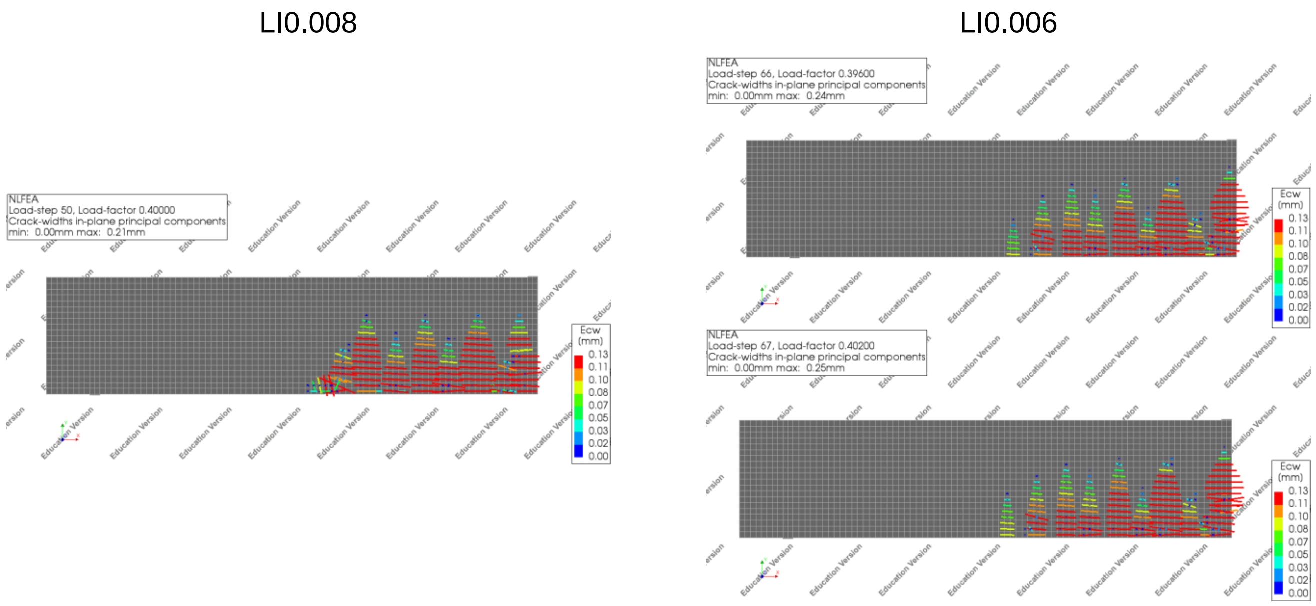

Figure 5.56 Crack Pattern Specimen H123A with Modified NR Method at δ = 6.66 mm (Shifting Point A)

LI0.008 LI0.006

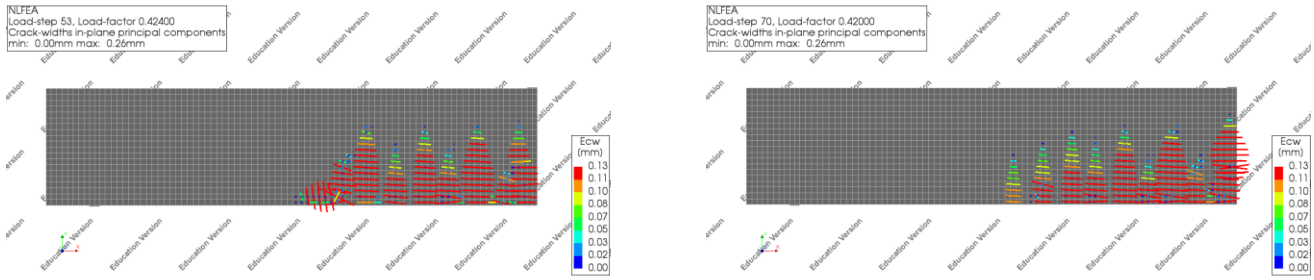

Figure 5.57 Crack Pattern Specimen H123A with Modified NR Method at δ = 7.06 mm (Shifting Point B)

LI0.008 LI0.006

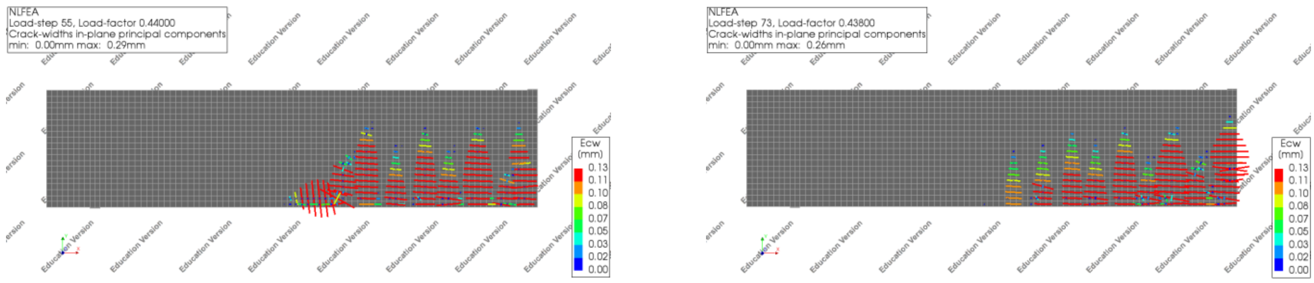

Figure 5.58 Crack Pattern Specimen H123A with Modified NR Method at δ = 7.33 mm (Shifting Point C)

LI0.008 LI0.006

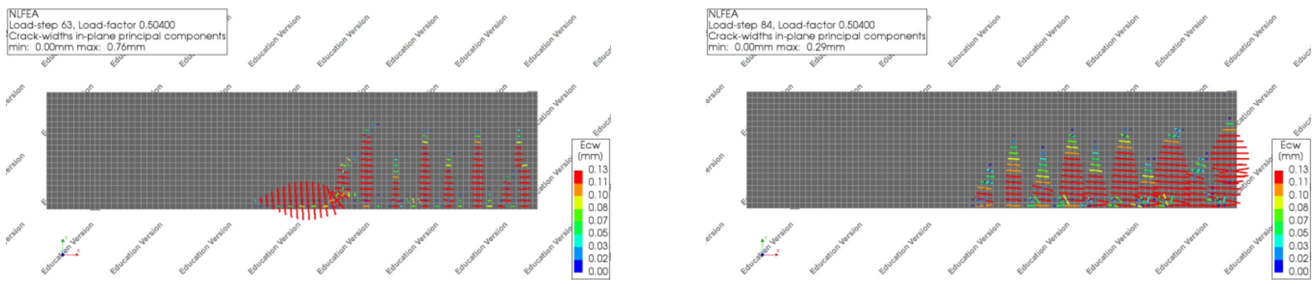

Figure 5.59 Crack Pattern Specimen H123A with Modified NR Method at δ = 8.41 mm (Shifting Point D)

LI0.008 LI0.006

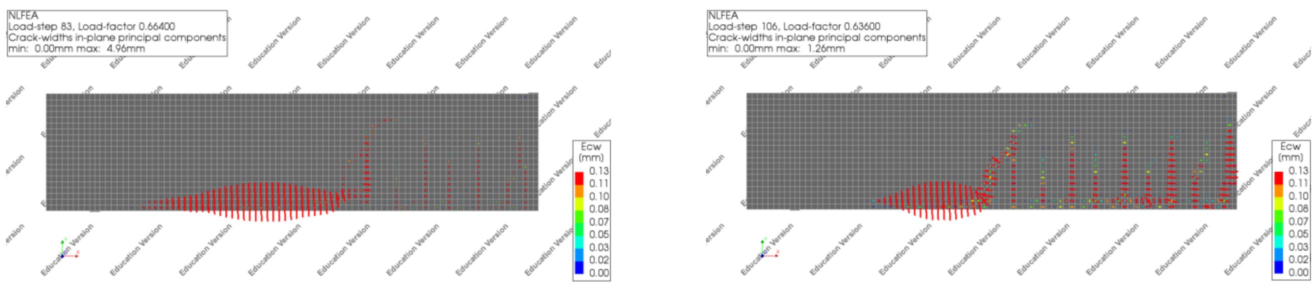

Figure 5.60 Crack Pattern Specimen H123A with Modified NR Method at Peak Load

In Figure 5.55, the relative energy variation of model H123A LI0.008 has an upward trend through all shifting points, while model H123A LI0.006 does not have a trend through all shifting points. The relative out-of-balance force of model H123A LI0.008 is constant through all shifting points. On the other hand, the relative out-of-balance force of model H123A LI0.006 does not have a trend through all shifting points.

In terms of crack pattern, model H123A LI0.008 and LI0.006 show a slight difference at shifting point A in Figure 5.56 where model H123A LI0.008 has developed a small dowel crack while model H123A LI0.006

does not have dowel crack yet. The dowel crack opening in model H123A LI0.008 is similar to the flexural crack opening at shifting point B in Figure 5.57. The dowel crack in model H123A LI0.008 starts to dominate the crack propagation in Figure 5.58 at shifting point C. On the other hand, model H123A LI0.006 does not develop any dowel crack up to shifting point D in Figure 5.59. This phenomenon can be correlated to the observation results for Figure 5.55 where the convergence state of model H123A LI0.006 does not have any trend because no dowel crack has been formed in the model. The relative energy variation increase through shifting point A to D in model H123A LI0.008 is correlated to the dowel crack propagation which resulted in more elements are cracked, thus increasing the relative energy variation on the respective steps on the shifting points. The starting point of the dowel crack propagation affected the crack pattern at the peak load in Figure 5.60, where the dowel crack has almost propagated to the support in model H123A LI0.008 compared to model H123A LI0.006.

Based on the observation for both specimen A123A1 and H123A, it can be concluded that variation on the peak load of models with the Modified Newton-Raphson method and different load increment is caused by the initiation of dowel crack formation. The formation of dowel crack can be identified by looking at the trend of the relative energy variation where the relative energy variation would be increasing as the dowel crack propagate and dominate the crack propagation process on the numerical model. The major types of propagating crack at certain steps can also be determined by observing the trend of the convergence state where no clear trend indicates flexural cracks are dominating the crack propagation process and a certain trend (constant/increasing) indicates that dowel crack starts to dominate the crack propagation process. The starting point of dowel crack propagation is considered important because it controls when the numerical models would reach their peak capacity and affect the crack pattern at the peak load. However, the degree of the influence of dowel crack propagation starting point is affected by the size of the specimen, where it has almost no influence in Figure 5.54 for the numerical model with specimen A123A1 while it has a significant influence in Figure 5.60 for the numerical model with specimen H123A.

5.4. Effect of Error Tolerance Variation

The influence of error tolerance can be observed in the peak load of the numerical models and the global behaviour of the beam. Furthermore, its influence on different types of iterative-incremental methods would also be observed. The observation would be done for results that have been post-processed with the additional criterion defined for each iterative-incremental method in 5.3 Effect of Load Increment Variation where an upper bound value for the convergence norms is used as a limit for accepting non-converged steps. The variation described in this subchapter is done for the error tolerance defined as an input to the numerical models, which separated converged and non-converged steps in the NLFEA. In this subchapter, this tolerance will be defined as lower bound tolerance. The analysis of the results is not going to be able to cover all variations of convergence level, because the focus of this subchapter is to give an insight on how error tolerance would be influencing the global behaviour of the beam, regardless of the convergence level of the NLFEA.

5.4.1 Effect of Error Tolerance Variation in Quasi-Newton Method

The first observation is done for numerical models with the Quasi-Newton method. The change in peak load distribution due to different values of lower bound value for energy tolerance can be observed in Figure 5.61 for specimens A123A1 and H123A.

The change in lower bound energy tolerance affects the peak load distribution significantly for both specimens. Less strict energy tolerance mostly causes larger peak load distribution. Figure 5.61 shows that the change in lower bound energy tolerance gives less impact to specimen A123A1 compared to specimen H123A. However, no trend can be observed in both specimen results.

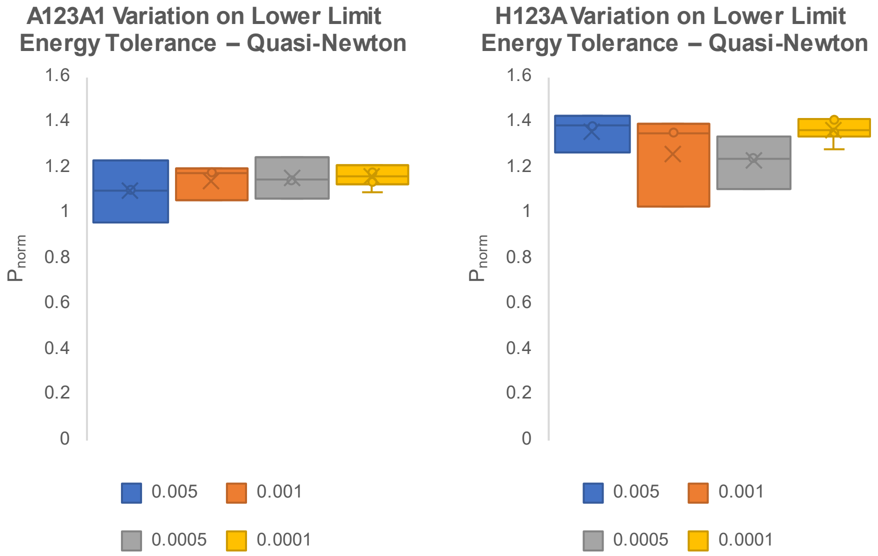

Figure 5.61 Peak Load Distribution for Quasi-Newton Method with Different Lower Bound Energy Tolerance

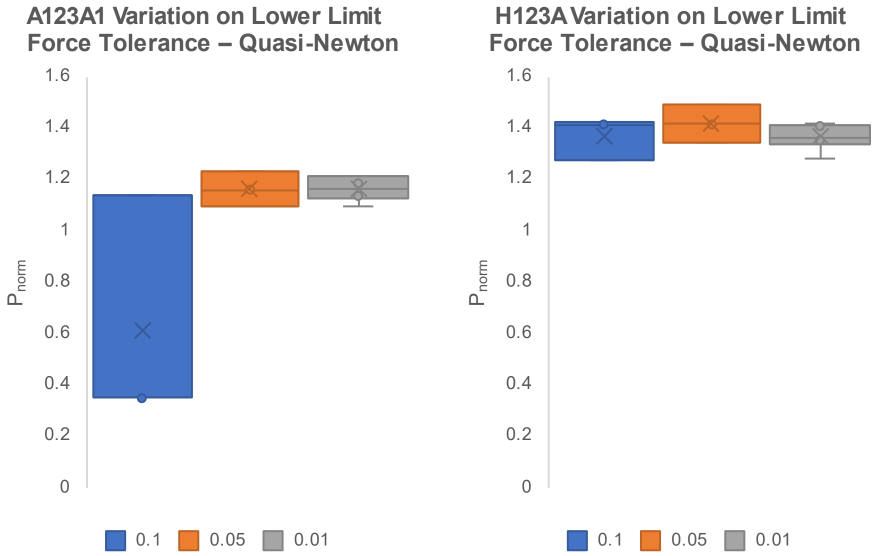

Figure 5.62 Peak Load Distribution for Quasi-Newton Method with Different Lower Bound Force Tolerance

When the level of strictness on the lower bound force tolerance is decreased, a significant change in the peak load distribution can also be observed in Figure 5.62. Figure 5.62 also shows that in most of the results, the size and the mean value of the peak load distribution does not change a lot. However, it can still be observed that the peak load distribution is larger when less strict lower bound force tolerance is applied on the numerical models. No trend can be observed in both specimen results.

The simulated global behaviour of the beam with the Quasi-Newton method is observed based on the results of NLFEA which has lower relative energy variation and relative out-of-balance force than the defined upper bound for both energy and force tolerance in subchapter 5.3.1 Effect of Load Increment Variation in Quasi-Newton Method. The observation of the simulated global behaviour of the beam will be done separately for different specimens. Figure 5.63 gives an illustration of the simulated global behaviour of the beam with the Quasi-Newton method based on the load-displacement curve for specimen A123A1.

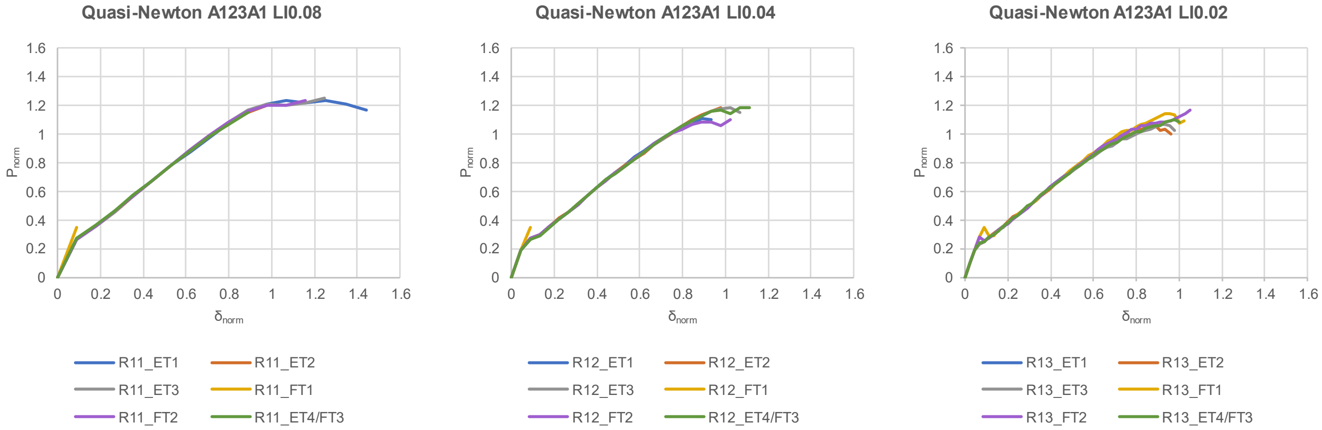

Figure 5.63 Load-displacement Curve for Error Tolerance Variance – A123A1 Quasi-Newton Method

Based on Figure 5.63, it can be said that the load-displacement curve for all variations of lower bound error tolerance for specimen A123A1 is independent of the prescribed lower bound error tolerance. The difference in the peak load estimation is caused by the pre-defined upper bound error tolerance. However, there are 2 phenomena that can be observed in Figure 5.63. The first phenomenon is non-linear behaviour cannot be simulated properly with high lower bound error tolerance for relative out-of-balance force. This can be seen in models A123A1 R11_FT1 and A123A1 R12_FT1 where one of the convergence norms has exceeded its upper bound tolerance at the first cracking occurrence. This phenomenon enlarges the peak load distribution, which can be seen in Figure 5.62. The second phenomenon is the first cracking occurrence does not influence the simulated non-linear behaviour of the model, which can be seen in Figure 5.63 where no significant deviation can be seen in the load-displacement curve. Overall, the effect of variation on the lower bound of error tolerance is insignificant to the simulated global behaviour of specimen A123A1.

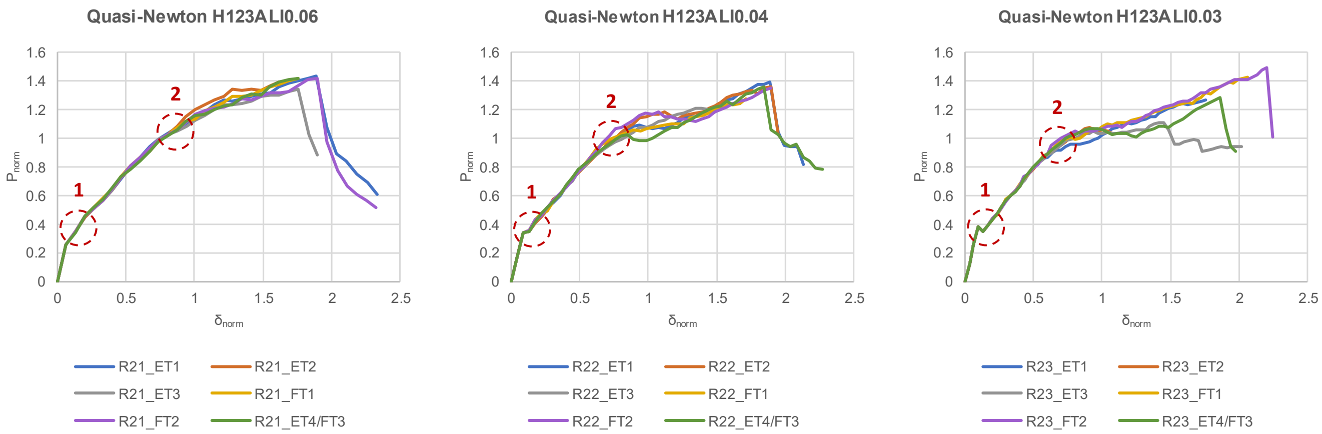

Figure 5.64 Load-displacement Curve for Error Tolerance Variance – H123A Quasi-Newton Method

Figure 5.64 gives an illustration of the simulated global behaviour of the beam with the Quasi-Newton method based on the load-displacement curve for specimen H123A. Based on Figure 5.64, it can be said that the load-displacement curve for all variations of lower bound error tolerance is dependent on the prescribed lower bound error tolerance. In the load-displacement curve in Figure 5.64, there are 2 critical points that show some deviation due to change in lower bound error tolerance. The first critical point is considered not important because the deviation in critical point 1 does not affect the overall simulated behaviour of the beam in the non-linear region. This can be seen by observing the load-displacement curve between critical point 1 and critical point 2, where the simulated non-linear behaviour is similar for all models with specimen H123A. On critical point 2, a significant deviation can be seen between the results of model H123A R23. The deviation on the curve is considered significant due to its effect on the simulated non-linear behaviour and the peak load of the model. Two models, ET3 and ET4/FT3 are chosen as the representative of all results of model H123A R23. The load-displacement curve for these models is given in Figure 5.65.

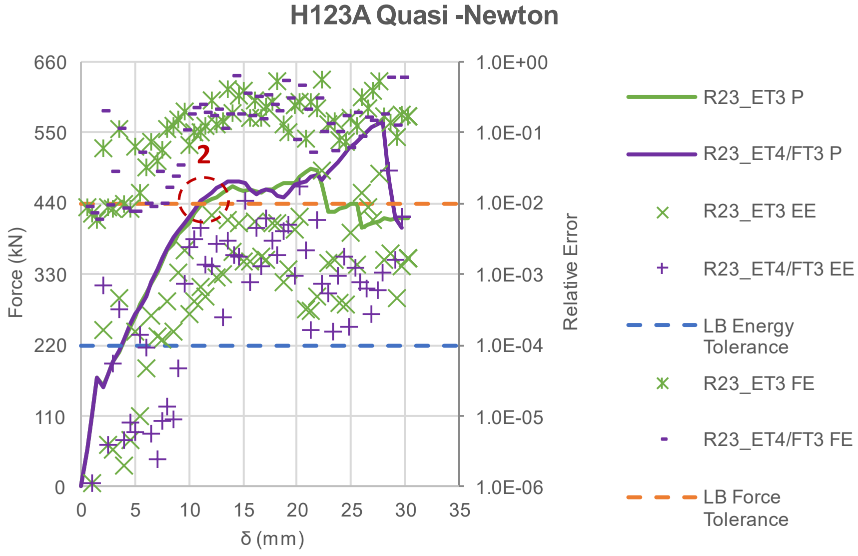

Figure 5.65 Load-displacement Curve Model H123A with the Convergence State for QN Method

In Figure 5.65, the lower bound of the convergence norms are based on the model code ET4/FT3. Based on Figure 5.65, most of the steps are converging in both relative energy variation and out-of-balance force. Furthermore, higher relative energy variation and out-of-balance force can be seen by comparing convergence state at δ = 10-20 mm to δ = 5-10 mm for model H123A R23_ET3 and δ = 10-30 mm to δ = 5-10 mm for model H123A R23_ET4/FT3, where the curve is near its peak.

In order to observe the simulated global behaviour on critical point 2, a detailed illustration for critical point 2 of model H123A R23 is given in Figure 5.66. 3 load steps are going to be observed in Figure 5.66. These load steps indicate the shift in the load-displacement curve and will be called shifting points A, B, and C for displacement at 11.03 mm, 11.54 mm, and 12.05 mm respectively.

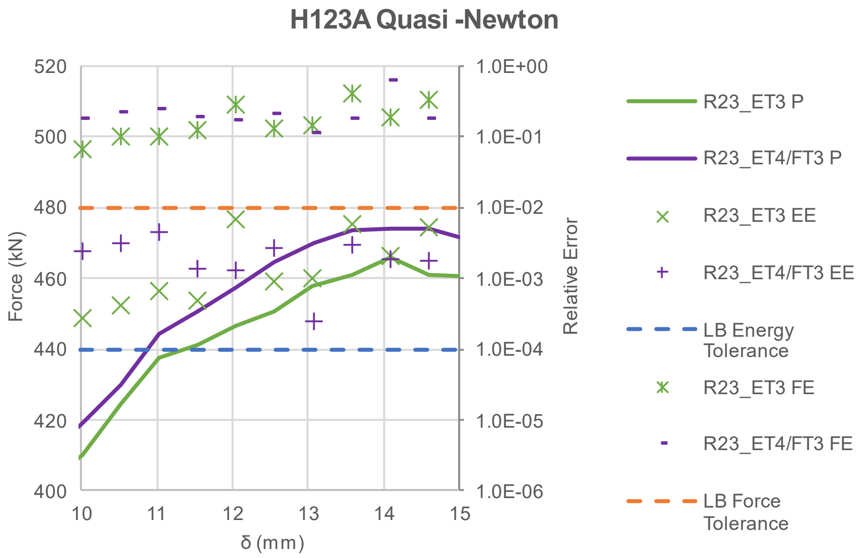

Figure 5.66 Load-displacement Curve on Critical Point 2 of Model H123A R23 for Quasi-Newton Method

ET3 ET4/FT3

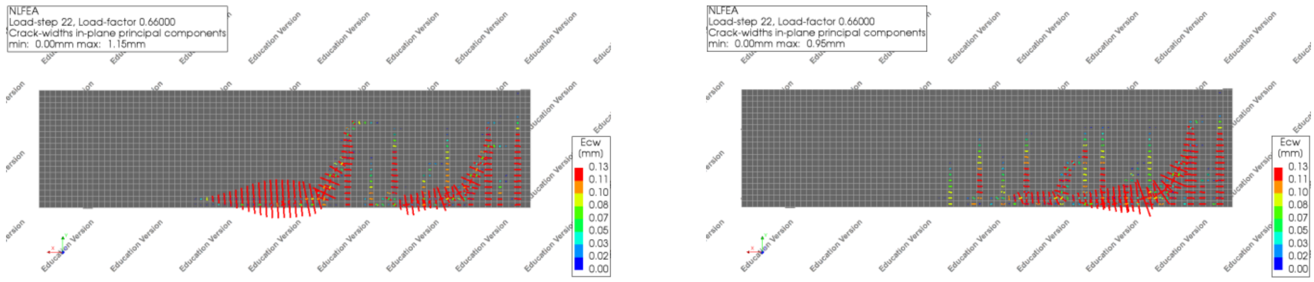

Figure 5.67 Crack Pattern Model H123A R23 for Err. Tol. Variation at δ = 11.03 mm (Shifting Point A)

ET3 ET4/FT3

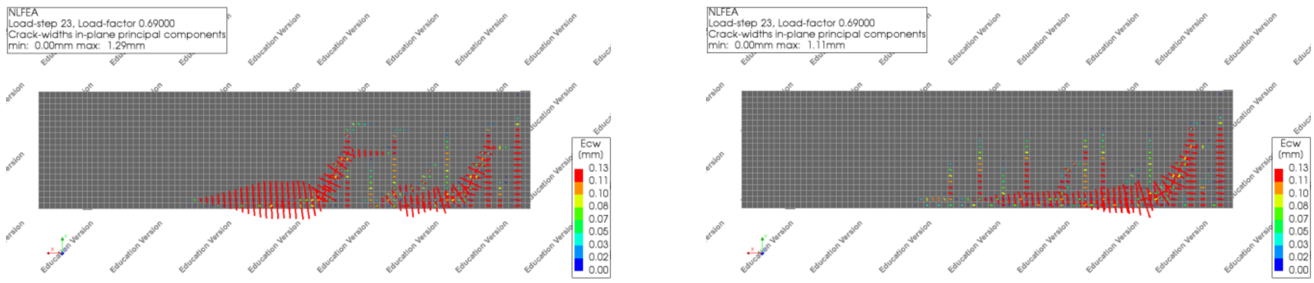

Figure 5.68 Crack Pattern Model H123A R23 for Err. Tol. Variation at δ = 11.54 mm (Shifting Point B)

ET3 ET4/FT3

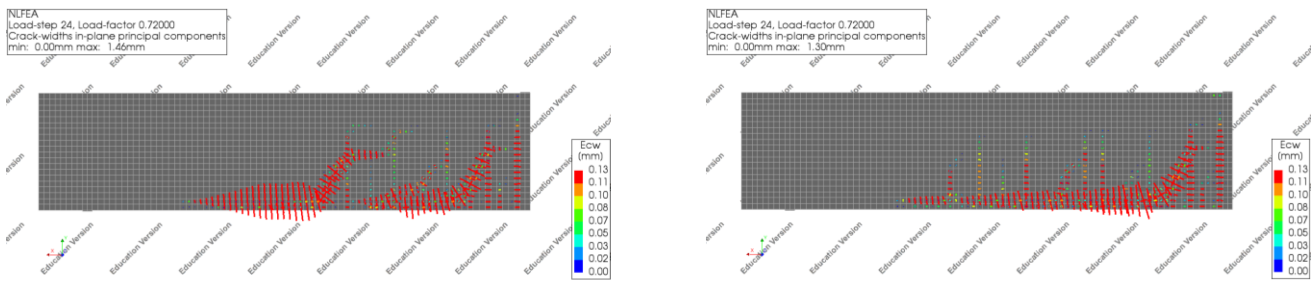

Figure 5.69 Crack Pattern Model H123A R23 for Err. Tol. Variation at δ = 12.05 mm (Shifting Point C)

ET3 ET4/FT3

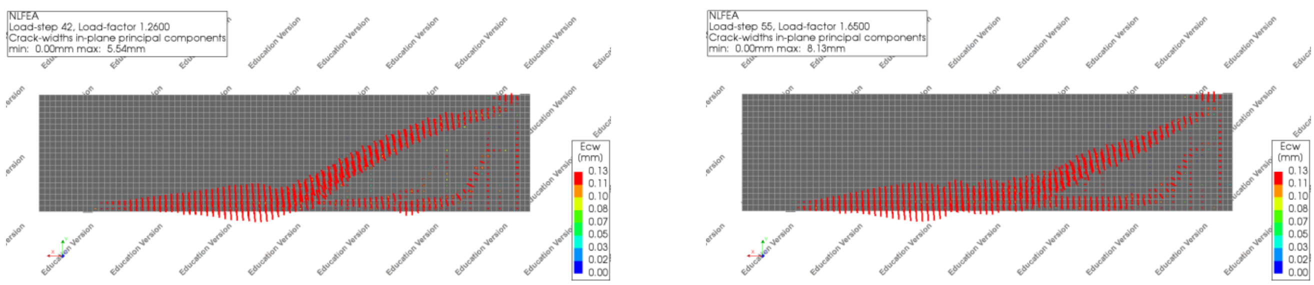

Figure 5.70 Crack Pattern Model H123A R23 for Err. Tol. Variation at Peak Load

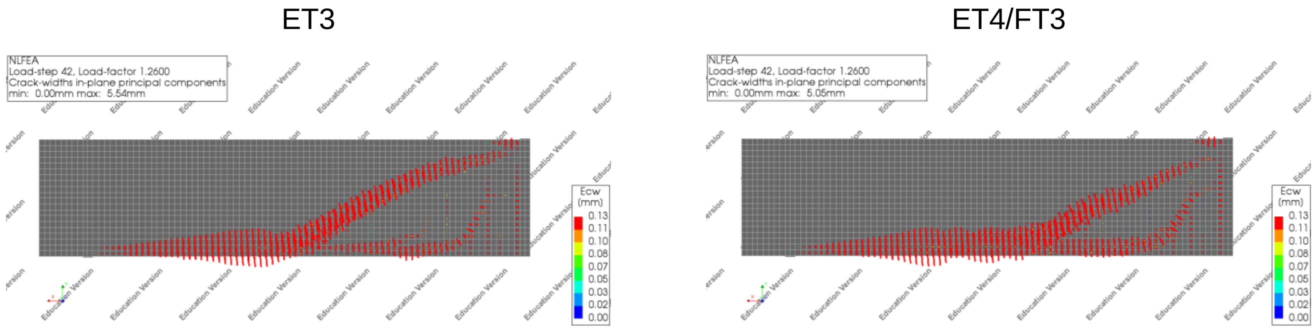

Figure 5.71 Crack Pattern of Model H123A R23 ET3 at Peak Load

The relative energy variation in model H123A R23 ET3 in Figure 5.66 is increasing through all shifting points. On the other hand, the relative energy variation is decreasing from shifting point A to shifting point C in model H123A R23 ET4/FT3. The relative out-of-balance force in Figure 5.66 is relatively constant for both models from shifting point A to shifting point C.

In terms of crack pattern, model H123A R23 ET3 and ET4/FT3 show similar crack progression in Figure 5.67, where both models have 2 inclined cracks with dowel crack. However, different crack progression can be seen from shifting point A to B, where the dowel cracks in model H123A R23 ET4/FT3 are connected and forming one major dowel crack, which can be seen in Figure 5.68. Furthermore, a significant difference in the maximum crack width can be seen as well on all shifting points. This difference still exists in Figure 5.69 in shifting point C for both models. Both models have a similar crack pattern at the peak load, as indicated in Figure 5.70. Model H123A R23 ET3 reached its peak sooner than model H123A R23 ET4/FT3 due to different locations of dowel crack, which can be seen in Figure 5.69, where one of the inclined cracks is formed in the middle of the span in model H123A R23 ET3. Its dowel crack has propagated up to three-quarters of the shear span, which indicates that model H123A R23 ET3 would reach its peak sooner than model H123A R23 ET4/FT3. This is proven by Figure 5.71 where model H123A R23 ET3 has been shattered into two parts while model H123A R23 ET4/FT3 is still intact. These differences cannot be seen in the convergence state of the model because of different lower bound error tolerance. Different lower bound error tolerance imposed different criteria for the NLFEA to consider a step as a converged step. At the early stage of analysis, the model enters the first cracking occurrence and the formation of flexural cracks. This means that the relative energy variation is directly correlated to tensile fracture energy, as the energy loss on the model is only caused by concrete tensile cracking. Higher relative energy variation at the early stages of the analysis causes different loss of tensile fracture energy, which resulted in different crack patterns and propagation.

Based on the observation for both specimen A123A1 and H123A, it can be concluded that the variation on the peak load of models with the Quasi-Newton method and different error tolerance is caused by different crack propagation on the models. Different crack propagation is caused by different lower bound energy tolerance prescribed on the model. This directly affected the number of cracked elements on the model, which controls the crack formation on the model. This effect cannot be observed in the trend of the convergence state of the models. However, this effect is size-dependent as this can only be observed in the numerical model for specimen H123A.

5.4.2 Effect of Error Tolerance Variation in Full Newton-Raphson Method

The second observation is done for numerical models with the Full Newton-Raphson method. The change in peak load distribution due to different values of lower bound value for energy tolerance can be observed in Figure 5.72 for specimens A123A1 and H123A.

The change in lower bound energy tolerance affects the peak load distribution significantly for specimen H123A, while the result for specimen A123A1 is less affected due to this change. Less strict energy tolerance causes larger peak load distribution for specimen A123A1 and smaller peak load distribution for specimen H123A, which can be seen in Figure 5.72. Furthermore, in the results of specimen H123A, a significant shift in the mean peak load distribution can also be seen, but the shift does not have a consistent trend. Figure

5.72 shows that the change in lower bound energy tolerance gives less impact to specimen A123A1 compared to specimen H123A. However, no trend can be observed in both specimen results.

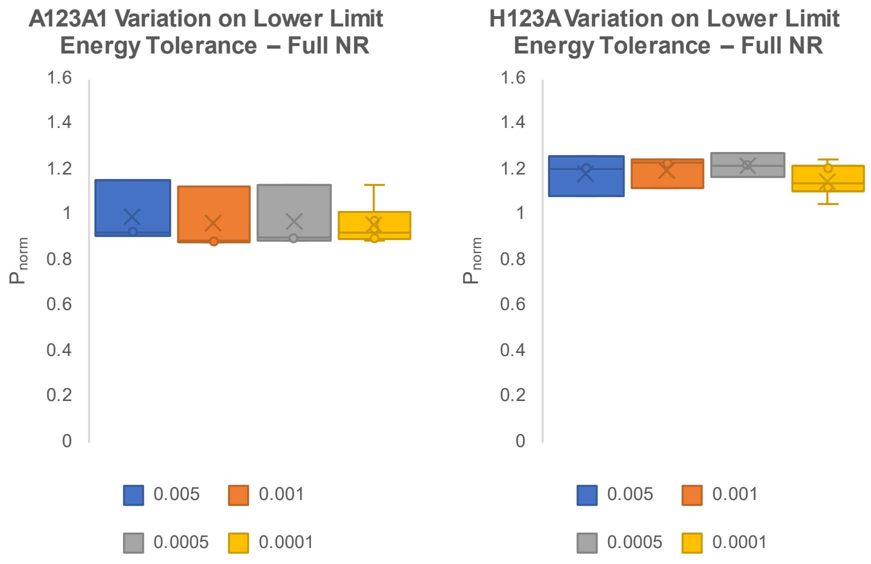

Figure 5.72 Peak Load Distribution for Full NR Method with Different Lower Bound Energy Tolerance

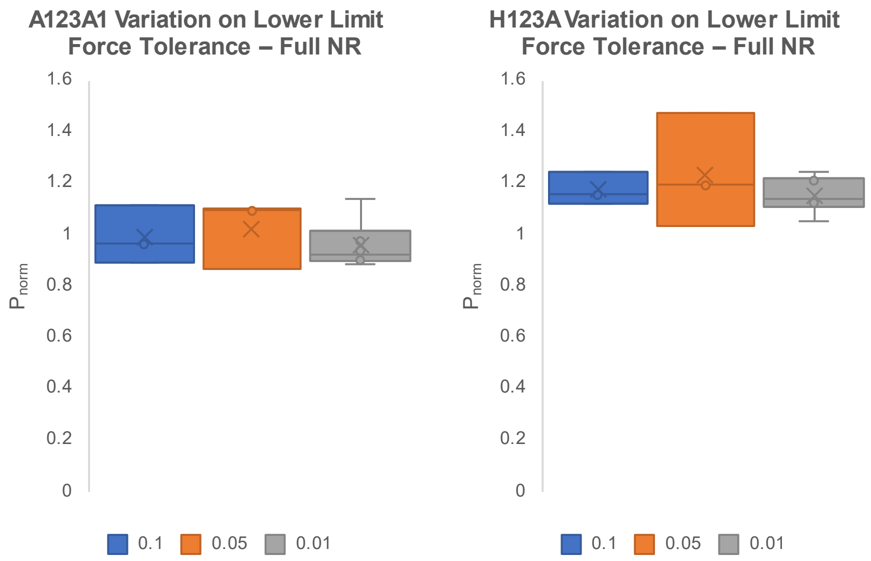

Figure 5.73 Peak Load Distribution for Full NR Method with Different Lower Bound Force Tolerance

When the level of strictness on the lower bound force tolerance is decreased, a significant change in the peak load distribution can also be observed in Figure 5.73. Figure 5.73 also shows that the size and the mean value of the peak load distribution do not change a lot for specimen A123A1, while significant change can be seen in the results for specimen H123A, especially at the peak load distribution. However, it can still be observed that the peak load distribution is larger when less strict lower bound force tolerance is applied on the numerical models for most of the results. No trend can be observed in both specimen results.

The simulated global behaviour of the beam with the Full Newton-Raphson method is observed based on the results of NLFEA which has lower relative energy variation and relative out-of-balance force than the defined upper bound for both energy and force tolerance in subchapter 5.3.2 Effect of Load Increment Variation in Full Newton-Raphson Method. The observation of the simulated global behaviour of the beam will be done separately for different specimens. Figure 5.74 gives an illustration of the simulated global behaviour of the beam with the Full Newton-Raphson method based on the load-displacement curve for specimen A123A1.

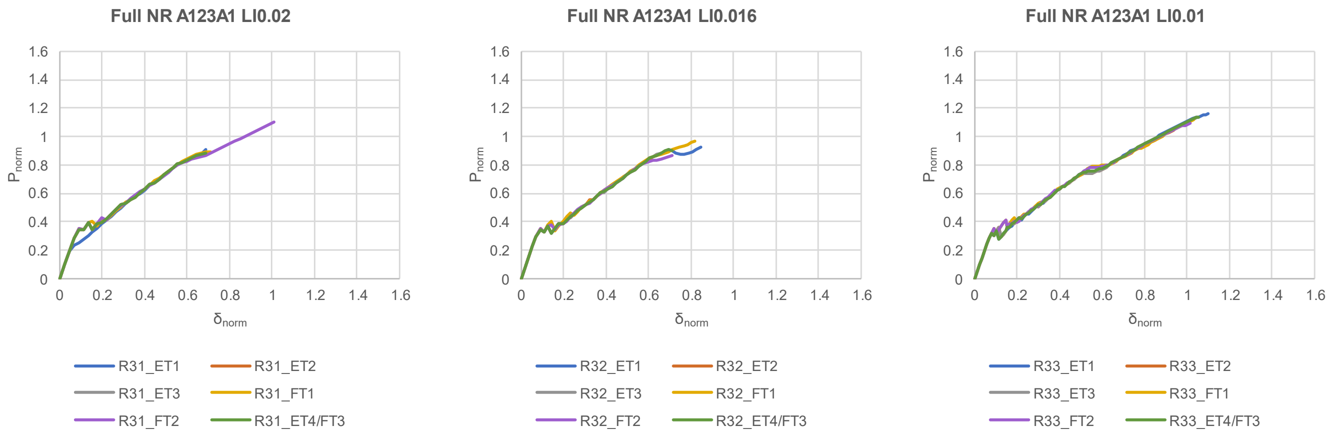

Figure 5.74 Load-displacement Curve for Error Tolerance Variance – A123A1 Full NR Method

Based on Figure 5.74, it can be said that the load-displacement curve for all variations of lower bound error tolerance for specimen A123A1 is independent of the prescribed lower bound error tolerance. The difference in the peak load estimation is caused by the pre-defined upper bound error tolerance. However, there is a phenomenon that can be observed in Figure 5.74. It can be said that the first cracking occurrence does not influence the simulated non-linear behaviour of the model, which can be seen in Figure 5.74 where no significant deviation can be seen in the load-displacement curve. Overall, the effect of variation on the lower bound of error tolerance is insignificant to the simulated global behaviour of specimen A123A1.

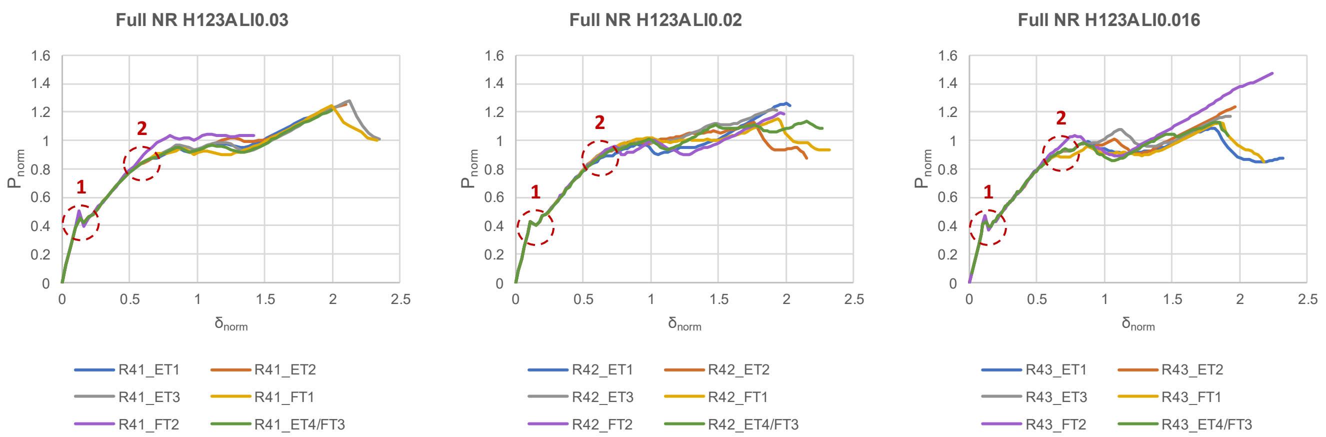

Figure 5.75 Load-displacement Curve for Error Tolerance Variance – H123A Full NR Method

Figure 5.75 gives an illustration of the simulated global behaviour of the beam with the Full Newton-Raphson method based on the load-displacement curve for specimen H123A. Based on Figure 5.75, it can be said that the load-displacement curve for all variations of lower bound error tolerance is dependent on the prescribed lower bound error tolerance. In the load-displacement curve in Figure 5.75, there are 2 critical points that show some deviation due to change in lower bound error tolerance. The first critical point is considered not important because the deviation in critical point 1 does not affect the overall simulated behaviour of the beam in the non-linear region. This can be seen by observing the load-displacement curve between critical point 1 and critical point 2, where the simulated non-linear behaviour is similar for all models with specimen H123A. On critical point 2, a significant deviation can be seen between the results of model H123A R23. The deviation on the curve is considered significant due to its effect on the simulated non-linear behaviour and the peak load of the model. Two sets of models, FT2 and ET4/FT3, and ET3 and ET4/FT3, are chosen as the representative of all results of model H123A R41 and R43 respectively. The load-displacement curve for these models is given in Figure 5.65.

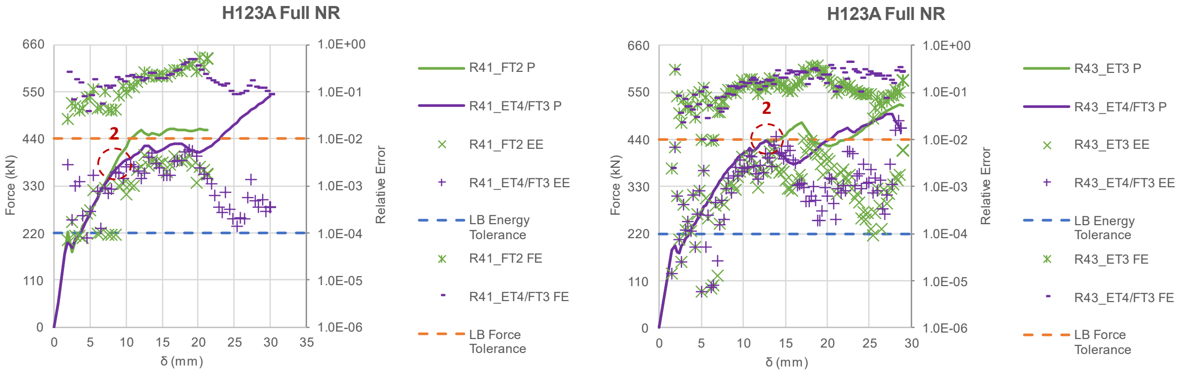

Figure 5.76 Load-displacement Curve Model H123A with the Convergence State for Full NR Method

In Figure 5.76, the lower bound of the convergence norms are based on the model H123A R41 and R43. Based on Figure 5.76, most of the steps are converging in the relative energy variation. Furthermore, higher relative energy variation and out-of-balance force can be seen by comparing convergence state at δ = 10-30 mm to δ = 5-10 mm for model H123A R41 and δ = 10-30 mm to δ = 5-10 mm for model H123A R43, where the curve is near its peak.

In order to observe the simulated global behaviour on critical point 2, a detailed illustration for critical point 2 is made for Figure 5.76. The first critical point 2 that is going to be observed is on model H123A R41, which is illustrated in Figure 5.77. 3 load steps are going to be observed in Figure 5.77. These load steps indicate the shift in the load-displacement curve and will be called shifting points A, B, and C for displacement at 6.49 mm, 7.00 mm, and 8.01 mm respectively.

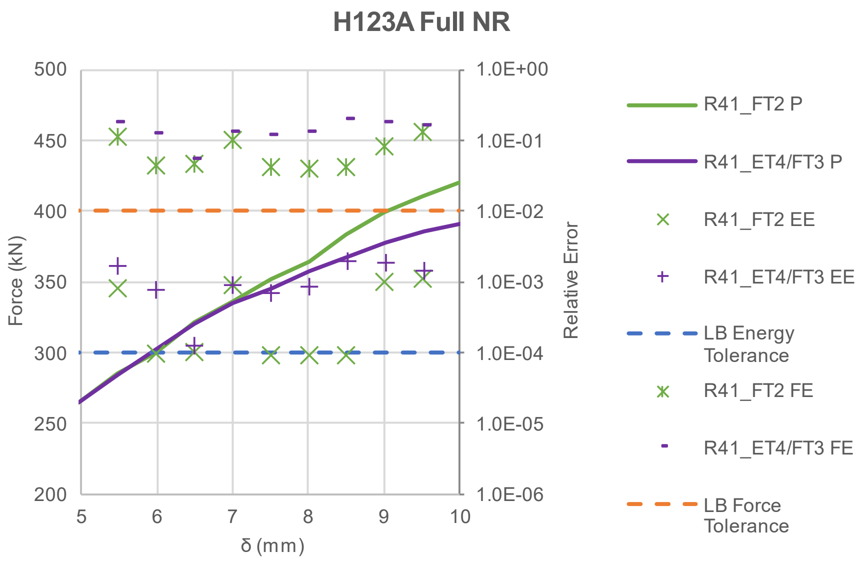

Figure 5.77 Load-displacement Curve on Critical Point 2 of Model H123A R41 for Full NR Method

FT2 ET4/FT3

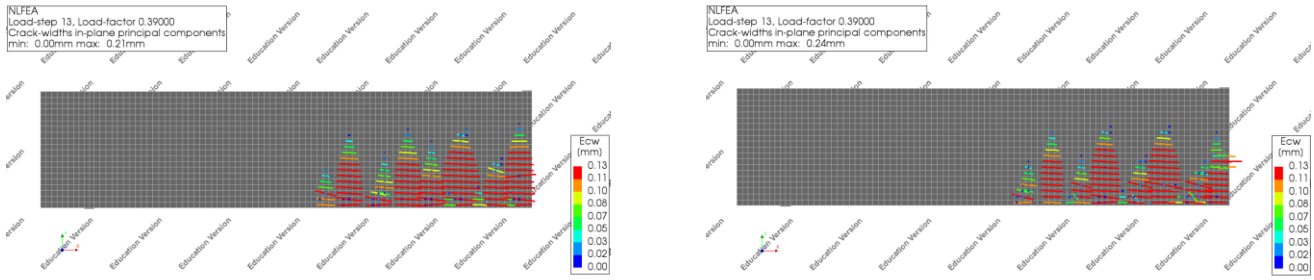

Figure 5.78 Crack Pattern Model H123A R41 for Err. Tol. Variation at δ = 6.49 mm (Shifting Point A)

FT2 ET4/FT3

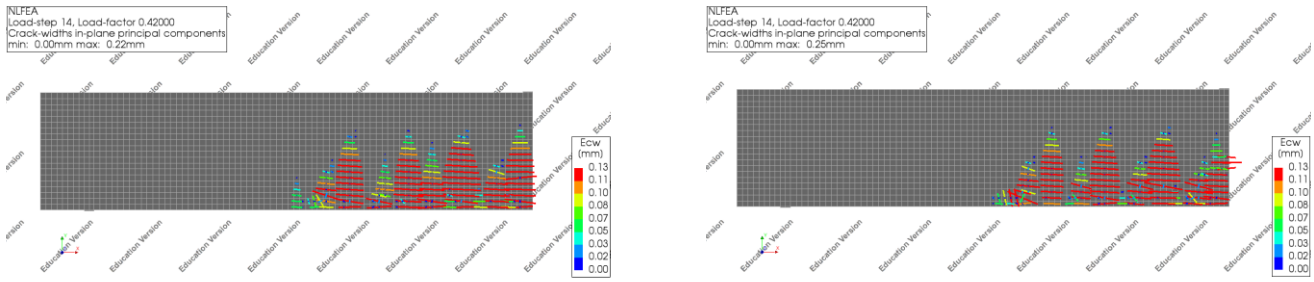

Figure 5.79 Crack Pattern Model H123A R41 for Err. Tol. Variation at δ = 7.00 mm (Shifting Point B)

FT2 ET4/FT3

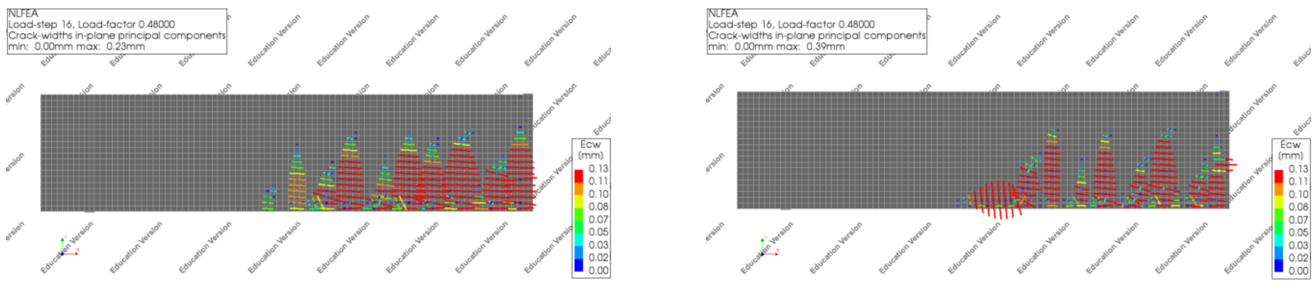

Figure 5.80 Crack Pattern Model H123A R41 for Err. Tol. Variation at δ = 8.01 mm (Shifting Point C)

FT2 ET4/FT3

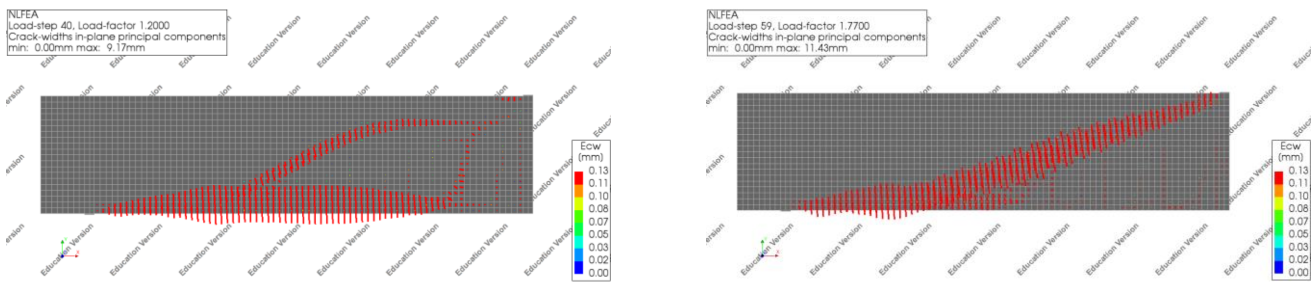

Figure 5.81 Crack Pattern Model H123A R41 for Err. Tol. Variation at Peak Load

The relative energy variation and out-of-balance force in model H123A R41 FT2 and ET4/FT3 in Figure 5.77 is constant through all shifting points. A significant difference in relative energy variation and out-of-balance force can be seen in shifting point C in Figure 5.77.

In terms of crack pattern, model H123A R41 FT2 and ET4/FT3 have a similar crack pattern in Figure 5.78 where the models only have flexural cracks in shifting point A. In shifting point B, no significant difference can be seen between both models in Figure 5.79, where model H123A R41 FT2 and ET4/FT3 has developed dowel crack. The formation of dowel crack in model H123A R41 ET4/FT3 in shifting point B led to dowel crack propagation in shifting point C in Figure 5.80 where the dowel crack starts to dominate the crack propagation process in model H123A R41 ET4/FT3, while this phenomenon does not happen in shifting point C of model H123A R41 FT2. This phenomenon can be correlated to the convergence state of the models. The significant difference in both relative energy variation and out-of-balance force is affecting the crack propagation direction. The difference in both relative energy variation and out-of-balance force is caused by different prescribed lower bound error tolerance, where the norms in model H123A R41 FT2 are converged to 0.0001 for energy tolerance and 0.05 for force tolerance. The difference in the prescribed lower bound error tolerance causes the model to find a different equilibrium state on model H123A FT2. However, this does not affect the crack pattern at the peak load of both models significantly in Figure 5.81.

The next critical point 2 that is going to be observed is on model H123A R43, which is illustrated in Figure 5.82. 3 load steps are going to be observed in Figure 5.82. These load steps indicate the shift in the load-displacement curve and will be called shifting points A, B, and C for displacement at 12.06 mm, 12.60 mm, and 13.96 mm respectively.

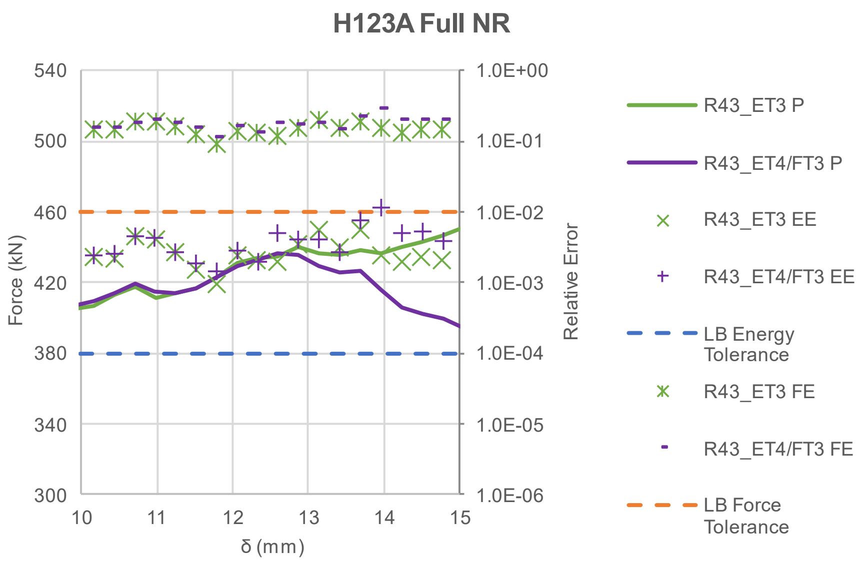

Figure 5.82 Load-displacement Curve on Critical Point 2 of Model H123A R43 for Full NR Method

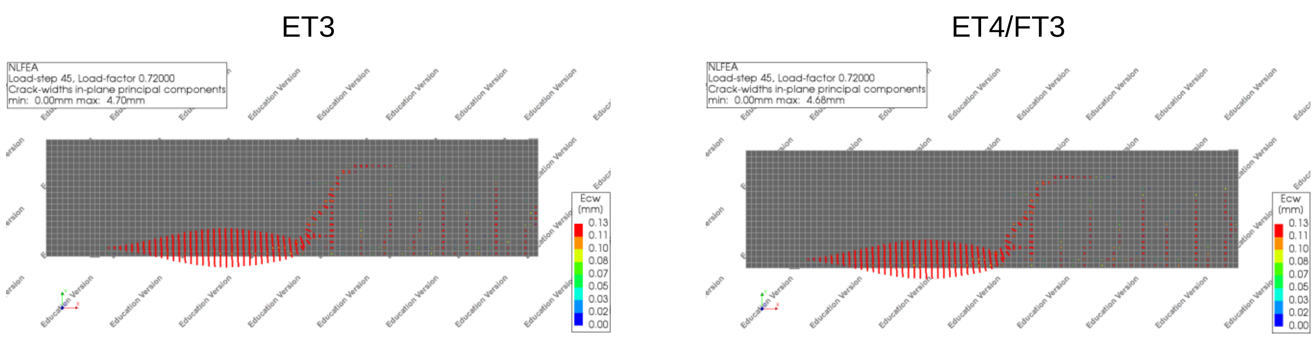

Figure 5.83 Crack Pattern Model H123A R43 for Err. Tol. Variation at δ = 12.06 mm (Shifting Point A)

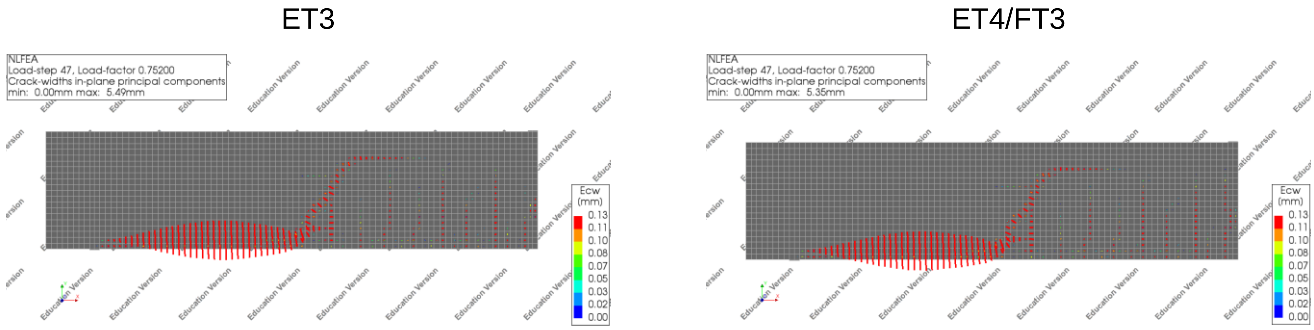

Figure 5.84 Crack Pattern Model H123A R43 for Err. Tol. Variation at δ = 12.60 mm (Shifting Point B)

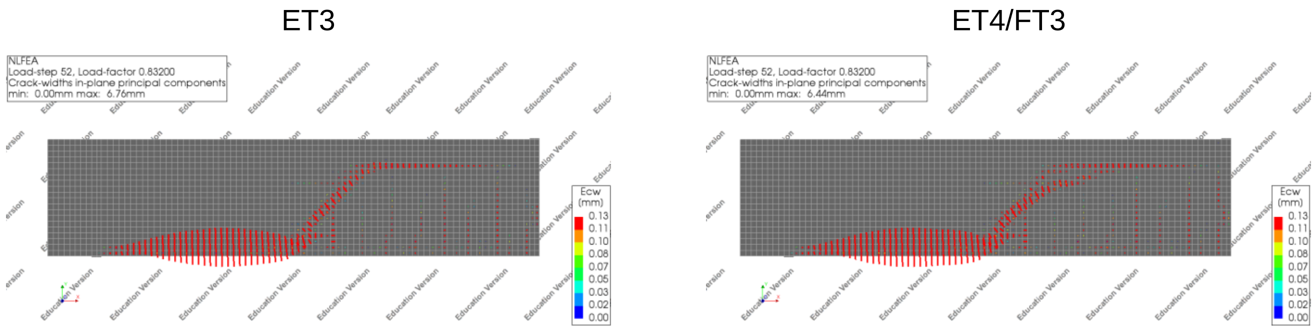

Figure 5.85 Crack Pattern Model H123A R43 for Err. Tol. Variation at δ = 13.96 mm (Shifting Point C)

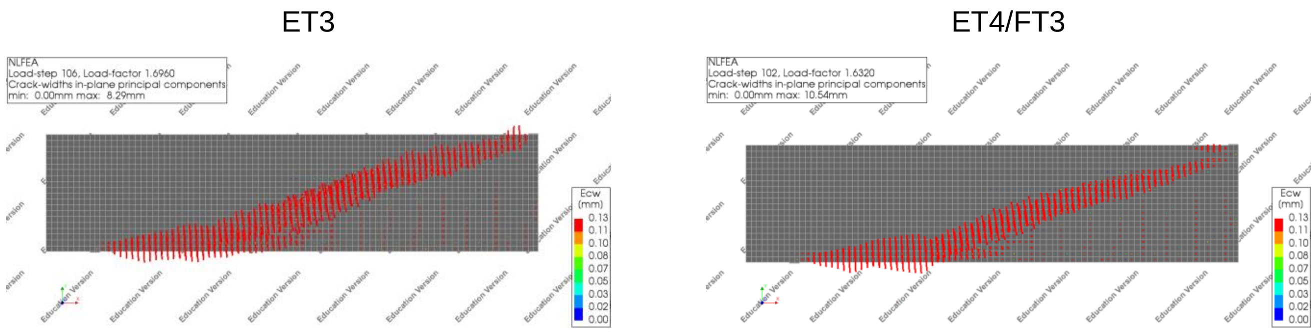

Figure 5.86 Crack Pattern Model H123A R43 for Err. Tol. Variation at Peak Load

The relative energy variation in model H123A R43 ET3 in Figure 5.82 is constant through all shifting points. On the other hand, the relative energy variation in model H123A R43 ET4/FT3 is increasing through all shifting points. The difference in relative energy variation is increasing between model H123A R43 ET3 and ET4/FT3 in Figure 5.82 from shifting point B to C. The relative out-of-balance force in both models is constant through all shifting points.

In terms of crack pattern, model H123A R23 ET3 and ET4/FT3 have similar crack propagation in shifting points A and B in Figure 5.83 and Figure 5.84. However, in shifting point C in Figure 5.85, the crack propagation changes in model H123A R23 ET4/FT3 where the second branch of the top horizontal crack formed below the first branch of the top horizontal crack. On the other hand, the crack propagation in model H123A R23 ET3 does not change from shifting point B to C. If this phenomenon is linked to the convergence state of the model, this indicates that a certain magnitude of relative energy variation caused different crack propagation directions. Based on Figure 5.82, as the relative energy variation of model H123A R23 ET3 is constant, the crack propagation direction is influenced in model H123A R23 ET4/FT3 when the step has a relative energy variation of more than 0.01, which is equal to 100 times the lower bound energy tolerance. Fortunately, this difference does not significantly influence the crack pattern at the peak load, which can be seen in Figure 5.86.

Based on the observation for both specimen A123A1 and H123A, it can be concluded that the variation on the peak load of models with the Full Newton-Raphson method and different error tolerance is caused by different crack propagation on the models. Different crack propagation is caused by a difference in the relative energy variation of the model. This directly affected the number of cracked elements on the model, which controls the crack formation on the model. However, the current data is not enough to define the boundary of the relative energy variation to prevent the change in crack propagation direction in the model. Moreover, the influence in the crack propagation direction is size-dependent as this can only be observed in the numerical model for specimen H123A.

5.4.3 Effect of Error Tolerance Variation in Modified Newton-Raphson Method

The last observation is done for numerical models with the Modified Newton-Raphson method. The change in peak load distribution due to different values of lower bound value for energy tolerance can be observed in Figure 5.87 for specimens A123A1 and H123A.

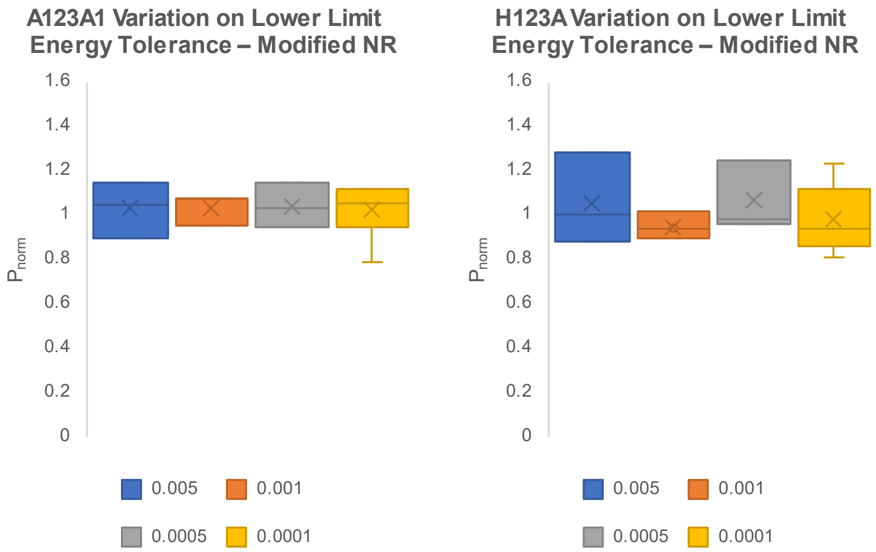

Figure 5.87 Peak Load Distribution for Modified NR Method with Different Lower Bound Energy Tolerance

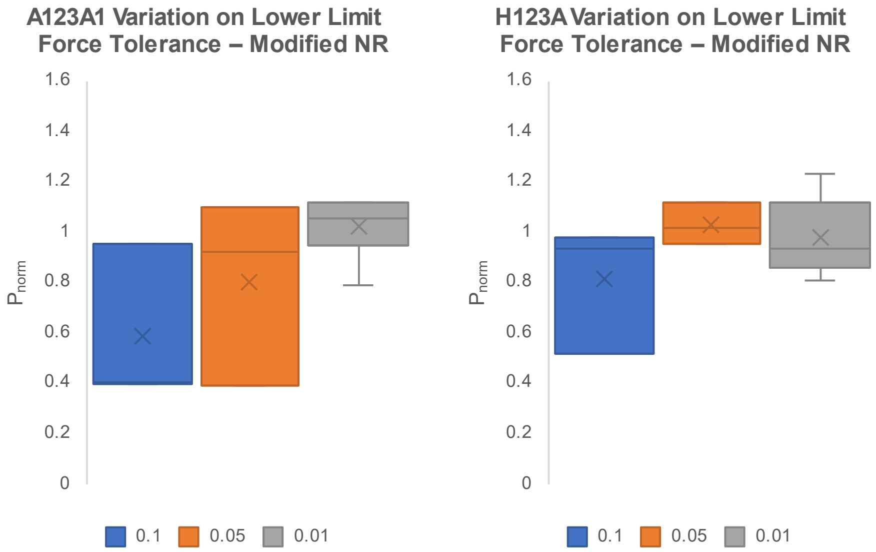

Figure 5.88 Peak Load Distribution for Modified NR Method with Different Lower Bound Force Tolerance

The change in lower bound energy tolerance affects the peak load distribution significantly for both specimens, which can be seen in Figure 5.87. The distribution of the peak load distribution is becoming smaller when the lower bound energy tolerance is increased up to 0.001. However, this trend changes when the lower bound energy tolerance is increased further to 0.005. A significant shift in the mean peak load distribution can also be seen for both specimens, but the shift does not have a consistent trend. Figure 5.87 shows that the change in lower bound energy tolerance gives less impact to specimen A123A1 compared to specimen H123A.

When the level of strictness on the lower bound force tolerance is decreased, a significant change in the peak load distribution can also be observed in Figure 5.88. The distribution of the peak load becomes larger after less strict lower bound force tolerance is used on the model for specimen A123A1. However, this is not the case for specimen H123A, where the peak load distribution is smaller when a lower bound of 0.05 is applied for force tolerance. An increase in the lower bound value for force tolerance results in larger peak load distribution.

The simulated global behaviour of the beam with the Modified Newton-Raphson method is observed based on the results of NLFEA which has lower relative energy variation and relative out-of-balance force than the defined upper bound for both energy and force tolerance in subchapter 5.3.3 Effect of Load Increment Variation in Modified Newton-Raphson Method. The observation of the simulated global behaviour of the beam will be done separately for different specimens. Figure 5.89 gives an illustration of the simulated global behaviour of the beam with the Modified Newton-Raphson method based on the load-displacement curve for specimen A123A1.

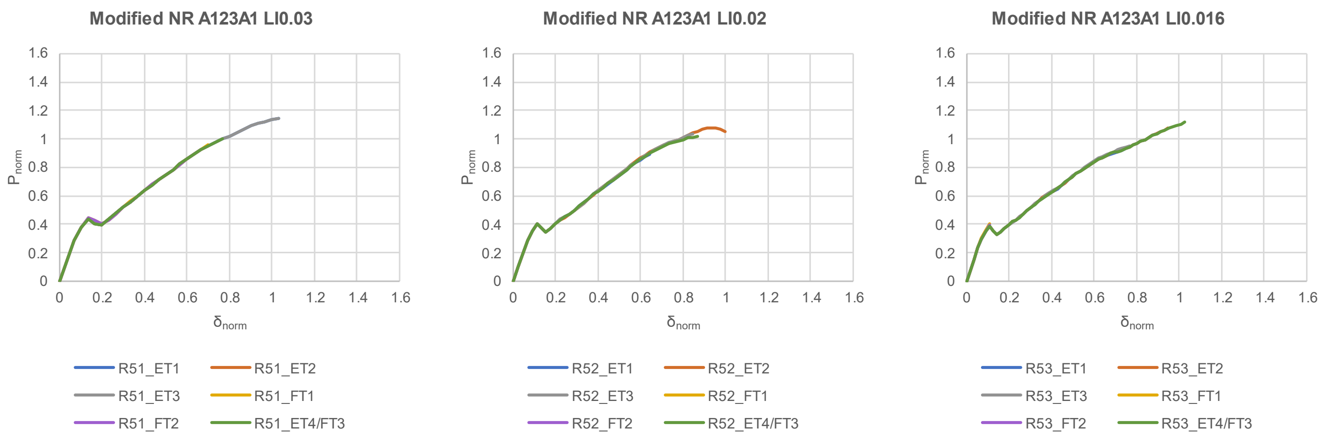

Figure 5.89 Load-displacement Curve for Error Tolerance Variance – A123A1 Modified NR Method

Based on Figure 5.89, it can be said that the load-displacement curve for all variations of lower bound error tolerance for specimen A123A1 is independent of the prescribed lower bound error tolerance. The difference in the peak load estimation is caused by the pre-defined upper bound error tolerance. Overall, the effect of variation on the lower bound of error tolerance is insignificant to the simulated global behaviour of specimen A123A1.

Figure 5.90 gives an illustration of the simulated global behaviour of the beam with the Modified Newton-Raphson method based on the load-displacement curve for specimen H123A. Based on Figure 5.90, it can be said that the load-displacement curve for all variations of lower bound error tolerance for specimen H123A is independent of the prescribed lower bound error tolerance. The difference in the peak load estimation is caused by the pre-defined upper bound error tolerance. However, there is a phenomenon that can be observed in Figure 5.90. It can be said that the first cracking occurrence does not influence the simulated non-linear behaviour of the model, which can be seen in Figure 5.90 where no significant deviation can be seen in the load-displacement curve. Overall, the effect of variation on the lower bound of error tolerance is insignificant to the simulated global behaviour of specimen H123A.

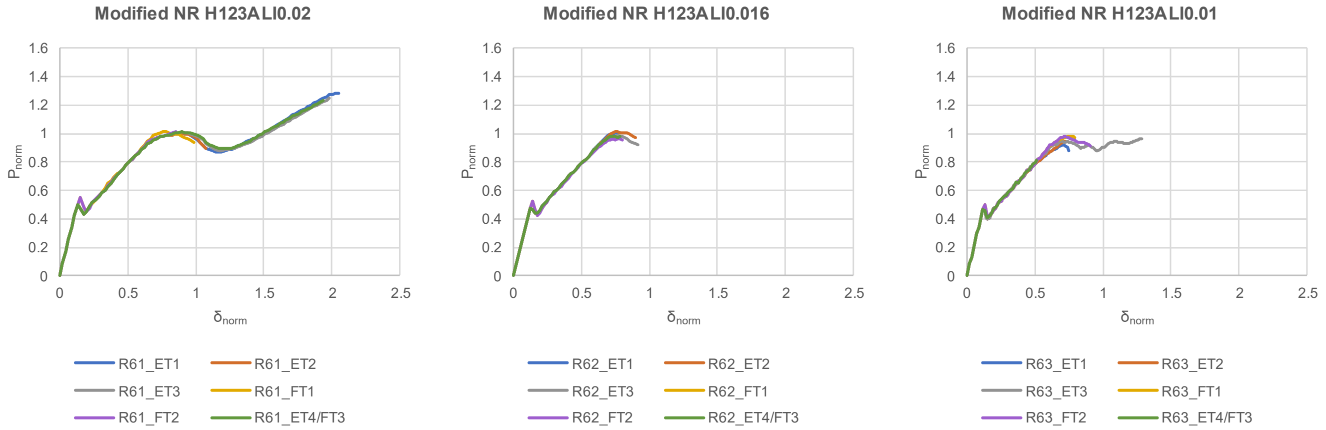

Figure 5.90 Load-displacement Curve for Error Tolerance Variance – H123A Modified NR Method

Based on the observation for both specimen A123A1 and H123A, it can be concluded that the numerical models with the Modified Newton-Raphson method are independent of the variation of the lower bound error tolerance. Furthermore, the independent behaviour towards the variation of the lower bound error tolerance is not size-dependent, where both models show similar behaviour when the numerical models are varied in the lower bound error tolerance.

5.5. Effect of Maximum Number of Iterations Variation

As there are a lot of steps that do not reach convergence and non-converged steps used the last output of the iterations, the maximum number of iterations is suspected to be influencing the peak load of the numerical models and the global behaviour of the beam. Furthermore, its influence is expected to be different for different types of iterative-incremental methods. Therefore, the effect on different iterative-incremental methods would also be observed. The observation would be done for results that have been post-processed with the additional criterion defined for each iterative-incremental method in 5.3 Effect of Load Increment Variation where an upper bound value for the convergence norms is used as a limit for accepting non-converged steps. The analysis of the results is not going to be able to cover all variations of convergence level, because the focus of this subchapter is to give an insight on how the maximum number of iterations would be influencing the global behaviour of the beam, regardless of the convergence level of the NLFEA.

5.5.1 Effect of Maximum Number of Iterations Variation in Quasi-Newton Method

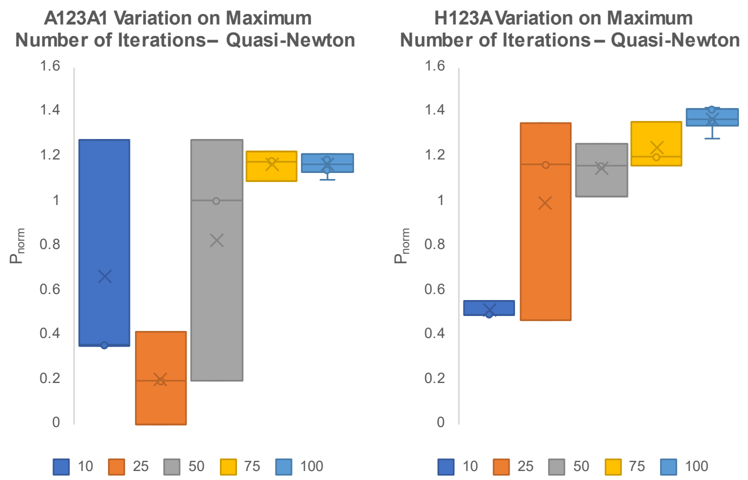

Figure 5.91 Peak Load Distribution for Quasi-Newton Method with Different Maximum Number of Iterations

The first observation is done for numerical models with the Quasi-Newton method. The change in peak load distribution due to different maximum numbers of iterations can be observed in Figure 5.91 for specimens A123A1 and H123A.

The peak load distribution for both specimens is significantly influenced by the variation of the maximum number of iterations. A significant change in peak load distribution can be seen in Figure 5.91 for specimen A123A1 starting from 75 iterations to 50 iterations and for H123A starting from 50 iterations to 25 iterations. No trend can be observed in the results of both specimens.

The simulated global behaviour of the beam with the Quasi-Newton method is observed based on the results of NLFEA which has lower relative energy variation and relative out-of-balance force than the defined upper bound for both energy and force tolerance in subchapter 5.3.1 Effect of Load Increment Variation in Quasi-Newton Method. The observation of the simulated global behaviour of the beam will be done separately for different specimens. Figure 5.92 gives an illustration of the simulated global behaviour of the beam with the Quasi-Newton method based on the load-displacement curve for specimen A123A1.

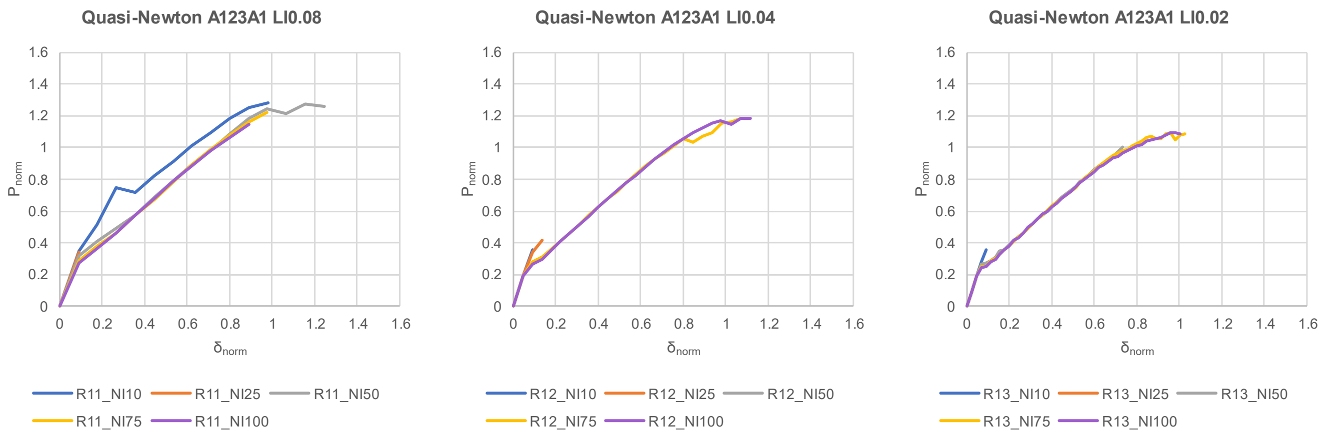

Figure 5.92 Load-displacement Curve for Maximum Iterations Variance – A123A1 Quasi-Newton Method

Based on Figure 5.92, it can be said that the load-displacement curve for all variations of the maximum number of iterations for specimen A123A1 is dependent on the prescribed maximum number of iterations. The difference in the peak load estimation is mostly caused by the pre-defined upper bound error tolerance. There are 2 phenomena that can be observed in Figure 5.92. The first phenomenon is non-linear behaviour cannot be simulated properly with a small maximum number of iterations. This can be seen in model A123A1 R11 NI25, R12 NI10, R12 NI25, R13 NI10, and R13 NI25 where one of the convergence norms has exceeded its upper bound tolerance at the first cracking occurrence. This phenomenon enlarges the peak load distribution, which can be seen in Figure 5.91. The second phenomenon is the first cracking occurrence does not influence the simulated non-linear behaviour of the model, except on model A123A1 R11 NI10, which can be seen in Figure 5.92 where no significant deviation can be seen in the load-displacement curve. Model A123A1 R11 NI10 is considered as an anomaly in this variation, as it is the only model that produces different results compared to other models. Model A123A1 R11 NI10 is considered an anomaly due to its significant difference in the simulated non-linear behaviour and the peak load of the model. In order to observe this model further, a comparison of two models, A123A1 R11 NI10 and NI100, is made based on the load-displacement curve in Figure 5.93.

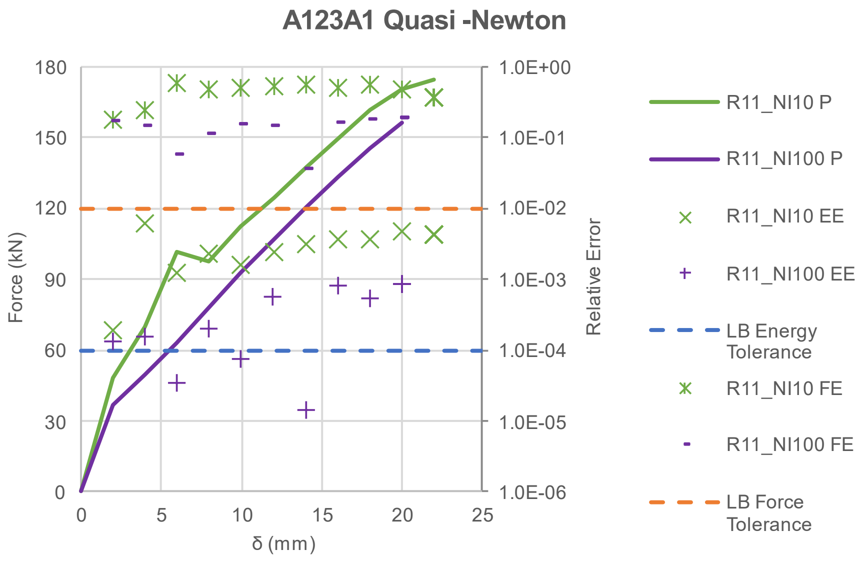

Figure 5.93 Load-displacement Curve Model A123A1 NI with the Convergence State for QN Method

Based on Figure 5.93, the relative energy variation and out-of-balance force are relatively constant for both models. However, no step is converging in model A123A1 R11 NI10 while there are some steps converging in model A123A1 R11 NI100.

In order to observe the deviation in the simulated global behaviour, a detailed illustration of model H123A R23 is given in Figure 5.94. The observation would be done for 3 load steps. These load steps indicate the shift in the load-displacement curve and will be called shifting points A, B, and C for displacement at 1.99 mm, 3.99 mm, and 7.99 mm respectively.

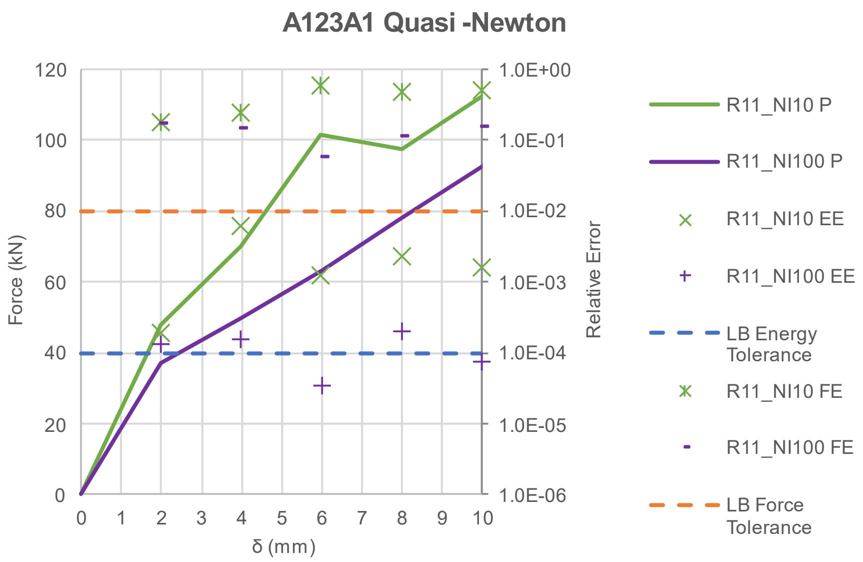

Figure 5.94 Load-displacement Curve on Critical Point 2 of Model H123A R11 NI for QN Method

NI10 NI100

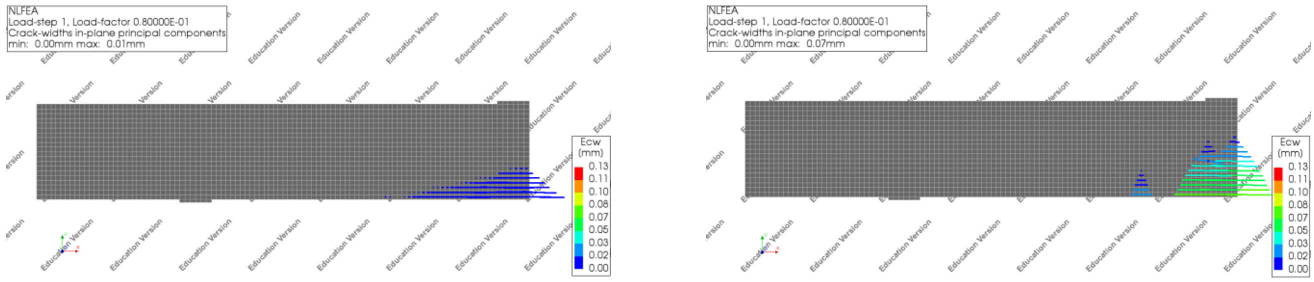

Figure 5.95 Crack Pattern Model A123A1 R11 for NI Variation at δ = 1.99 mm (Shifting Point A)

NI10 NI100

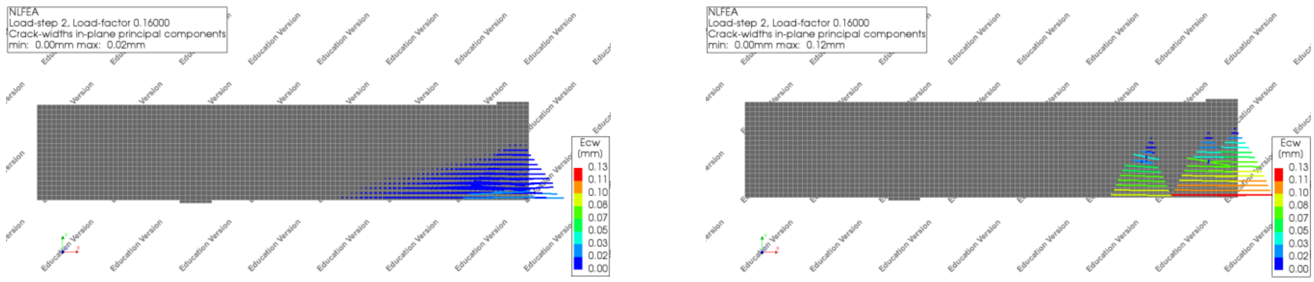

Figure 5.96 Crack Pattern Model A123A1 R11 for NI Variation at δ = 3.99 mm (Shifting Point B)

NI10 NI100

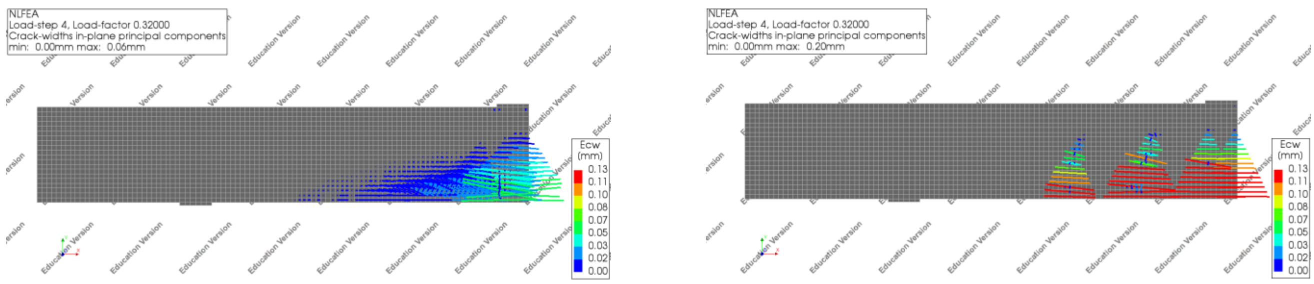

Figure 5.97 Crack Pattern Model A123A1 R11 for NI Variation at δ = 7.99 mm (Shifting Point C)

NI10 NI100

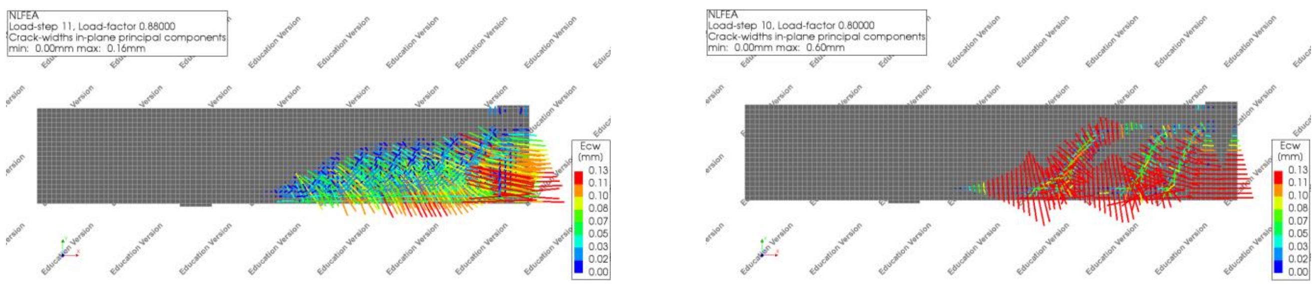

Figure 5.98 Crack Pattern Model A123A1 R11 for NI Variation at Peak Load

The relative energy variation in model A123A1 R11 NI10 in Figure 5.94 is significantly larger in all shifting points compared to model A123A1 R11 NI100. The relative out-of-balance force is also significantly larger in model A123A1 R11 NI10 compared to model A123A1 R11 NI100, but the differences are not as large as differences in relative energy variation.

In terms of crack pattern, model A123A1 R11 NI10 and NI100 have a significant difference in the crack propagation where model A123A1 R11 NI10 has distributed small flexural cracks while model A123A1 R11

NI100 has 3 single flexural cracks, which can be seen in shifting point A in Figure 5.95. Shifting point B and C in Figure 5.96 and Figure 5.97 also shows that the crack propagation of both models is different, where model A123A1 R11 NI10 continue to create distributed small flexural cracks while model A123A1 R11 NI100 is propagating single flexural cracks. This resulted in a significant difference in the maximum crack width in all shifting points between both models. The crack pattern at the peak load is also different, where model A123A1 R11 NI10 fails due to flexural cracks while model A123A1 R11 NI100 fails due to flexural shear cracks. This phenomenon can be correlated to the convergence state of the models. The significant difference in relative energy variation in model A123A1 R11 NI10 is caused by multiple openings of small cracks. The significant difference in relative out-of-balance force can be related to a different type of crack propagation. This correlation can be verified by the observation results of critical point 2 for numerical models with the Quasi-Newton method, where in Figure 5.11 (specimen A123A1) and Figure 5.17 (specimen H123A), a similar magnitude of the relative out-of-balance force is reflected in the similarity of the cracking progression on the numerical models in Figure 5.12, Figure 5.13, Figure 5.14 and Figure 5.15 for specimen A123A1 and Figure 5.18, Figure 5.19, Figure 5.20 and Figure 5.21 for specimen H123A. As there is no other shifting point in model A123A1 R11 NI10 where the crack propagation behaviour change, this phenomenon affected the simulated crack pattern at the peak load in Figure 5.98.

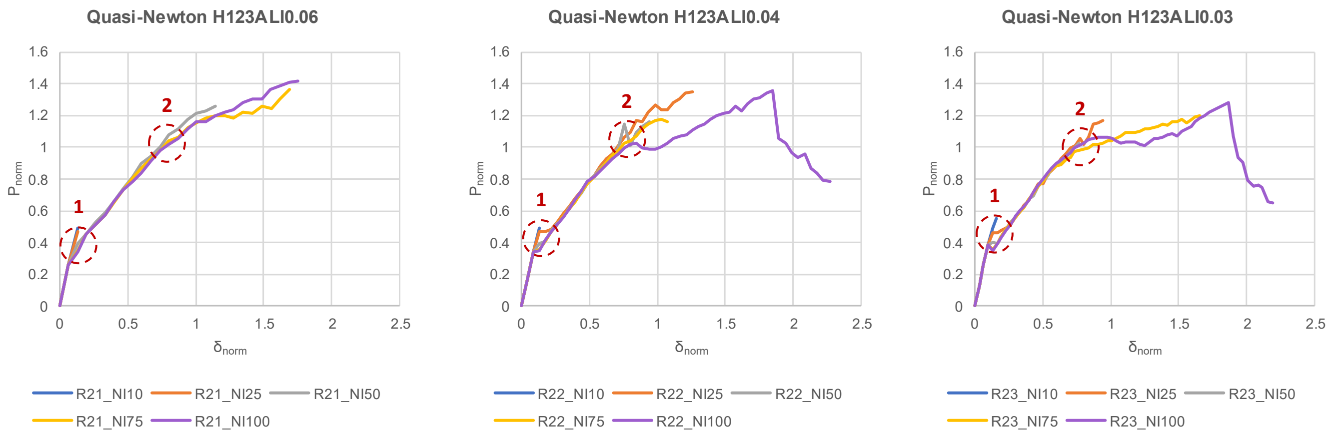

Figure 5.99 Load-displacement Curve for Maximum Iterations Variance – H123A Quasi-Newton Method

The next observation is done for numerical models for specimen H123A. Figure 5.99 gives an illustration of the simulated global behaviour of the beam with the Quasi-Newton method based on the load-displacement curve for specimen H123A. Based on Figure 5.99, it can be said that the load-displacement curve for all variations of the maximum number of iterations is dependent on the prescribed maximum number of iterations. The first observation that can be derived from Figure 5.99 is non-linear behaviour cannot be simulated properly with a small maximum number of iterations. This can be seen in model H123A R21 NI10, R21 NI25, R22 NI10, and R23 NI10 where one of the convergence norms has exceeded its upper bound tolerance at the first cracking occurrence. Another observation can be done based on the defined critical points in Figure 5.99. There are 2 critical points that show some deviation due to changes in the maximum number of iterations. The first critical point is considered not important because the deviation in critical point 1 does not affect the overall simulated behaviour of the beam in the non-linear region. This can be seen by observing the load-displacement curve between critical point 1 and critical point 2, where the simulated non-linear behaviour is similar for all models with specimen H123A. On critical point 2, a significant deviation can be seen between the results of model H123A R22 and R23. The deviation on the curve is considered significant due to its effect on the simulated non-linear behaviour and the peak load of the model. Three sets of models, NI25, NI75 and NI100, are chosen as the representative of all results of models H123A R22 and R23. The load-displacement curve for these models is given in Figure 5.100.

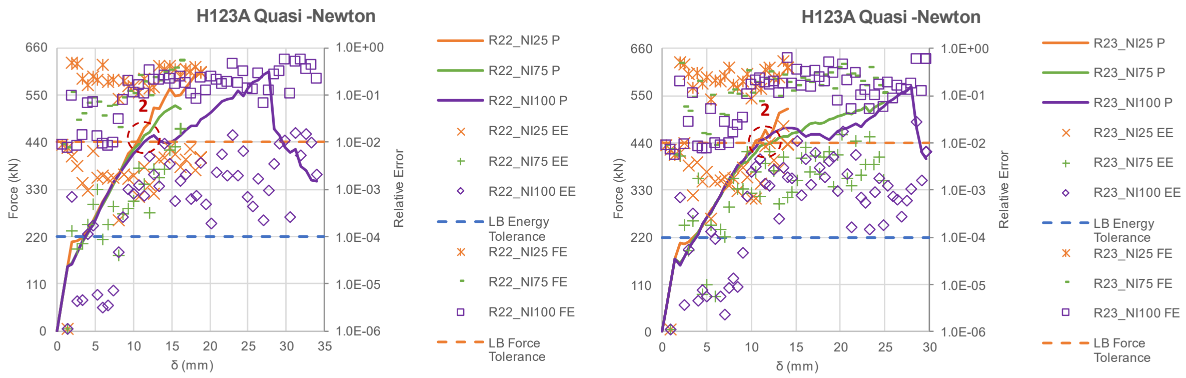

Figure 5.100 Load-displacement Curve Model H123A NI with the Convergence State for QN Method

Based on Figure 5.100, most of the steps are converging in both relative energy variation and out-of-balance force. Furthermore, higher relative energy variation and out-of-balance force can be seen by comparing convergence state at δ = 10-30 mm to δ = 5-10 mm for model H123A R22 and R23, where the curve is near its peak.

In order to observe the simulated global behaviour on critical point 2, a detailed illustration for critical point 2 is made for Figure 5.100. The first critical point 2 that is going to be observed is on model H123A R22, which is illustrated in Figure 5.101. 3 load steps are going to be observed in Figure 5.101. These load steps indicate the shift in the load-displacement curve and will be called shifting points A, B, and C for displacement at 7.34 mm, 8.02 mm, and 9.36 mm respectively.

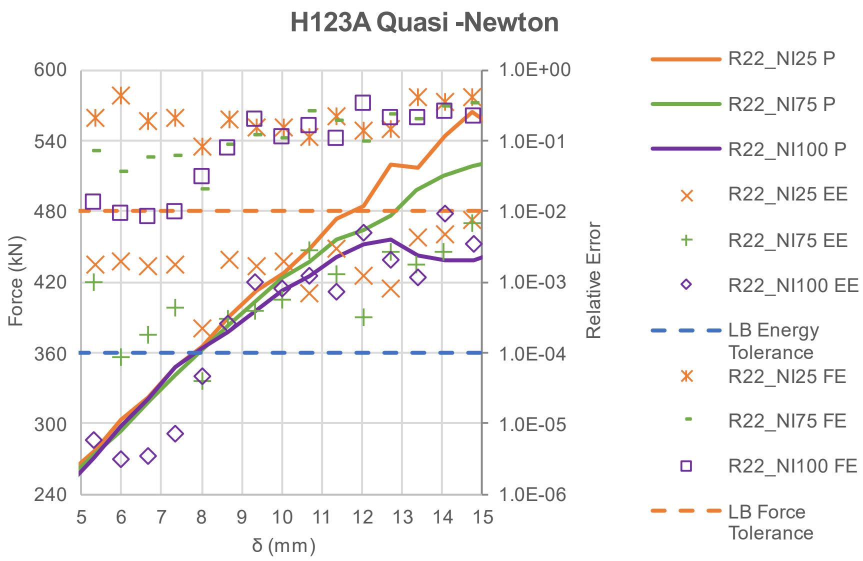

Figure 5.101 Load-displacement Curve on Critical Point 2 of Model H123A R22 NI for QN Method

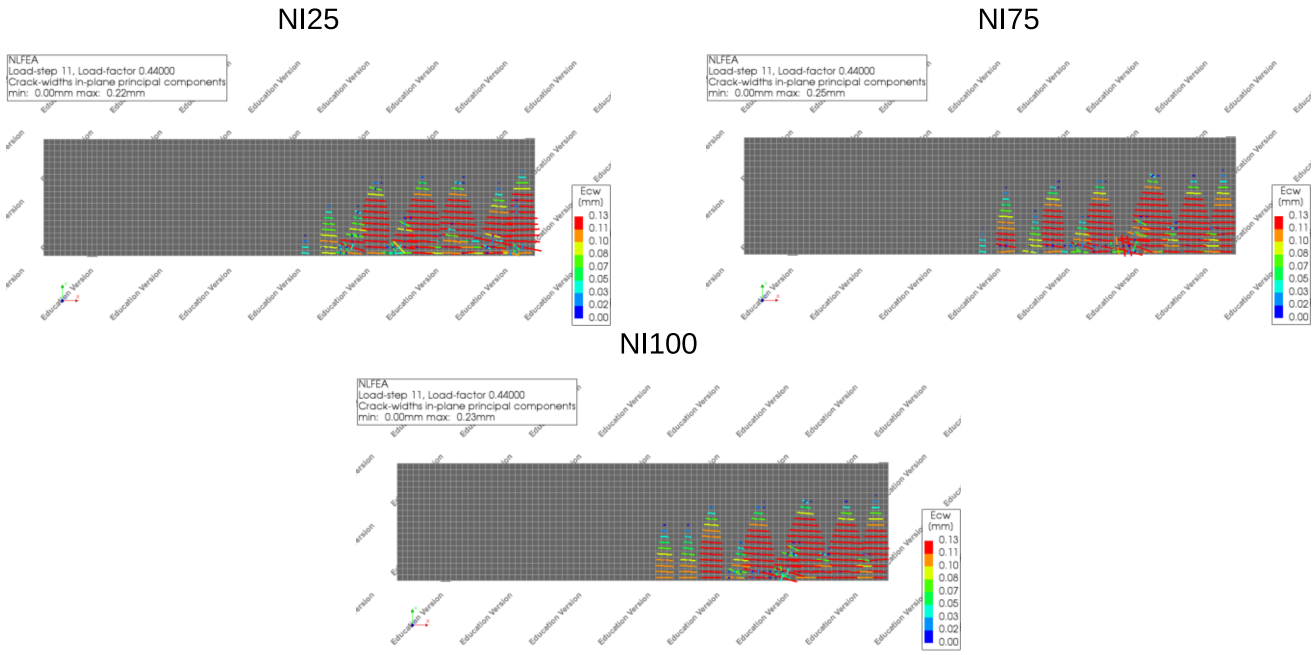

Figure 5.102 Crack Pattern Model H123A R22 for NI Variation at δ = 7.34 mm (Shifting Point A)

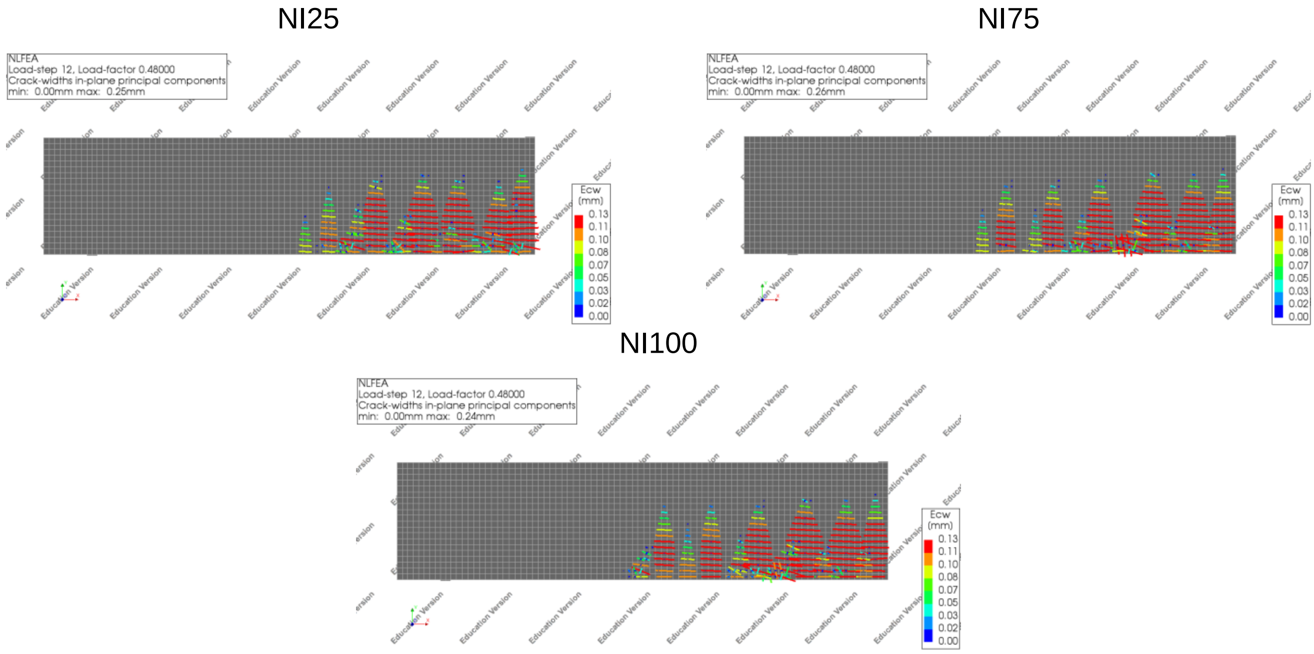

Figure 5.103 Crack Pattern Model H123A R22 for NI Variation at δ = 8.02 mm (Shifting Point B)

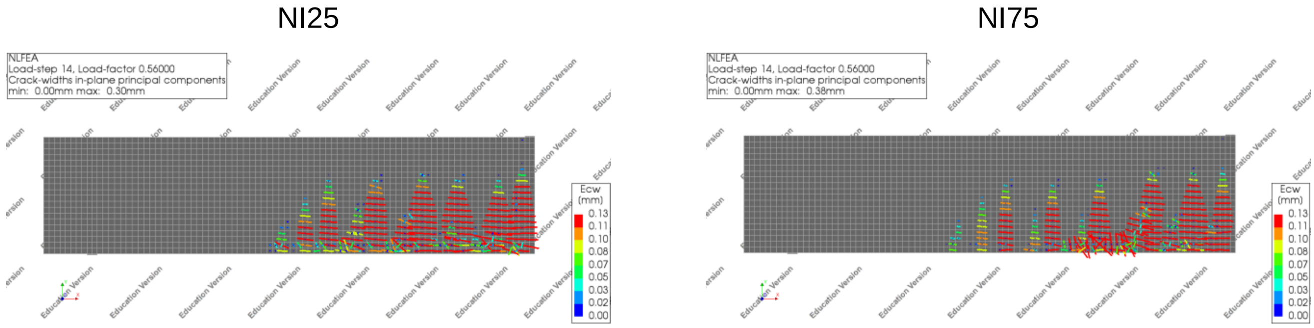

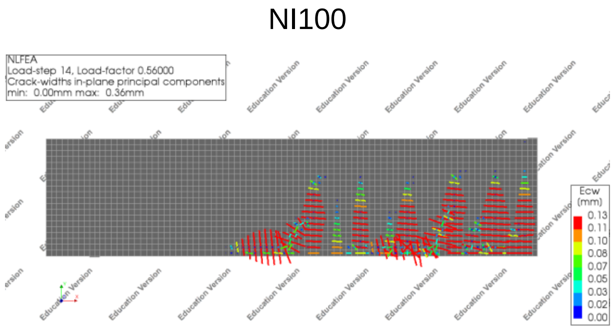

Figure 5.104 Crack Pattern Model H123A R22 for NI Variation at δ = 9.36 mm (Shifting Point C)

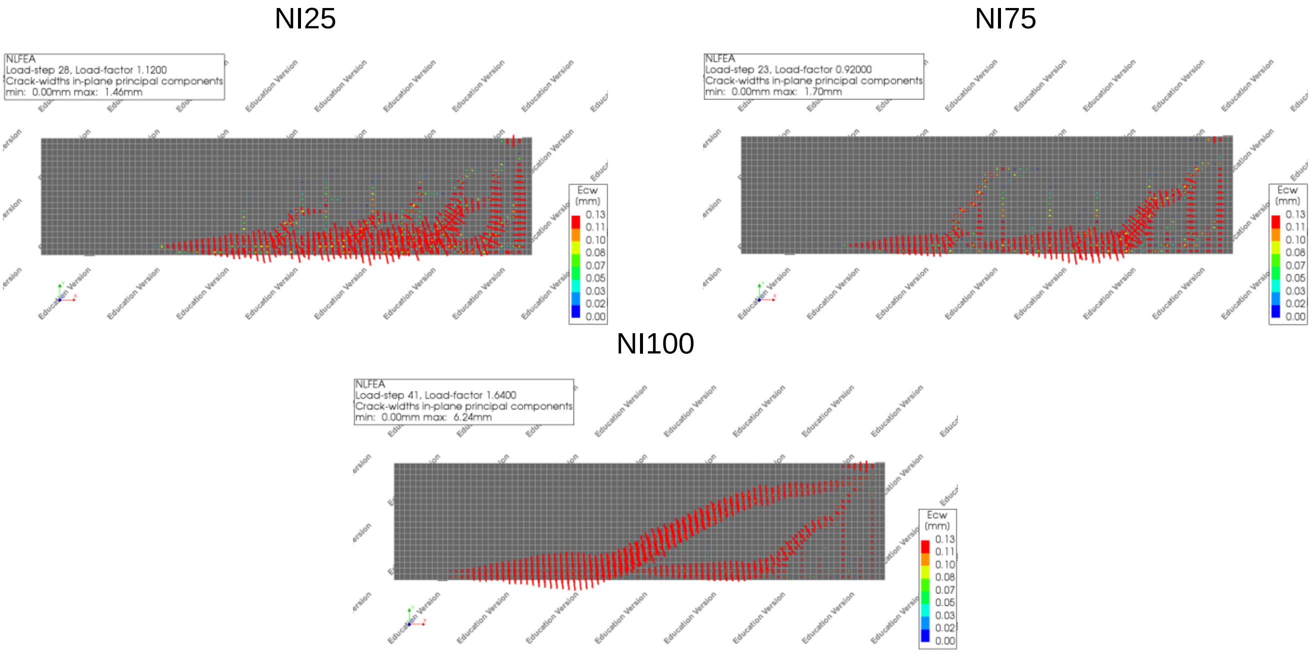

Figure 5.105 Crack Pattern Model H123A R22 for NI Variation at Peak Load

The relative energy variation and out-of-balance force in model H123A R22 NI25 and NI75 in Figure 5.101 are relatively constant through all shifting points. On the other hand, the relative energy variation and out-of-balance force are increasing from shifting point A to shifting point C in model H123A R22 NI100. In all shifting points, the relative energy variation and out-of-balance force of model H123A R22 NI25 is higher compared to model H123A R22 NI75.

In terms of crack pattern, models H123A R22 NI25, NI75 and NI100 show no significant difference in the crack pattern on shifting point A in Figure 5.102. The crack pattern starts to change for model H123A R22 NI75 and NI100 on shifting point B in Figure 5.103 where dowel crack starts to form while dowel crack has not formed in model H123A R22 NI25. On shifting point C in Figure 5.104, the type of propagating crack changes from flexural crack to dowel crack for model H123A R22 NI100, while the flexural crack propagation continues in model H123A R22 NI25 and NI75. These phenomena can be correlated to the convergence state of the models. The absence of dowel crack in model H123A R22 NI25 is related to the difference in relative energy variation and out-of-balance force where model H123A R22 NI25 is not converged while other models converged on this shifting point, resulting in a slightly different crack pattern. The domination of dowel crack can be seen on the trend of the convergence state of model H123A R22 NI100 where a significant increase in both relative energy variation and out-of-balance force signifies the change in the type of propagating crack. The difference in the relative energy variation and out-of-balance force between model H123A R22 NI25 and NI75 are also seen in the slight difference in the crack pattern, which implies that the difference in the relative energy variation and out-of-balance force is insignificant to the models. However, the formation of the dowel crack is influencing the crack pattern at the peak load in Figure 5.105 where both model H123A R22 NI25 and NI75 have an incomplete flexural shear crack while model H123A R22 NI100 has a fully formed flexural shear crack.

The next critical point 2 that is going to be observed is on model H123A R23, which is illustrated in Figure 5.106. 3 load steps are going to be observed in Figure 5.106. These load steps indicate the shift in the load-displacement curve and will be called shifting points A, B, and C for displacement at 8.51 mm, 9.02 mm, and 10.03 mm respectively.

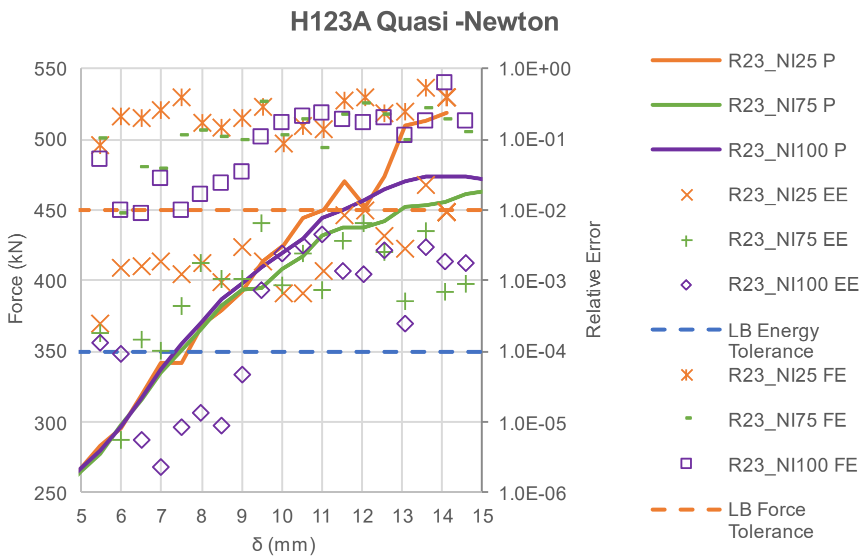

Figure 5.106 Load-displacement Curve on Critical Point 2 of Model H123A R23 NI for QN Method

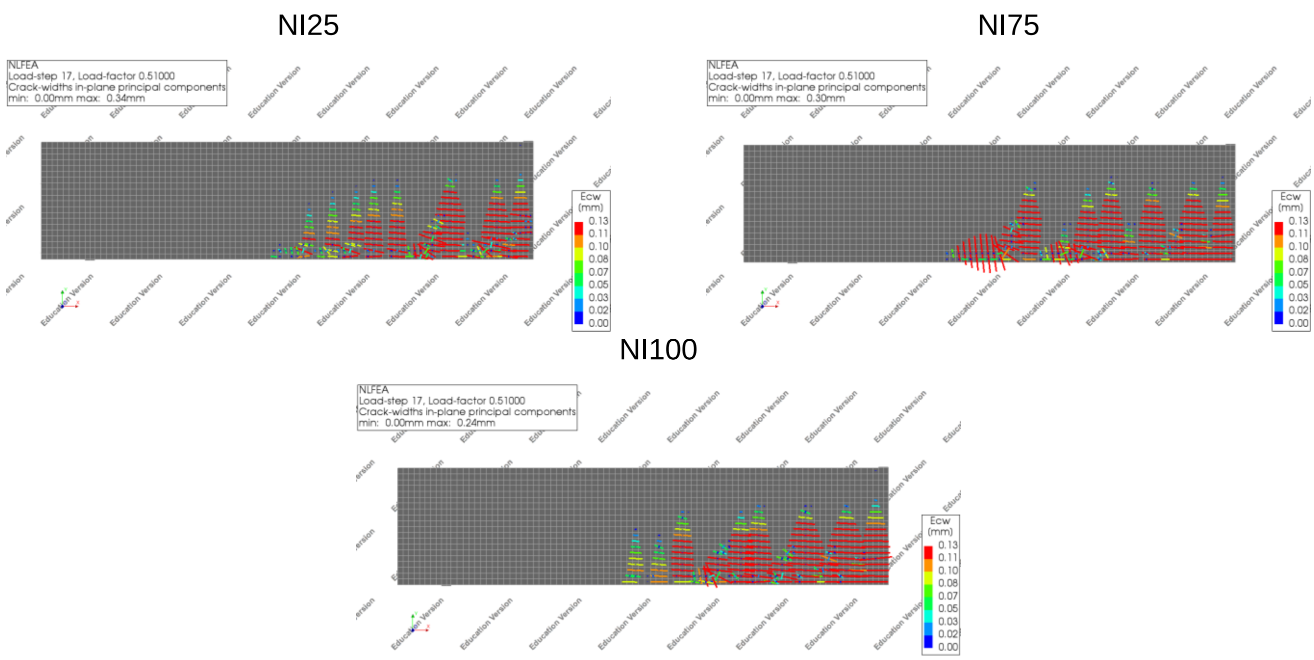

Figure 5.107 Crack Pattern Model H123A R23 for NI Variation at δ = 8.51 mm (Shifting Point A)

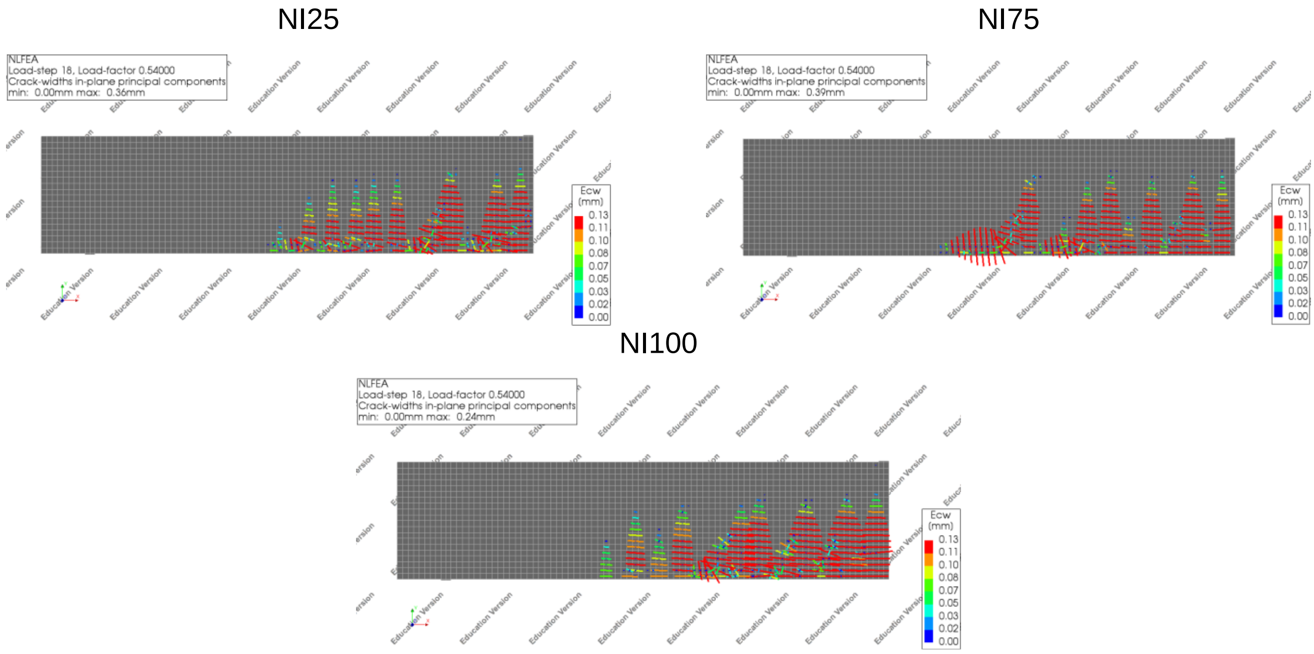

Figure 5.108 Crack Pattern Model H123A R23 for NI Variation at δ = 9.02 mm (Shifting Point B)

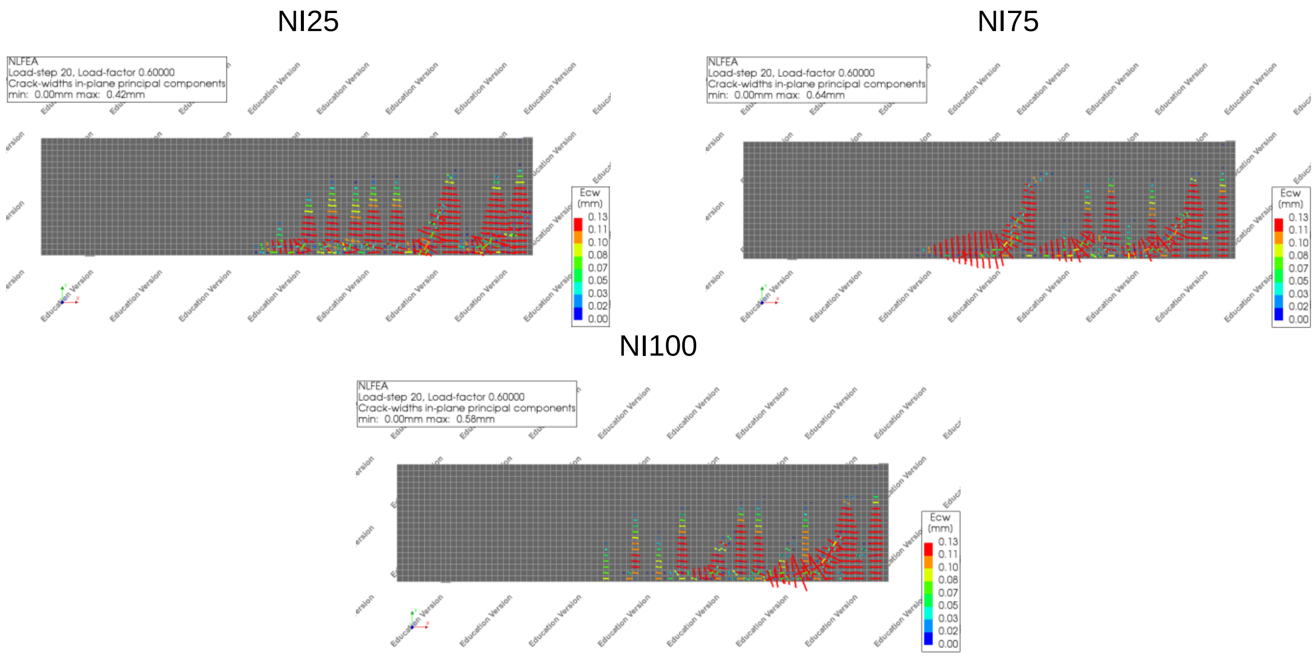

Figure 5.109 Crack Pattern Model H123A R23 for NI Variation at δ = 10.03 mm (Shifting Point C)

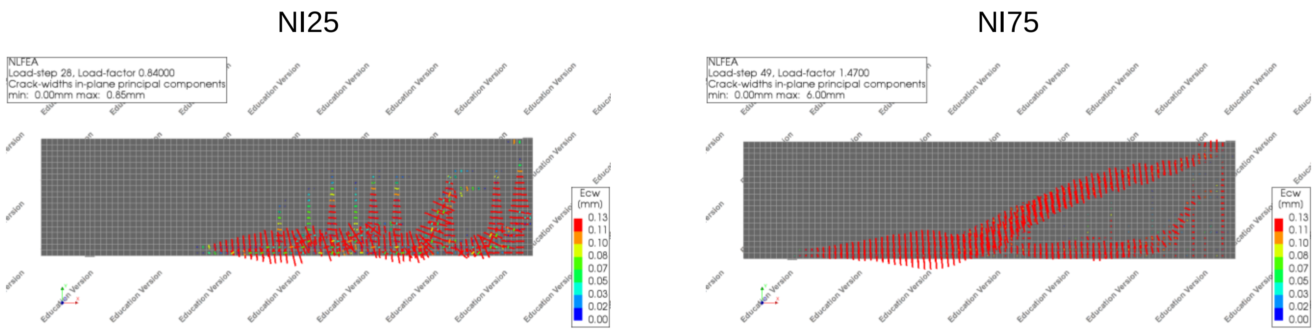

NI100

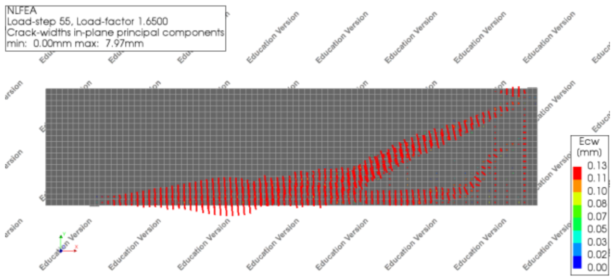

Figure 5.110 Crack Pattern Model H123A R23 for NI Variation at Peak Load

The relative energy variation and out-of-balance force in model H123A R23 NI25 and NI75 in Figure 5.106 are relatively constant through all shifting points. On the other hand, the relative energy variation and out-of-balance force are increasing from shifting point A to shifting point C in model H123A R22 NI100. A slight difference in the relative energy variation and out-of-balance force between model H123A R22 NI25 and NI75 can only be observed in shifting point B.

In terms of crack pattern, models H123A R23 NI25 and N100 show a similar crack pattern, several single flexural cracks with small dowel crack on shifting point A in Figure 5.107. On the other hand, model H123A R23 NI75 shows a slightly different crack pattern where several single flexural cracks with major dowel cracks can be observed in shifting point A in Figure 5.107. In shifting point B, the type of propagating crack starts to change in model H123A R23 NI100 where dowel crack becomes more dominant, which is similar to the crack propagation process in model H123A R23 NI75 in Figure 5.108. In shifting point C, the rate of dowel crack propagation in model H123A R23 NI75 is higher compared to model H123A R23 NI100, which can be known by observing the crack pattern and the maximum crack width in Figure 5.109. On the other hand, the dowel crack in model H123A R23 NI25 has not become the dominant crack propagation in shifting points B and C. This phenomenon can be correlated to the convergence state of the models. The increase of both relative energy variation and out-of-balance force indirectly implied the change in the type of propagating crack in model H123A R23 NI75, which is also found in the observation of Figure 5.101 for model H123A R22 NI25, NI75 and NI100. The change in the type of propagating crack in model H123A R23 NI100 is not as major as model H123A R23 NI75, resulted in the constant trend of both relative energy variation and out-of-balance force. However, the different types of propagating crack between model H123A R23 NI100 and NI25 can be noticed in the relative energy variation and out-of-balance force at shifting point B, where the relative energy variation and out-of-balance force is lower in model H123A R23 NI100 compared to model H123A R23 NI25. It can be said that a certain level of relative energy variation and out-of-balance force could affect the crack pattern, where in this case is influencing the type of propagating crack. The change in the type of propagating crack in the model is influencing the crack pattern at the peak load in Figure 5.110 where model H123A R23 NI25 has an incomplete flexural shear crack while both model H123A R23 NI75 and NI100 have fully formed flexural shear crack.

Based on the observation for both specimen A123A1 and H123A, it can be concluded that the variation on the peak load of models with the Quasi-Newton method and different maximum number of iterations is caused by the change in both relative energy variation and out-of-balance force. If the change in both relative energy variation and out-of-balance force reached a certain magnitude, then it would influence the type of propagating crack that would be affecting the crack pattern at the peak load and the magnitude of the peak load. However, the current data is not enough to define the boundary of the relative energy variation and out-of-balance force to prevent the change in the dominating type of propagating crack in the model. The influence of the maximum number of iterations is size-dependent as this phenomenon mainly observed in the numerical model for specimen H123A. The influence of the maximum number of iterations in the numerical model for specimen A123A can be eliminated by prescribing a minimum value of 50 for the maximum number of iterations.

5.5.2 Effect of Maximum Number of Iterations Variation in Full Newton-Raphson Method

The second observation is done for numerical models with the Full Newton-Raphson method. The change in peak load distribution due to different maximum numbers of iterations can be observed in Figure 5.111 for specimens A123A1 and H123A.

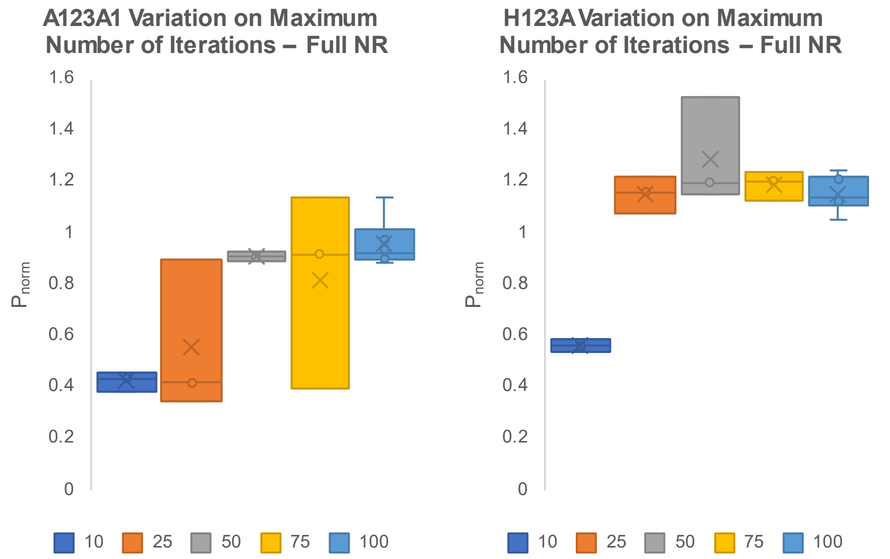

Figure 5.111 Peak Load Distribution for Full NR Method with Different Maximum Number of Iterations

The peak load distribution for both specimens is significantly influenced by the variation of the maximum number of iterations. A significant change in peak load distribution can be seen in Figure 5.111 for specimen A123A1 starting from 100 iterations to 75 iterations and for H123A starting from 75 iterations to 50 iterations. No trend can be observed in the results of both specimens.

The simulated global behaviour of the beam with the Full Newton-Raphson method is observed based on the results of NLFEA which has lower relative energy variation and relative out-of-balance force than the defined upper bound for both energy and force tolerance in subchapter 5.3.2 Effect of Load Increment Variation in Full Newton-Raphson Method. The observation of the simulated global behaviour of the beam will be done separately for different specimens. Figure 5.112 gives an illustration of the simulated global behaviour of the beam with the Full Newton-Raphson method based on the load-displacement curve for specimen A123A1.

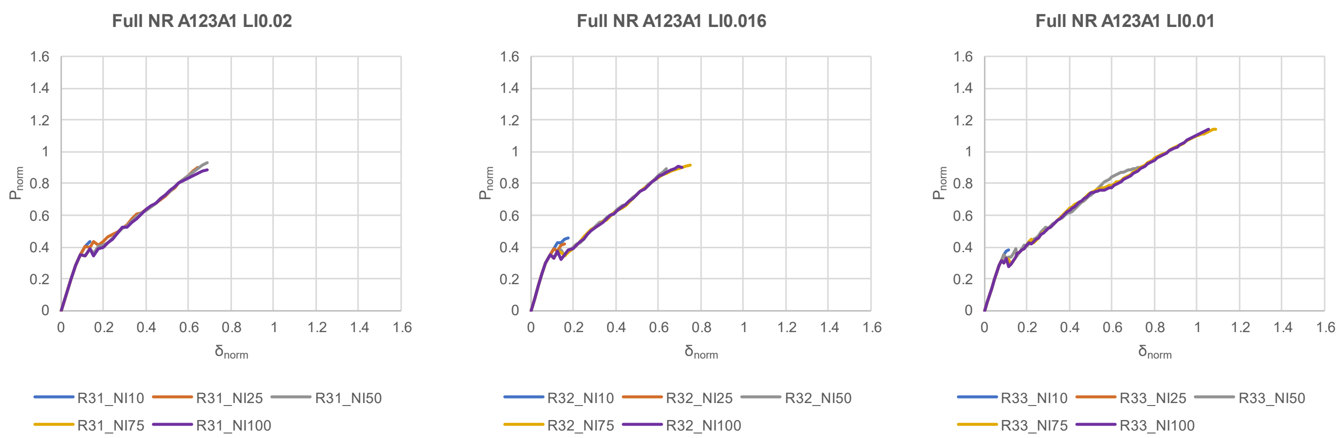

Figure 5.112 Load-displacement Curve for Maximum Iterations Variance – A123A1 Full NR Method

Based on Figure 5.112, it can be said that the load-displacement curve for all variations of the maximum number of iterations for specimen A123A1 is independent of the prescribed maximum number of iterations. The difference in the peak load estimation is caused by the pre-defined upper bound error tolerance. However, there are two phenomena that can be observed in Figure 5.112. The first phenomenon is non-linear behaviour cannot be simulated properly with a small maximum number of iterations. This can be seen in model A123A1 R31 NI10, R31 NI75, R32 NI10, R32 NI25, R33 NI10, and R33 NI25 where one of the convergence norms has exceeded its upper bound tolerance at the first cracking occurrence. This phenomenon enlarges the peak load distribution, which can be seen in Figure 5.111. The second phenomenon is the first cracking occurrence does not influence the simulated non-linear behaviour of the model, which can be seen in Figure 5.112 where no significant deviation can be seen in the load-displacement curve. Overall, the effect of variation on the maximum number of iterations is insignificant to the simulated global behaviour of specimen A123A1.

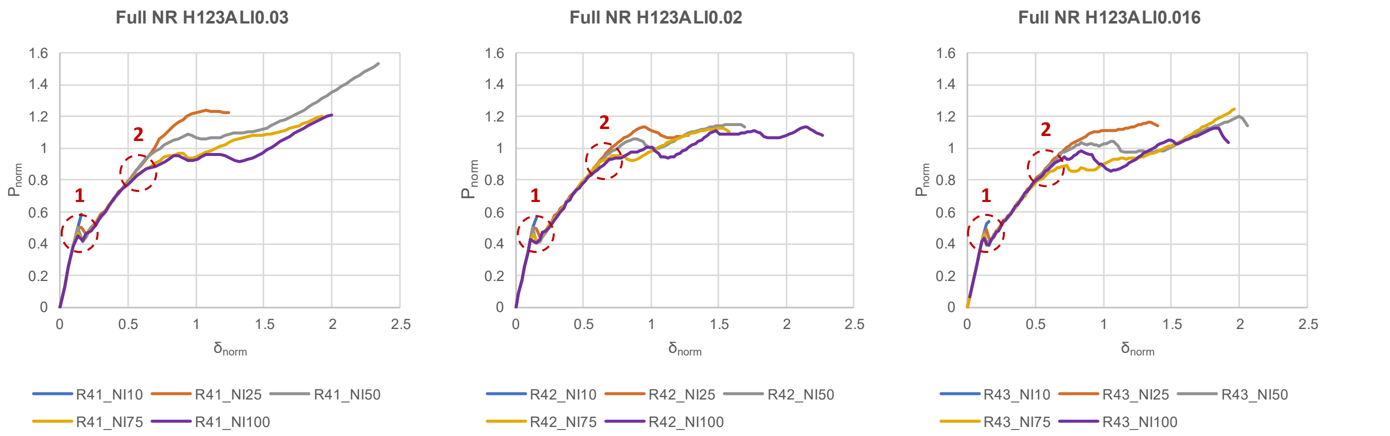

Figure 5.113 Load-displacement Curve for Maximum Iterations Variance – H123A Full NR Method

Figure 5.113 gives an illustration of the simulated global behaviour of the beam with the Full Newton-Raphson method based on the load-displacement curve for specimen H123A. Based on Figure 5.113, it can be said that the load-displacement curve for all variations of the maximum number of iterations is dependent on the prescribed maximum number of iterations. In the load-displacement curve in Figure 5.113, there are 2 critical points that show some deviation due to change in the maximum number of iterations. The first critical point is considered not important because the deviation in critical point 1 does not affect the overall simulated behaviour of the beam in the non-linear region. This can be seen by observing the load-displacement curve between critical point 1 and critical point 2, where the simulated non-linear behaviour is similar for all models with specimen H123A. On critical point 2, a significant deviation can be seen between the results of models H123A R41 and R43. The deviation on the curve is considered significant due to its effect on the simulated non-linear behaviour and the peak load of the model. Two sets of models, NI25 and NI100, are chosen as the representative of all results of model H123A R41 and R43 respectively. The load-displacement curve for these models is given in Figure 5.114.

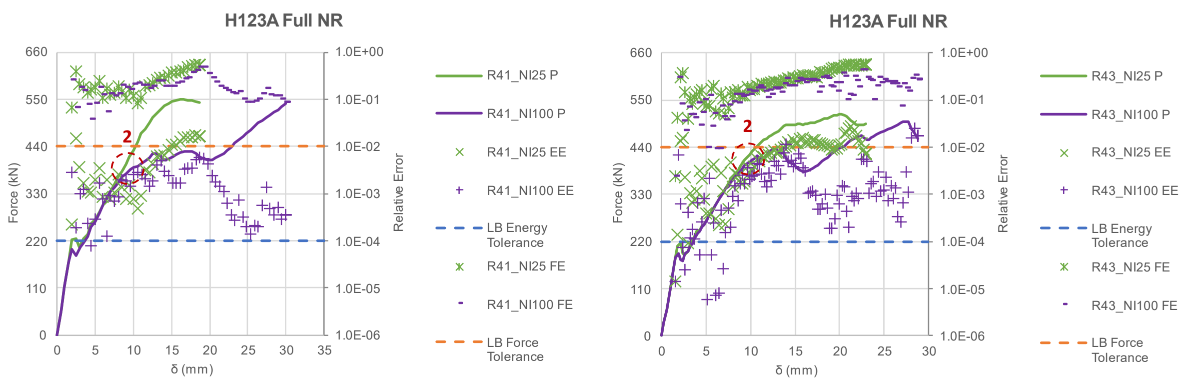

Figure 5.114 Load-displacement Curve Model H123A NI with the Convergence State for Full NR Method

Based on Figure 5.114, most of the steps are converging in the relative energy variation. Furthermore, higher relative energy variation and out-of-balance force can be seen by comparing convergence state at δ = 10-20 mm to δ = 5-10 mm for model H123A R41 and δ = 10-30 mm to δ = 5-10 mm for model H123A R43, where the curve is near its peak.

To observe the simulated global behaviour on critical point 2, a detailed illustration for critical point 2 is made for Figure 5.114. The first critical point 2 that is going to be observed is on model H123A R41, which is illustrated in Figure 5.115. 3 load steps are going to be observed in Figure 5.115. These load steps indicate the shift in the load-displacement curve and will be called shifting points A, B, and C for displacement at 6.49 mm, 7.00 mm, and 7.50 mm respectively.

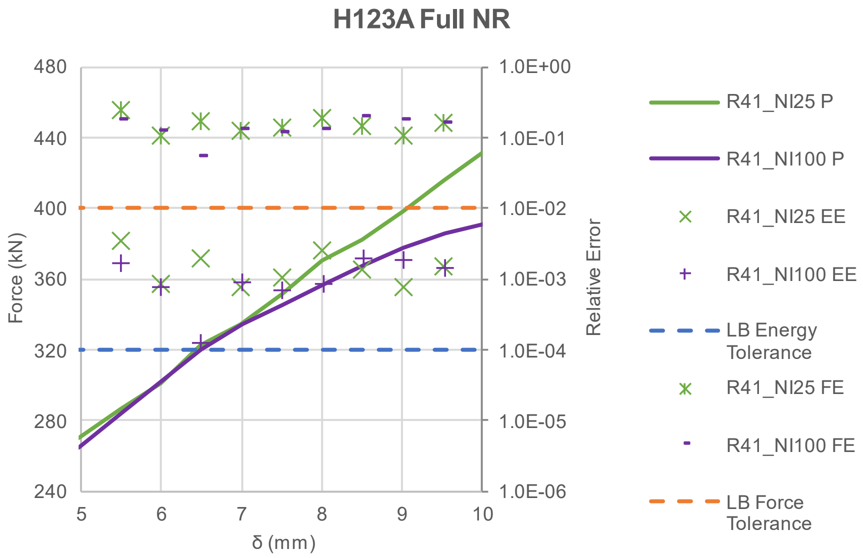

Figure 5.115 Load-displacement Curve on Critical Point 2 of Model H123A R41 NI for Full NR Method

NI25 NI100

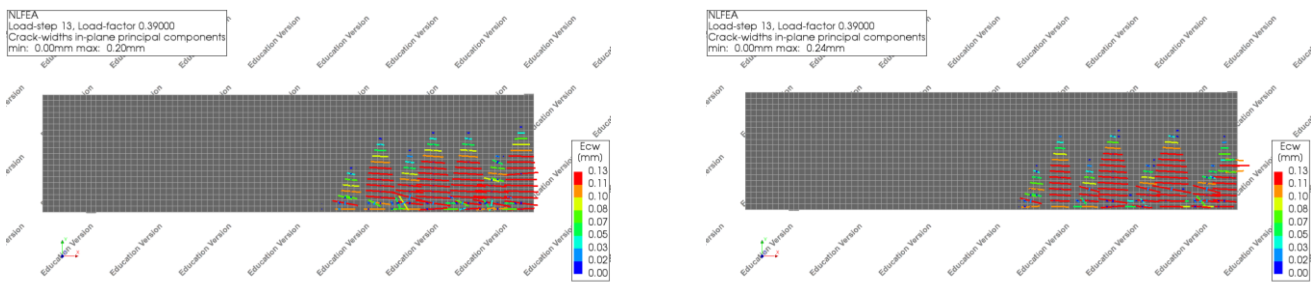

Figure 5.116 Crack Pattern Model H123A R41 for NI Variation at δ = 6.49 mm (Shifting Point A)

NI25 NI100

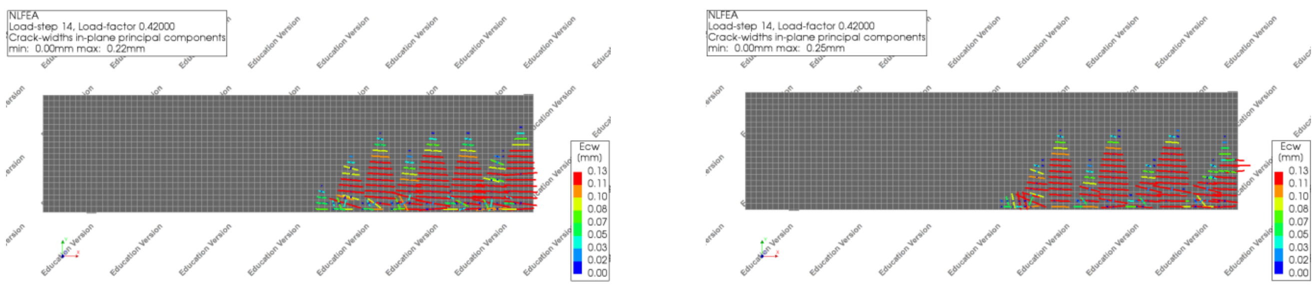

Figure 5.117 Crack Pattern Model H123A R41 for NI Variation at δ = 7.00 mm (Shifting Point B)

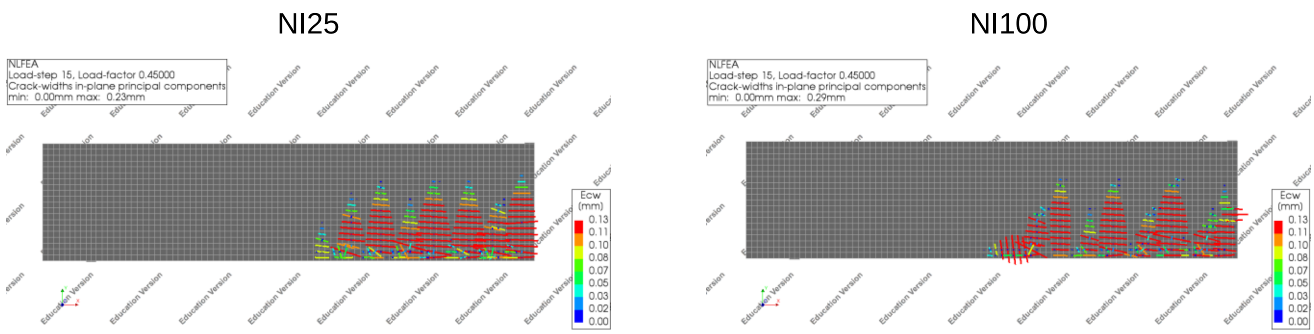

Figure 5.118 Crack Pattern Model H123A R41 for NI Variation at δ = 7.50 mm (Shifting Point C)

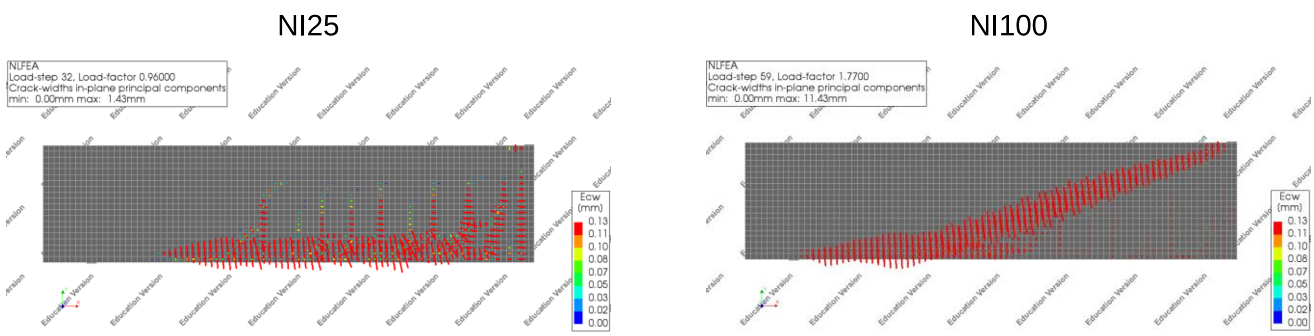

Figure 5.119 Crack Pattern Model H123A R41 for NI Variation at Peak Load

The relative energy variation and out-of-balance force in model H123A R41 NI25 in Figure 5.115 is relatively constant through all shifting points. On the other hand, the relative energy variation and out-of-balance force in model H123A R41 NI100 are increasing through all shifting points. A significant difference in relative energy variation and out-of-balance force can be seen in shifting point A and a slight difference in shifting point C.

In terms of crack pattern, model H123A R41 NI25 and NI100 have a similar crack pattern in shifting points A and B, as indicated in Figure 5.116 and Figure 5.117. The only noticeable difference in shifting point B is the formation of the dowel crack in model H123A R41 NI100. In shifting point C, the dowel crack propagation is becoming more dominant in model H123A R41 NI100, while model H123A R41 NI25 has not formed any dowel crack, which can be seen in Figure 5.118. This phenomenon can be observed in the trend of the convergence state of the model, where the increasing trend of both relative energy variation and out-of-balance force resulted in the formation of dowel crack while the constant trend means the flexural crack is still propagating. This phenomenon is also affecting the crack pattern at the peak load in Figure 5.119 where model H123A R41 NI25 has an incomplete flexural shear crack while model H123A R41 NI100 has a fully formed flexural shear crack.

The next critical point 2 that is going to be observed is on model H123A R43, which is illustrated in Figure 5.120. 3 load steps are going to be observed in Figure 5.120. These load steps indicate the shift in the load-displacement curve and will be called shifting points A, B, C, and D for displacement at 6.65 mm, 7.19 mm, 7.73 mm, and 9.08 mm respectively.

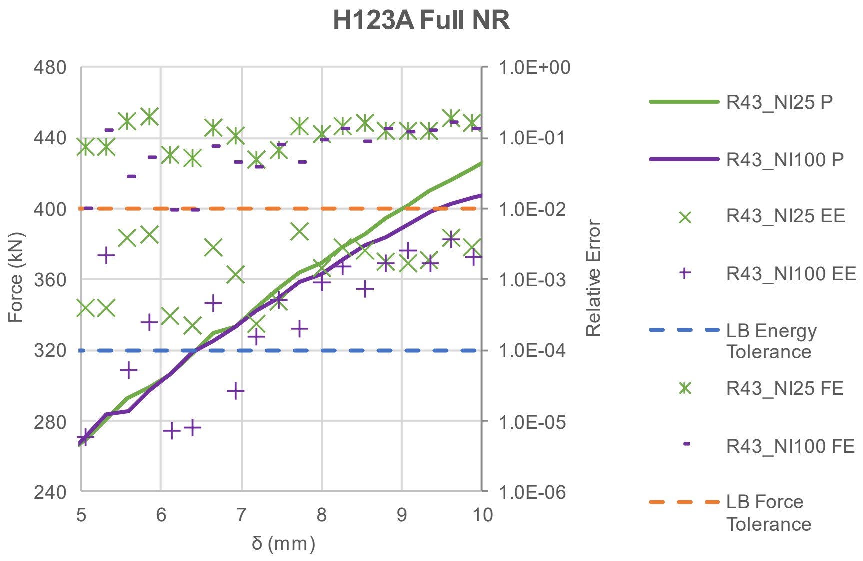

Figure 5.120 Load-displacement Curve on Critical Point 2 of Model H123A R43 NI for Full NR Method

NI25 NI100

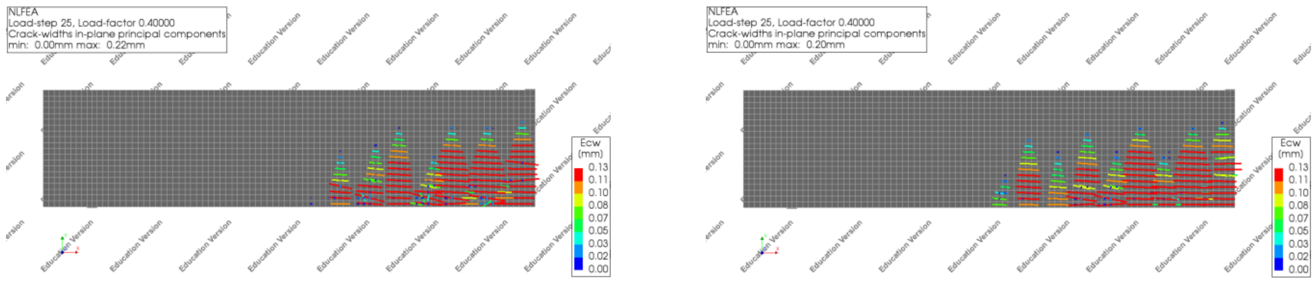

Figure 5.121 Crack Pattern Model H123A R43 for NI Variation at δ = 6.65 mm (Shifting Point A)

NI25 NI100

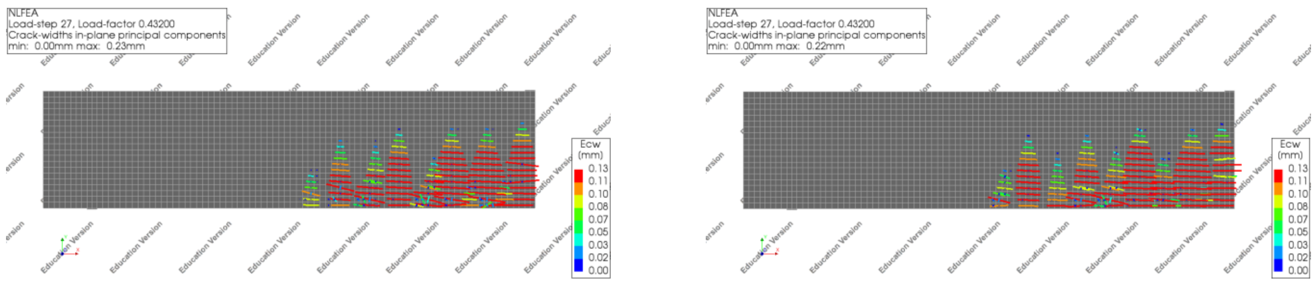

Figure 5.122 Crack Pattern Model H123A R43 for NI Variation at δ = 7.19 mm (Shifting Point B)

NI25 NI100

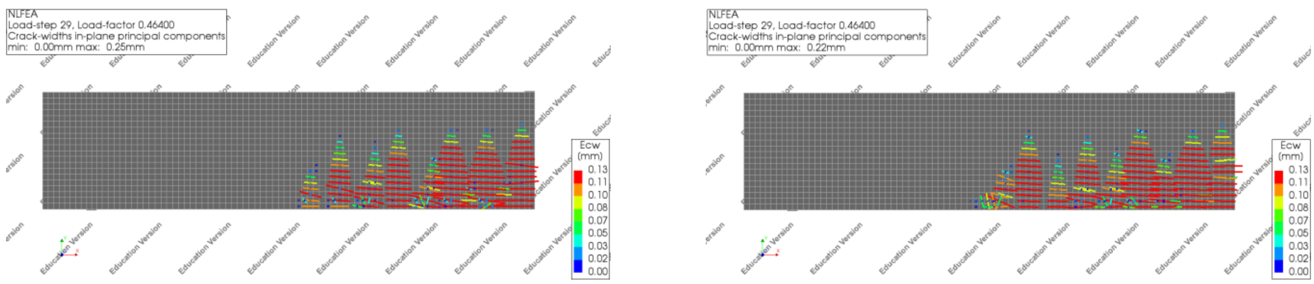

Figure 5.123 Crack Pattern Model H123A R43 for NI Variation at δ = 7.73 mm (Shifting Point C)

NI25 NI100

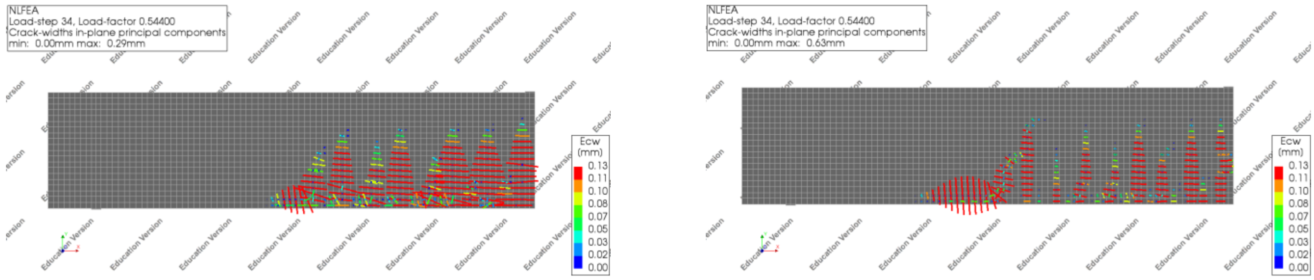

Figure 5.124 Crack Pattern Model H123A R43 for NI Variation at δ = 9.08 mm (Shifting Point D)

NI25 NI100

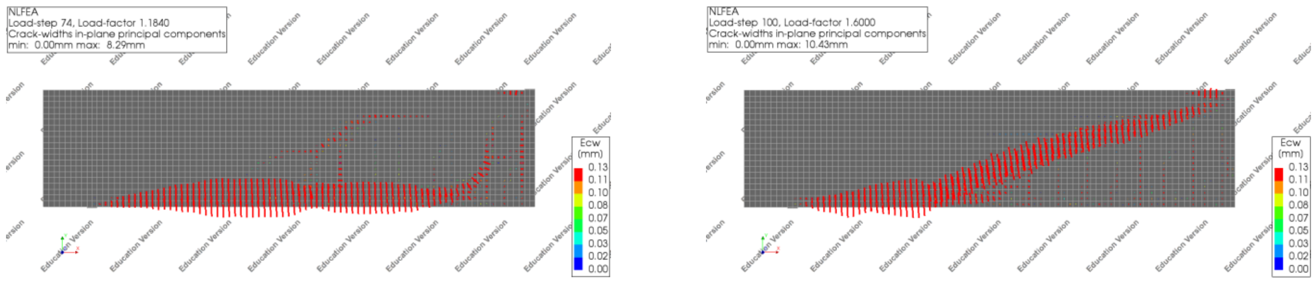

Figure 5.125 Crack Pattern Model H123A R43 for NI Variation at Peak Load

The relative energy variation and out-of-balance force in model H123A R43 NI25 in Figure 5.120 is significantly changing through all shifting points where no trend can be observed. On the other hand, the relative energy variation and out-of-balance force in model H123A R43 NI100 are relatively constant from shifting point A to shifting point C and then followed by an increase from shifting point C to D.

In terms of crack pattern, model H123A R43 NI25 and NI100 have a similar crack pattern at shifting points A and B in Figure 5.121 and Figure 5.122 respectively. Model H123A R43 NI100 starts to develop dowel crack at shifting point C in Figure 5.123 and the dowel crack propagation is becoming more dominant in shifting point D in Figure 5.124. However, the dowel crack has not developed in shifting point C in Figure 5.123 for model H123A R43 NI25 and just starts to propagate in shifting point D in Figure 5.124. This phenomenon can be correlated to the convergence state of the model, where the increase in the relative energy variation and out-of-balance force resulted in the formation of dowel crack in model H123A R43 NI100. This correlation can be validated by observing the convergence behaviour in model H123A R43 NI25 where no trend can be observed in all shifting points because there is no formation of the dowel crack yet. Furthermore, the formation of the dowel crack also causes an increase in the relative energy variation and out-of-balance force in model H123A R43 NI25 after shifting point D, which can be observed in Figure 5.115. The formation of dowel crack affected the crack pattern at the peak load in Figure 5.125 where model H123A R23 NI25 has an incomplete flexural shear crack formation due to late dowel crack propagation, while model H123A R23 NI100 has a fully formed flexural shear crack.

Based on the observation for both specimen A123A1 and H123A, it can be concluded that the variation on the peak load of models with the Full Newton-Raphson method and different maximum number of iterations is caused by different load level that initiates the formation of dowel crack on the models. Different dowel crack initiation is caused by a different moment of trend changing in the convergence state, where a certain level of increment on the relative energy variation and out-of-balance force resulted in the formation of the dowel crack. This directly affected the crack formation process on the model, and as a result affecting the crack formation at the peak load. However, this effect is size-dependent as this can only be observed in the numerical model for specimen H123A.

5.5.3 Effect of Maximum Number of Iterations Variation in Modified Newton-Raphson Method

The last observation is done for numerical models with the Modified Newton-Raphson method. The change in peak load distribution due to different maximum numbers of iterations can be observed in Figure 5.126 for specimens A123A1 and H123A.

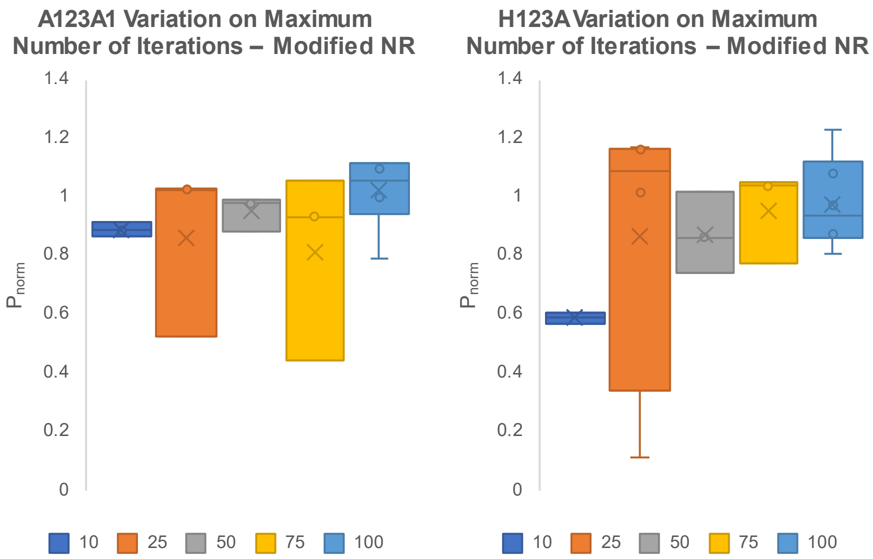

Figure 5.126 Peak Load Distribution for Modified NR Method with Different Maximum Number of Iterations

The peak load distribution for both specimens is significantly influenced by the variation of the maximum number of iterations. A significant change in peak load distribution can be seen in Figure 5.111 for specimen A123A1 starting from 100 iterations to 75 iterations and for H123A starting from 50 iterations to 25 iterations. No trend can be observed in the results of both specimens.

The simulated global behaviour of the beam with the Modified Newton-Raphson method is observed based on the results of NLFEA which has lower relative energy variation and relative out-of-balance force than the defined upper bound for both energy and force tolerance in subchapter 5.3.3 Effect of Load Increment Variation in Modified Newton-Raphson Method. The observation of the simulated global behaviour of the beam will be done separately for different specimens. Figure 5.127 gives an illustration of the simulated global behaviour of the beam with the Modified Newton-Raphson method based on the load-displacement curve for specimen A123A1.

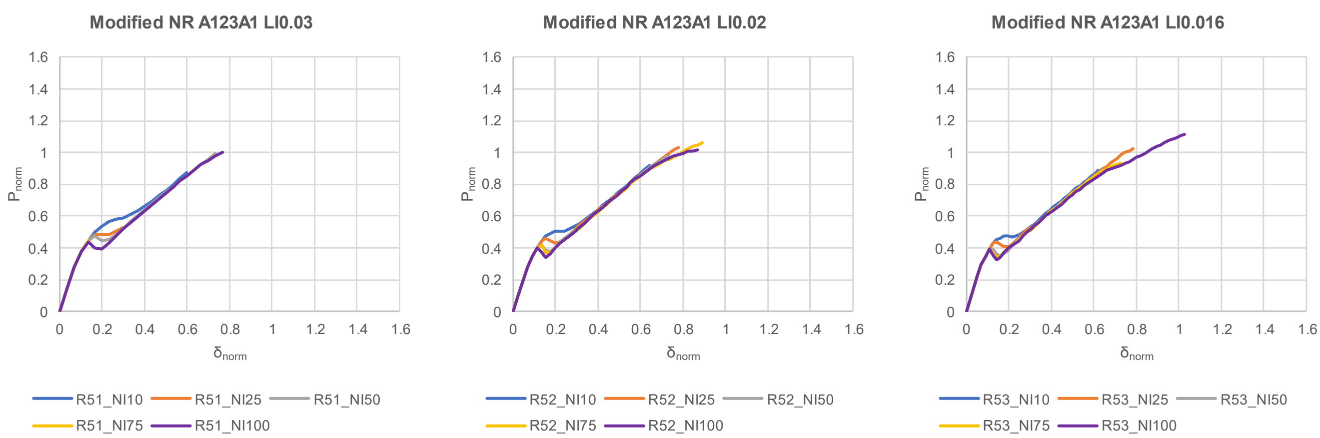

Figure 5.127 Load-displacement Curve for Maximum Iterations Variance – A123A1 Modified NR Method

Based on Figure 5.127, it can be said that the load-displacement curve for all variations of the maximum number of iterations for specimen A123A1 is independent of the prescribed maximum number of iterations. The difference in the peak load estimation is caused by the pre-defined upper bound error tolerance. However, there is a phenomenon that can be observed in Figure 5.127. It can be said that the first cracking occurrence does not influence the simulated non-linear behaviour of the model, which can be seen in Figure 5.127 where no significant deviation can be seen in the load-displacement curve. Overall, the effect of variation on the maximum number of iterations is insignificant to the simulated global behaviour of specimen A123A1.

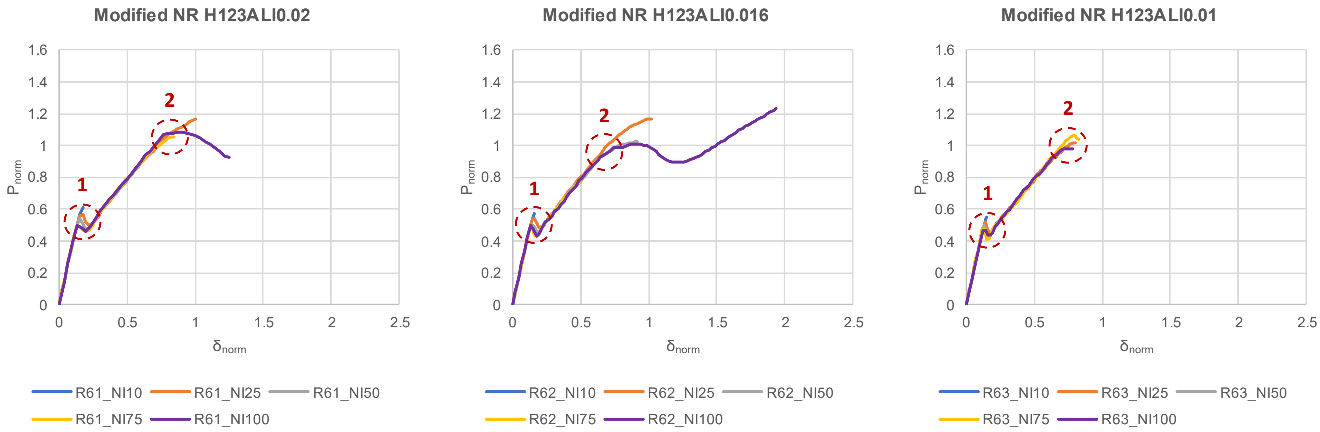

Figure 5.128 Load-displacement Curve for Maximum Iterations Variance – H123A Modified NR Method

Figure 5.128 gives an illustration of the simulated global behaviour of the beam with the Modified Newton-Raphson method based on the load-displacement curve for specimen H123A. Based on Figure 5.128, it can be said that the load-displacement curve for all variations of the maximum number of iterations is dependent on the prescribed maximum number of iterations. The first observation that can be derived from Figure 5.128 is non-linear behaviour cannot be simulated properly with a small maximum number of iterations. This can be seen in models H123A R61 NI10, R62 NI10, and R63 NI10 where one of the convergence norms has exceeded its upper bound tolerance at the first cracking occurrence. Another observation can be done based on the defined critical points in Figure 5.128. There are 2 critical points that show some deviation due to changes in the maximum number of iterations. The first critical point is considered not important because the deviation in critical point 1 does not affect the overall simulated behaviour of the beam in the non-linear region. This can be seen by observing the load-displacement curve between critical point 1 and critical point 2, where the simulated non-linear behaviour is similar for all models with specimen H123A. On critical point 2, a significant deviation can be seen between the results of model H123A R61 and R62. The deviation on the curve is considered significant due to its effect on the simulated non-linear behaviour and the peak load of the model. Two sets of models, NI25 and NI100, are chosen as the representative of all results of model H123A R61 and R62. The load-displacement curve for these models is given in Figure 5.129.

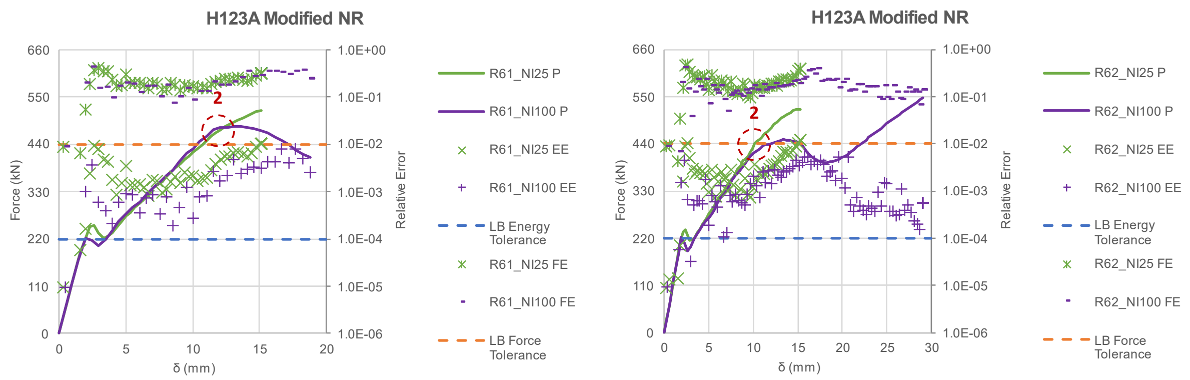

Figure 5.129 Load-displacement Curve Model H123A NI with the Convergence State for Modified NR Method

Based on Figure 5.129, most of the steps are not converging in any convergence norms. Furthermore, higher relative energy variation and out-of-balance force can be seen by comparing convergence state at δ = 10-20 mm to δ = 5-10 mm for model H123A R61, δ = 10-15 mm to δ = 5-10 mm for model H123A R62 NI25, and δ = 10-30 mm to δ = 5-10 mm for model H123A R62 NI100, where the curve is near its peak.

In order to observe the simulated global behaviour on critical point 2, a detailed illustration for critical point 2 is made for Figure 5.129. The first critical point 2 that is going to be observed is on model H123A R61, which is illustrated in Figure 5.130. 3 load steps are going to be observed in Figure 5.130. These load steps indicate the shift in the load-displacement curve and will be called shifting points A, B, and C for displacement at 12.06 mm, 12.40 mm, and 13.07 mm respectively.

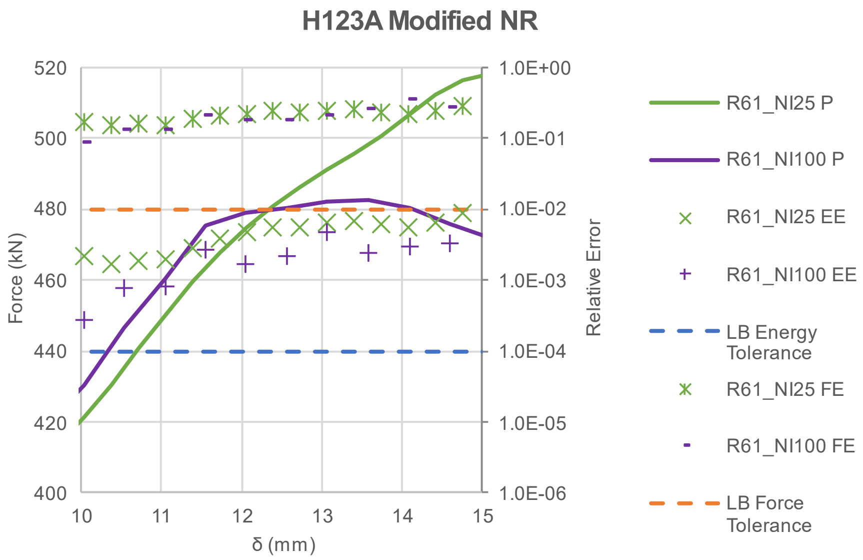

Figure 5.130 Load-displacement Curve on Critical Point 2 of Model H123A R61 NI for Modified NR Method

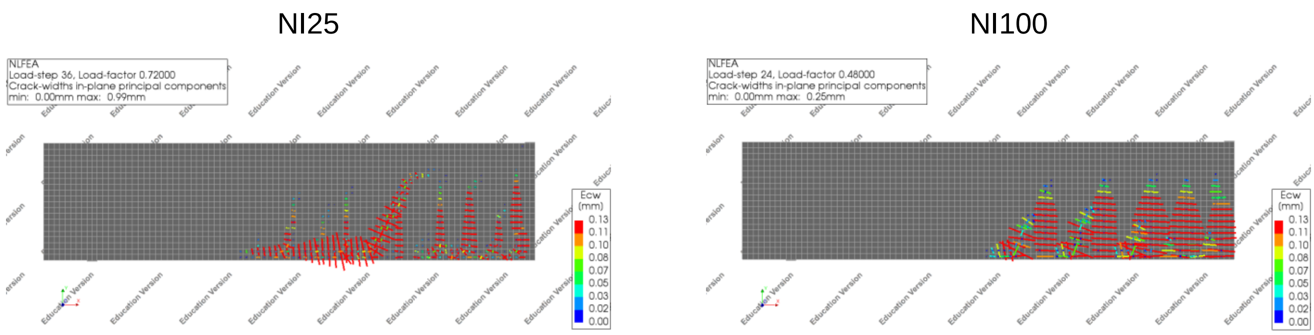

Figure 5.131 Crack Pattern Model H123A R61 for NI Variation at δ = 12.06 mm (Shifting Point A)

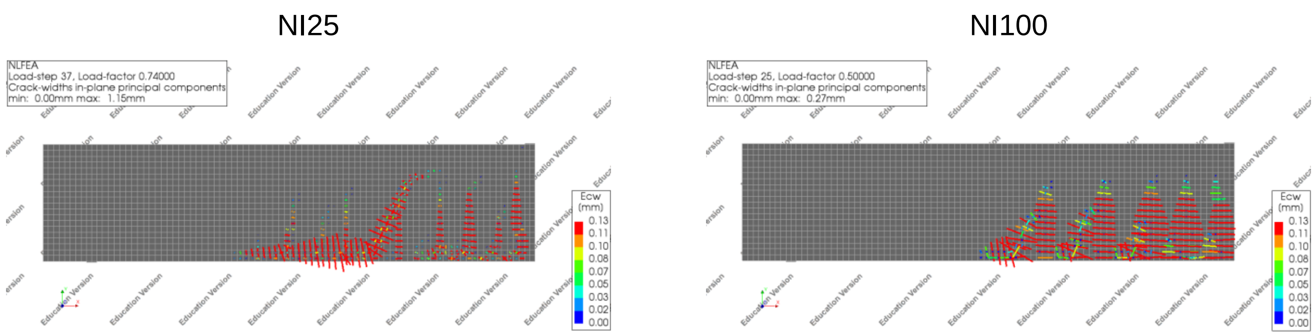

Figure 5.132 Crack Pattern Model H123A R61 for NI Variation at δ = 12.40 mm (Shifting Point B)

NI25 NI100

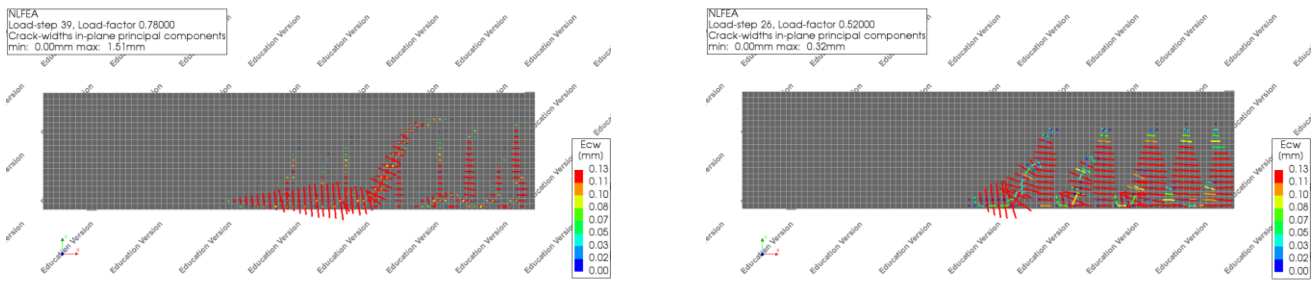

Figure 5.133 Crack Pattern Model H123A R61 for NI Variation at δ = 13.07 mm (Shifting Point C)

NI25 NI100

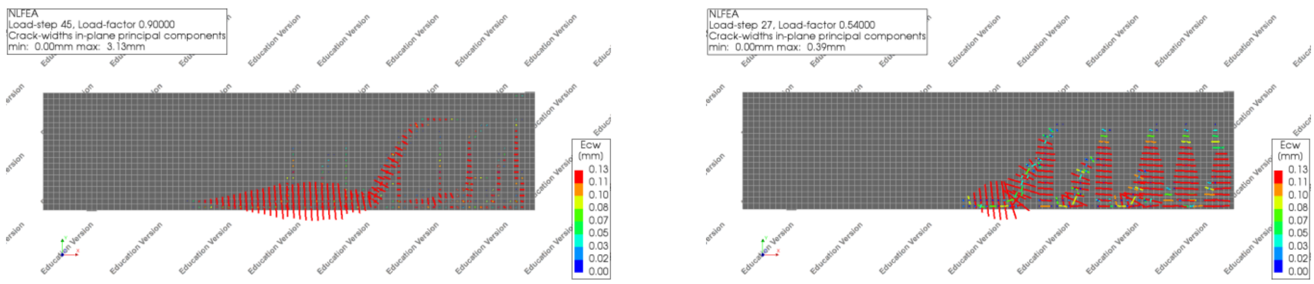

Figure 5.134 Crack Pattern Model H123A R61 for NI Variation at Peak Load

The relative energy variation and out-of-balance force in model H123A R61 NI25 and NI100 in Figure 5.130 is slightly increasing through all shifting points. The relative energy variation of model H123A R61 NI25 is slightly higher compared to model H123A R61 NI100.

In terms of crack pattern, model H123A R61 NI25 has a different crack pattern compared to model H123A R61 NI100 where the dowel crack has dominated the crack propagation and the inclined crack has been formed in model H123A R61 NI25, while model H123A R61 NI100 is still developing the flexural cracks and the dowel crack has just formed. This difference can be seen in all shifting points in Figure 5.131, Figure 5.132, and Figure 5.133. Furthermore, a significant difference can also be seen in the maximum crack width in all shifting points. These differences influenced the crack pattern at the peak load significantly in Figure 5.134 where model H123A NI25 developed an almost fully formed flexural shear crack while model H123A NI100 developed flexural cracks in combination with small dowel crack. These phenomena cannot be seen in the convergence state of the model where both models have similar trends and similar magnitude of relative energy variation and out-of-balance force.

The next critical point 2 that is going to be observed is on model H123A R62, which is illustrated in Figure 5.135. 3 load steps are going to be observed in Figure 5.135. These load steps indicate the shift in the load-displacement curve and will be called shifting points A, B, C, and D for displacement at 7.20 mm, 8.01 mm, 10.16 mm, and 10.98 mm respectively.

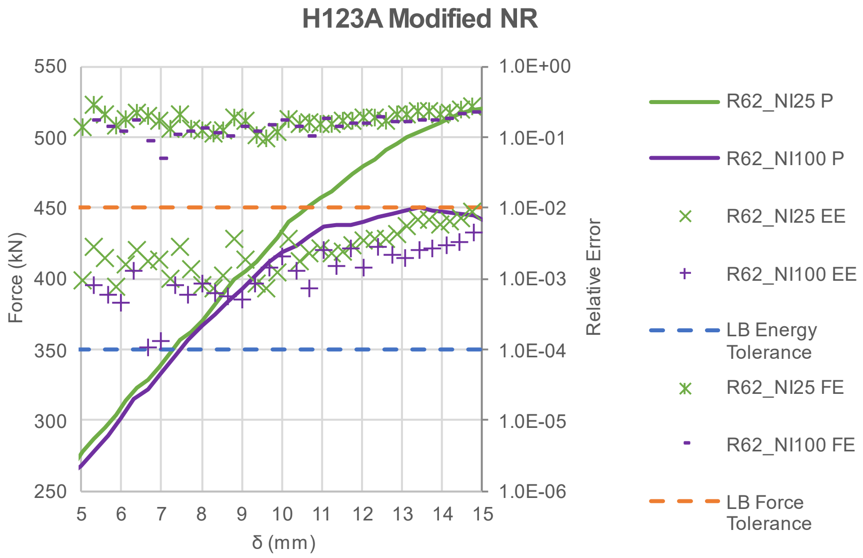

Figure 5.135 Load-displacement Curve on Critical Point 2 of Model H123A R62 NI for Modified NR Method

NI25 NI100

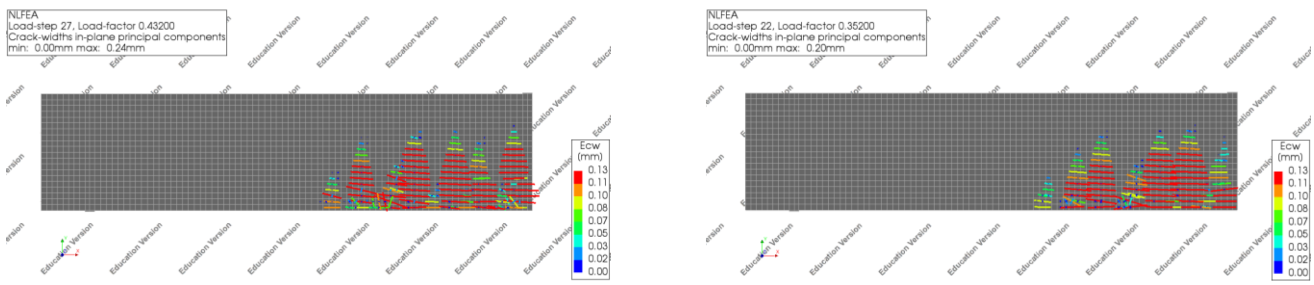

Figure 5.136 Crack Pattern Model H123A R62 for NI Variation at δ = 7.20 mm (Shifting Point A)

NI25 NI100

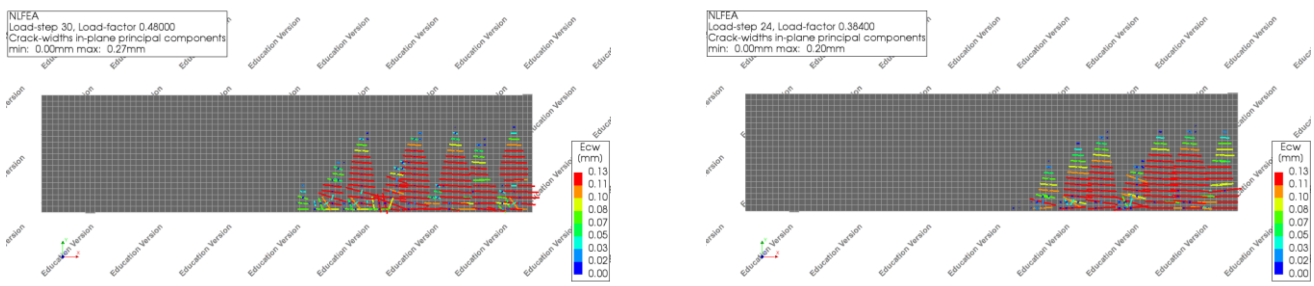

Figure 5.137 Crack Pattern Model H123A R62 for NI Variation at δ = 8.01 mm (Shifting Point B)

NI25 NI100

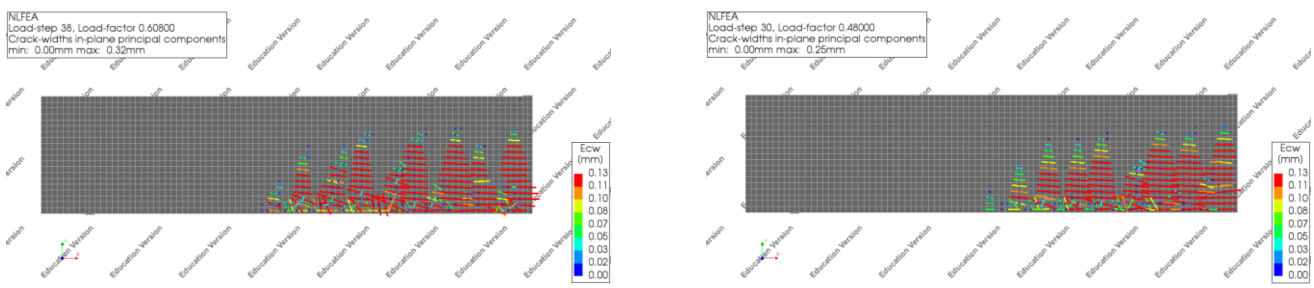

Figure 5.138 Crack Pattern Model H123A R62 for NI Variation at δ = 10.16 mm (Shifting Point C)

NI25 NI100

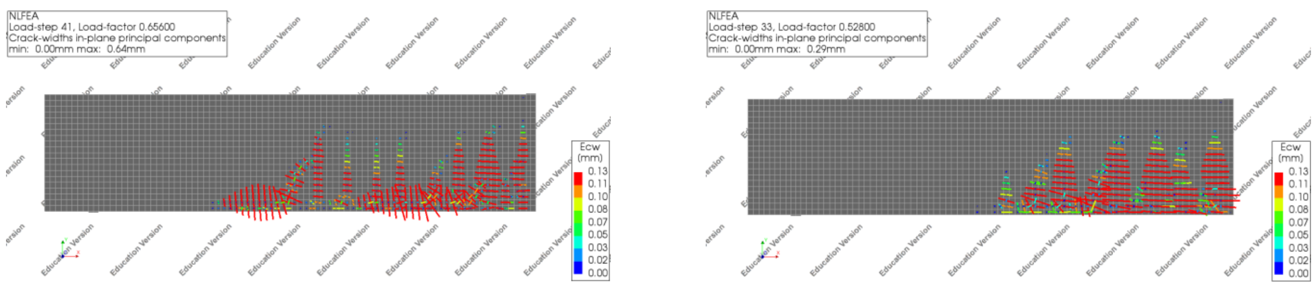

Figure 5.139 Crack Pattern Model H123A R62 for NI Variation at δ = 10.98 mm (Shifting Point D)

NI25 NI100

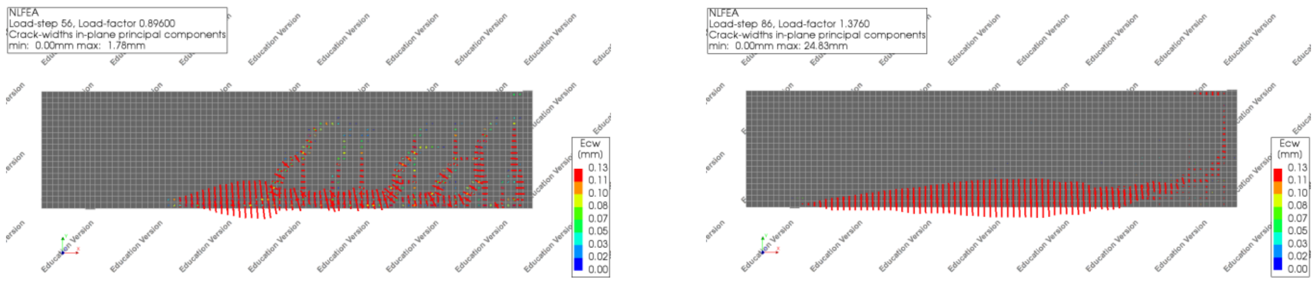

Figure 5.140 Crack Pattern Model H123A R62 for NI Variation at Peak Load

The relative energy variation in model H123A R62 NI25 and NI100 in Figure 5.135 is relatively increasing through all shifting points. The relative out-of-balance force in Figure 5.135 is relatively constant for both models from shifting point A to shifting point C.

In terms of crack pattern, model H123A R62 NI25 and NI100 have a similar crack pattern in shifting point A (Figure 5.136) and shifting point B (Figure 5.137). In shifting point C, the dowel crack in model H123A R62 NI25 starts propagating more compared to model H123A R62 NI100, which can be observed in Figure 5.138. In shifting point D in Figure 5.139, the type of propagating crack in model H123A R62 NI25 changes to dowel crack propagation while model H123A R62 NI100 has not reached this state yet. This phenomenon cannot be seen in the convergence state of the model, where both models have similar trends and similar magnitude of relative energy variation and out-of-balance force. However, this phenomenon does not affect the crack pattern at the peak load significantly in Figure 5.140.

Based on the observation for both specimen A123A1 and H123A, it can be concluded that the variation on the peak load of models with the Modified Newton-Raphson method and different maximum number of iterations is caused by the different crack patterns on the models at the same displacement. The different crack pattern is caused by different amount of iterations on each step on the model. The number of iterations is becoming a crucial factor in the NLFEA because most of the steps are not converging. It is well known that Modified Newton-Raphson evaluates the stiffness matrix only on the first iteration of the steps, based on the previous steps, and the rest of the iterations is used only to sharpen the prediction of displacement and force on the model. When the numerical model has most of the steps not converging, the deviation of the stiffness matrix prediction is controlled by the model condition of the previous steps, which is dependent on the iterations done for the respective steps. Small deviation on the crack formation on one of the load steps will result in a completely different crack pattern, which can be seen in the numerical models with specimen H123A, even when the deviation on the load-displacement curve is negligible. Hence, it could be said that the crack propagation process is heavily dependent on the maximum number of iterations per step. Furthermore, this effect is size-dependent as this can only be observed in the numerical model for specimen H123A.

5.6. The Formation of Dowel Crack vs The Convergence State

In order to understand the causal relationship between the formation of dowel crack and the convergence state of the numerical model, the first aspect that must be explained is how the dowel crack formed. The formation of the dowel crack can be explained by observing the stress state of the simulated model before and after the formation of the dowel crack. The explanation for the formation of dowel crack will be done by using model H123A R41_ET4/ET3 (or the same as model H123A LI0.03). The load-displacement curve is given in Figure 5.141 and the stress state will be observed in three points, which is referred to as shifting points A, B, and C, with displacement equal to 6.49 mm, 7.00 mm, and 8.01 mm respectively.

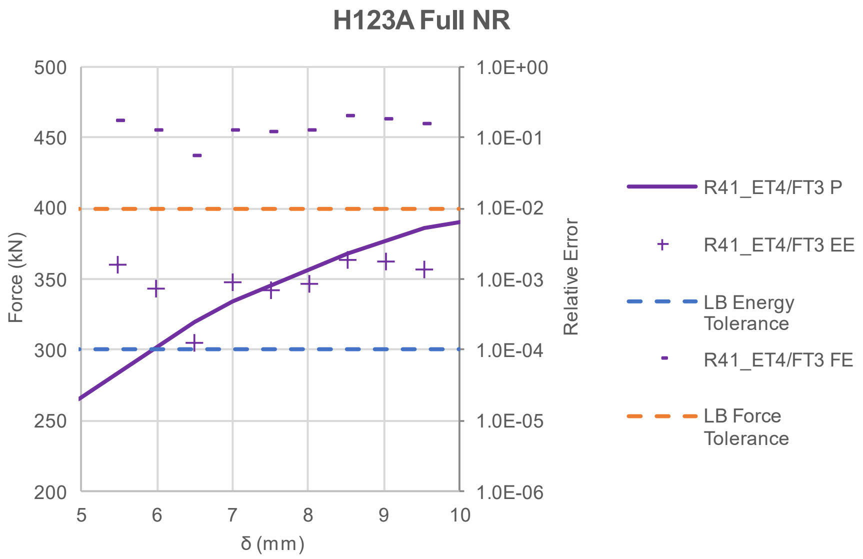

Figure 5.141 Load-displacement Curve of Model H123A R41 ET4/FT3 with δ = 5-10 mm

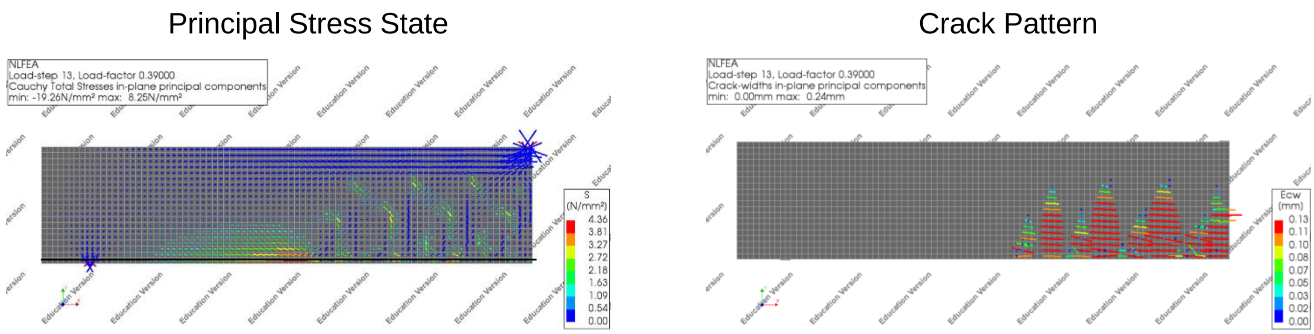

Figure 5.142 Stress State of Model H123A R41 ET4/FT3 at δ = 6.49 mm (Shifting Point A)

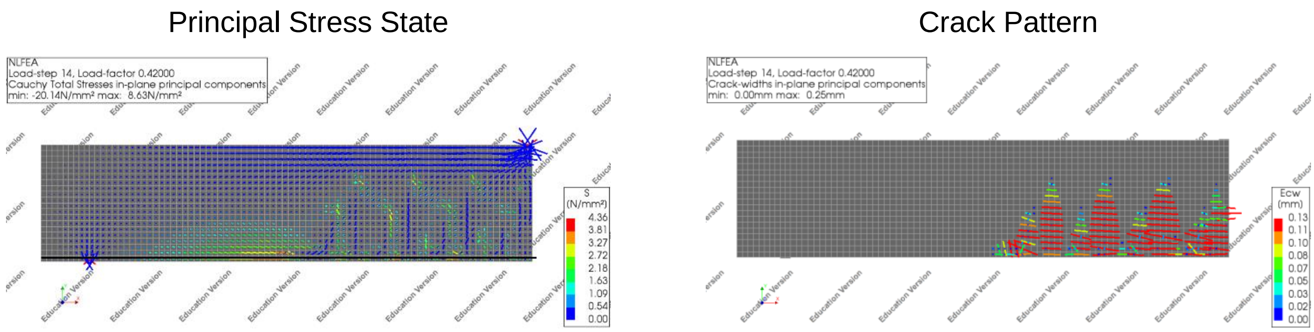

Figure 5.143 Stress State of Model H123A R41 ET4/FT3 at δ = 7.00 mm (Shifting Point B)

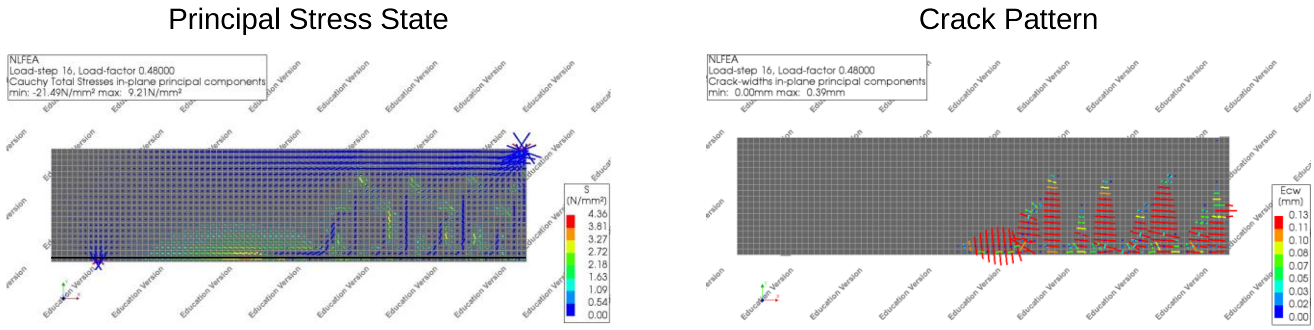

Figure 5.144 Stress State of Model H123A R41 ET4/FT3 at δ = 8.01 mm (Shifting Point C)

The initiation of dowel crack is caused by the existence of flexural cracks on the beam in Figure 5.142. The flexural crack forms a discontinuity on the bottom part of the beam, where no stress can be transferred through the cracks after exceeding the ultimate tensile crack width. Therefore, the tensile stress is distributed through the reinforcement, which causes the principal direction of the concrete element above the reinforcement to rotate. The rotation of the principal direction introduces vertical stress, which resulted in splitting failure around the reinforcement due to insufficient strength and area of the concrete below the bar. Furthermore, it can be noticed that at the tip of the dowel crack, there is a concentration of tensile stress, which cause the dowel crack continues to propagate, which can be seen in Figure 5.143. At this stage, there is no additional flexural crack propagation anymore and the dowel crack will continue propagating to the support, which can be seen in Figure 5.144. The rate of the dowel crack propagation is based on the simulated concrete strain value above the reinforcement.

The second aspect that will be explained is the convergence state. In this thesis, the convergence state that will be checked with the convergence criteria are the level of relative energy variation and out-of-balance force on each step in the NLFEA. In order to reach convergence in the NLFEA in this case, both force and energy tolerance must be satisfied. Further details about the convergence state are given in subchapter 2.1.

The causal relation between the formation of dowel crack and convergence state can be analysed by observing Figure 5.141. As there are no converged steps in the analysis between displacement equal to 5-10 mm, high relative energy variation and out-of-balance force can be spotted. As both relative energy variation and out-of-balance force are related to the internal force, it can be said that variation of relative energy variation and out-of-balance force is due to change in internal force, assuming that the displacement remains constant/have a non-significant change. The change in internal force is caused by different stress-strain conditions of the element in the numerical model. The sudden change in the stress-strain condition of the model will lead to an excessive change of the principal stress-strain direction and magnitude on the element above the reinforcement. This happens when the dowel crack starts to form and propagate in the numerical model. Therefore, it can be said that the formation of the dowel crack results in bad convergence. The influence on the convergence state is different in every iterative-incremental method, as it has a different method on how it calculates the global stiffness matrix of the numerical model. Furthermore, this proves that the result of NLFEA is dependent on the numerical parameters such as load increment, error tolerance, and the maximum number of iterations due to the bad convergence, as these parameters indirectly contribute to determining the error found on each step in the analysis.

The causal relation between the formation of dowel crack and convergence state can be verified by observing the principal strain condition of Figure 5.77. In Figure 5.145, the principal strain direction at the low-end of the inclined crack is similar for both models. In model H123A R41 FT2, an additional flexural crack is formed at shifting point B, causing a small difference in both relative energy variation and out-of-balance force in Figure 5.77 when compared to model H123A R41 ET4/FT3. As the principal strain direction starts rotating in model H123A R41 ET4/FT3, the dowel crack continues propagating and become more apparent at shifting point C in Figure 5.147. The excessive rotation of the principal strain direction increases the relative energy variation and out-of-balance force in model H123A R41 ET4/FT3, which in turn gives a higher difference in both energy variation and out-of-balance force when compared to model H123A R41 FT2. The effect of excessive rotation of the principal strain can be analysed further by observing Figure 5.148. In the element above the reinforcement, the excessive rotation of the principal strain is also accompanied by the sudden change of the principal strain. The sudden change of the principal strain causes a drop of tensile stress in the principal direction where the tensile stress and fracture energy is reduced to zero. The sudden energy release contributes to the high energy variation. The drop of tensile stress reduces the internal force, which in turn increase the out-of-balance force.

FT2 ET4/FT3

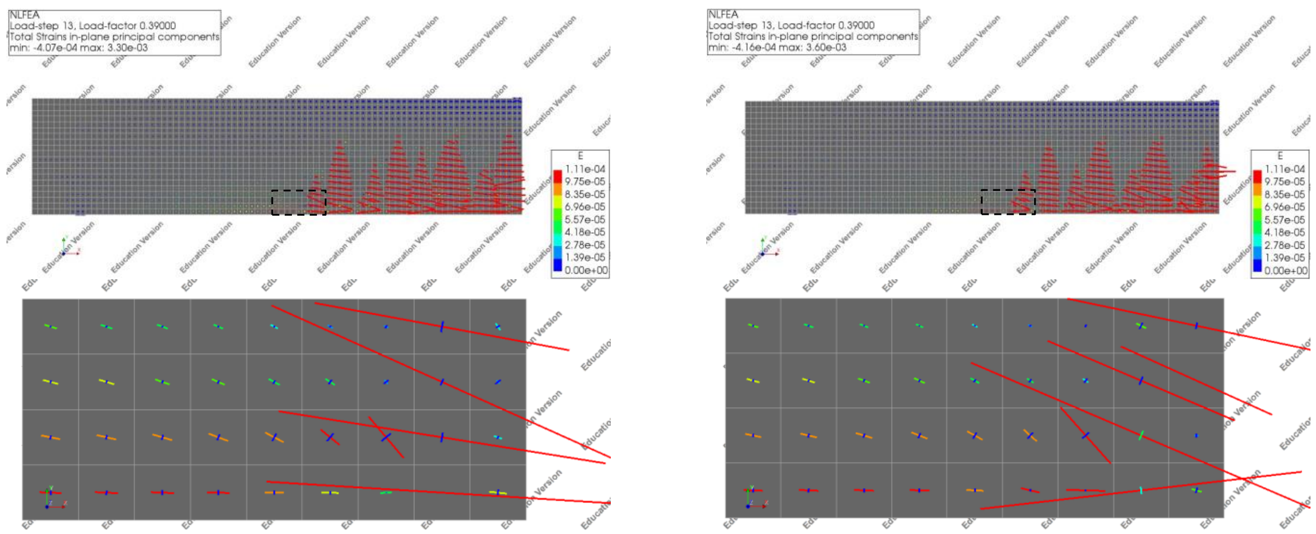

Figure 5.145 Principal Strain in Model H123A R41 at δ = 6.49 mm (Shifting Point A)

FT2 ET4/FT3

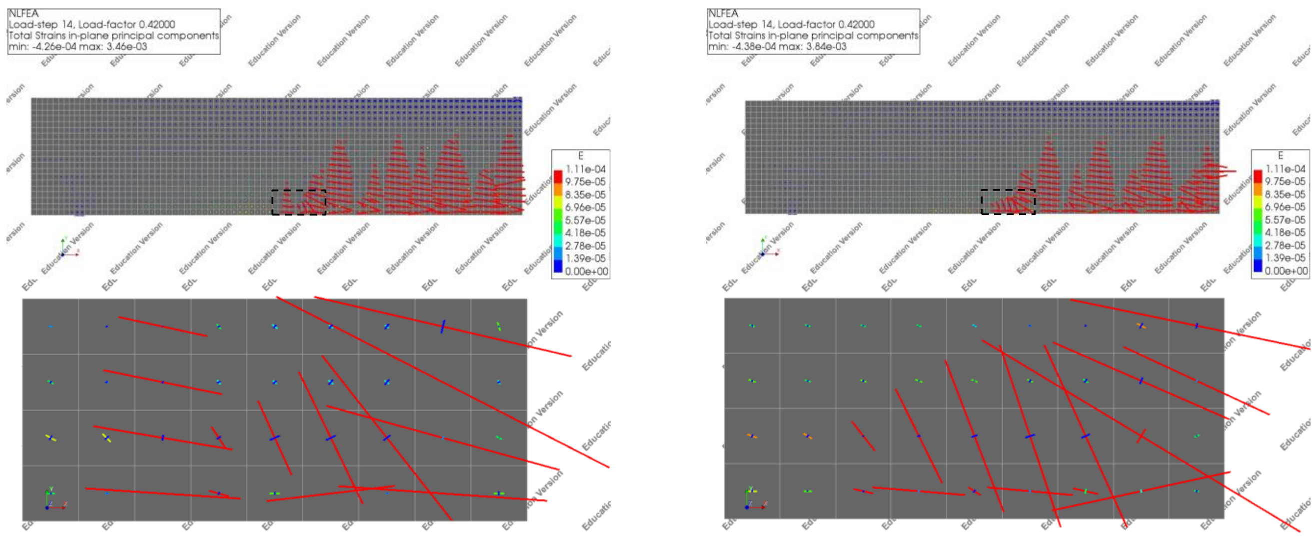

Figure 5.146 Principal Strain Model H123A R41 at δ = 7.00 mm (Shifting Point B)

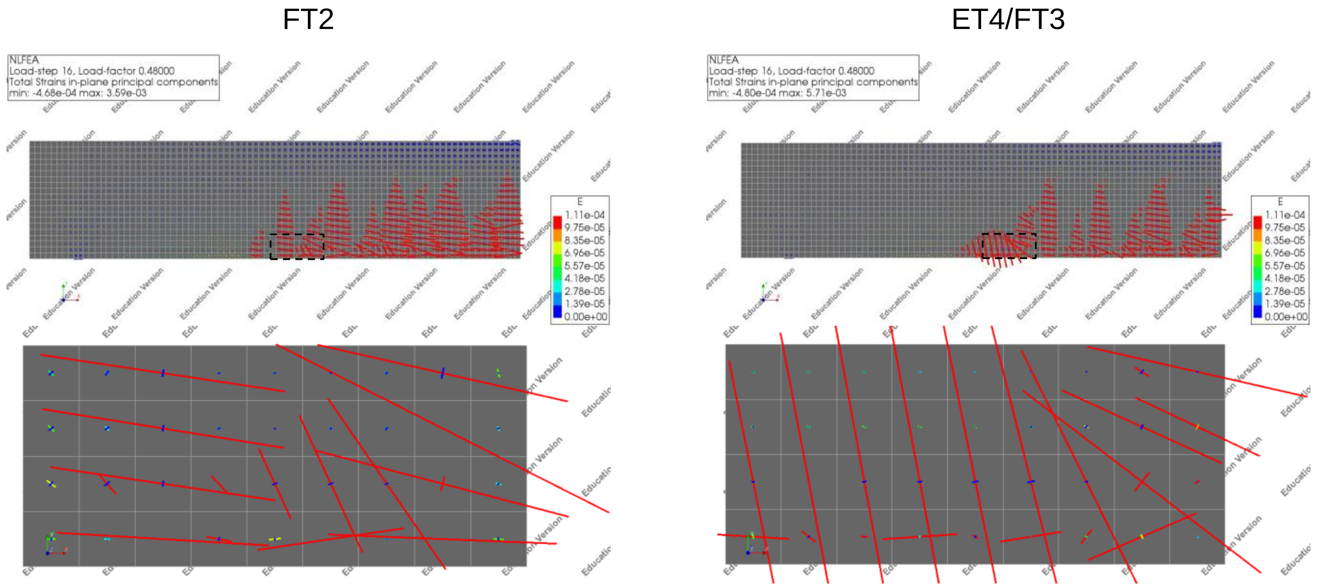

Figure 5.147 Principal Strain Model H123A R41 at δ = 8.01 mm (Shifting Point C)

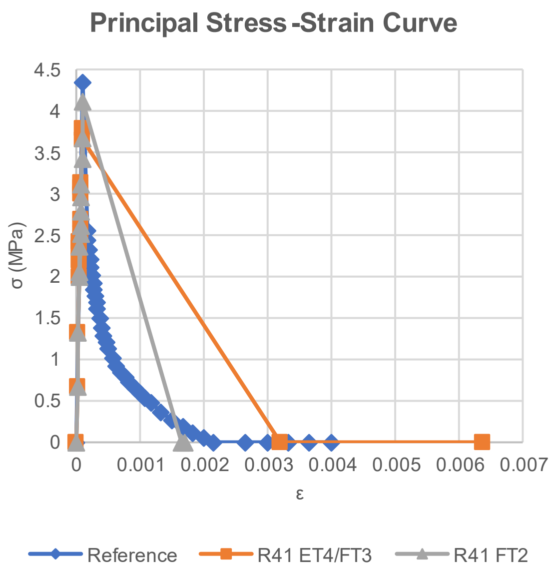

Figure 5.148 Principal Stress-Strain Curve of Element above the Reinforcement

5.7. Derivation of Convergence Criteria

Based on the study that has been done for three types of iterative-incremental analysis procedure, Quasi-Newton, Full Newton-Raphson, and Modified Newton-Raphson, it can be concluded that the derivation of the convergence criteria will not be able to create a single set of criteria that can be used for all non-linear analysis. The difference between each analysis would be discussed in this subchapter and a recommendation would be given on which configuration should be used for each analysis and which analysis should be used for simulating shear failure of the concrete beam.

In each analysis procedure, some numerical models stopped in the middle of the analysis due to a reason. Overall, two problems arise in the NLFEA, the dominator of plasticity matrix equal to zero due to huge loss of bond-slip capacity over the shear span, causing instability on the numerical model, and divergence due to large relative energy variation (equal or larger than 10^4) and out-of-balance force (equal or larger than 10^4). The peak load of several numerical models is affected by these problems. No consistent trend can be seen when observing this effect, except for model A123A1 LI0.01 with the Full Newton-Raphson method. The influence of the NLFEA problem is disappearing after the energy tolerance is loosen to 0.001 or the maximum number of iterations per step is reduced to 50. As there are no other models that have the same phenomena as model A123A1 LI0.01 and no significant influence can be seen in the observation of change in load increment, error tolerance, and the maximum number of iterations, this phenomenon is considered negligible for this case. The summary of the numerical models that experience these problems are given in Table 5.5.

Table 5.5 Summary of Convergence State of Numerical Models at the Last Step

Problem	1A*	1B*	1*	2A*	2B*	2*
Variation of Load Increment						
Quasi-Newton – Crisfield	0	0	0	0	0	0
Full Newton-Raphson	6 [11]** LI0.01, LI0.008, LI0.006***	1 [2]**	7 [13]**	0	0	0
Modified Newton-Raphson	6 [11]** LI0.016, LI0.01, LI0.006***	5 [7]** LI0.008***	11 [18]**	0	1 [3]**	1 [3]**
Variation of Error Tolerance						
Quasi-Newton – Crisfield	0	0	0	0	0	0
Full Newton-Raphson	15 R31_FT2, R32_ET2, R33_ET3, R33_FT1, R33_FT2***	1	16	0	0	0
Modified Newton-Raphson	15 R51_ET1, R51_ET3, R51_FT2, R52_ET2***	4 R62_ET3, R62_FT1***	19	0	5 R62_ET1***	5
Variation of Maximum Number of Iterations						
Quasi-Newton – Crisfield	0	0	0	0	0	0
Full Newton-Raphson	12 R31_NI25, R33_NI75***	3 R41_NI50***	15	0	0	0
Modified Newton-Raphson	12	7 R63_NI50***	19	0	4	4

* (1) Denominator of plasticity matrix equal to zero
(2) Divergence
(A) Numerical model for specimen A123A1
(B) Numerical model for specimen H123A

** 1[2] = 1 model experiences the problem within the optimal range and 2 models experience the problem within the load increment range of 0.1-0.004
Optimal range for Quasi-Newton Method = 0.1-0.02
Optimal range for Full Newton-Raphson Method = 0.03-0.006
Optimal range for Modified Newton-Raphson Method = 0.03-0.006

*** The problem on the respective numerical model affects the magnitude of the peak load in the optimal range

In terms of the influence of the load increment, all methods are dependent on the prescribed load increment on the numerical models. A different set of ranges of load increment is used for each method to attain consistent results with a certain range of peak load distribution. The overview of the peak range comparison between different methods can be seen in Table 5.6. The smallest peak range can be obtained with the Quasi-Newton method, while the largest peak range is attained from the Modified Newton-Raphson method. However, it must be noted that the Quasi-Newton method has the most loosen convergence tolerance while the Modified Newton-Raphson method has the tightest convergence tolerance. If the Quasi-Newton method is compared to Full Newton-Raphson, it can be seen that the difference in the peak range is relatively small, but significant overestimation can be seen in the numerical model with the Quasi-Newton method.

Table 5.6 Quantitative Comparison between Different Iterative-incremental Analysis Method

Iterative-Incremental Analysis Method	Range of Load Increment	Energy Tolerance	Force Tolerance	Peak Range Specimen A123A1	Peak Range Specimen H123A
Quasi-Newton – Crisfield	0.1-0.02	0.0001-0.04	0.01-0.68	1.096-1.214	1.283-1.420
Full Newton-Raphson	0.03-0.006	0.0001-0.03	0.01-0.58	0.887-1.140	1.055-1.246
Modified Newton-Raphson	0.03-0.006	0.0001-0.012	0.01-0.54	0.791-1.121	0.809-1.231

When comparing each method qualitatively in order to see the influence of the load increment, each method has different factors that affected the simulated global behaviour of the beam. In the numerical model with the Quasi-Newton method, the change in load increment causes a change in the rate of crack propagation on the model that can be seen in the convergence state based on the change in trend from constant to linear growth. In the numerical model with the Full and Modified Newton-Raphson method, the change in load increment is caused by the initiation of dowel crack on the model that can be identified from the sudden increase in the relative energy variation and out-of-balance force. However, the influence of the load increment in the model with the Modified Newton-Raphson method is more complex, as it also affects the crack pattern at the peak load and size-dependent. Based on this observation, it can be said that the change in load increment affects the simulated cracking process on the beam.

In terms of the influence of the predefined error tolerance in the numerical model, each method has a similar factor that affected the simulated global behaviour of the beam. In the numerical model with the Quasi-Newton and Full Newton-Raphson method, the change in the lower bound error tolerance causes different crack propagation on the model that cannot be observed clearly on the convergence state of the numerical model. Different crack propagation is directly correlated to the change in the predefined energy tolerance, where the change in lower bound energy tolerance affect the number of cracked elements and change the crack formation process. Furthermore, this effect is size-dependent. On the other hand, the numerical model with Modified Newton-Raphson does not show this behaviour. Based on this observation, it can be said that the Modified Newton-Raphson method has a better performance compared to other methods when the predefined error tolerance is varied. However, it must be noted that in Table 5.6, the numerical model with the Modified Newton-Raphson method has a total of 24 out of 30 models (excluding the model reference ET4/FT3) that has a problem at the last step.

In terms of the influence of the maximum number of iterations in the numerical model, each method has different factors that affected the simulated global behaviour of the beam. In the numerical model with the Quasi-Newton method, the change in the maximum number of iterations affects the relative energy variation and out-of-balance force, causing changes in the type of propagating crack. This resulted in a different crack pattern at the peak load and influence the magnitude of the peak load. In the numerical model with the Full Newton-Raphson method, the change in the maximum number of iterations gives the same phenomenon as the change in load increment, where the initiation of the dowel crack is affected due to different levels of relative error in the convergence state. In the numerical model with the Modified Newton-Raphson method, the change in the maximum number of iterations causes different crack patterns at the same displacement level due to deviation on the relative energy variation and out-of-balance force of the numerical model. The deviation in the relative energy variation and out-of-balance force depends heavily on the maximum number of iterations, as most of the steps are not converging. Furthermore, the influence of the maximum number of iterations in the numerical model with any method is size-dependent. Based on this observation, it can be said that the change in the maximum number of iterations affects the simulated cracking process of the beam. However, the impact of this change is more severe in the numerical model with the Modified Newton-Raphson method.

According to these observations, it can be concluded that all methods have similar dependency behaviour to the load increment, predefined error tolerance and the maximum number of iterations with different degrees of influence. The influence of these dependencies is most severe in the numerical model with the Modified Newton-Raphson method, which makes this method is not recommended to be used for simulating shear failure in concrete beams. The influence of these dependencies in the numerical model with Quasi-Newton and Full Newton-Raphson is similar, but the use of Full Newton-Raphson is more recommended compared to Quasi-Newton because the peak load is less overestimated in the numerical model with Full Newton-Raphson.

5.8. Rotating vs Fixed Crack Model

As the problem of formation of the dowel crack is caused by excessive rotation of the principal strain of the elements above the reinforcement, the numerical model with a fixed crack model that has been modelled in chapter 4 is observed to see whether the use of different types of cracking model can solve the problem related to the formation of the dowel crack. The observation will be done for both specimens. The first observation is done for specimen A123A1. The load-displacement curve of numerical models of specimen A123A1 with rotating and fixed crack model is given in Figure 5.149.

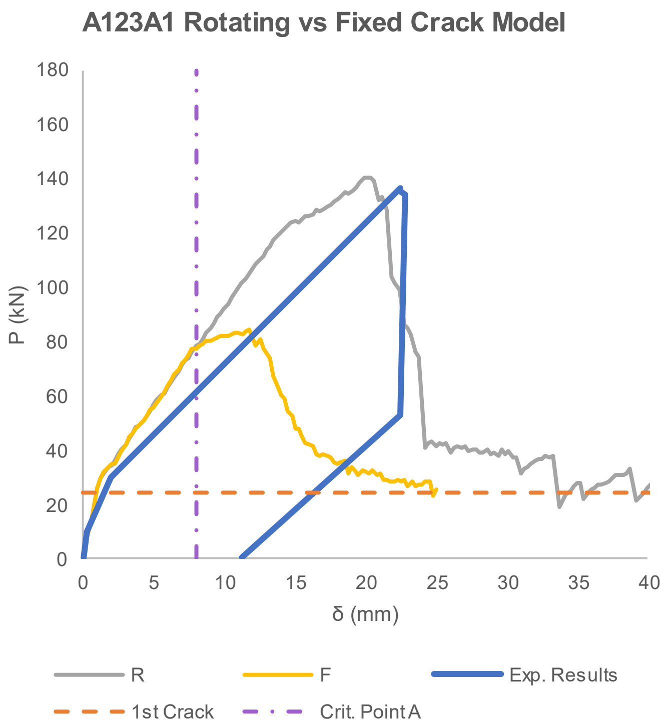

Figure 5.149 Load-displacement Curve of model A123A1 with Different Cracking Models

Figure 5.149 indicates that there is a significant difference in the peak load between model A123A1 R and F, where model A123A1 F gives significant underestimation of the peak load compared to the experimental result. Further observation on the cracking progression in the model is needed in order to understand this phenomenon. Critical point A is defined as the point where the numerical model with the fixed crack model starts deviating. The most important difference between the rotating and fixed crack models is the model of the shear retention factor. The shear retention factor in the rotating crack model is calculated implicitly while it is calculated explicitly in the fixed crack model with an explicit function. The process of change in the shear retention factor can be observed indirectly from the crack strain progression parallel to the crack opening. The crack strain in the perpendicular direction also needed to be observed in order to see whether the opening of the crack happens at the same time on the different crack models. The crack strain in the perpendicular $(Eknn)$ and parallel $(Gknt)$ to the crack opening is observed in the load step before critical point A to after critical point A.

R F

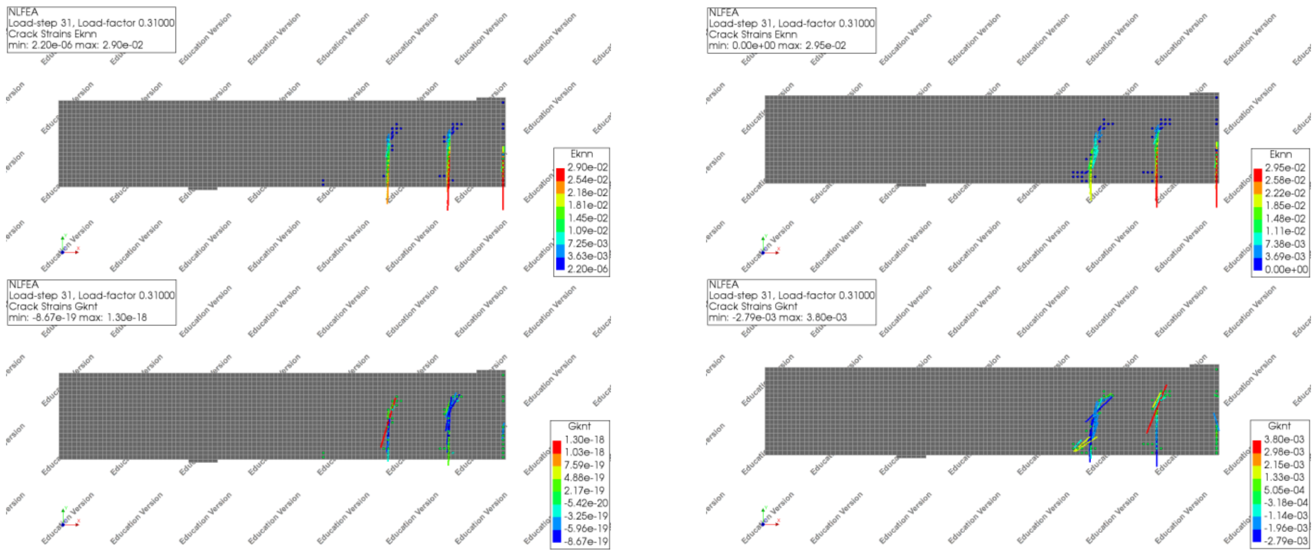

Figure 5.150 Crack Strain in model A123A1 before Critical Point A (Load Step 31)

R F

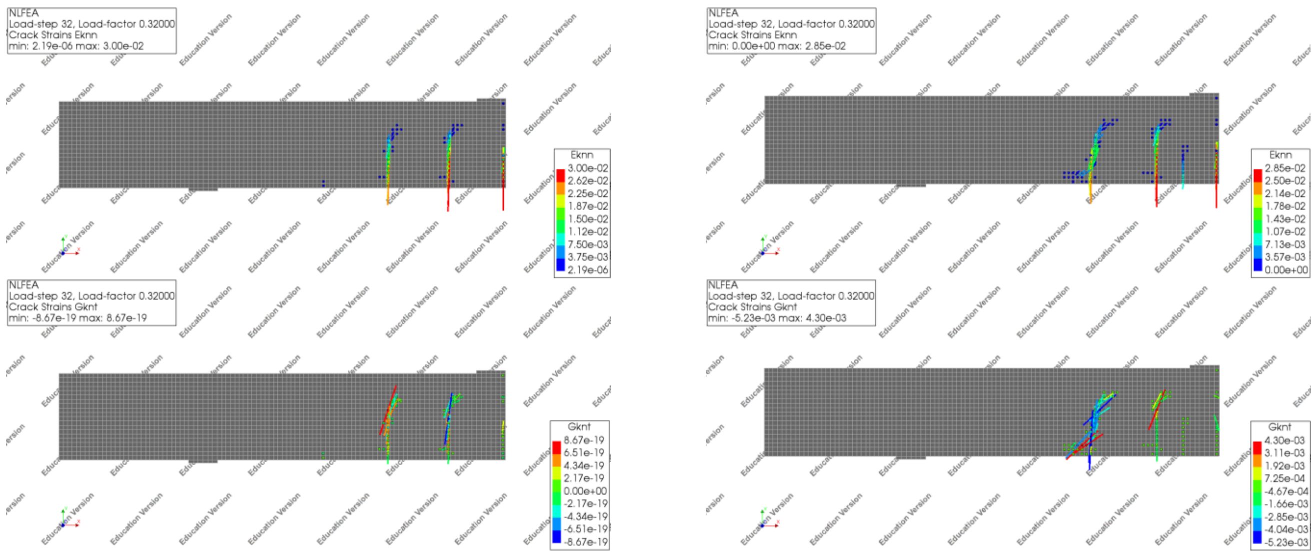

Figure 5.151 Crack Strain in model A123A1 at Critical Point A (Load Step 32)

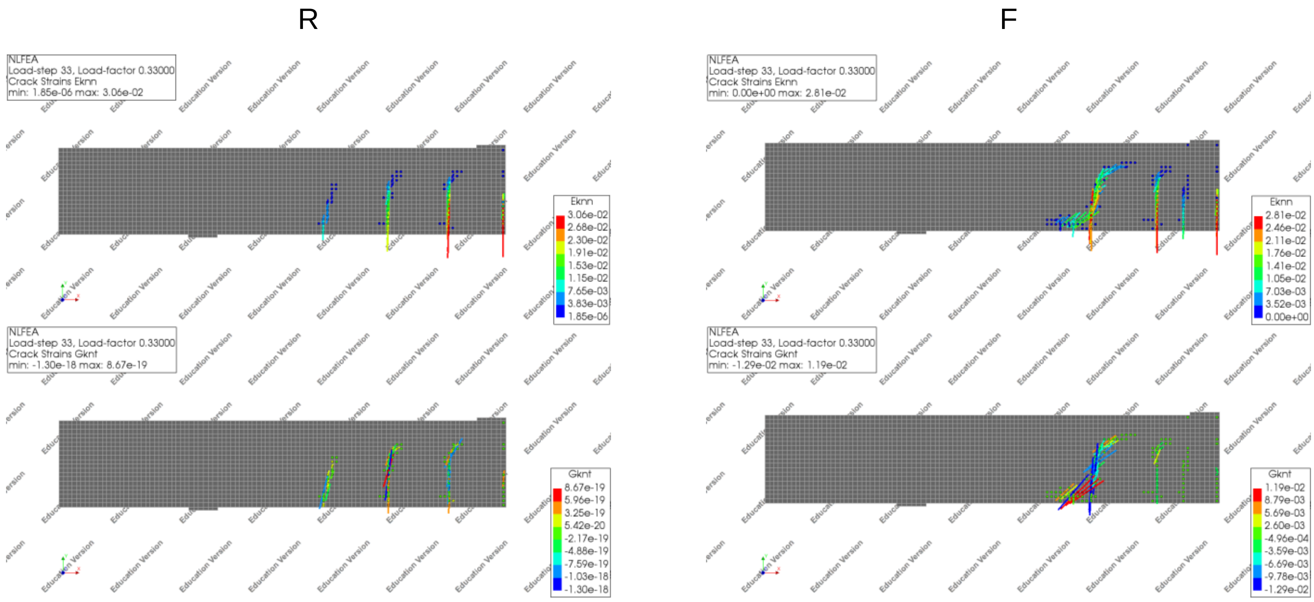

Figure 5.152 Crack Strain in model A123A1 after Critical Point A (Load Step 33)

Before critical point A in Figure 5.150, it can be seen that there is a significant difference in the crack strain $Gknt$ between model A123A1 R and F. Model A123A1 R has a smaller crack strain $Gknt$ compared to model A123A1 F. Furthermore, the crack strain $Gknt$ in model A123A1 F is comparable in magnitude to the crack strain $Eknn$ and small dowel crack has been formed. At critical point A in Figure 5.151, the crack strain $Gknt$ in the inclined flexural crack increase significantly in model A123A1 F while no significant change can be seen in the crack strain $Gknt$ in model A123A1 R. The crack strain $Gknt$ in model A123A1 F increase further and the dowel crack propagation also starts to dominate the cracking propagation process in Figure 5.152 after critical point A. No significant change in the crack strain $Eknn$ can be seen between both models in Figure 5.150, Figure 5.151 and Figure 5.152. The excessive change in the crack strain $Gknt$ does not exist in model A123A1 R in this stage of the analysis, which cause the load capacity of model A123A1 R to keep increasing while model A123A1 F reach its peak.

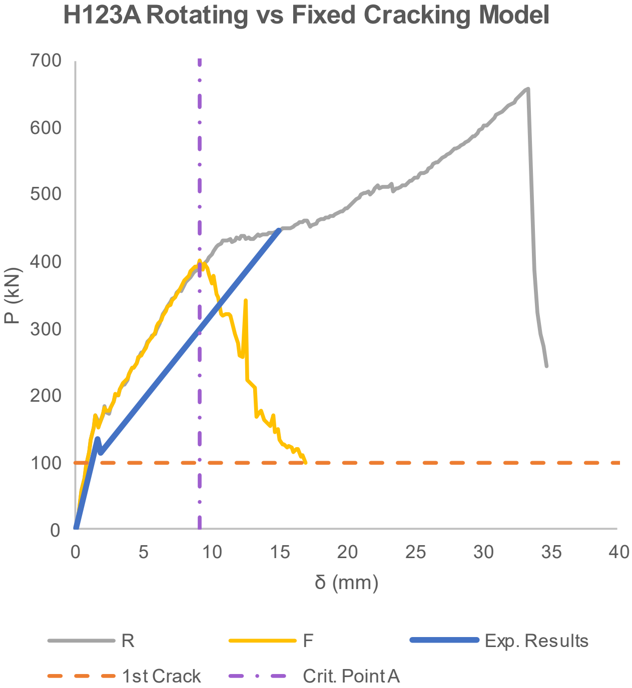

Figure 5.153 Load-displacement Curve of model H123A with Different Cracking Models

The next observation is done for the model with specimen H123A. The load-displacement curve of numerical models of specimen H123A with rotating and fixed crack model is given in Figure 5.153. Figure 5.153 indicates that there is a significant difference in the peak load between model H123A R and F, where model H123A F gives an underestimation of the peak load compared to the experimental result. Further observation on the cracking progression in the model is needed in order to understand this phenomenon. Critical point A is defined as the point where the numerical model with the fixed crack model starts deviating. The crack strain in the perpendicular $(Eknn)$ and parallel $(Gknt)$ to the crack opening is observed in the load step before critical point A to after critical point A.

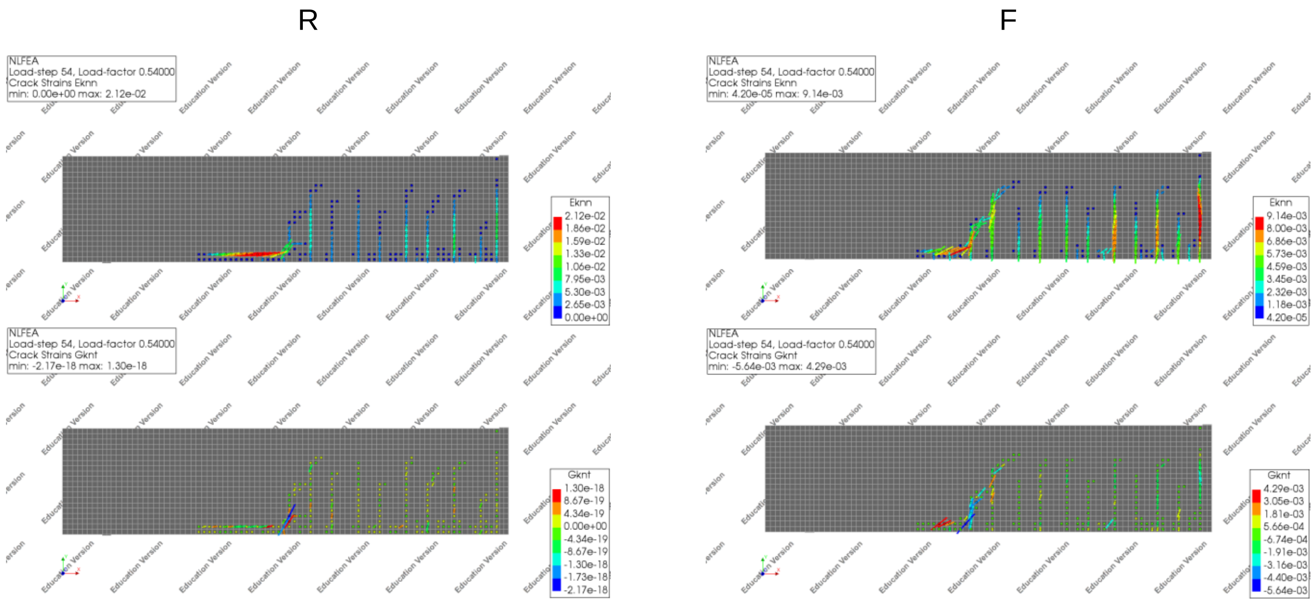

Figure 5.154 Crack Strain in model H123A before Critical Point A (Load Step 54)

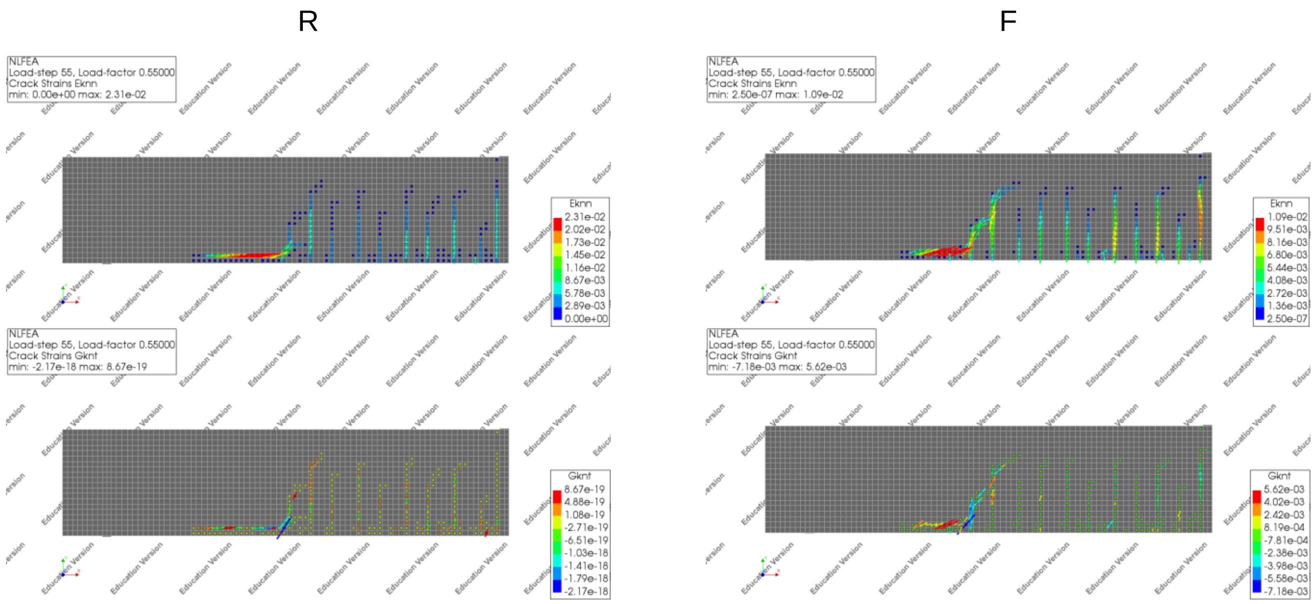

Figure 5.155 Crack Strain in model H123A at Critical Point A (Load Step 55)

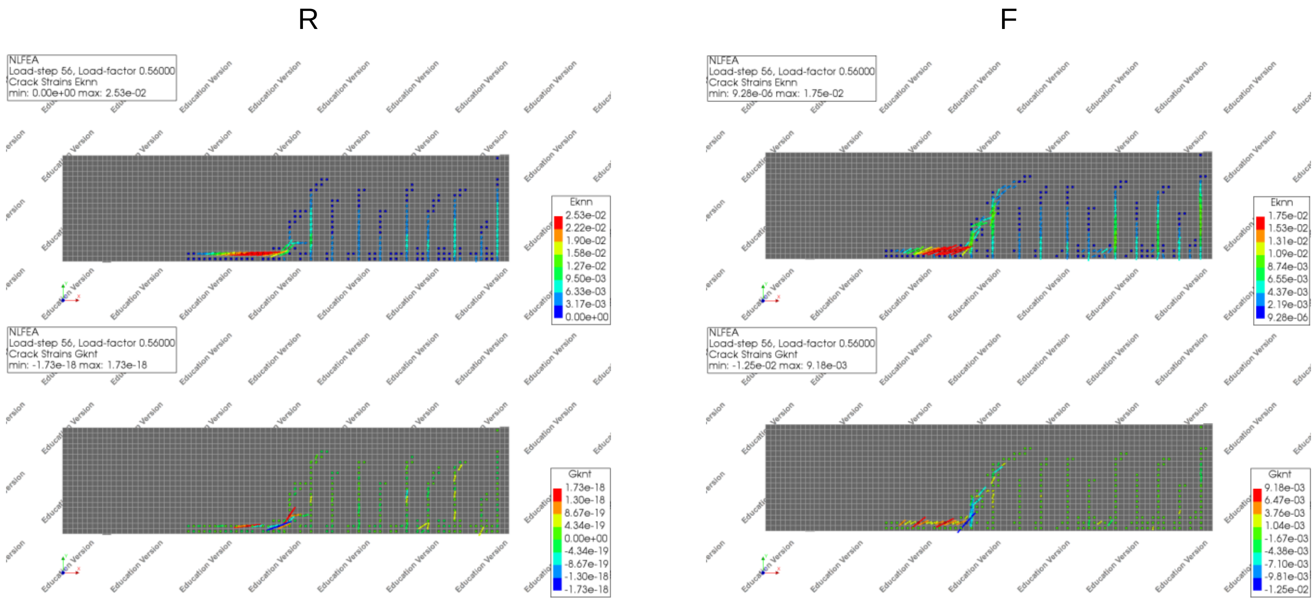

Figure 5.156 Crack Strain in model H123A after Critical Point A (Load Step 56)

Before critical point A in Figure 5.154, it can be seen that there is a significant difference in the crack strain $Gknt$ between model H123A R and F. Model H123A R has a smaller crack strain $Gknt$ compared to model H123A F. Furthermore, the crack strain $Gknt$ in model H123A F is comparable in magnitude to the crack strain $Eknn$. At the critical point A in Figure 5.155, the crack strain $Gknt$ in the inclined flexural crack increase significantly in model H123A F and the dowel crack propagation also starts to dominate the cracking propagation process, while no significant change can be seen in the crack strain $Gknt$ in model H123A R. The crack strain $Gknt$ in model H123A F increase further in Figure 5.156 after critical point A. No significant change in the crack strain $Eknn$ can be seen between both models in Figure 5.154, Figure 5.155 and Figure 5.156. The excessive change in the crack strain $Gknt$ does not exist in model H123A R in this stage of the analysis, which causes the load capacity of model H123A R to keep increasing while model H123A F reaches its peak.

Based on the observation of both specimens with different crack models, the use of fixed crack in the numerical model will not be able to solve the problem related to the formation of dowel crack because of the excessive change in the crack strain $Gknt$. The change of crack strain $Gknt$ represents the change in the shear retention factor on the element. The shear retention loss on the element above the reinforcement is too excessive, therefore causing a premature failure of the numerical model.

5.9. Summary

The sensitivity analysis is done for three different parameters, load increment, error tolerance and the maximum number of iterations. The sensitivity study of load increment is performed by studying 11 variations of load increment ratios (load increment/experimental peak load) from 0.1 to 0.004. The sensitivity study of error tolerance is performed by studying 6 variations of error tolerance from 0.0001 to 0.005. The sensitivity study of the maximum number of iterations is performed by studying 5 variations from 10 iterations to 100 iterations. The sensitivity study of error tolerance and the maximum number of iterations is also varied with 3 different load increments ratios for each specimen. The details of these sub-variations are given in Table 5.4. All studies are done for 3 different iterative-incremental procedures, Quasi-Newton (Crisfield), Full Newton-Raphson, and Modified Newton-Raphson. The study is mainly using the numerical model with the rotating crack model.

The use of different load increments, error tolerance and the maximum number of iterations cause a variation of the calculated peak load. Different peak load distributions are achieved with the different methods of iterative-incremental analysis. The distribution of the peak load is tried to be reduced by applying an upper value of error tolerance, which in turn gives a range of error tolerance instead of a single value of error tolerance. This treatment is only done to the results of NLFEA with different load increments as it will need more than three sub-variations of load step per variation in order to have a more representative data distribution, which consumed more than the available time. Furthermore, the necessity of studying the distribution of the data for both variations (error tolerance and the maximum number of iterations) has not been identified yet, which means that the study of both variations will be focused on the dependency of these variations to the global behaviour. The overview of the peak load distribution within the optimum range of load increment in combination with a certain level of accepted error tolerance can be seen in Table 5.6.

The behaviour related to the load increment, error tolerance and the maximum number of iterations is different for a different iterative-incremental procedure with different degrees of influence as well. The change in the load increment mainly affects the propagation of the dowel crack. However, additional effects can be seen in different iterative-incremental analysis methods. In numerical models with the Quasi-Newton method, the change of load increment also affects the propagation rate of the inclined crack. In numerical models with the Modified Newton-Raphson method, the change of load increment also affects the crack pattern at the peak load on model H123A, which indicates that the additional effect in this method is size-dependent. Furthermore, the change in load increment also has an impact on the trend of the convergence state (the relative energy variation and out-of-balance force) of the analysis where the trend changes from constant/random to linear growth. It must be noted that 7 out of 14 models with the Full Newton-Raphson method have a problem at the last step of the analysis where the denominator of plasticity matrix becomes equal to zero and all models with the Modified Newton-Raphson method have a problem at the last step of the analysis where the denominator of plasticity matrix also becomes equal to zero or divergence occurs.

The change in the predefined error tolerance mainly affects the propagation of inclined and dowel crack in numerical models with the Quasi-Newton and Full Newton-Raphson methods. This effect can be considered size-dependent as the effect can only be observed in the simulation of specimen H123A. The change in the predefined error tolerance affects the criteria of the analysis steps to be considered as converged steps, which cause the model to find a different equilibrium path in the analysis. On the other hand, numerical models with the Modified Newton-Raphson method do not exhibit this phenomenon. The Modified Newton-Raphson method has a better performance compared to the other methods. However, it must be noted that 5 out of 30 models (excluding the model reference ET4/FT3) have a problem at the last step of the analysis where divergence occurs.

The change in the maximum number of iterations mainly affects the initiation of the dowel crack in numerical models. This effect can be considered size-dependent as the effect can only be observed in the simulation of specimen H123A. Several additional effects can be seen in different iterative-incremental analysis methods. In the numerical model with the Quasi-Newton method, the change in the maximum number of iterations also affects the propagation of the dowel crack, which in turn change the crack pattern at the peak load. In the numerical model with the Modified Newton-Raphson method, the change in the maximum number of iterations affects both initiation and propagation of the inclined and dowel crack, which produce different crack patterns at the same displacement level. Furthermore, the change in the maximum number of iterations also has an impact on the convergence state where the relative error level of both energy variation and out-of-balance force increases significantly because most of the steps are not converging. This causes the relative error level to be heavily dependent on the maximum number of iterations per step and the equilibrium path becomes sensitive to the change of the relative error level. It must be noted that 15 out of 24 models (excluding the model reference NI100) with the Full Newton-Raphson method have a problem at the last step of the analysis where the denominator of plasticity matrix becomes equal to zero and 23 out of 25 models (excluding the model reference NI100) with Modified Newton-Raphson method have a problem at the last step of the analysis where the denominator of plasticity matrix also becomes equal to zero or divergence occurs.

Based on all observations, the main source of all peak load variations with different numerical parameters is connected to the formation of the dowel crack. The sudden change in the stress-strain condition of the model will lead to excessive rotation of the principal strain direction on the element which causes premature dowel crack opening in the numerical model. This problem causes bad convergence in the later stage of analysis and influences the iterative-incremental method differently due to different methods of forming the global stiffness matrix of the numerical model. The use of the fixed crack model in the numerical model will not be able to solve the problem related to the formation of dowel crack because of the excessive change in the shear retention factor on the elements where dowel crack is formed and propagating, which lead to premature failure of the beam.

As all methods are influenced at different levels, a single set of criteria cannot be formed for all non-linear analyses with a different iterative-incremental method. The Full Newton-Raphson is recommended to be used for simulating shear failure in the reinforced concrete beam without shear reinforcement. This method should be combined with a range of load increment ratio (load increment/experimental peak load) of 0.03-0.006, an error tolerance of $G_{err} = 0.0001$ and $F_{err} = 0.01$, and accepting non-converged steps if the relative energy variation and out-of-balance force of the corresponding step are below 0.03 and 0.58 respectively, in order to have a peak load ratio ranging from 0.887-1.140 for specimen A123A1 and 1.055-1.246 for specimen H123A.

6 Sensitivity Analysis of Mesh Size

After solving the convergence problem, the investigation of the numerical size effect continues by studying the effect of using different sizes of mesh in the numerical model. The numerical configuration and details of the mesh size variation are given in subchapter 6.1. The change in the simulated overall behaviour of the numerical model is investigated in subchapter 6.3. Based on the observation and analysis in subchapter 6.3, the change in mesh size is causing a change in the rate of the dowel crack propagation. The correlation and the causal relationship between the rate of the dowel crack propagation and the mesh size are studied in subchapter 6.4. The study regarding mesh size is concluded in subchapter 6.5 by examining which mesh size is sufficient to be used for simulating shear failure in the reinforced concrete beam without shear reinforcement. It must be noted that any figure with a crack pattern, such as Figure 6.4, is only used to be studied qualitatively. The value of Ecw always indicates a range from uncracked element $(Ecw=0)$ to fully cracked element $(Ecw=CW_{t,u})$. A fully cracked element is defined as an element which has lost all its fracture energy. The value of Ecw should not be used as a reference for any study related to the experimental crack width because it does not consider the effect of localised reinforcement, which should have decreased the crack opening around the reinforcement.

6.1. Case Study Details for Mesh Dependency Study

After solving the problem regarding convergence, the next phenomenon that will be studied is related to the mesh size. As mentioned in subchapter 3.5, the numerical size effect is always closely correlated to the mesh size dependency and one of the ways to minimize the numerical size effect is to limit the mesh size used on the numerical model. There are two types of limits that have been discussed in chapter 3, the limit based on the minimum number of elements per height and minimum size of the mesh. In the Guidelines for Nonlinear Finite Element Analysis of Concrete Structures (Hendriks & Roosen, 2020), the limit based on the minimum number of elements per height is used. In order to clarify the limit, the variation of the results due to changes in mesh size must be studied.

In order to study the dependency of NLFEA results on the mesh size, 4 variations are made based on the number of elements per height. An additional variation is created in order to see whether the minimum size of the mesh should be used as a reference for the limit or not. These variations can be seen in Table 6.1. The specimens used for the study are the same as specimens defined in chapter 4 Identification of Problem Related to Convergence. All material properties and beam geometry would also be the same as defined in subchapter 4.1 Experimental Set-Up for Convergence Problem Identification, except for the top reinforcement, which is excluded from the model. The load step and convergence norms are also the same as defined in Table 4.10 except for the load increment/total number of steps.

Table 6.1 Model Variation 5

Code	Element Size (mm)		Size Ratio		Load Increment Ratio	Cracking Model	Iterative-Incremental Method
	A123A1	H123A	A123A1	H123A			
M15	15	-	$h/20$	-	0.03	Rotating	Full Newton-Raphson
M20	20	-	$h/15$	-			
M30	30	30	$h/10$	$h/40$			
M50	50	-	$h/6$	-			
M60	-	60	-	$h/20$			
M80	-	80	-	$h/15$			
M120	-	120	-	$h/10$			

Code	Element Size (mm)		Size Ratio		Load Increment Ratio	Cracking Model	Iterative-Incremental Method
	A123A1	H123A	A123A1	H123A			
M200	-	200	-	$h/6$			

6.2. Analysis Method for Studying the Mesh Size

The sensitivity analysis will be done in two stages. The first stage is to observe the global behaviour of the simulated beam and the convergence state of the analysis with different mesh sizes. The purpose of this stage is to find whether there is a connection between change in the global behaviour to the change in the convergence state of the analysis and how it affects the numerical model with different mesh sizes.

Two types of global behaviour are going to be observed in this stage, the load-displacement curve and the crack propagation process. The process of flexural shear crack formation has been studied and clarified into 4 steps in subchapter 4.5 Correlation of Crack Propagation to the Beam Global Response. Understanding the process of flexural shear crack formation will help identify the influence of mesh size and its connection to the convergence state as well. At the end of the first stage, the correlation and causal relationship of the mesh size to the change in the global behaviour will be analysed in order to have an insight of what is the root of the problem. The influence of the convergence state that has been found in subchapter 5.6 The Formation of Dowel Crack vs The Convergence State will also be used to help this study.

The last stage is to derive new mesh size criteria that should be satisfied in order to have a numerical model which can simulate the correct failure mode. This stage evaluates all results from the previous stage of the analysis and tries to derive a set of criteria that can be used in any case.

6.3. Effect of Mesh Size Variation

The change due to different mesh sizes is studied in terms of the global behaviour and the maximum crack width. The study of global behaviour is explaining on how does global behaviour changes as the mesh size change. A problem related to the maximum crack width is found in the study of the global behaviour, where the maximum crack width reaches an unrealistic value at the peak load in all numerical models. The study of the maximum crack width will try to reduce this value by applying another criterion to the post-processing of the results, see its effect on the load-displacement curve and the global behaviour at the peak load and try deriving a rule of thumb for evaluating the load-displacement curve.

6.3.1 The Study of Global Behaviour of the Beam with Different Mesh Size

The simulated global behaviour of the beam is observed based on the results of NLFEA which has lower relative energy variation and relative out-of-balance force than the defined upper bound for both energy and force tolerance in subchapter 5.3.2 Effect of Load Increment Variation in Full Newton-Raphson Method. The first phase of observation for the simulated global behaviour of the beam will be done separately for different specimens. Figure 6.1 gives an illustration of the simulated global behaviour of the beam with different mesh sizes based on the load-displacement curve.

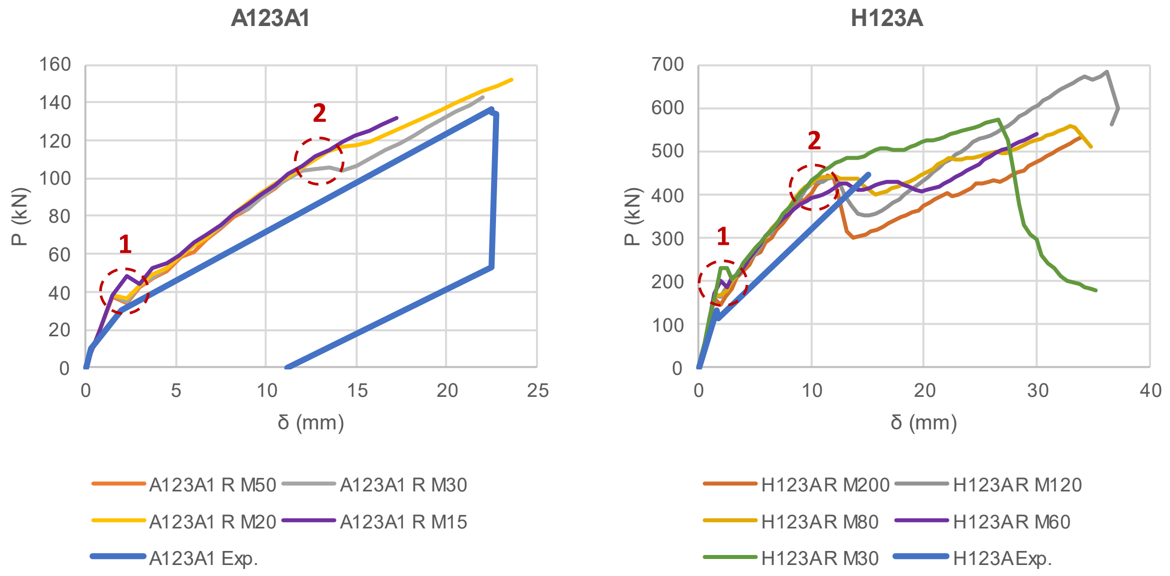

Figure 6.1 Load-displacement Curve with Different Mesh Size

In the load-displacement curve in Figure 6.1, there are 2 critical points that show some deviation due to change in mesh size. The first critical point is considered not important because the deviation in critical point 1 does not affect the overall simulated behaviour of the beam in the non-linear region. This can be seen by observing the load-displacement curve between critical point 1 and critical point 2, where the simulated non-linear behaviour is similar for all models with specimen A123A1 and H123A. On critical point 2, a significant deviation can be seen between the results on both specimens. The deviation on the curve is considered significant due to its effect on the simulated non-linear behaviour and the peak load of the model. Two models, M30 and M20, are chosen as the representative of all results for specimen A123A1 and three models, M80, M60, and M30, for specimen H123A. The load-displacement curve for these models is given in Figure 6.2.

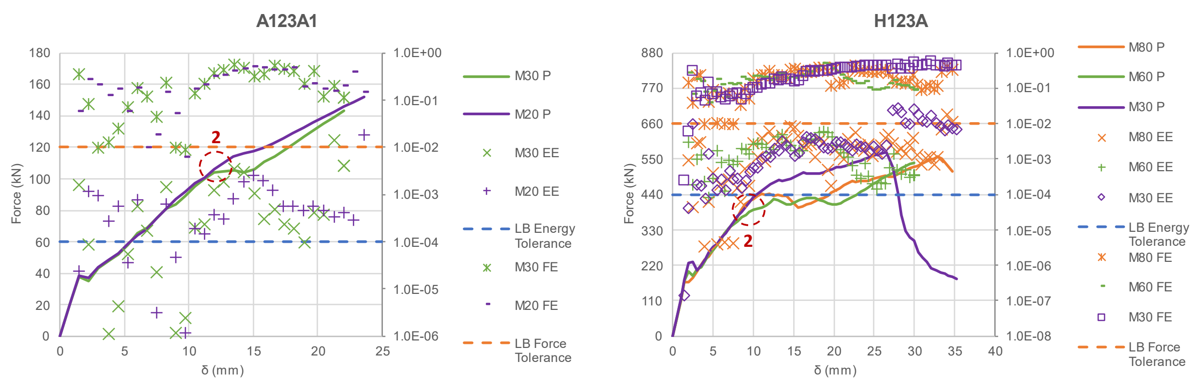

Figure 6.2 Load-displacement Curve with Convergence State for Different Mesh Size

Figure 5.30 indicates that most of the steps are converging in relative energy variation for model simulating specimen A123A1 and H123A. Furthermore, an increase in the relative energy variation and out-of-balance force can be seen around critical point 2 by observing convergence state at δ = 10-15 mm in specimen A123A1 and δ = 5-15 mm in specimen H123A.

The first critical point 2 that would be analysed is for specimen A123A1. Detailed illustration for critical point 2 of specimen A123A1 is given in Figure 6.3. 4 load steps are going to be observed in Figure 6.3. These load steps indicate the shift in the load-displacement curve and will be called shifting points A, B, C, and D for displacement at 11.23 mm, 11.98 mm, 12.73 mm, and 13.49 mm respectively.

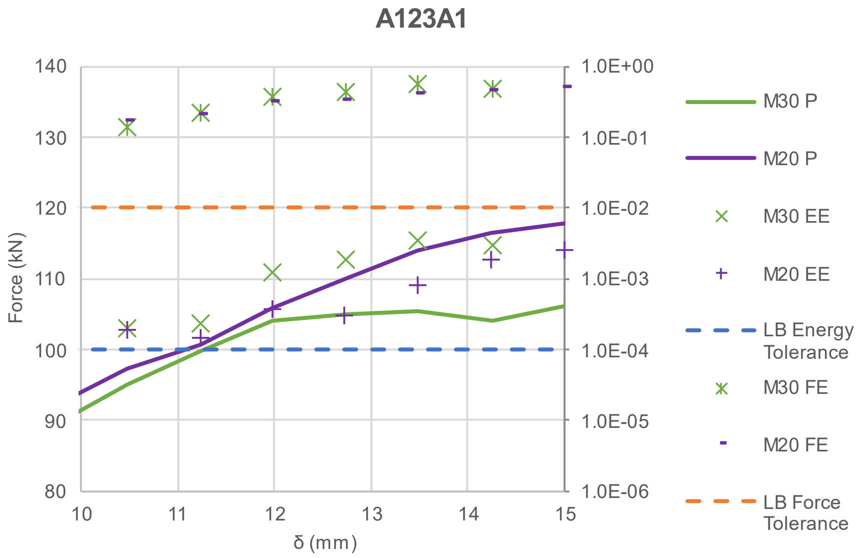

Figure 6.3 Load-displacement Curve on Critical Point 2 of Model A123A1

M30 M20

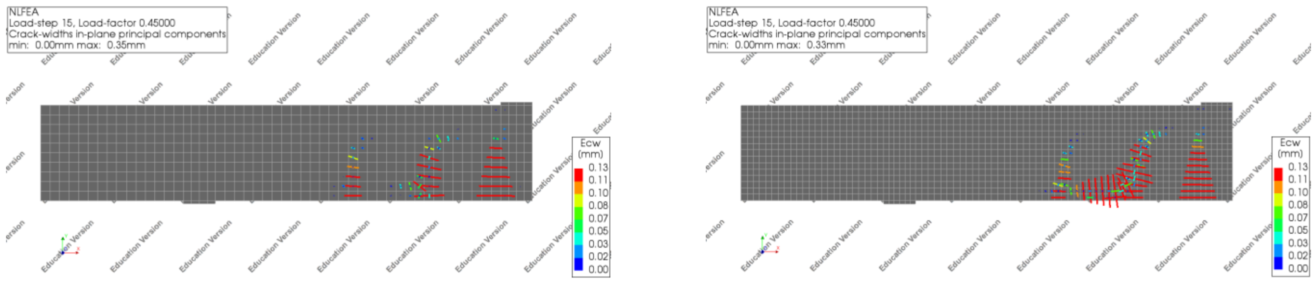

Figure 6.4 Crack Pattern Model A123A1 for Different Mesh Size at δ = 11.23 mm (Shifting Point A)

M30 M20

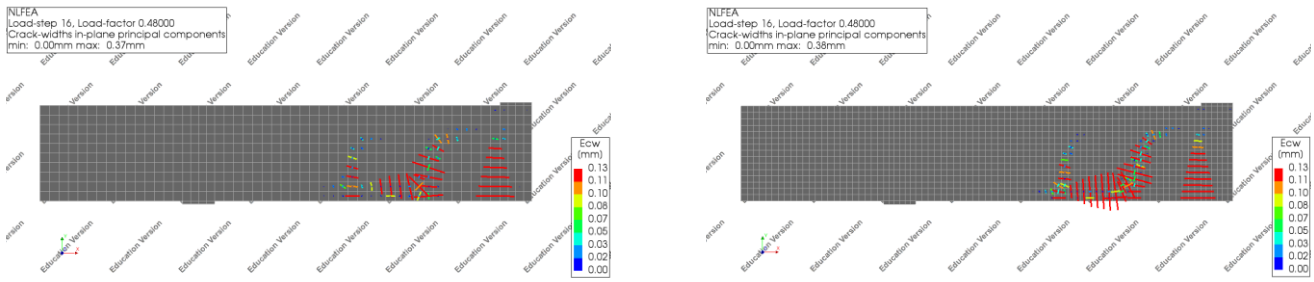

Figure 6.5 Crack Pattern Model A123A1 for Different Mesh Size at δ = 11.98 mm (Shifting Point B)

M30 M20

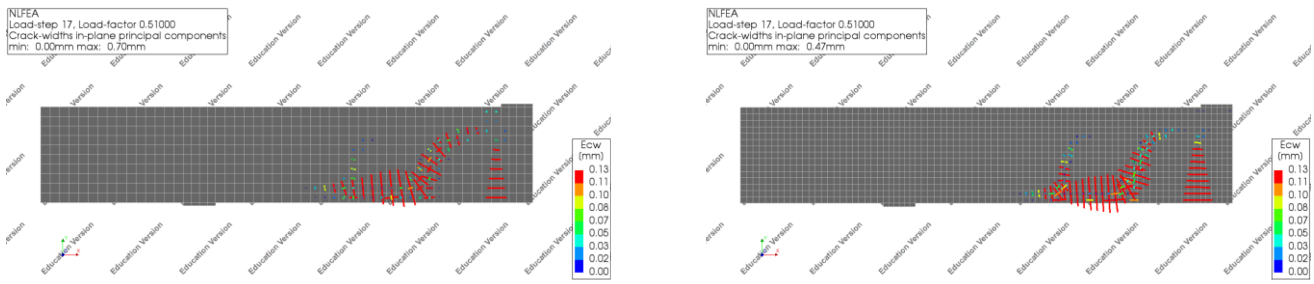

Figure 6.6 Crack Pattern Model A123A1 for Different Mesh Size at δ = 12.73 mm (Shifting Point C)

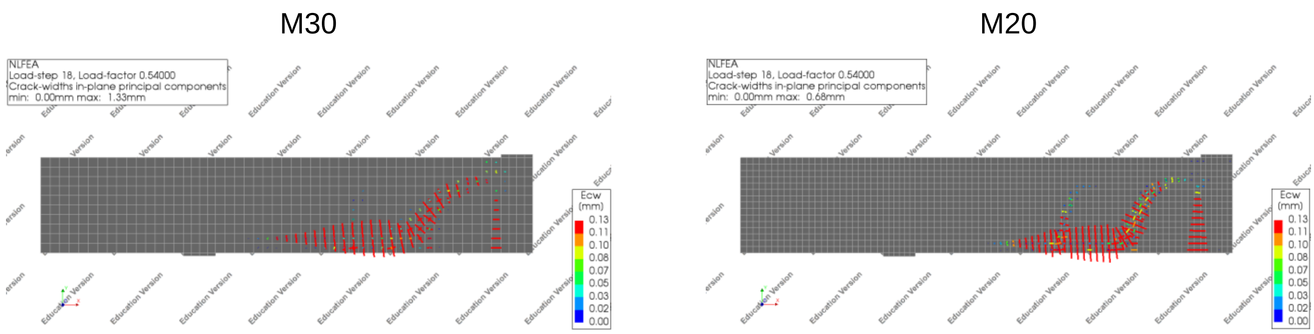

Figure 6.7 Crack Pattern Model A123A1 for Different Mesh Size at δ = 13.49 mm (Shifting Point D)

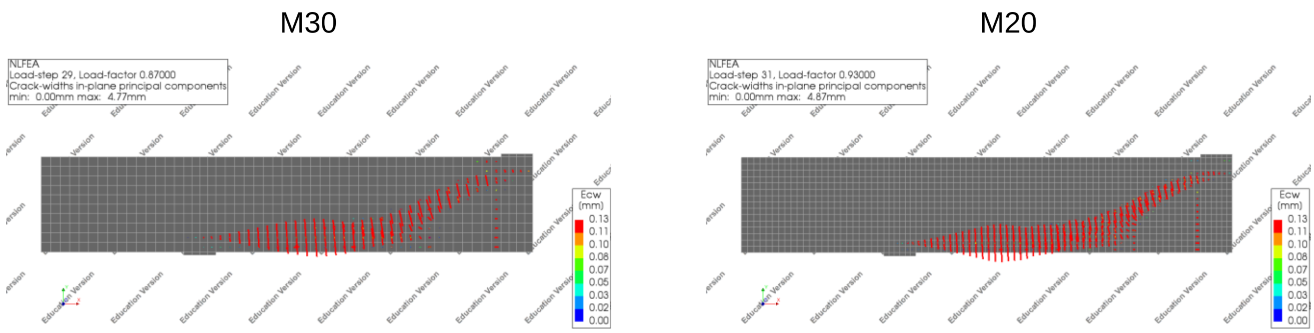

Figure 6.8 Crack Pattern Model A123A1 for Different Mesh Size at Peak Load

The relative energy variation and out-of-balance force in Figure 6.3 are increasing for model A123A1 M30 and M20 from shifting point A to shifting point D. However, the rate of increment of relative energy variation is higher compared to the relative out-of-balance force. The difference in the relative energy variation between model A123A1 M30 and M20 is growing from shifting point A to shifting point D, while the difference in the out-of-balance force in both models is very small in all shifting points.

In terms of crack pattern, models A123A1 M30 and M20 have similar crack progression at shifting point A in Figure 6.4. However, it must be noted that model A123A1 M30 has a smaller opening of dowel crack compared to model A123A1 M20. In shifting point B, the dowel crack propagates faster in model A123A1 M30 compared to model A123A1 M20. This can be seen in Figure 6.5 where the maximum crack width and the tensor size in both specimens is comparable. This trend continues in Figure 6.6 and Figure 6.7 where a significant increase can be seen in the maximum crack width between shifting point B to C and shifting point C to D. This phenomenon can also be seen in Figure 6.3 where the relative energy variation in model A123A1 M30 is higher compared to A123A1 M20. The relative energy variation in model A123A1 M30 is higher due to larger differences in cracked elements between the corresponding step to the previous step. As the rate of crack propagation increase, the number of cracked elements also increase significantly and leads to higher relative energy variation. Based on this observation, it can be seen that the dowel crack propagation is less stable in model A123A1 M30 compared to model A123A1 M20. Fortunately, this phenomenon does not affect the crack pattern at the peak load in Figure 6.8.

The next critical point 2 in Figure 6.2 that would be analysed is for specimen H123A. Detailed illustration for critical point 2 of specimen H123A is given in Figure 6.9. 5 load steps are going to be observed in Figure 6.9. These load steps indicate the shift in the load-displacement curve and will be called shifting points A, B, C, D, and E for displacement at 6.47 mm, 6.98 mm, 7.98 mm, 9.49 mm, and 10.50 mm respectively.

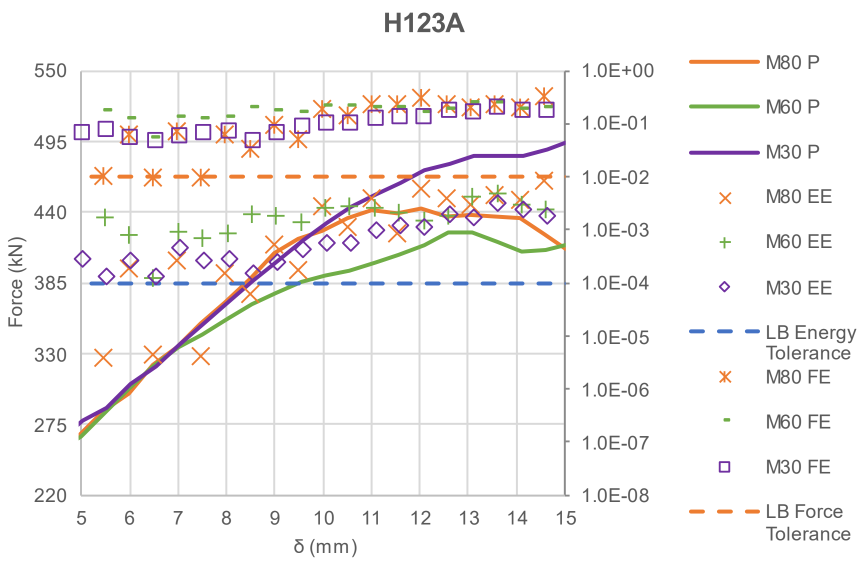

Figure 6.9 Load-displacement Curve on Critical Point 2 of Model H123A

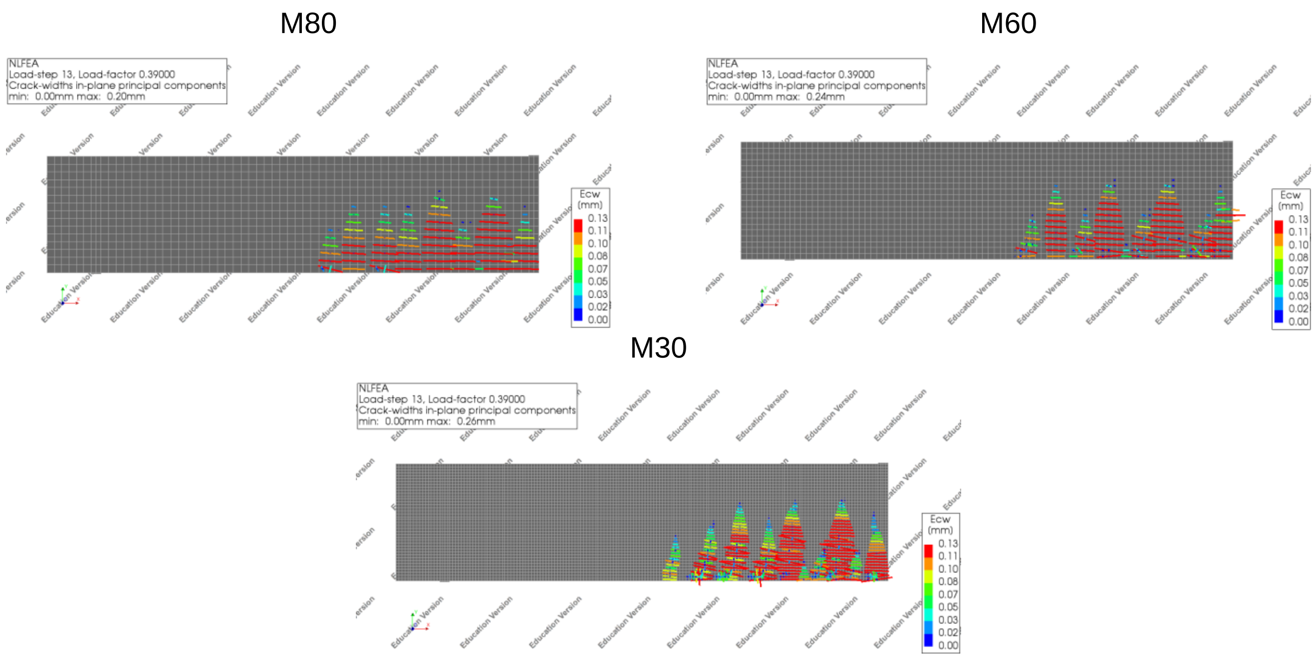

Figure 6.10 Crack Pattern Model H123A for Different Mesh Size at δ = 6.47 mm (Shifting Point A)

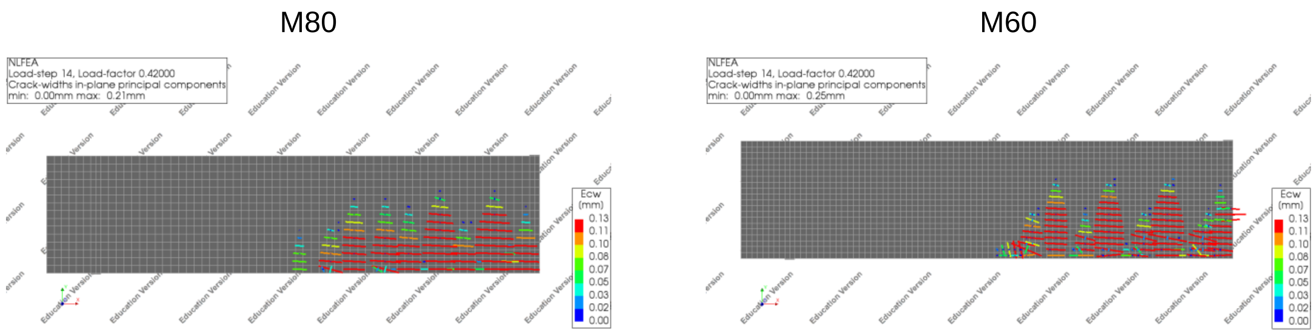

M30

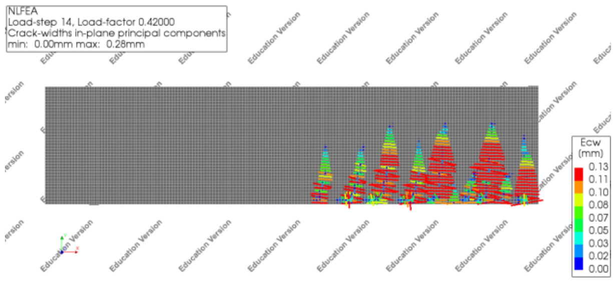

Figure 6.11 Crack Pattern Model H123A for Different Mesh Size at δ = 6.98 mm (Shifting Point B)

M80

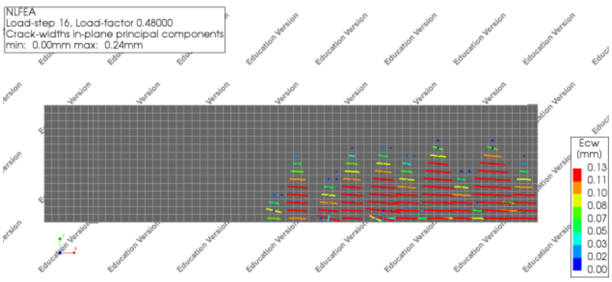

M60

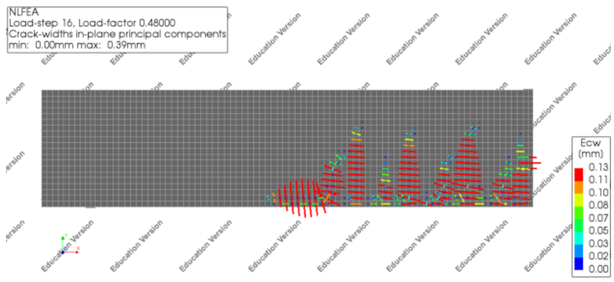

M30

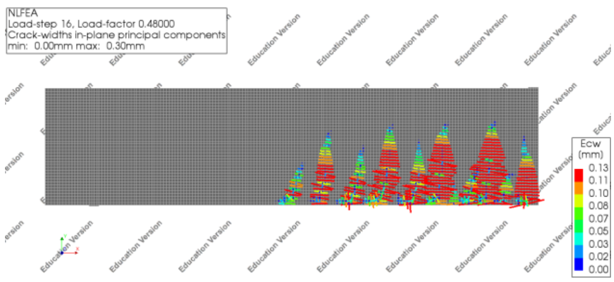

Figure 6.12 Crack Pattern Model H123A for Different Mesh Size at δ = 7.98 mm (Shifting Point C)

M80

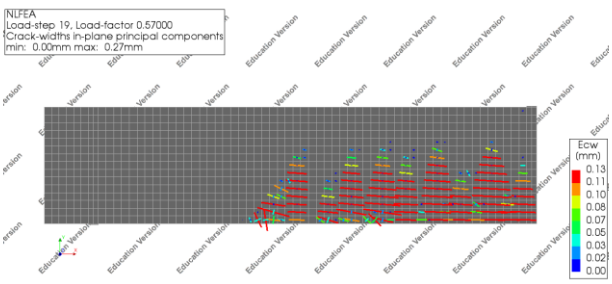

M60

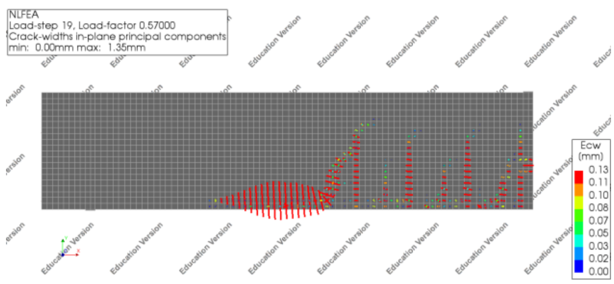

M30

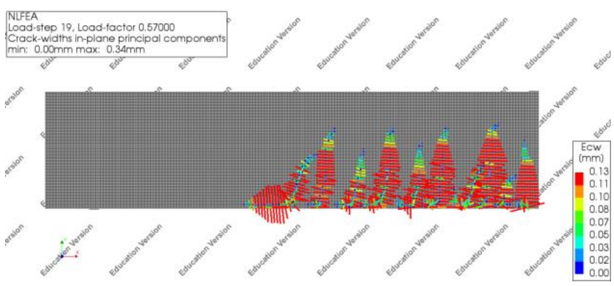

Figure 6.13 Crack Pattern Model H123A for Different Mesh Size at δ = 9.49 mm (Shifting Point D)

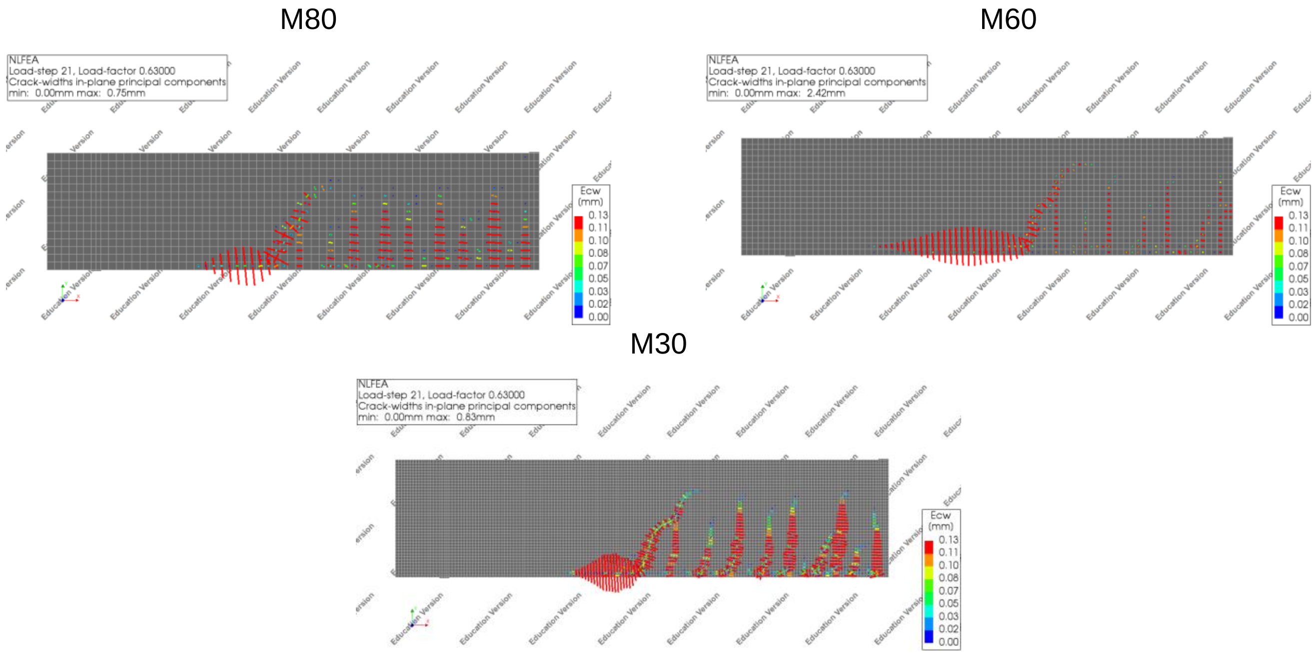

Figure 6.14 Crack Pattern Model H123A for Different Mesh Size at δ = 10.50 mm (Shifting Point E)

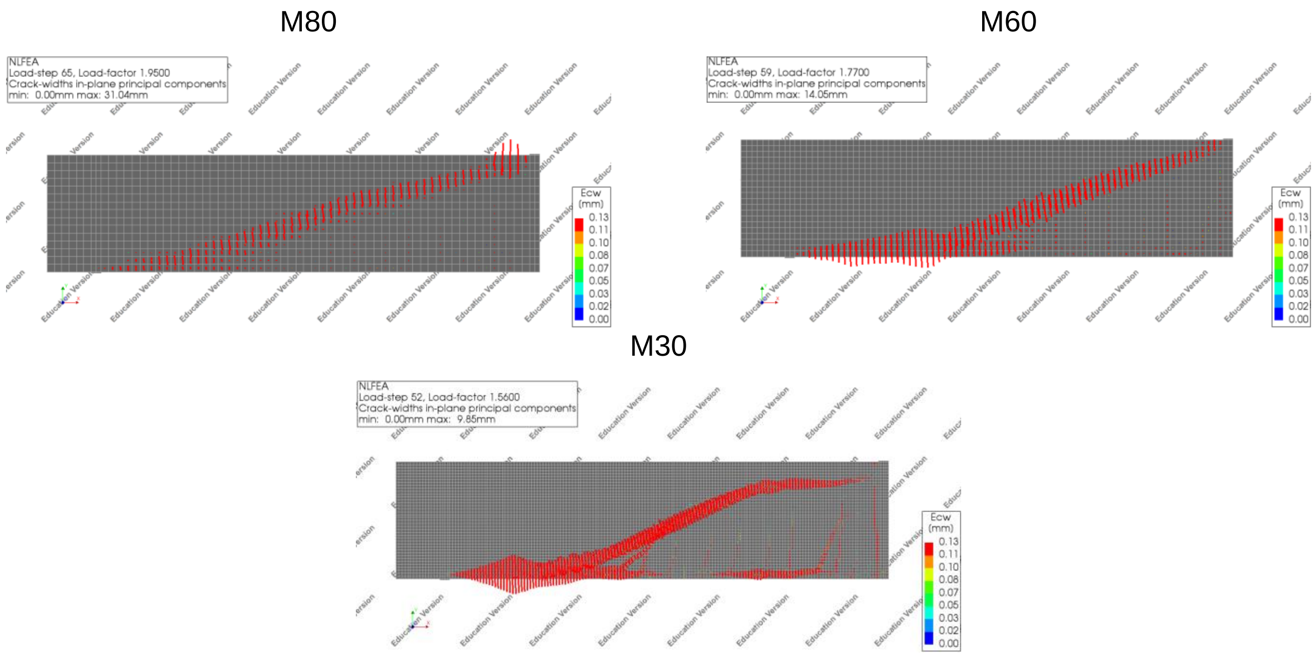

Figure 6.15 Crack Pattern Model H123A for Different Mesh Size at Peak Load

The relative energy variation and out-of-balance force in models H123A M80, M60 and M30 in Figure 6.9 is relatively constant from shifting point A to shifting point C. The relative energy variation of model H123A M60 is always higher compared to other models. From shifting point C to shifting point E, the relative energy variation and out-of-balance force of models H123A M80 and M30 are relatively increasing. A significant increase in the relative energy variation and out-of-balance force in model H123A M80 can be seen from shifting point D to E, while this phenomenon does not exist in model H123A M30.

In terms of crack pattern, models H123A M80, M60, and M30 show similar crack progression at shifting point A, while a bigger crack opening can be seen as the mesh size transition from 80 mm to 30 mm in Figure 6.10. A small dowel crack opening can be seen in model H123A M30, while no dowel crack can be seen in other models. In shifting point B, model H123A M60 starts developing dowel crack while no significant change can be seen in other model's crack patterns in Figure 6.11. The formation of dowel crack in model H123A M60 becomes more dominant in shifting point C in Figure 6.12, which cause a significant increase in the maximum crack width, while other models are still governed by flexural crack propagation. The formation of dowel crack in model H123A M30 becomes more dominant in shifting point D in Figure 6.13, while model H123A M80 is still governed by flexural crack propagation. The dowel crack starts propagating in model H123A M80 at shifting point E. However, it must be noted that the dowel crack propagation in model H123A M80 is less stable compared to other models, which can be seen by comparing the maximum crack width of Figure 6.13 and Figure 6.14 where the difference maximum crack width of model H123A M80 and M30 changes rapidly from shifting point D to E. The change in maximum crack width in model H123A M60 due to dowel crack propagation, which can be seen by observing Figure 6.11 and Figure 6.12, is more stable compared to model H123A M80 and less stable compared to model H123A M30. This phenomenon can be correlated to the convergence state of the models. It can be seen that if the relative energy variation in the model exceeds a certain threshold, the dowel crack will start propagating. All models surpassed this threshold at different shifting points, where model H123A M80 exceed the threshold at shifting point E, model H123A M60 at shifting point B, and model H123A M30 at shifting point D. If the observation is focused on this phenomenon at each shifting point, the threshold of the relative energy variation that causes the formation of the dowel crack is 0.001. The relative energy variation of model H123A M60 is higher compared to other models due to the formation of dowel crack, which adds more cracked elements to the model. The sudden increase of relative energy variation at shifting point E in model H123A M80 is due to the sudden increase in the number of cracked elements compared to the previous steps, which can be seen by comparing Figure 6.13 and Figure 6.14. Based on this observation, it can be said that in the case of simulating specimen H123A, the numerical model with a small mesh size has more stable crack propagation compared numerical model with a larger mesh size. However, this phenomenon does not affect the crack pattern at the peak load in Figure 6.15.

Based on the observation for both specimen A123A1 and H123A, it can be concluded that changing the mesh size would cause a change in the dowel crack propagation. Finer mesh would lead to more stable dowel crack propagation where the increment of the crack width between each load step becomes smaller. More stable crack propagation leads to a constant increase of the load capacity, which can be seen in Figure 6.1 whereas the mesh size reduces, the point where the stiffness change became less pronounce and completely disappeared after a certain size of the mesh is used. Furthermore, this phenomenon also implied that the initiation of dowel crack become less pronounced in the load-displacement curve of the numerical model with finer mesh. However, the formation of dowel crack can still be seen in the convergence state of the model where the formation of dowel crack is signified by the sudden increase in the relative energy variation of the model. The shifting point of this phenomenon is considered important because the shifting point controls when the numerical models would reach their peak capacity.

6.3.2 The Study of the Maximum Crack Width with Different Mesh Size

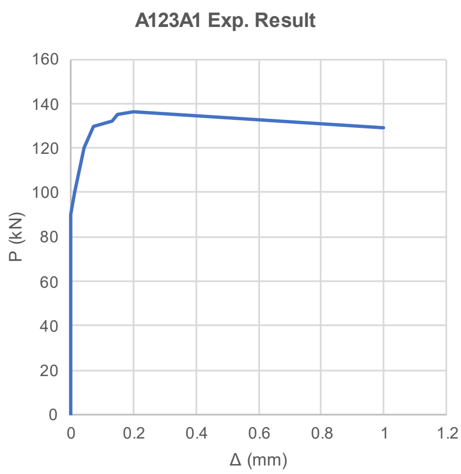

Figure 6.16 Experimental Result of Shear Displacement of Specimen A123A1

Source: (Koekkoek & Yang, 2016)

As the numerical model usually reached an un-realistic magnitude of maximum crack width, which can be seen in Figure 6.8 and Figure 6.15. The term "un-realistic" is used due to a significant difference in the crack opening compared to the experimental result, which can be seen in Figure 6.16. In the experimental result, the peak load is reached when the vertical crack opening of specimen A123A1 is equal to 0.2 mm. The progression of the vertical crack opening on the major flexural shear crack of the numerical model must be observed further. The vertical crack opening is going to be referred as the shear displacement in this report. The observation is done by analysing the load vs shear displacement at the mid-height of the major flexural shear crack opening in Figure 6.17.

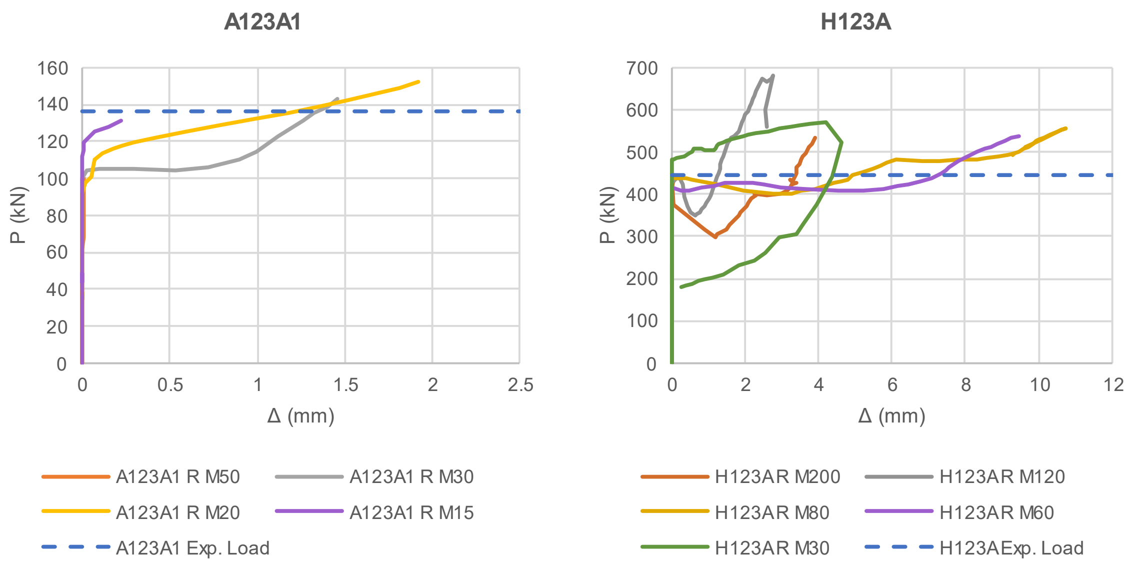

Figure 6.17 The Simulated Shear Displacement Progression as the Load Increase

Based on Figure 6.17, it can be seen that the shear displacement starts increasing after a certain magnitude of load applied on the beam. In the numerical model with specimen A123A1, the shear displacement can increase up to 2 mm before reaching failure. On the other hand, the numerical model with specimen H123A shows that the shear displacement can increase up to 11 mm before reaching failure. Several models for specimen A123A1 and all models for specimen H123A overestimated the peak load due to excessive vertical crack propagation. In order to solve this problem, Figure 6.18 is plotted to see the load increase at the early stage of the vertical cracking.

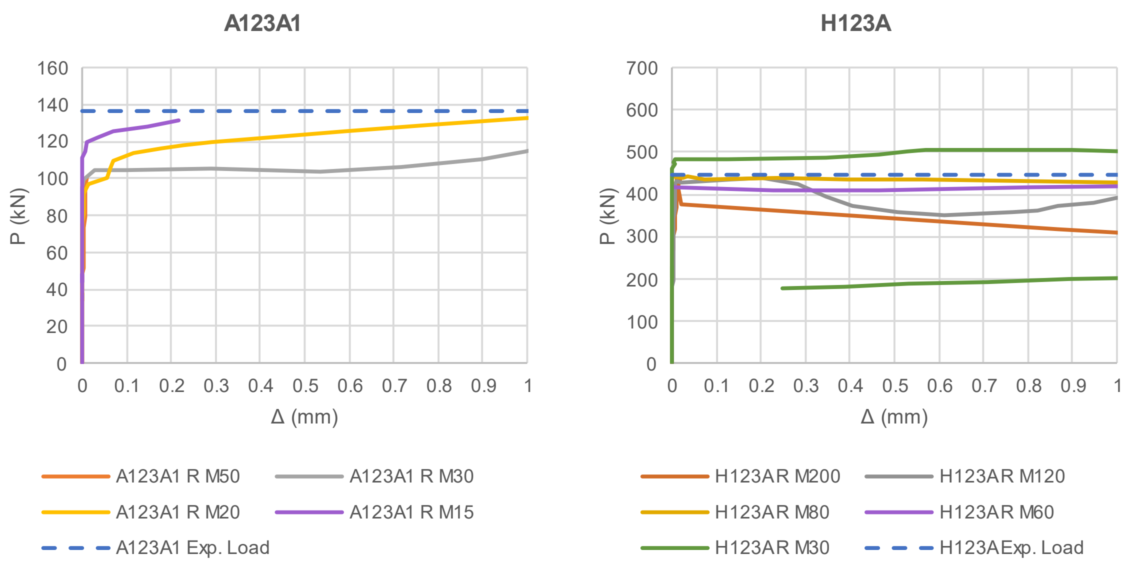

Figure 6.18 The Simulated Vertical Crack Width Progression up to 1 mm

When the shear displacement is limited up to 1 mm, the maximum load capacity of the beam is underestimated in most of the models for both specimens in Figure 6.18. In the NLFEA, each concrete element is assigned with a specific material behaviour where the ultimate tensile crack width can be calculated. The ultimate tensile crack width is defined as the crack width where all fracture energy of the element has been consumed, which can be calculated by multiplying the ultimate tensile strain with the mesh size. The ultimate tensile strain is calculated based on Guidelines for Nonlinear Finite Element Analysis of Concrete Structures (Hendriks & Roosen, 2020). For both specimens, the ultimate tensile crack width is roughly equal to 0.13 mm, which is similar to the maximum vertical crack opening of the experimental result in Figure 6.16. If the ultimate tensile crack width is used for post-processing in combination with the previously defined convergence criteria, the peak load is reduced in most of the models, which can be seen in Figure 6.19.

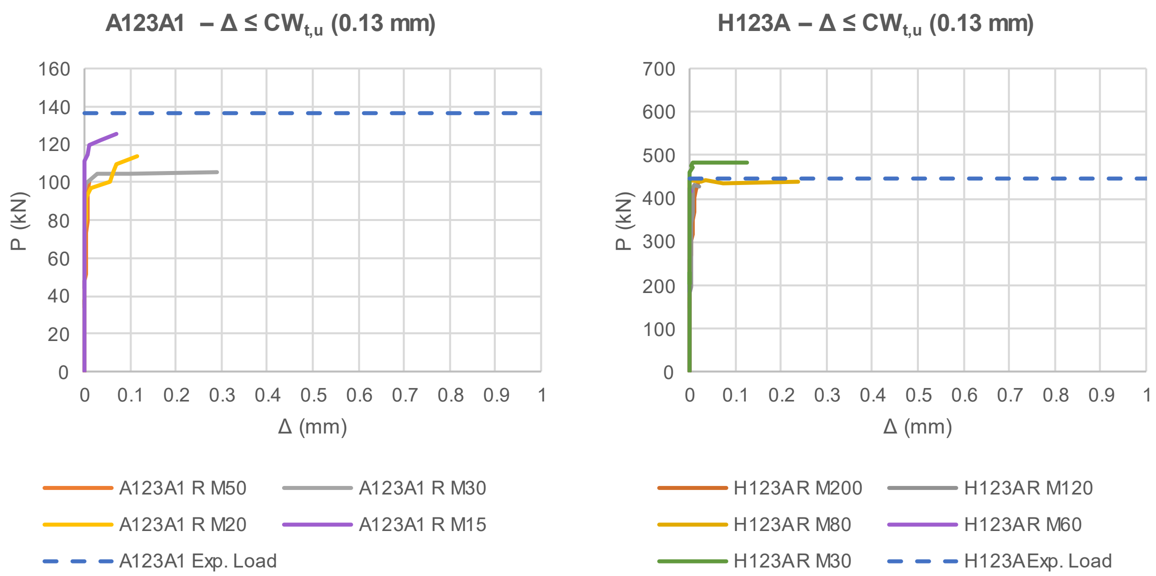

Figure 6.19 The Simulated Shear Displacement Progression up to Ultimate Tensile Crack

Table 6.2 Peak Load with Shear Displacement ≤ 0.13 mm

Code	Element Size (mm)		Size Ratio		Peak Load* (kN)		Peak Load Ratio**	
	A123A1	H123A	A123A1	H123A	A123A1	H123A	A123A1	H123A
M15	15	-	h/20	-	125.30	-	0.92	-
M20	20	-	h/15	-	114.02	-	0.84	-
M30	30	30	h/10	h/40	104.98	484.31	0.77	1.09
M50	50	-	h/6	-	100.25	-	0.73	-
M60	-	60	-	h/20	-	424.25	-	0.95
M80	-	80	-	h/15	-	443.11	-	1.00
M120	-	120	-	h/10	-	430.96	-	0.97
M200	-	200	-	h/6	-	445.27	-	1.00

* The peak load is referred to as the maximum load that a beam can be sustained based on the result of simulation with NLFEA
** The peak load ratio is calculated based on the peak load of the numerical models divided by experimental peak load

Figure 6.19 shows that most of the peak load predictions in the models are underestimated. The exact value of the peak load in the model can be observed in Table 6.2. In order to have a satisfactory simulated result, the behaviour of the load-displacement curve should be observed, and the simulated failure mode must be in accordance with the experimental results. The modified load-displacement curve can be seen in Figure 6.20.

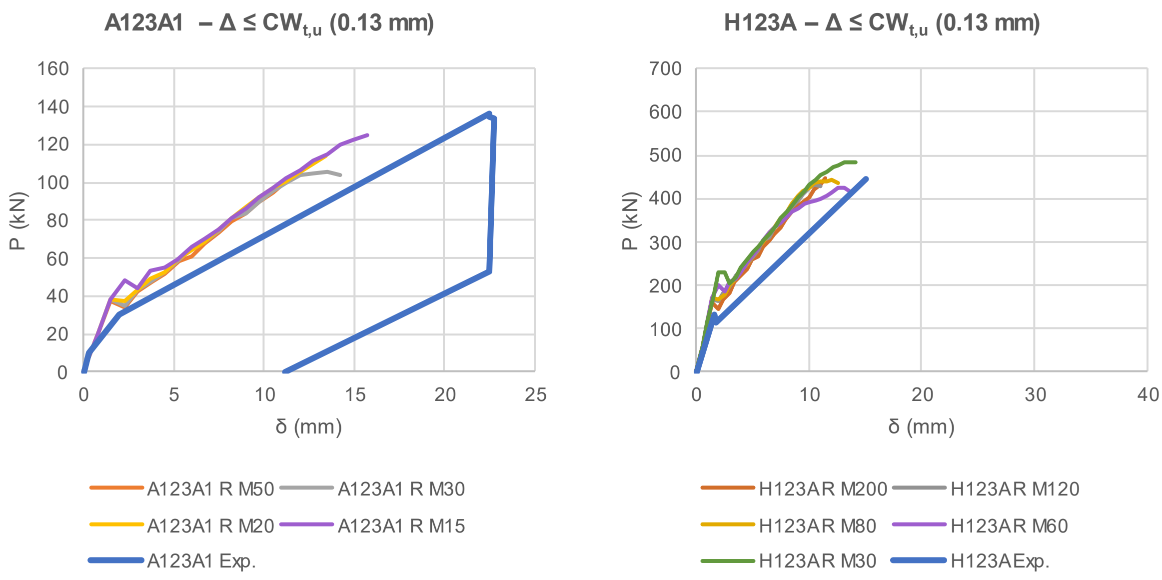

Figure 6.20 Load-displacement Curve with $\Delta \leq CW_{t,u}$

If Figure 6.20 is compared to Figure 6.1, it can be seen that the first peak of Figure 6.1 corresponds to the peak of Figure 6.20 in the numerical model for specimen H123A. Therefore, it is recommended to use the first peak found on the load-displacement curve as the peak load of the numerical models. As almost all models give an underestimated peak load, the next aspect that needed to be verified is the simulated failure mode.

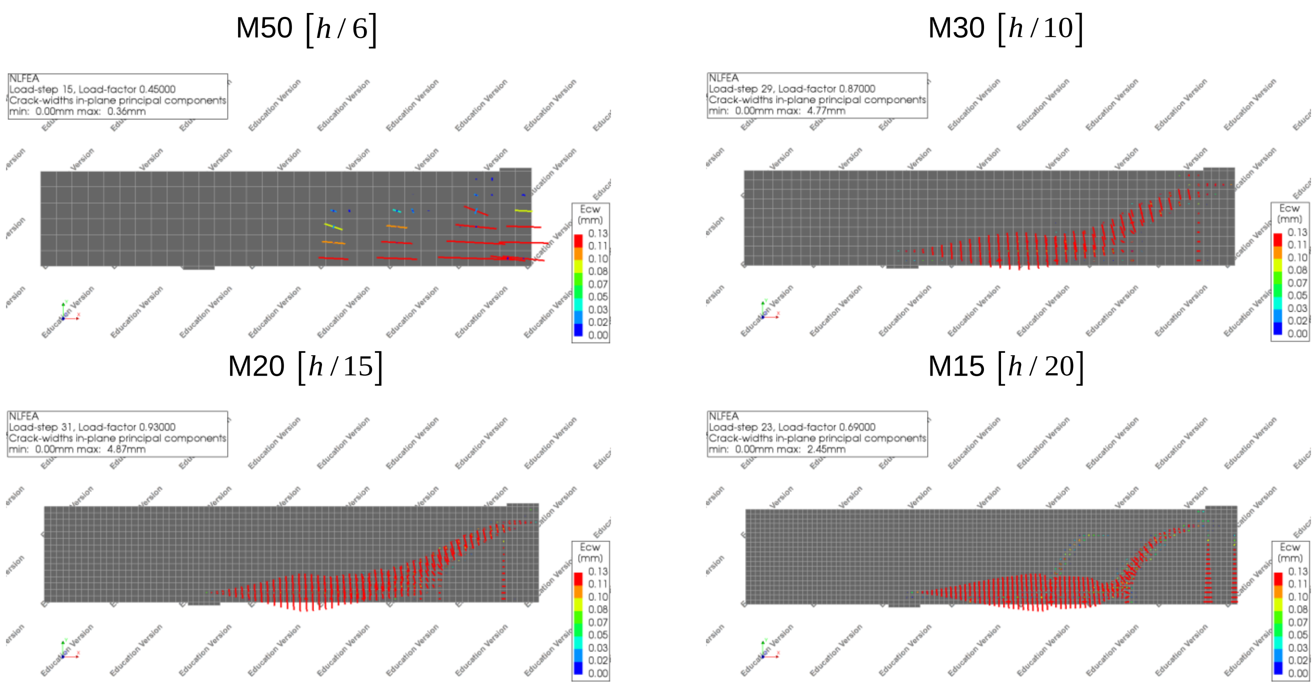

Figure 6.21 Crack Pattern Model A123A1 for Different Mesh Size at Peak Load of Figure 6.1

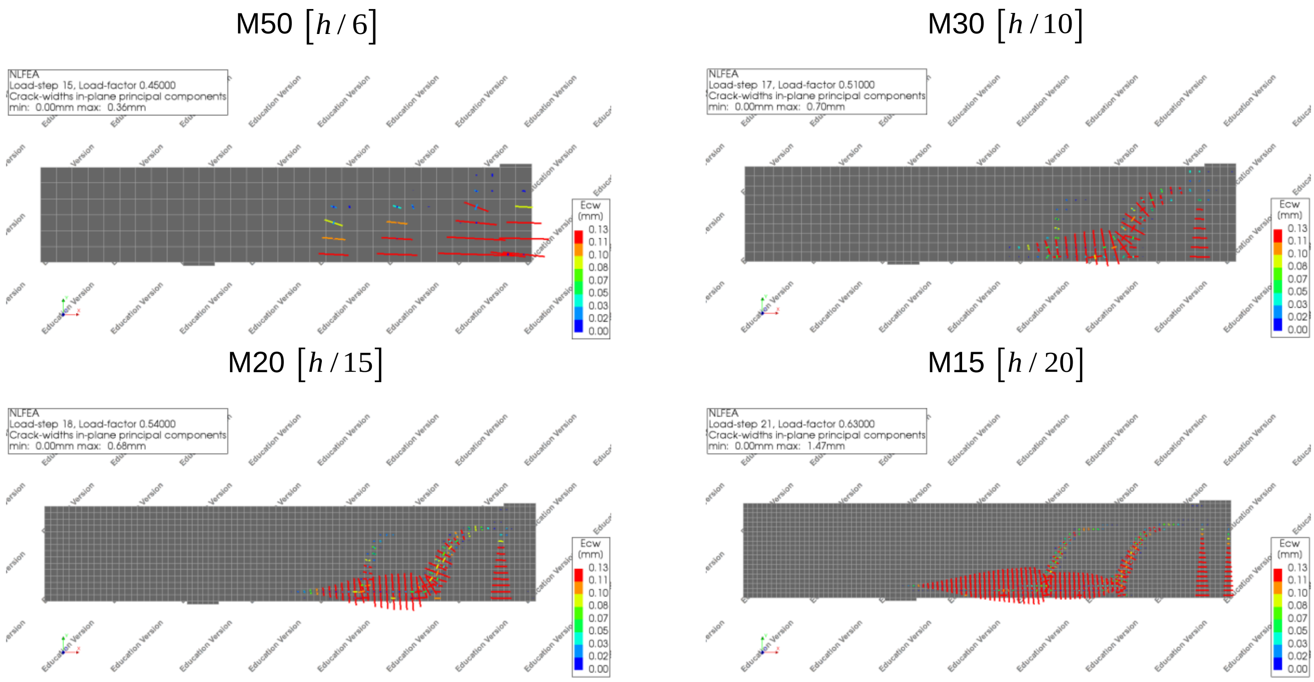

Figure 6.22 Crack Pattern Model A123A1 for Different Mesh Size at Peak Load of Figure 6.20

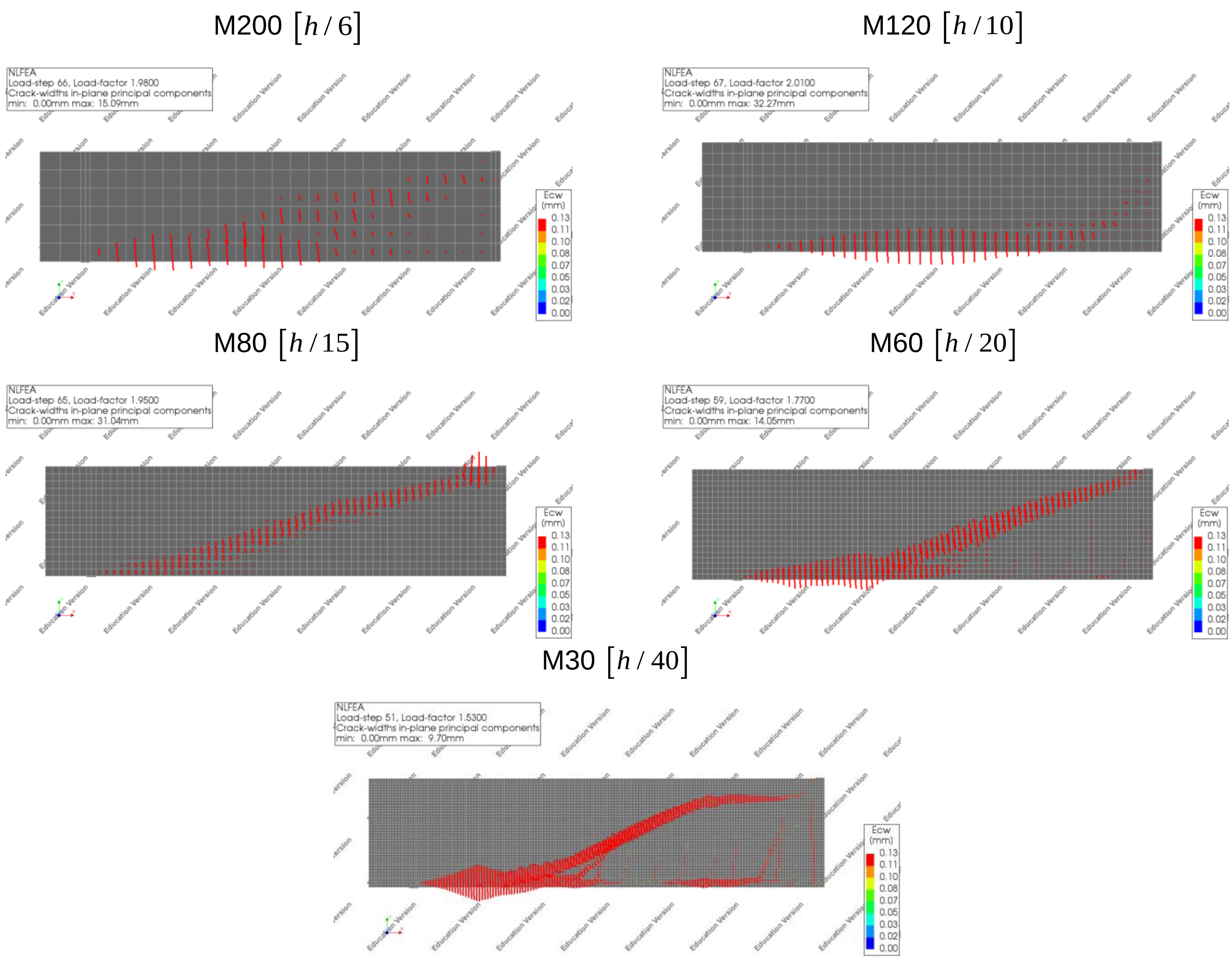

Figure 6.23 Crack Pattern Model H123A for Different Mesh Size at Peak Load of Figure 6.1

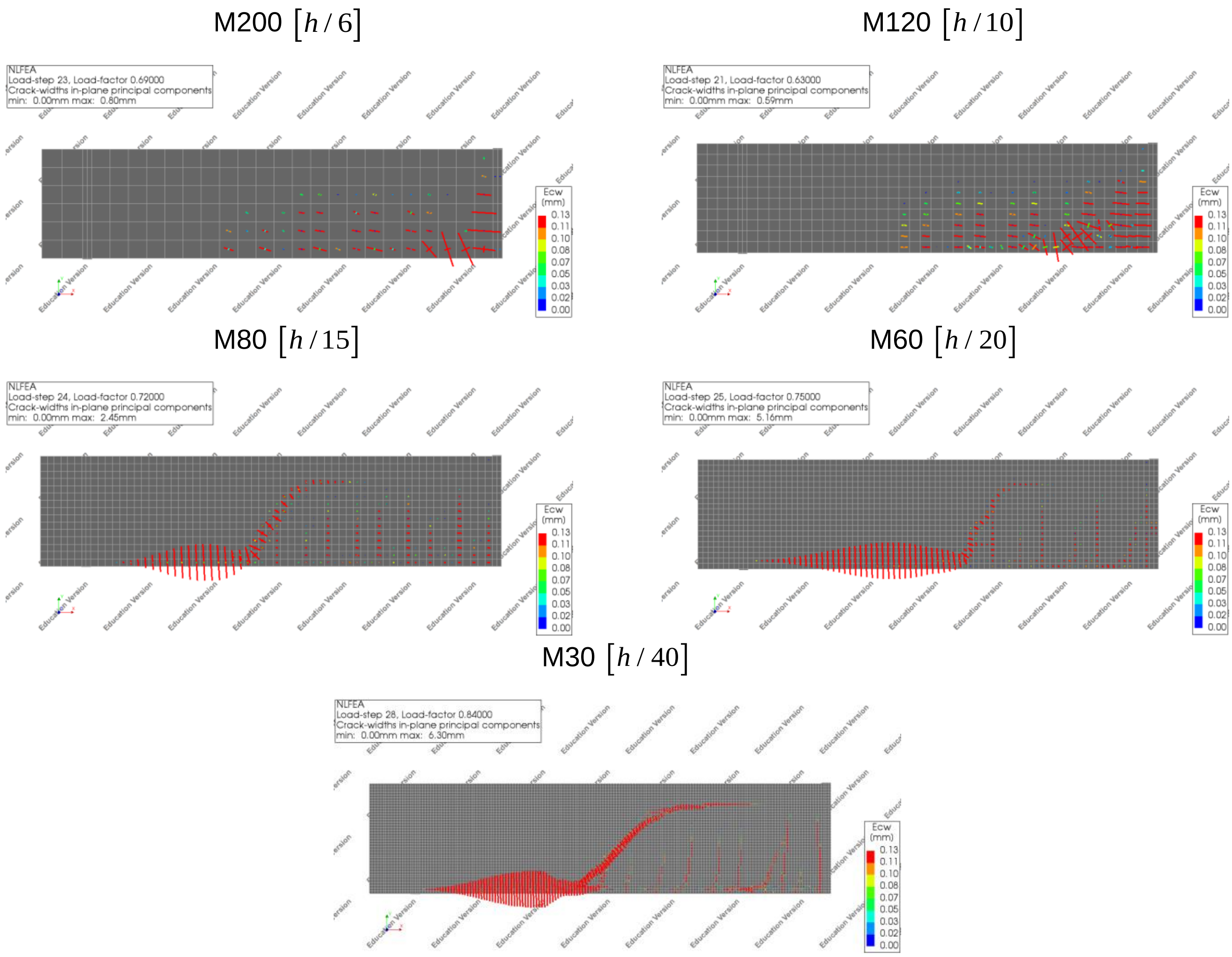

Figure 6.24 Crack Pattern Model H123A for Different Mesh Size at Peak Load of Figure 6.20

Figure 6.22 and Figure 6.24 illustrate the crack pattern for the model with specimen A123A1 and H123A respectively, for the defined peak in Figure 6.20. Figure 6.21 and Figure 6.23 illustrate the crack pattern for the model with specimen A123A1 and H123A respectively, for the defined peak in Figure 6.1. It can be seen that the numerical model with mesh size equal to 50 mm for specimen A123A1 cannot simulate the failure mode properly in any models either referring to Figure 6.1 or Figure 6.20. The same phenomenon can also be seen in the numerical model with mesh size equal to 200 mm and 120 mm for specimen H123A referring to Figure 6.20, while the numerical model for specimen H123A with any mesh can simulate the failure mode properly if the peak is referring to Figure 6.1. Furthermore, it can be seen that as the mesh size decrease, the flexural shear crack appearance becomes more obvious in the model.

6.4. The Rate of Dowel Crack Propagation vs Mesh Size

The relation between the rate of dowel crack propagation and mesh size can be understood by observing the crack propagation length of the numerical model. The crack propagation length can be indirectly seen from the strain development of the element above the reinforcement on the shear span. Model A123A1 M30 and M20 are used for the observation. 4 load steps are chosen to be observed according to Figure 6.3, where the load-displacement curve starts to deviate. The illustration of the strain development and the crack length of the element above the reinforcement is given in Figure 6.25 and Figure 6.26 respectively.

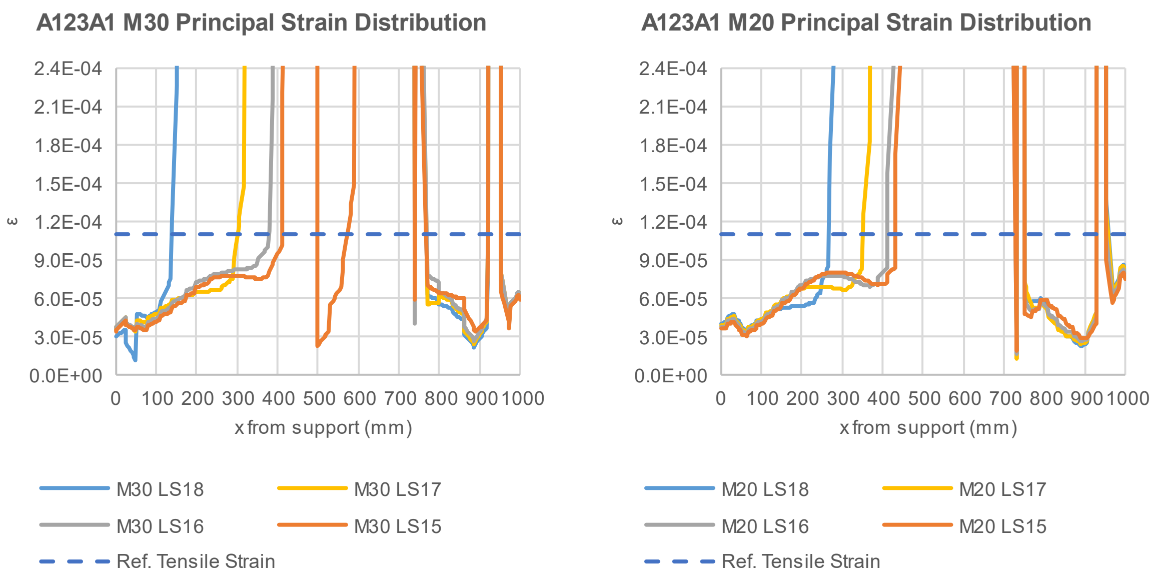

Figure 6.25 Strain Development of Numerical Models with Different Mesh Size

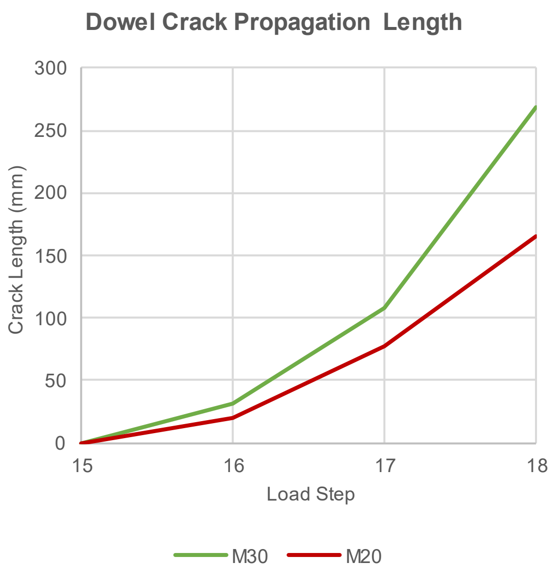

Figure 6.26 Length of Dowel Crack for Numerical Models with Different Mesh Size

This figure is made by referring to Figure 6.25 from $x = 0$ to $x = 400$ mm

From load steps 15 to 16, the strain increases at $x = 0$ to $x = 400$ mm is similar for both models, which is reflected in the length of the dowel crack as well. The strain starts to develop faster in model A123A1 M30 compared to model A123A1 M20 from load steps 16 to 17, which also cause the dowel crack length to have a larger increase in model A123A1 M20. A larger difference in the strain development and dowel crack length between model A123A1 M30 and M20 can be seen from load steps 17 to 18. The change in the rate of strain development and dowel crack length can be explained with an illustration in Figure 6.27.

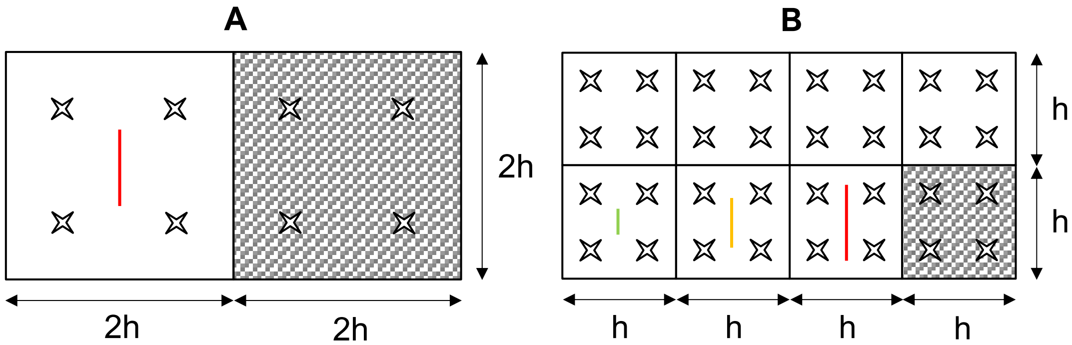

Figure 6.27 Illustration of Stress State of the Element above the Reinforcement*

* the stars indicate the integration points, the red, orange and green lines with their size indicate the magnitude of the tensile stress.

Assume that illustrations A and B in Figure 6.27 are the magnified version of the element above the reinforcement when the formation of the dowel crack has started. If one of the integration points has reached the reference tensile strain in Figure 6.25, then the element is considered cracked, as the tensor of either stress or strain is usually represented by only one line in NLFEA. In illustration A, the crack development length is equal to 2h while in illustration B is equal to h at the formation of the dowel crack. The difference in the crack development length will continue as the dowel crack propagates, causing the model represented with illustration A to have dowel crack propagating to the support faster compared to the model represented with illustration B. Furthermore, the area of the cracked element is larger in illustration A compared to B, resulting in different equilibrium conditions which increase the probability of higher stress in the adjacent element for illustration A in order to compensate for the stress loss on the respective element. This phenomenon is becoming more apparent in the strain development in Figure 6.25 due to the effect of excessive change of the principal stress-strain direction and magnitude, which is described in subchapter 5.6.

6.5. Derivation of Mesh Size Criteria

In order to derive the mesh size criteria, two aspects are going to be considered, the qualitative aspects of the results of NLFEA and the quantitative value of the peak load from the results of NLFEA. In terms of the qualitative aspect, as mentioned in subchapter 6.3 Effect of Mesh Size Variation, the use of smaller mesh size changes the rate of dowel crack propagation and affects the initiation of the dowel crack formation. These phenomena cause the peak load variation between numerical models with different mesh sizes. Furthermore, the crack pattern at the peak load is not affected in most cases.

Table 6.3 Comparison of Peak Load with and without Shear Displacement Criterion

Code	Size Ratio		Peak Load 1* (kN)		Peak Load 2** (kN)		Peak Load 1 Ratio*		Peak Load 2 Ratio**	
	A123A1	H123A	A123A1	H123A	A123A1	H123A	A123A1	H123A	A123A1	H123A
M15	h/20	-	131.41	-	125.30	-	0.96	-	0.92	-
M20	h/15	-	151.96	-	114.02	-	1.11	-	0.84	-
M30	h/10	h/40	142.98	572.44	104.98	484.31	1.05	1.29	0.77	1.09
M50	h/6	-	100.25	-	100.25	-	0.73	-	0.73	-
M60	-	h/20	-	539.14	-	424.25	-	1.21	-	0.95
M80	-	h/15	-	557.58	-	443.11	-	1.25	-	1.00
M120	-	h/10	-	682.20	-	430.96	-	1.53	-	0.97
M200	-	h/6	-	534.02	-	445.27	-	1.20	-	1.00

* Peak Load 1 is defined as the peak load obtained from the load-displacement curve without satisfying the shear displacement criterion ≤ $CW_{t,u}$

** Peak Load 2 is defined as the peak load obtained from the load-displacement curve with satisfying the shear displacement criterion ≤ $CW_{t,u}$

When the quantitative value is observed, there is a large distribution on the peak load with different mesh. The information regarding the peak load is given in Table 6.3. The peak load ratio distribution for specimen A123A1 and H123A is equal to 0.73-1.11 and 1.20-1.53 respectively. These distributions can be reduced by introducing an additional criterion related to the vertical crack width, where the peak load ratio distribution is changed to 0.73-0.92 for specimen A123A1 and 0.95-1.09 for specimen H123A. However, the change in the peak load distribution also impacted the simulated failure mode of the models. In subchapter 6.3 Effect of Mesh Size Variation, the use of shear displacement criterion resulted in wrong failure mode at the peak load for numerical model with mesh size equal to 50 mm for specimen A123A1 and mesh size equal to 200 mm and 120 mm for specimen H123A. This indicates that the numerical model with a mesh size ratio less than $h/15$ cannot simulate shear failure mode properly. Therefore, it is recommended to use a mesh size ratio larger than $h/15$. The use of maximum mesh size is not given as a recommendation because the use of small maximum mesh size resulted in a huge number of elements on large beams, such as specimen H123A, which increase the computation time significantly and does not give any additional advantage to the results compared to numerical model with a smaller number of elements/larger mesh size.

6.6. Summary

The sensitivity analysis is done for a total of 9 variations of mesh size, which consist of 4 variations of mesh size ranging from 15 mm $(h/20)$ to 50 mm $(h/6)$ and 5 variations ranging from 30 mm $(h/40)$ to 200 mm $(h/6)$ for the numerical model with specimen A123A1 and H123A respectively. The study is mainly using the numerical model with the rotating crack model and applying the convergence criteria from chapter 5.

The mesh size influences the initiation and propagation of the dowel crack. The initiation of the dowel crack begins at different load levels with a random pattern. The initiation can be identified from observing the convergence state of the analysis where the initiation of the dowel crack is usually accompanied by a sudden increase in the relative energy variation. The propagation of the dowel crack becomes more stable as the size of the mesh becomes smaller. The stability of the dowel crack propagation is identified from the increment of the crack width between each load step where small increments equal higher stability.

As explained in subchapter 5.6, the initiation of the dowel crack propagation is varying in the different models due to the sudden change in the stress-strain condition of the model, which leads to excessive rotation of the principal strain direction in the element and causes premature dowel crack opening in the numerical model. This also affects the convergence state where the bad convergence can be seen in the later stage of the NLFEA.

The mesh size is influencing the propagation of the dowel crack due to different equilibrium conditions found in the numerical models with different mesh sizes. The numerical model with a large element size has a bigger dowel crack opening compared to the numerical model with a small element size. This phenomenon causes two other phenomena. The first phenomenon is that the change in the simulated non-linear stiffness becomes more apparent in the load-displacement curve as the element size is increased. The second phenomenon is that the formation of the dowel crack becomes more pronounced as the element size increase. These phenomena are becoming more apparent due to the effect of excessive rotation of the principal strain, which is described in subchapter 5.6.

Almost all numerical model variations are able to simulate the correct failure, but at the peak load, the numerical models predict an excessive crack opening of the major flexural shear crack. In order to reduce the crack opening, another criterion is used in the post-processing where the analysis steps are considered valid if the shear displacement of the major flexural shear crack (Δ) in the numerical model at the corresponding step is below the ultimate tensile crack width $(CW_{t,u})$, which is calculated from the Guidelines for Nonlinear Finite Element Analysis of Concrete Structures (Hendriks & Roosen, 2020). The ultimate tensile crack width of both specimens is equal to 0.13 mm. However, the failure mode at the peak load changes due to this process and a mesh size ratio larger than $h/15$ is required in order to have the correct simulated failure mode. A maximum mesh size ratio is not defined as the use of small maximum mesh size resulted in a huge number of elements in large beams, such as specimen H123A, which increases the computation time significantly and does not give any additional advantage to the results compared to numerical models with a smaller number of elements or larger mesh size. It must be noted that the minimum mesh size ratio is only derived based on two specimens and further study is needed to determine whether the ratio should be increased or can be decreased.

7 Conclusion and Recommendation

7.1. Overview of the Study

The numerical simulations of flexural shear failure in reinforced concrete beams without shear reinforcement in NLFEA show a large scatter of results in terms of peak load. This study is trying to investigate the cause of this phenomenon and how to increase both the accuracy and precision of the results. The investigation is done for two beams specimen which fails in flexural shear. The investigation is strictly limited to cases with similar shear slenderness (a/d). These beams have a total height (h) of 300 mm and 1200 mm, a shear span (a) of 1000 mm and 4500 mm, and shear slenderness (a/d) of 3.70 and 3.91 respectively.

The study is divided into three stages:

1. The first stage is done to investigate how the flexural shear failure mode can be obtained with NLFEA by studying the results of 16 models with different numerical configurations of the following variables:
   a. Cracking model (Rotating and Fixed crack model)
   b. Reinforcement configuration (With or without top reinforcement)
   c. Convergence criteria (Energy and Force)
   d. Incremental iterative analysis methods (Quasi-Newton, Full Newton-Raphson and Modified Newton-Raphson)

   It was found that bad convergence was achieved at the later stage of the analysis and by not accepting non-converged steps, the results became dependent on the convergence state of the analysis where different peak loads were achieved in different numerical configurations for a single case study.

2. The second stage is done to investigate the influence of different numerical parameters on the results of NLFEA and whether these dependencies have an influence on the convergence state of the analysis. All load steps are accepted in this stage, regardless of their convergence state, and the rotating crack model is used in these numerical models. The investigation is done for the following numerical parameters:
   a. Load increment ratio (0.004 to 0.1 times the experimental total deformation)
   b. Error tolerance (Energy and Force Tolerance with 0.0001-0.005)
   c. Maximum Number of Iterations (10 to 100 per load step)

   It was found that the results of NLFEA were dependent on these numerical parameters due to its influence in the process of initiation and propagation of dowel crack on each analysis. This happens due to a sudden change in the stress-strain condition of the numerical model when a dowel crack initiates and propagates. As a result, the principal stress-strain of the element above the reinforcement change its direction and magnitude excessively, causing a bad convergence in the later stage of the analysis.

   An additional study is done by replacing the crack model with a fixed crack model with a damage-based shear retention model. It was found that this did not solve the problem due to the excessive change in the shear retention factor on the elements where dowel crack is formed and propagating, which lead to premature failure of the beam.

3. The third stage is done to investigate the influence of the mesh size on the results of NLFEA. The numerical models use the rotating crack model and the results are evaluated with the convergence criteria developed in the second stage. The investigation is done for the following variations:
   a. Specimen A123A1 with $h = 300$ mm: $h/20 - h/6$ (h_{ele}: 15, 20, 30, 50 mm)
   b. Specimen H123A with $h = 1200$ mm: $h/40 - h/6$ (h_{ele}: 30, 60, 80, 120, 200 mm)

   It was found that the results of NLFEA were dependent on the mesh size due to the difference in initiation and propagation rate of dowel crack. The difference in dowel crack initiation is caused by the excessive change of the principal stress-strain on the element above the reinforcement, as mentioned in the previous stage. The difference in dowel crack propagation rate is caused by different increments of the dowel crack length between each load step, where the dowel crack length is following the size of the mesh. This cause the dowel crack length to varies with different mesh, making the dowel crack longer in the numerical model with a larger mesh size. Furthermore, the difference in dowel crack length also affects the equilibrium conditions found by the numerical model where a different load capacity can be found at the same level of displacement.

7.2. Conclusions

Based on the study that has been performed, the following conclusions can be drawn:

1. The use of different values for the numerical parameters, such as load increment, error tolerance, and the maximum number of iterations influence the initiation and propagation of the dowel crack. This causes an excessive change of the principal stress-strain direction and magnitude on the element above the reinforcement. As a result, convergence is difficult to achieve in the later stage of analysis. However, it is not necessary to reach convergence at each load step, as it is still possible to simulate the shear failure mode with sufficient accuracy with the recommended choice of numerical parameters.

2. The result of NLFEA is dependent on the numerical parameters such as load increment, error tolerance, and the maximum number of iterations, as the error found on each step in the analysis is determined based on the chosen value of these parameters in the numerical model. These parameters are also used to define the magnitude of the accepted errors in the critical steps that could not converge. As a result, the accumulation of the error eventually influences the simulated peak load.

3. The excessive change of principal stress-strain is influencing the iterative-incremental method differently due to different methods of forming the global stiffness matrix of the numerical model.

4. The use of the fixed crack model with damage-based shear retention model in the numerical model is not able to solve the excessive change of principal stress-strain on the element above the reinforcement due to the excessive change in the shear retention factor on the elements where dowel crack is formed and propagating, which lead to premature failure of the beam.

5. The use of different sizes of mesh influences the initiation and propagation rate of the dowel crack. The initiation of the dowel crack causes an excessive change of the principal stress-strain direction and magnitude on the element above the reinforcement. The propagation rate of the dowel crack is dependent on the mesh size where a smaller increment of the dowel crack length between each load step can be achieved with a reduction of the size of the mesh.

6. Numerical models with very large mesh sizes cannot simulate the development of flexural shear crack properly and give an overestimation of the shear displacement on the crack opening.

7.3. Recommendation for Practice

Based on the study that has been performed, the following recommendations are given to reach a reliable simulation of shear failure for members without shear reinforcement:

1. The use of Full Newton-Raphson is recommended for the simulation of shear failure with NLFEA, as it gives the smallest variation of the peak load ratio (P_{norm}), ranging from $0.887-1.140$ for specimen A123A1 and $1.055-1.246$ for specimen H123A, compared to the other iterative-incremental method when the analysis is done with a load increment ratio (load increment/experimental peak load) within $0.03-0.006$ and an error tolerance of $G_{err}=0.0001$ and $F_{err}=0.01$. Non-converged steps can still be

accepted if the relative energy variation and out-of-balance force of the corresponding step are below 0.03 and 0.58 respectively. Further detail of the comparison of the peak load ratio variation with different iterative-incremental methods is given in Table 5.6.

2. An additional criterion can be added to the evaluation of the acceptable analysis step in order to prevent an excessive crack opening on the major flexural shear crack at the peak load. The analysis step can still be considered valid if the shear displacement on the major flexural shear crack (Δ) on the respective step is below the ultimate tensile crack width $(CW_{t,u})$, which can be calculated from the Guidelines for Nonlinear Finite Element Analysis of Concrete Structures (Hendriks & Roosen, 2020).

3. The mesh size should be smaller than $h/15$ to simulate the flexural shear failure correctly with a realistic crack opening. The mesh size should only be sufficiently smaller than the limit, as decreasing the mesh size will also increase the computation time and based on the study that has been performed, no significant improvement can be seen in the result.

7.4. Recommendations for Further Study

Based on the study that has been performed, the following recommendations are given for further study related to this topic:

1. The study indicates that the dependency of the result to the numerical parameters is the initiation and formation of the dowel crack. Further analysis should be performed to understand how does the stress-strain in the element just above the reinforcement changes after the flexural shear crack is formed and its correlation to the crack development of the corresponding flexural crack.

2. As the study is limited to two specimens with comparable shear slenderness, the convergence criteria and the mesh size criteria should be tested for more specimens with a different shear span (a), beam depth (d) and shear slenderness (a/d) in order to see whether it gives satisfactory results or the criteria needs further modification.

3. Based on the results of the study, the use of the rotating crack model with the Full Newton-Raphson method still causes a certain level of overestimation in the peak load ratio. Further analysis should be done on how each component of NLFEA works in order to understand the reason behind this phenomenon. This can be done by performing sensitivity analysis for all parameters of the model in order to determine the necessity of each parameter. This could also help reduce the number of non-linearities, which will result in shorter computational time and increase the number of converged steps in NLFEA.

4. The use of the fixed crack model with damage-based shear retention model results in excessive loss of shear retention factor. Further study is needed to identify the cause of this phenomenon and whether the use of different shear retention models can solve this problem. Sensitivity analysis can also be done afterwards in order to see its dependency on the numerical parameters, such as load increment, error tolerance, the maximum number of iterations and mesh size.

Bibliography

An, X., Maekawa, K., & Okamura, H. (1997). Numerical Simulation of Size Effect in Shear Strength of RC Beams. *ResearchGate*.

Balakrishnan, S., & Murray, D. W. (1986). *Finite Element Prediction of Reinforced Concrete Behavior.* Edmonton: Department of Civil Engineering University of Alberta.

Balakrishnan, S., Elwi, A. E., & Murray, D. W. (1988). Effect of Modeling on NLFE Analysis of Concrete Structures. *ASCE: Journal of Structural Engineering*.

Bažant, Z. P., & Kazemi, M. T. (1991). Size Effect on Diagonal Shear Failure of Beams without Stirrups. *ACI Structural Journal 88(3)*, 268-276.

Bazant, Z. P., & Oh, B. H. (1983). Crack Band Theory for Fracture of Concrete. *Materiaux et Constructions*.

Bazant, Z. P., & Yu, Q. (2009). Universal Size Effect Law and Effect of Crack Depth on Quasi-Brittle Structure Strength. *ASCE: Journal of Engineering Mechanics*.

Bazant, Z. P., Ozbolt, J., & Eligehausen, R. (1994). Fracture Size Effect: Review of Evidence for Concrete Structures. *ASCE*.

Borst, R. d., & Nauta, P. (1985). Non-Orthogonal Cracks in a Smeared Finite Element Model. *Emerald: Engineering Computations*.

Broujerdian, V., & Kazemi, M. T. (2016). Nonlinear Finite Element Modeling of Shear-Critical Reinforced Concrete Beams using a Set of Interactive Constitutive Laws. *Springer Link*.

Cervenka, J., Cervenka, V., & Laserna, S. (2018). On Crack Band Model in Finite Element Analysis of Concrete Fracture in Engineering Practice. *Elsevier: Engineering Fracture Mechanics* .

Cervenka, V., Cervenka, J., Pukl, R., & Sajdlova, T. (2016). Prediction of Shear Failure of Large Beam based on Fracture Mechanics. *Research Gate*. doi:10.21012/FC9.029

Channakeshava, C., & Iyengar, K. T. (1988). Elasto-Plastic Cracking Analysis of Reinforced Concrete. *ASCE: Journal of Structural Engineering*.

Choi, C.-K., & Kwak, H.-G. (1990). The Effect of Finite Element Mesh Size in Nonlinear Analysis of Reinforced Concrete Structures. *Computer and Structures*.

Collins, M. P., & Kuchma, D. A. (1999). How Safe are Our Large, Lightly Reinforced Concrete Beams, Slabs, and Footings? *ACI Structural Journal 96(4)*, 482-490.

Cook, R. D. (1995). *Finite Element Modeling for Stress Analysis.* Canada: John Wiley & Sons, Inc.

Cook, R. D., Malkus, D. S., Plesha, M. E., & Witt, R. J. (2002). *Concepts and Applications of Finite Element Analysis: Fourth Edition.* John Wiley & Sons, Inc.

De Putter, A. (2020). *Towards A Uniform and Optimal Approach for Safe NLFEA of Reinforced Concrete Beams: Quantification of the Accuracy of Multiple Solution Strategies using A Large Number of Samples.* Delft: TU Delft.

DeCoursey, W. J. (2003). *Statistics and Probability for Engineering Applications with Microsoft Excel.* Elsevier Science (USA).

Deng, Q., Yi, W.-J., & Tang, F.-J. (2017). Effect of Coarse Aggregate Size on Shear Behavior of Beams without Shear Reinforcement. *ACI Structural Journal: Technical Paper*.

DIANA FEA. (2020). *DIANA Finite Element Analysis*. Retrieved from User Manual -- Release 10.4: https://dianafea.com/manuals/d104/Diana.html

Fenwick, R. C., & Paulay, T. (1968). Mechanisms of shear resistance of concrete beams. *ASCE: Structural Division Vol. 94 No. 10*, 2325-2350.

Fisker, J., & Hagsten, L. G. (2016). Mechanical Model for the Shear Capacity of R/C Beams without Stirrups: A Proposal based on Limit Analysis. *Elsevier: Engineering Structures*.

Hendriks, M. A., & Roosen, M. A. (2020). *Guideline for Nonlinear Finite Element Analysis of Concrete Structures.* Rijkswaterstaat Centre for Infrastructure.

Huang, Z., Lü, Z., Song, S., Tu, Y., Blanksvärd, T., Sas, G., & Elfgren, L. (2018). Finite Element Analysis of Shear Deformation in Reinforced Concrete Shear-Critical Beams. *Structure and Infrastructure Engineering, Taylor and Francis Group*. doi:10.1080/15732479.2017.1360915

Huber, P., & Kollegger, J. (2014). Numerical Simulation of Shear Behaviour of Reinforced Concrete Beams with and without Flanges. *ResearchGate*. doi:10.1201/b16645-119

Ismail, K. S., Guadagnini, M., & Pilakoutas, K. (2016). Numerical Investigation of the Shear Strength of RC Deep Beams using the Microplane Model. *ASCE: Journal of Structural Engineering*. doi:10.1061/(ASCE)ST.1943-541X.0001552

Kani, G. N. (1967). How Safe are Our Large Reinforced Concrete Beams. *ACI Journal 64(3)*, 128-141.

Khalfallah, S., Charif, A., & Naimi, M. (2004). Nonlinear Analysis of Reinforced Concrete Structures using A New Constitutive Model.

Koekkoek, R. T., & Yang, Y. (2016). *Measurement Report on the Transition between Flexural and Shear Failure of RC Beams without Shear Reinforcement.* Delft: Delft University of Technology.

Malm, R., & Holmgren, J. (2008). Cracking in Deep Beams owing to Shear Loading. Part 2: Non-Linear Analysis. *Magazine of Concrete Research*. doi:10.1680/macr.2008.60.5.381

Pruijssers, A. F. (1988). *Aggregate Interlock and Dowel Action under Monotonic and Cyclic Loading.* Delft: Delft University Press.

Rots, J. G., & Blaauwendraad, J. (1989). Crack Models for Concrete: Discrete or Smeared? Fixed, Multi-Directional or Rotating? *HERON*, 5.

Sarkhosh, R., Uijl, J. A., Braam, C. R., & Walraven, J. C. (2010). *Shear Capacity of Concrete Beams without Shear Reinforcement under Sustained Loads - Literature Survey.* Delft: Stevin Laboratory - Concrete Structures, Delft University of Technology.

Sato, Y., Tadokoro, T., & Ueda, T. (2004). Diagonal Tensile Failure Mechanism of Reinforced Concrete Beams. *Japan Concrete Institute: Journal of Advanced Concrete Technology*.

Shayanfar, M. A., Kheyroddin, A., & Mirza, M. S. (1997). Element Size Effects in Nonlinear Analysis of Reinforced Concrete Members. *Elsevier Science: Computers and Structures*.

Slobbe, A. T., Hendriks, M. A., & Rots, J. G. (2013). Systematic Assessment of Directional Mesh Bias with Periodic Boundary Conditions: Applied to the Crack Band Model. *Elsevier: Engineering Fracture Mechanics*.

Slowik, M., & Smarzewski, P. (2014). Numerical Modelling of Diagonal Cracks in Concrete Beams. *Archives of Civil Engineering*. doi:10.2478/ace-2014-0021

Syroka-Korol, E., & Tejchman, J. (2014). Experimental Investigations of Size Effect in Reinforced Concrete Beams Failing by Shear. *Elsevier: Engineering Structures*.

Tavio. (2008). Element Size Effects in Nonlinear Analysis of Reinforced Concrete Beams without Web Reinforcement. *IPTEK, The Journal for Technology and Science*.

Teshome, T. T. (2019). Model Uncertainty of Non-Linear Finite Element Analysis of Reinforced Concrete Beams without Shear Reinforcement: Examining the Effect of Modelling Strategies and Modes of Failure. *Repository TU Delft: MSc Thesis*.

Tran, N. L. (2020). A Mechanical Model for the Shear Capacity of Slender Reinforced Concrete Members without Shear Reinforcement. *Elsevier: Engineering Structures*.

Vecchio, F. J., & Shim, W. (2004). Experimental and Analytical Reexamination of Classic Concrete Beam Tests. *ASCE: Journal of Structural Engineering*.

Walraven, J. C. (1980). Aggregate Interlock: A Theoretical and Experimental Analysis. *Repository TU Delft: PhD Thesis*.

Yang, Y. (2014). Shear Behaviour of Reinforced Concrete Members without Shear Reinforcement: A New Look at an Old Problem. *Repository TU Delft: PhD Thesis*.

Yang, Y. (2020). *Shear Behaviour of Deep RC Slab Strips (Beams) with Low Reinforcement Ratio.* Delft: Delft University of Technology.

Yang, Y., Boer, A. d., & Uijl, J. d. (2021). Postdiction of the Flexural Shear Capacity of a Deep Beam. *Taylor & Francis*, 208-215.